Universidad de Salamanca

Instituto de Biología Molecular y Celular del Cáncer

Non-muscle Myosin II: New mechanisms of regulation and functional characterization of *MYH9* pathological variants

Tesis doctoral

Clara Llorente González

Salamanca, 2022

Miguel Vicente-Manzanares, Doctor en Ciencias Químicas,

CERTIFICA:

Que Clara Llorente González, graduada en Bioquímica por la Universidad Autónoma de Madrid, ha realizado bajo mi dirección el trabajo de investigación correspondiente a su Tesis Doctoral con el título:

Non-muscle Myosin II: New mechanisms of regulation and functional characterization of *MYH9* pathological variants

Revisado este trabajo, el que suscribe considera el trabajo realizado satisfactorio y autoriza su presentación para ser evaluado por el tribunal correspondiente.

Y para que así conste y a los efectos oportunos, firma el presente certificado en Salamanca a

Firmado digitalmente por VICENTE MANZANARES MIGUEL - 50728204W
Nombre de reconocimiento (DN): c=ES, serialNumber=IDCES-50728204W, givenName=MIGUEL, sn=VICENTE MANZANARES, cn=VICENTE MANZANARES MIGUEL - 50728204W
Fecha: 2022.10.19 08:48:35 +01'00'

Fdo. Dr. Miguel Vicente Manzanares

En recuerdo de mi abuela,
y de su fortaleza

Summary

Generation of mechanical forces is essential for multiple biological processes, e.g tissue formation and homeostasis, cell migration and division, etc. Class II myosins generate most of these forces. Myosin II is expressed in muscle and non-muscle cells as different paralogs. These proteins are endowed with actin-binding and ATPase-mediated contraction activities. Additionally, they organize into polymers (myosin filaments) that exert forces through the concerted movement of actin filaments. There are three paralogs of non-muscle myosin II (NMII), NMII-A, NMII-B and NMII-C. Together with actin filaments, NMII participates in the generation of multiple cellular structures that support mechanical stresses and exert traction forces. These actomyosin structures are involved in the maintenance of cellular integrity during cell migration and division, etc. Since NMII function relies on its assembly into filaments and its binding to actin, these steps are tightly regulated.

This work is divided in two parts. First, we characterize a new mode of regulation through Tyr phosphorylation on the regulatory light chain of NMII. This phosphorylation prevents the formation of a functional NMII units, repressing its assembly into filaments. In the second part, we delineate new aspects of NMII functionality by characterizing several mutations that affect diverse functional domains of the NMII-A paralog. Appearance of these mutations causes a group of disorders collectively named *MYH9*-related diseases (*MYH9*-RD). We showed that the mutations translate into specific alterations of NMII-A stability in filaments and cellular functions that depend on actin, e.g. adhesion dynamics. Additionally, we characterize the morphological and functional alterations of primary leukocytes from a patient with the *MYH9* variant c.3486G>T (R1162S). We found morphological alterations in activated T cells, monocyte-derived dendritic cells and neutrophils. We also found that the inclusion bodies observed in neutrophils, which characterize *MYH9*-RD, are in fact the result of a defective disassembly of NMII-A structures.

Resumen

La generación de fuerzas mecánicas es esencial para múltiples procesos biológicos, e.g. homeostasis y formación de tejidos, migración y división celular, etc. Las miosinas de clase II generan la mayoría de estas fuerzas. La miosina II se expresa en células musculares y no musculares como parálogos diferentes. Estas proteínas están dotadas de sitios de unión a actina y de capacidad contrácil mediada por la hidrólisis de ATP. Además, se organizan en polímeros que ejercen fuerzas a través del movimiento concertado de filamentos de actina. La forma no muscular de miosina II (NMII) aparece como tres parálogos, NMII-A, NMII-B and NMII-C. Junto con los filamentos de actina, NMII participa en la generación de estructuras celulares que soportan tensión y ejercen fuerzas de tracción. Estas estructuras participan en el mantenimiento de la integridad celular, e.g durante la migración celular y la división, etc. Debido a que la función de NMII depende de su ensamblaje en filamentos y su unión a actina, estos procesos están muy regulados.

Este trabajo está dividido en dos partes. En la primera, caracterizamos un nuevo modo de regulación por la fosforilación de tirosina en la cadena ligera reguladora de NMII. Esta fosforilación impide la formación de unidades funcionales de NMII, inhibiendo su ensamblaje en filamentos. En la segunda parte, definimos nuevos aspectos de la función de NMII mediante la caracterización de mutaciones que afectan dominios funcionales del parálogo NMII-A. La aparición de estas mutaciones causa las enfermedades asociadas al gen *MYH9* (*MYH9*-RD). Demostramos que las mutaciones se traducen en alteraciones de la estabilidad de NMII-A en filamentos. Además, caracterizamos las alteraciones morfológicas y funcionales de leucocitos primarios de un paciente con la variante c.3486G>T (R1162S) del gen *MYH9*, observando alteraciones morfológicas en linfocitos T activados, células dendríticas derivadas de monocitos y neutrófilos. También hemos comprobado que los cuerpos de inclusión que se observan en neutrófilos y que caracterizan estas enfermedades, son el resultado de un desensamblaje deficiente de estructuras de NMII-A.

Contents

List of Figures

List of Tables

1 Introduction

1.1 Class II Myosins

Class II myosins belong to the myosin superfamily of actin-based molecular motors. Most members of this superfamily display an actin-binding ATPase motor domain followed by a neck domain, which acts as a lever arm, transforming the conformational changes derived from ATP hydrolysis into movement along actin filaments. The neck domain also contains specific sequences (IQ sequences) that serve as binding sites for regulatory light chains (see next section). The tail domain at the C-terminal end is highly variable in length and sequence, becoming a regulatory hotspot and a crucial domain that determines myosin function among the members of this superfamily (Beach et al., 2017; Krendel and Mooseker, 2005).

Even with a highly conserved motor domain, the actin-dependent ATPase activity, the velocity to slide actin filaments or the processivity (the ability of a myosin to undergo subsequent steps on actin without detaching) vary greatly among myosins, providing a wide range of cellular functions such as cargo transport, strain sensing and tension generation, organelle subcellular positioning, actomyosin-dependent cytoskeletal rearrangements and adhesion among others (Heissler and Sellers, 2016; Mooseker and Foth, 2007).

Class II myosins are also termed "conventional" myosins, as they were the first described members of the myosin superfamily, isolated as a viscous fraction from muscle extracts (Engelhardt and Lyubimova, 1939). Mammalian non muscle myosin II belongs to this class, along with *Acanthamoeba* or *Dictyostelium* myosins, yeast myosins, skeletal or cardiac myosins and vertebrate smooth muscle myosins (Sellers, 2000). Specific molecular features of this myosin class include the presence of an SH3 motif in the motor region (Fujita-Becker et al., 2006) and the ability to bind two

light chains per heavy chain through IQ-motifs (Mitchell et al., 1989). However, the most relevant feature of this family is its ability to form supramolecular structures by multimerization.

Class II myosins display a long α-helical rod-like tail domain that enables dimerization in an anti-parallel fashion, and further organization into larger-order bundles. Owing to this bipolar arrangement, myosin can bind actin filaments at both ends, and the conformational movement upon ATP hydrolysis translates into actin filament sliding, shortening or contraction and the generation of mechanical force. This mechanism enables muscle contraction and actomyosin-based cytoskeletal reorganization in response to different cellular stimuli (Landsverk and Epstein, 2005). While muscle myosin is activated by calcium binding to its light chain, vertebrate smooth muscle and non-muscle class II myosins are activated by phosphorylation of the regulatory light chain (Conti and Adelstein, 2008; Cremo and Hartshorne, 2007; Gordon et al., 2000).

1.2 Non muscle myosin II structure

The functional unit of non-muscle myosin II is a hexamer composed of two heavy chains (MHCII) intertwined with each other through a long coiled-coil region, two essential light chains (ELC, encoded by the *MYL6* gene) and two regulatory light chains (RLC, encoded by the *MYL12A/B* genes), depicted in **Figure 1**. There are several variants of MHCII encoded in different genes. These are: MHCII-A (encoded by gene *MYH9*), MHCII-B (encoded by gene *MYH10*) and MHCII-C (encoded by gene *MYH14*). The organization of the *MYH9*, *MYH10*, *MYH14* genes is virtually identical, indicating that the three genes evolved from ancestral duplication (Berg et al., 2001; Sellers, 2000). For nomenclature purposes throughout the present work, we refer to the protein products of the *MYH9/10/14* genes (i.e., MHCII-A, II-B, II-C) as isoforms. We refer to the fully formed hexamers (NMII-A, NMII-B, NMII-C), including their light chains (ELC and RLC are common to all the isoforms) as paralogs.

The motor (head) domain of MHCII contains the actin-binding and Mg^{2+}/actin-dependent ATPase activity. The neck domain acts as a movable hinge that enables the conformational changes supporting myosin head swinging. It also has binding domains (IQ-motifs) for the four light chains, two sites on each heavy chain. The

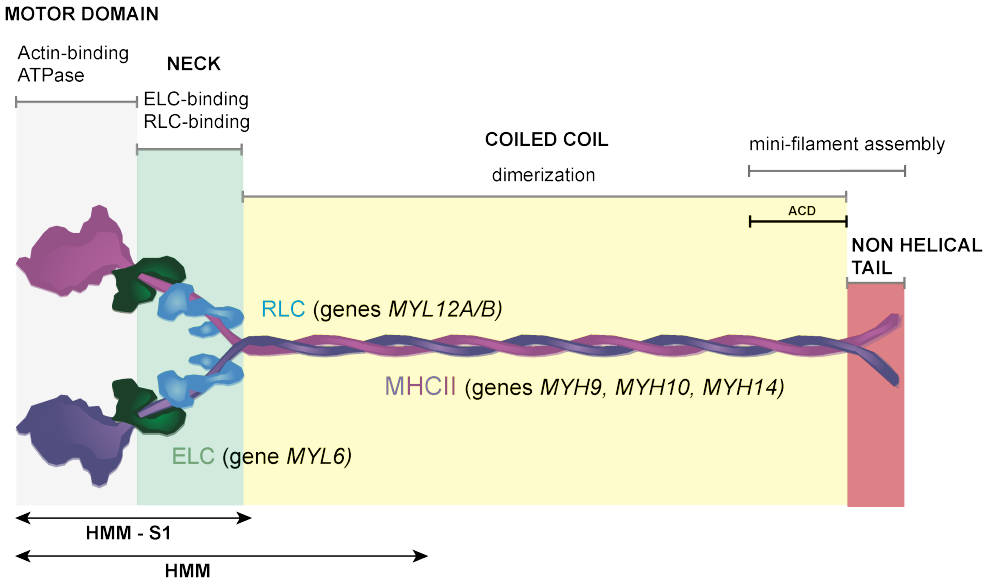

Figure 1: Schematic representation of NMII functional unit. The NMII hexamer is composed by two heavy chains intertwined through their coiled-coil region (pink and purple, the two different colors are used to enhance visualization, but they do not represent molecular differences), and four light chains, two essential (ELC, dark green) and two regulatory (blue). The functional domains of MHCII are depicted in bold. The motor domain contains the ATP catalytic and actin binding sites. The neck contains two IQ-motifs per heavy chain, IQ1 and IQ2, which act as docking sequences for ELC and RLC, respectively. The bulk of the coiled-coil domain contains sequence stretches displaying net negative and positive charge in an alternate manner that enable heavy chain dimerization. The end of the coiled-coil region is the ACD, which controls mini-filament oligomerization and stability. Heavy meromyosin (HMM) is a two-headed myosin fragment, and HMM-S1 is a single-headed myosin subfragment-1, both used in kinetic studies. Figure modified from (Asensio-Juárez et al., 2020).

ELC binds to an IQ motif closer to the N-terminus while the RLC binds to an adjacent IQ-like motif next to it, but closer to the coiled coil. Both light chains serve a structural purpose, although RLC also modulates the ATPase function of the heavy chain. The tail domain is most divergent between paralogs and contains a long coiled-coil region responsible for MHCII dimerization into a rod-like structure that supports the formation of the NMII hexamer. This region displays patterns of alternating charge (Atkinson and Stewart, 1992; McLachlan and Karn, 1983; Ricketson et al., 2010) that sustain hexamer parallel and antiparallel interactions with other NMII units, thereby enabling NMII assembly into higher order filaments. The tail region ends in a non-helical tailpiece (NHT), which is highly divergent among isoforms and regulates filament formation through protein–protein interactions and/or phosphorylation (Even-Faitelson and Ravid, 2006; Juanes-Garcia et al., 2015).

The folding of this complex structure requires the presence of chaperones. This

has been well-characterized in muscle myosins, which undergo constant turnover due to the disruption of and damage to myosin contractile units ("sarcomeres") caused by continuous strain. Myosin II folding seems a very complex and cell type-dependent process; just the motor domain of muscle myosin II undergoes a multistep folding process that transits through multiple transitional states and only reach completion in muscle cells (Chow et al., 2002).

Folding of both invertebrate and vertebrate muscle myosin II molecules is catalyzed by chaperones, specifically ubiquitous heat-shock proteins 90 (Hsp90) and 70 (Hsp70) supported by members of the UNC-45 family. UNC-45 consists of an N-terminal tetratricopeptide repeat (TPR) domain that enables its binding to Hsp90 and Hsp70 (Barral et al., 2002), a central domain and neck domain, followed by a conserved C-terminal UCS domain that interacts with the motor domain of myosin II (Barral et al., 2002; Gazda et al., 2013; Price et al., 2002). Non-vertebrates have a single UNC-45 protein, whereas vertebrates express two UNC-45 isoforms: muscle-specific UNC-45b and a non-muscle isoform, UNC-45a (Anderson et al., 2008; Price et al., 2002). UNC-45b colocalizes with myosin II in myofibrils and is required for their proper assembly in *Xenopus*, zebrafish, and mouse cardiac and/or skeletal muscles (Chen et al., 2012; Etard et al., 2008; Geach and Zimmerman, 2010; Srikakulam et al., 2008; Wohlgemuth et al., 2007). UNC-45a was recently described to participate in the initial steps of folding and stress fiber assembly of non-muscle myosin II-A (Lehtimaki et al., 2017b).

Together, the motor kinetics and assembly properties of NMII tail jointly determine the specific function and working capacity of NMII. NMII paralogs display 60-80% of amino acid sequence identity and a high level of structural conservation that accounts for some overlapping cellular functions (Wang et al., 2011), however, there are differences in the motor activity and assembly behavior among NMII paralogs that will provide actomyosin structures with some non-redundant properties.

This was initially illustrated by the effects of abrogation of the different NMII paralogs in mouse models. MHCII-A abrogation is lethal by embryonic day (E)6.5, with a defect in cell adhesion and a failure to organize a polarized functional visceral endoderm, which indicates that one of the functions of this paralog is the maintenance of epithelial monolayer integrity (Conti et al., 2004). Systemic MHCII-B deletion causes cardiac and brain defects. While most embryos died around E14.5, some

animals are born; but those die perinatally (Tullio et al., 1997, 2001). The brain defects are caused by defective adhesion and migration and include hydrocephalus and altered final destination of the migration of various neuronal cell progenitors. Mice lacking MHCII-C do not display any apparent phenotype unless the dose of MHCII-B is also reduced (Ma et al., 2010), suggesting that the function of NMII-B can compensate for the loss of NMII-C.

1.3 The motor domain: mechanism of filament sliding and force generation

NMII-based actin filament sliding can be described in terms of the swinging cross-bridge model (Spudich, 2001). This model is shown in **Figure 2**. Briefly, ATP-bound NMII is free, that is, not associated with the actin filament. When ATP is hydrolyzed by the Mg^{2+}/actin-dependent ATPase activity of the head domain, NMII increases its affinity for the actin filament. The release of the resulting phosphate triggers a conformational movement that, while bound to actin, causes the sliding of the actin filament with respect to the NMII (10 nm/step on average). The exchange of ADP for ATP restarts the cycle.

NMII organization into ensembles (filaments) allows the association to actin filaments over multiple ATPase cycles and the generation of mechanical work, defined as the amount of energy transferred by the mechanical force induced by the conformational change of the myosin head into the filament along its displacement. However, the extent and type of mechanical work is determined, in part, by the paralog-specific composition of these actomyosin structures. Although all NMII paralogs undergo the cycle described above, their kinetics differ due to differences in the amino acid composition of the motor domain.

NMII-A has the highest ATPase rate of the three non-muscle paralogs. The duty ratio, defined as the time of the cycle a given myosin head spends bound to actin, is the lowest (5-20%) for NMII-A, and similar to muscle myosins. Conversely, NMII-B has a much higher duty ratio (20-40%) and the duty ratio of NMII-C is intermediate between NMII-A and NMII-B, and splicing-dependent (Heissler and Manstein, 2011). The duty ratio of the NMII isoforms is load-dependent, which

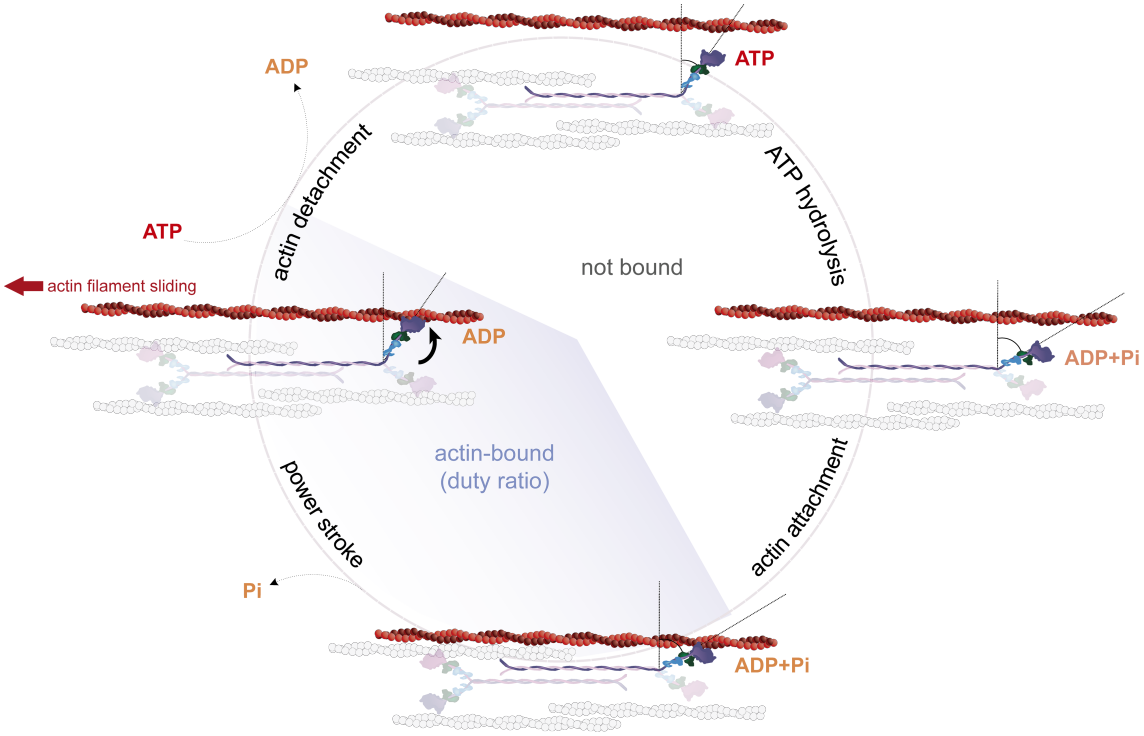

Figure 2: The swinging cross-bridge model. Image depicts the cycle of NMII interaction with ATP and actin filaments. For the sake of simplicity, only one heavy chain is highlighted (purple), although the concerted action of several heads from multiple NMIIs molecules takes place (light colors). The NMII-ATP complex has low affinity for actin filaments. ATP hydrolysis allows heavy chain binding to the actin filament. Subsequent phosphate release (Pi) produces the conformational change (dark arrow) of the head (shown by the angle change with respect to the actin filaments) that generates actin filament sliding. The image also includes the exchange of ADP for ATP that restarts the cycle. Note that this cycle is represented as four symmetric stages, although the actual amount of time the NMII spends in one or another conformation is paralog-dependent (see text for details).

means that forces against the power stroke can slow ADP release down, therefore increasing the duration of the myosin-actin interaction. This catch-bond behavior is particularly characteristic of NMII-B (Kovacs et al., 2007).

Overall, the motor kinetic differences described above make NMII-A the fastest paralog in terms of cycle completion and thus filament displacement. By the time NMII-B completes one cycle, NMII-A would have cycled several times. This suggests that NMII-A is more adequate for overall force generation. On the other hand, the fact that NMII-B spends more time strongly attached to actin filaments (due to its slower ADP release rate) coupled to its increased catch-bond behavior makes this paralog better suited for force, strain, and structure buildup in non-muscle cells (Schiffhauer et al., 2016, 2019).

1.4 Fine-tune regulation of NMII assembly cycle

Myosin II function is very tightly regulated due to its critical importance as the major generator of mechanical forces inside cells. Regulation takes place across multiple levels, including changes to the conformation; control of the ATPase activity and/or actin binding; formation of bipolar filaments; and growth, stability, and disassembly of larger order mini filaments.

1.4.1 Regulation of NMII Conformation and its ATPase Activity: RLC phosphorylation and the conformational switch

Within cells, NMII undergoes constant polymerization and depolymerization. NMII can be found either in a folded, autoinhibited conformation (10S) or an extended, assembly-competent form (6S), originally distinguished by their different sedimentation coefficient in ultracentrifugation experiments (Craig et al., 1983).

The ability to fold into an autoinhibited, compact, conformation (10S) is a regulatory step that controls NMII activity by defining the amount of active NMII that can exert force. This mechanism is conserved in all conventional myosins, having also been described for smooth, cardiac, and skeletal muscle myosins (Jung et al., 2008; Wendt et al., 1999). In this conformation, both heads establish asymmetric interactions with each other, blocking the heads' actin and nucleotide binding site (**Figure 3a**). The tail folds at two hinge regions, so that the second hinge binds RLCs at the neck, stabilizing the compact conformation and preventing filament assembly (Burgess et al., 2007; Jung et al., 2011; Salzameda et al., 2006). Deletion studies have shown that this interaction prevents spontaneous filament assembly, since the removal of either RLC binding site (Breckenridge et al., 2009) or RLC-interacting hinge region (Kiboku et al., 2013) causes NMII over-assembly.

Phosphorylation of RLC on Serine 19 (S19) by NMII activation signals disrupts the compact conformation (Suzuki et al., 1985) and boosts NMII ATPase activity and the conformational extension ("opening") of the molecule (6S conformation), which becomes assembly competent and thus able to incorporate into filaments (**Figure 3b**) (Adelstein and Conti, 1975; Craig et al., 1983; Trybus and Lowey, 1984).

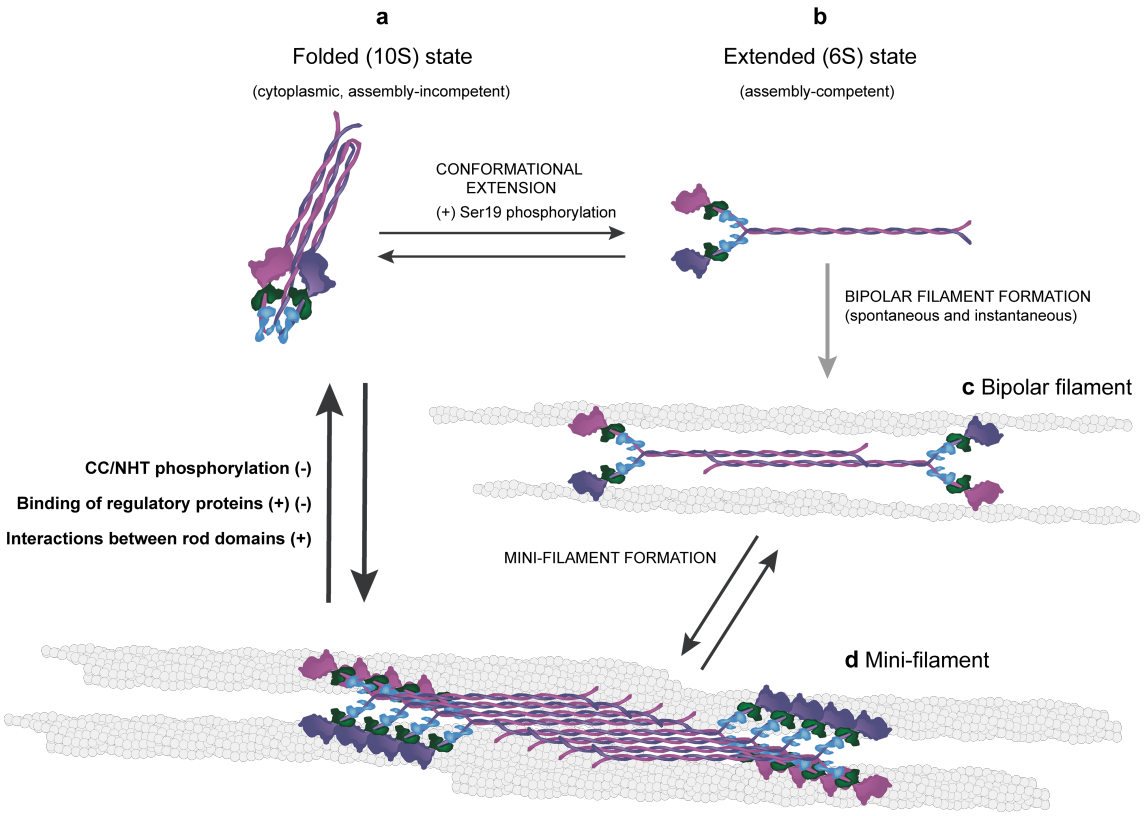

Figure 3: Scheme of NMII assembly/disassembly cycle. The figure depicts the main conformational states of NMII, regardless of the paralog. **(a)** The folded (10S) state. NMII is autoinhibited by head-head and head-tail interactions. This conformation enables cytoplasmic transport of NMII by diffusion-dependent mechanisms. **(b)** The extended (6S) state is triggered by S19 phosphorylation of RLC, which disrupts the intramolecular interactions of the folded state. This assembly-competent conformation is unstable by itself, and rapidly dimerizes into **(c)** bipolar filaments, or reverts to the 10S conformation. **(d)** NMII mini-filaments, that contain between 6-30 NMII monomers. Phosphorylation of the coiled-coil (CC) and/or the non-helical tail (NHT) in general, cause filaments instability and promote NMII disassembly. Figure modified from (Garrido-Casado et al., 2021)

There is evidence that both RLC chains have to be phosphorylated to disrupt RLC-tail interactions (Salzameda et al., 2006) and extend the molecule (Jung et al., 2008; Yang et al., 2019). Different kinases may phosphorylate RLC on S19 (reviewed in (Garrido-Casado et al., 2021)), most notably myosin light chain kinase (MLCK) (Ikebe and Hartshorne, 1985a) and Rho-associated kinase (ROCK) (Amano et al., 1996). Although ROCK can phosphorylate RLC on S19 directly (Amano et al., 1996), it mainly acts through the phosphorylation and inactivation of MYPT1, the catalytic subunit of a RLC phosphatase (Kimura et al., 1996). Additional phosphorylation of Thr18 contributes to extension of the hexamer (Ikebe et al., 1988), increases myosin II actin-dependent ATPase activity (Ikebe et al., 1986) and favors

the stabilization of NMII filaments, which controls cell polarity and adhesion dynamics (Vicente-Manzanares and Horwitz, 2010; Vicente-Manzanares et al., 2008). The resulting 6S extended conformation is unstable by itself (**Figure 3c**), thus it rapidly dimerizes into antiparallel bipolar structures that can eventually grow into higher order filaments (**Figure 3d**), containing 20–30 hexamers and with a filament length of approximately 300 nm (Craig and Woodhead, 2006; Dasbiswas et al., 2018).

The interconversion between these two conformations ($10S \leftrightarrow 6S$) regulates NMII filament distribution *in vivo* (Breckenridge et al., 2009; Kiboku et al., 2013). The compact 10S conformation likely enables the long range diffusion of myosin, which can be incorporated into other subcellular compartments if/when needed (Breckenridge et al., 2009). In that sense, *in vitro* experiments have also shown that myosin monomers can form folded antiparallel oligomers of two or more molecules before extending into an assembly-competent form (Liu et al., 2017). These data suggest that, in a cellular context, this mechanism could not only apply to monomers, but also to myosin oligomers. These complexes could switch back and forth between a diffusible, assembly-incompetent form and an assembly-competent form that could be rapidly recycled and assembled upon RLC phosphorylation.

Other post-translational modifications of RLC also regulate NMII ability to form filaments. Phosphorylation of S1 and S2 by PKC inhibits the function of NMII by decreasing the binding of NMII to actin filaments (Komatsu and Ikebe, 2007; Nishikawa et al., 1984). In platelets, this phosphorylation is necessary for NMII-A disassembly and reorganization in response to platelet-derived growth factor (Komatsu and Ikebe, 2007). In mesenchymal cells, this mechanism prevents actomyosin assembly at the leading edge during chemotaxis (Asokan et al., 2014). In addition, Tyrosine (Y) phosphorylation of the RLC on residues Y142 and Y155 in response to EGF was described by Krebs and coworkers over 30 years ago (Gallis et al., 1983), but its function in live cells has remained unexplored. While RLC phosphorylation controls NMII availability and readiness to assemble by supporting the conformational switch, it is the tail domain that primarily mediate the assembly-disassembly of myosin filaments and their subcellular localization (Vicente-Manzanares et al., 2008).

1.4.2 Regulation of Bipolar Filament Formation and Higher Order Mini-Filament Assembly and Disassembly: the tail domain

NMII dimerization and bundling into higher order mini filaments occurs through electrostatic interactions between alternatively charged (negative and positive) regions along the tail of the hexamer. Specifically, there is a critical and highly conserved positively charged region, the "assembly critical domain" (ACD) at the end of the coiled coil domain. The ACD can interact with negatively charged regions distributed along the tail in other NMII molecules (Cohen and Parry, 1998; Dulyaninova and Bresnick, 2013). Experimental data as well as modeling support the notion that NMII establishes electrostatic interactions to form parallel and anti-parallel arrays with well-defined periodicity. This is due to the amino acid sequence of specific regions within the coiled coil domain of NMII (Kaufmann and Schwarz, 2020; Nakasawa et al., 2005; Ricketson et al., 2010). The current thinking is that, upon RLC phosphorylation, the NMII hexamer adopts a 6S conformation, which is highly unstable. Thus, it either increases its stability by forming electrostatic bonds with similarly open 6S forms, or it rapidly folds back into the more stable 10S form.

Classical immunofluorescence examination of NMII isoforms across cells and tissues has contributed to the notion that filaments are relatively stable. However, quantitative microscopy approaches such as fluorescence recovery after photo bleaching have shown that filaments rapidly exchange NMII hexamers, that is, hexamers from the filaments are replaced by hexamers that are in non-filamentous form in the cytoplasm (Vicente-Manzanares et al., 2007), which must rapidly undergo the $10S \rightarrow 6S$ conversion.

Filaments also undergo RLC exchange. Exchanged RLC may be part of NMII hexamer turnover, or it may be released from the NMII hexamer and replaced with free, cytoplasmic RLC. Although direct evidence is lacking, RLC is likely to exist unassociated to NMII, either free or bound to proteins other than NMII. This is supported by the fact that RLC has additional binding partners, e.g., Myo18, calponin or NMDA receptors (Bajaj et al., 2009; Guzik-Lendrum et al., 2013; Szymanski and Goyal, 1999). Other, more indirect, proof also supports the existence of free RLC. For instance, MHCII binds acidic liposomes through its RLC binding site, promoting

the dissociation of the RLC (Liu et al., 2016), which likely becomes free. Thus, it is likely that photobleaching of RLC in filaments probably measures both components (NMII exchange in and out of filaments; and RLC in and out of NMII hexamers), particularly since the fractional recovery of fluorescent RLC (>80%) is higher than those of any of the MHCII isoforms (∼55% for MHCII-A; ∼ 30% for MHCII-B and MHCII-C) (Vicente-Manzanares et al., 2007; Zhang et al., 2018).

The coiled coil domain that enables dimerization is followed by a non-helical domain that constitutes the tailpiece of the hexamer. Sequence alignment reveals that this is the most diverse region among NMII and SMM heavy chains. Homology in this region is almost non-existent, whereas it is up to 90% in the motor and coiled coil domains. Additionally, electrostatic studies indicate that the tailpiece does not dimerize, but likely remains untethered from the main NMII structure (Kaufmann and Schwarz, 2020). Importantly, the end of the coiled coil and the non-helical tailpiece account for paralog-specific regulation, which will define the paralogs' differences in filament dynamics in cells, as well as their distinct intracellular localization.

Phosphorylation and/or binding to regulatory proteins affect the establishment and/or maintenance of the aforementioned electrostatic interactions between the ACD domains. When these events occur in hexamers within filaments, they promote their instability, triggering filament disassembly and thus contributing to cytoskeletal reorganization and plasticity (**Figure 3**). Several kinases phosphorylate NMII-A (and II-B and II-C) on the last portion of the coiled coil domain and/or the non-helical tailpieces. These kinases include protein kinase C (PKC), transient receptor potential melastatin 7 (TRPM7) and casein kinase II (CKII) (Clark et al., 2008; Dulyaninova and Bresnick, 2013; Even-Faitelson and Ravid, 2006).

Due to the large divergence between isoforms in these regions, different residues have specific functions. Here, for the purpose and focus of this thesis, we only discuss NMII-A, not NMII-B or II-C. S1917 of MHCII-A lies close to the ACD of NMII-A. Its phosphorylation by PKC controls the role of NMII-A in mastocyte degranulation (Ludowyke et al., 2006). S1943, located in the NHT domain, is phosphorylated by CK-II. S1943 phosphorylation dictates the level of NMII-A incorporated into filaments and the organization of NMII-A assemblies (Dulyaninova et al., 2007, 2005). In mesenchymal stem cells, S1943 acts as a mechanosensor, becoming non-phosphorylated when cells are plated on stiffer substrates. This increases NMII-A

assembly and enables NMII-B-dependent migratory polarization (Raab et al., 2012). Several other proteins have been reported to bind and regulate NMII-A filament assembly, including, lethal giant larvae, myosin binding protein H and LIMCH1 and Myo18. There are excellent reviews on this matter (Dulyaninova and Bresnick, 2013; Pecci et al., 2018).

1.5 The organization of actomyosin structures

Actomyosin structures are continuously under intense reorganization, allowing cells to adapt and react to different stimuli. The mechanical properties of actomyosin arrays are defined by the geometry of actin filaments and by the relative composition of actin binding proteins to meet the needs of specific cellular functions or cell types. There are various types of myosin-containing cellular structures. We will focus on two of them: the actomyosin meshwork that makes up the cytoskeletal component of the cell cortex and the stress fibers observed in migrating mesenchymal cells. Both structures participate in the maintenance of mechanical integrity and coordinated movement of the cell.

1.5.1 The cell cortex

The cortex is a thin, crosslinked actomyosin network immediately beneath the plasma membrane. A mix of bundled straight and branched filaments of variable mesh size defines its structure, which may display subtle differences depending on the cell type (Morone et al., 2006). Myosin motors localized at the cortex exert contractile forces in the meshwork, playing a central role in the control of cell shape.

The cellular cortex originates from *de novo* nucleation of Arp2/3-dependent branched actin networks and linear filaments polymerized by formins, e.g. mDia1 (Bovellan et al., 2014). It also features many actin-binding proteins involved in filament bundling and crosslinking (α-actinin, filamin, fimbrin) as well as contractility (myosin, tropomyosin, tropomodulin) and connection to plasma membrane receptors (for example, members of the ezrin–radixin–moesin [ERM] family, filamin) (Biro et al., 2013).

The components of cell cortex are characterized by fast turnover: actin filaments turn over within a minute, while the dynamics of actin crosslinkers and myosin II are usually 5-10 times faster than actin turnover. This ability to undergo remodeling

within seconds makes the cortex simultaneously rigid and highly plastic, which seems essential to its function (Salbreux et al., 2012).

1.5.2 Stress fibers in cell migration

At the leading edge of migrating cells, protrusion results from the balance of Arp2/3-driven actin polymerization opposed by the retrograde flow of actin caused by protrusion itself (Ponti et al., 2004; Gardel et al., 2008). NMII assembly often starts at these protrusive cell edges (Choi et al., 2008) where it binds to branched actin networks (**Figure 4A-B**). Recently assembled NMII mini-filaments are highly dynamic, displaying multiple splitting and fusion events. As NMII filaments move inwards coupled to the actin retrograde flow, splitting events give rise to new nucleation points and the subsequent incorporation of NMII molecules (Beach et al., 2017; Fenix et al., 2016).

Filament fusion and concatenation coupled to NMII contractile activity enables the restructuration of the actin network into aligned actomyosin bundles of mixed polarity such as transverse arcs (Burnette et al., 2011; Hotulainen and Lappalainen, 2006; Spira et al., 2017; Tojkander et al., 2015) and ventral stress fibers (**Figure 4A-B**). These contractile arrays differ in the degree of actomyosin bundling and their ability to interact with focal adhesions. Transverse arcs are curved actomyosin bundles that move inwards parallel to the leading edge and coupled to the retrograde flow. They are linked to focal adhesions through dorsal stress fibers. Dorsal stress fibers are derived from formin-driven actin structures and are devoid of NMII, thus they are not contractile. However, they interact with focal adhesions and allow the transmission of myosin-dependent forces from transverse arcs. Ventral stress fibers result from the fusion of transverse arcs and dorsal stress fibers and localize parallel to the direction of migration (Lehtimaki et al., 2017a). Other stress fibers seem to evolve from myosin-driven reorganization of the actin cortex, preferentially underneath the nucleus (Lehtimäki et al., 2021).

1.5.3 The mechanical properties of actomyosin arrays

The mechanical properties of the different actomyosin arrays vary greatly. The scale of contractile power depends on several factors, including the geometry of the actin filaments, the nature of the cross-linking proteins within the structure as well

as their relative abundance, particularly regarding NMII (Blanchoin et al., 2014; Koenderink and Paluch, 2018). For example, actin crosslinkers such as fimbrin and α-actinin organize actin filaments in a parallel and antiparallel manner, therefore promoting myosin assembly and a more contractile behavior (Laporte et al., 2012).

The geometry of the actin filaments provides selective regulation and behavior upon myosin II-dependent contraction. The rate of contraction is slower for branched actin networks than for antiparallel filaments, and both are sensitive to myosin-dependent contraction and subsequent reorganization or disassembly; while parallel actin filaments are not (Reymann et al., 2012).

The degree of actin crosslinking also defines the mechanical output of myosin II-dependent contraction. In actomyosin networks, a low concentration of crosslinkers does not provide sufficient contact points to transmit myosin II-driven forces, whereas a high density of actin crosslinkers increases the rigidity component, which limits the scale of contraction (Ennomani et al., 2016; Reymann et al., 2012). Besides actin networks, the same limitations have been observed in actomyosin bundles enriched in α-actinin (Hu et al., 2019).

In addition to changes in protein abundance, connectivity can also be modulated through changes in crosslinking activity or turnover rates. Actomyosin networks undergo continuous component exchange to sustain a dynamic, contractile steady state (Kelkar et al., 2020; Koenderink and Paluch, 2018; Salbreux et al., 2012). Turnover rates range from seconds for crosslinkers (Mukhina et al., 2007; Reichl et al., 2008) to tens of seconds for actin filaments and myosin (Fritzsche et al., 2013; Guha et al., 2005; Khalilgharibi et al., 2019). On the contrary, myosin turnover in actomyosin bundles lies in the order of hundreds of seconds to tens of minutes (Horvath et al., 2020; Shutova et al., 2017; Vicente-Manzanares et al., 2008). *In vitro* experiments and *in silico* models show that removal of any network component, or altering turnover, translates into the collapse of the network under myosin-driven contraction (Ennomani et al., 2016; Hiraiwa and Salbreux, 2016; McFadden et al., 2017).

Actin filament turnover is driven either by ADF/cofilin or myosin II-dependent contraction. Cofilin induces actin turnover by severing actin filaments and creating branching points. On the other hand, stresses driven by NMII contraction in the absence of continuous polymerization of actin structures lead to the remodeling of actin arrays or the collapse of actin structures, and therefore to active stress decay

(McFadden et al., 2017), which correlates well with observation of the leading edge of migrating cells, which collapses under myosin II-driven tension when polymerization decreases or stops (Choi et al., 2008).

Crosslinking proteins that counteract filament rearrangements could mitigate this process but, in some cases, their behavior is also modified by mechanical tension. The turnover of actin crosslinkers can be modified under strain, locally adapting the composition of these networks in response to mechanical cues. For example, fascin decreases the lifetime of its bond to actin under load (Alvarado et al., 2013), which excludes this crosslinker from regions of high stress. Conversely, α-actinin 4 or filamin become enriched in high stress regions due to their catch-bond behavior under strain (Schiffhauer et al., 2016). The same catch-bond behavior is observed for the NMII-B paralog (Nagy et al., 2013; Rosenfeld et al., 2003).

Actomyosin networks maintain mechanical homeostasis throughout the cell cortex, providing resistance against rupture upon biological phenomena that locally strain the plasma membrane, e.g. cell migration, or division. In this manner, actomyosin networks support and transmit large scale contractile forces during these phenomena, e.g. cell body translocation in migrating cells (Svitkina et al., 1997); apical constriction of epithelial cells (Seri et al., 2003); or cytokinesis (Spira et al., 2017). On the other hand, transverse arcs and ventral stress fibers exert modest mechanical forces, but absorb and dissipate tension to a greater extent than actin-NMII networks due to their increased organization and alignment to coordinate and transmit physical cues. These structures are better suited to respond to mechanical stimuli originating in the cellular environment and to remodel the surrounding tissue (Hinz et al., 2001; Pellegrin and Mellor, 2007), participating in cellular processes such as adhesion-dependent migration, the maintenance of endothelial barrier integrity, or myofibril assembly (Burridge and Wittchen, 2013; Sanger et al., 2005; Tojkander et al., 2012; Wong et al., 1983).

In the next section we review how NMII paralogs influence the mechanical properties of the best-characterized actomyosin arrays: actomyosin networks and stress fibers.

1.5.4 NMII paralogs contribute to the mechanical properties of actomyosin arrays

Apart from its role in generating forces and mechanical tension, NMII-mediated contractility participates in the active turnover of actin structures, mainly through the mechanical breakdown of actin filaments under tension, generating new assembly points (Haviv et al., 2008; Murrell and Gardel, 2012; Reymann et al., 2012; Vogel et al., 2013; Wilson et al., 2010).

Additionally, there are differences in the dynamic behavior of NMII paralogs that specify their functions in actomyosin arrays. These differences rely mostly on variations on the disassembly rates from filaments, since activation signals that determine NMII assembly readiness are similar among paralogs and depend on RLC phosphorylation and monomer interactions through the ACD domains, which are highly conserved.

The regulatory factors that control NMII disassembly act, mainly, through the end of the coiled coil domain, a more versatile region that endow each paralog with specific dynamic behaviors. NMII-A displays higher disassembly rates than NMII-B and NMII-C (Sandquist and Means, 2008; Vicente-Manzanares et al., 2008). In addition to its higher catalytic activity and faster *in vitro* actin filament sliding (Heissler and Manstein, 2011; Kelley et al., 1996), faster disassembly enables NMII-A to generate highly contractile structures. Conversely, NMII-B mainly plays scaffold roles, as determined by its higher duty ratio and slower exchange in filaments, which makes it more adequate to bear tension rather than to produce force.

The different dynamic behavior of the NMII paralogs affect their specific subcellular localization and function. This has been extensively studied in transversal and ventral stress fibers in mesenchymal migration (Kolega, 2003; Maupin et al., 1994; Shutova et al., 2017; Vicente-Manzanares et al., 2008, 2007). In the context of cortical actomyosin networks, some work has been done towards deciphering their role during cytokinesis and the maintenance of cortical stability (Ma et al., 2020; Taneja et al., 2020; Taneja and Burnette, 2019). We have selected two examples to illustrate how the dynamic properties of these paralogs determine the subcellular localization and the mechanical properties of the arrays in which they are.

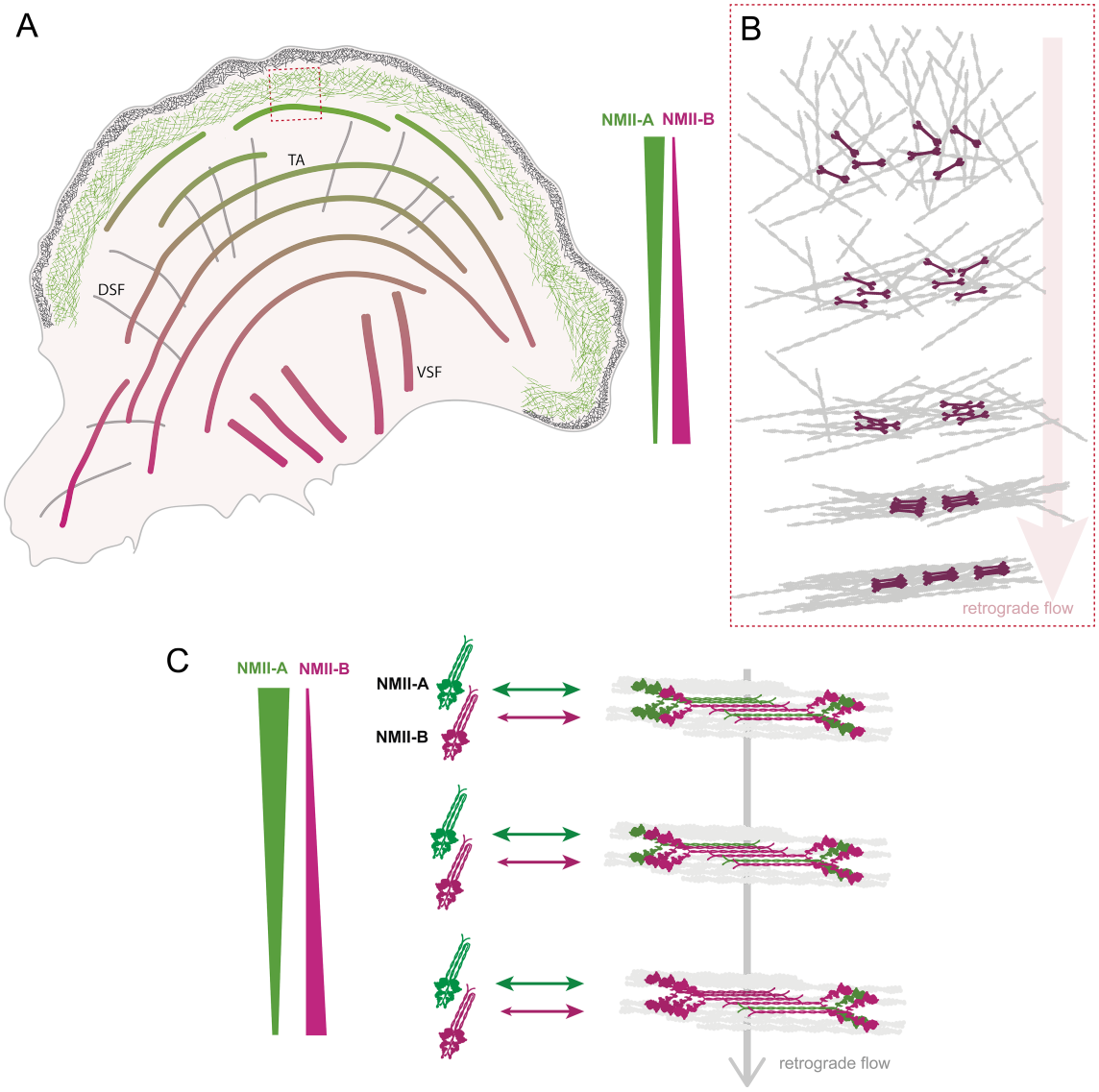

Figure 4: Scheme of the spatiotemporal evolution of cellular actomyosin arrays. **(A)** Schematic representation of actomyosin arrays in a polarized cell on a flat surface. Transverse arcs (TA) and ventral stress fibers (VSF) are color-coded in relation to their relative composition regarding NMII-A and NMII-B paralogs. Dorsal stress fibers (DSF), which do not have NMII and are therefore non-contractile, are depicted in light grey. **(B)** Details of the molecular events that lead to the initial bundling of actomyosin structures. Newly assembled myosin filaments bind to randomly oriented actin filaments producing an actomyosin contractile network at the leading edge. Subsequent cycles of NMII contraction promote sliding and the coalignment of actin and NMII filaments, yielding incipient bundles. Progressive bundling and NMII staggering lead to the development of small, sarcomere-like structures. Forces in the axis of the filament length lead to the fusion of NMII stacks to older bundles. **(C)** Mechanism of paralog sorting. NMII-A and NMII-B can co-assemble in the nascent structures at the leading edge. However, the faster turnover rate of NMII-A (that is, its return to the 10S conformation) allows its recycling into newly assembled structures in anterior regions, while the more stable behavior of NMII-B leads to its gradual accumulation in older filaments, localized in more central regions or at the back of the cell because of the retrograde flow of actomyosin structures.

NMII paralogs in stress fibers

In the context of a migrating cell as depicted in **Figure 4**, NMII-A and NMII-B can co-assemble close to the leading edge (Beach et al., 2017). However, NMII-A displays a faster turnover rate (**Figure 4C**, green arrows) (Vicente-Manzanares et al., 2007). This feature allows NMII-A to be easily redirected to newly assembled NMII filaments at the front, while NMII-B, due to its increased duty ratio and stability in filaments (Vicente-Manzanares et al., 2008), remains bound to stress fibers that continue to fuse and mature inwards coupled to actin retrograde flow. Consequently, NMII-A is enriched in more dynamic actomyosin structures appearing at the leading edge, such as branched actin networks as they evolve towards transverse arcs, while NMII-B becomes enriched in older, more central and mature ventral stress fibers (**Figure 4B**) (Shutova et al., 2017; Shutova and Svitkina, 2018).

The sorting of the different paralogs along these actomyosin arrays (actin networks and fibers) creates a polarized cytoskeleton that enables different cellular functions: Transverse arcs, enriched in NMII-A, display high contractile activity which is needed to support lamellipodial (Burnette et al., 2011) and adhesion (Cai et al., 2006; Vicente-Manzanares et al., 2007) growth. On the other hand, the high abundance of NMII-B in ventral stress fibers endows these structures with high stability, which can be further increased upon load (Nagy et al., 2013; Rosenfeld et al., 2003). These characteristics make these structures better suited for cellular processes such as polarity maintenance (Lo et al., 2004; Vicente-Manzanares et al., 2008), morphogenesis, mechanosensing and nuclear translocation in 3D environments (Thomas et al., 2015).

NMII paralogs in actomyosin networks

To illustrate the specific contribution of NMII paralogs to cortical actomyosin networks, we focus on NMII function during cytokinesis (Mabuchi and Okuno, 1977). Initially, NMII local activation at the equatorial plane of a dividing cell drives contraction and coalescence of cortical actin networks into more organized actin arrays, which contain aligned actin bundles and NMII distributed into stacks. NMII-dependent alignment of these structures allows the application of higher forces, ingression of the cleavage furrow and efficient scission of the two nascent cells.

During this process, cells suffer a drastic increase in intracellular pressure, often

alleviated by blebbing events. NMII contributes to stabilize the tension in the cortical actomyosin network and to control the frequency and size of blebbing events that otherwise will hamper cytokinesis by creating spindle oscillation and cytokinetic instability. Knock-down experiments have revealed different contributions of the NMII paralogs to this process. Depletion of NMII-A induced slower ingression rates and a lack of blebbing events, which suggest a reduction of intracellular pressure. NMII-B stacks also appeared disorganized at the contractile ring. NMII-B depletion, however, increased overall cortical tension due to uncontrolled NMII-A-driven contraction, generating cortical instability, an increase in bleb frequency and a failure to end abscission due to spindle oscillation (Taneja et al., 2020).

This result and others (Ma et al., 2020; Weissenbruch et al., 2022, 2021; Yamamoto et al., 2019) highlight the fact that generation of cortical tension is the major function of NMII-A; while NMII-B seems to regulate the actomyosin networks (and fibers) by stabilizing NMII-A induced tension. However, NMII-B is also recruited to sites of elevated cortical tension (Schiffhauer et al., 2019), indicating that, whereas its role in cortical force generation is more limited, it is also highly mechanosensitive and responds to external force by locally creating structures that grow upon tension buildup. This is also illustrated by the unique phenotype of the *MYH10*-depleted mouse model, which exhibits structural failure at points of high force application and tension buildup, e.g. the ventricular septum (Tullio et al., 1997).

In summary, the combination of the geometry, crosslinking composition and density, NMII activation state, and relative, localized, abundance of NMII paralogs determines the mechanical properties of different actomyosin arrays in eukaryotic cells.

1.6 Myosin II-related pathologies

The first myosin II mutation shown to cause human disease was identified in β-cardiac myosin (*MYH7* gene)(Geisterfer-Lowrance et al., 1990). This myosin subtype is expressed in both cardiac and slow skeletal muscle as well as in developing muscle fibers. In the adult heart, it mainly localizes in the ventricles. The mutation localized in the motor domain, and its appearance caused hypertrophic cardiomyopathy (HCM). Since then, more than 1000 mutations have been identified on stri-

ated myosin, including β-cardiac myosin (*MYH7*), α-cardiac (*MYH6*), embryonic (*MYH3*) and adult fast myosin (*MYH2*) (Parker and Peckham, 2020).

MYH7 mutations mainly cause HCM, but also other cardiomyopathies such as dilated cardiomyopathy (DCM) or left ventricular non-compaction, which is a loss of organization and packing of cardiomyocytes during myocardium development. *MYH6* mutations also cause HCM and DCM. Most of the defects are missense mutations located in various functional domains of myosin heavy chain, but more frequently in the motor domain, the converter region and the first amino acids of the coiled coil domain, which are known to stabilize the shutdown state of myosin II (Alamo et al., 2017; Parker and Peckham, 2020). In addition to mutations in the heavy chain of striated myosin, pathogenic variants of the essential (*MYL3*) and regulatory (*MYL2*) light chains also cause HCM (Alcalai et al., 2008).

There are several pathological variants associated with mutations in the heavy chain of two non-muscle myosin II paralogs, NMII-C (*MYH14*) and NMII-A (*MYH9*). *MYH14* mutations cause autosomal dominant non-syndromic hearing loss, with an onset age later than 20 years old (Hiramatsu et al., 2021). Additionally, there is a pathological variant associated with peripheral neuropathy due to a defect in mitochondrial fission (Almutawa et al., 2019), consistent with a defect in mitochondrial fission caused by *MYH14* depletion in cells in which MHCII-C (protein product of the *MYH14* gene) represents less than 1% of the total NMII (Kage et al., 2022). The mutations in NMII-C locate in all functional domains of the heavy chain, with no specific genotype–phenotype correlation among the domains, although two cases of congenital hearing loss associated with variants in the N-terminal region, the motor domain (Hiramatsu et al., 2021).

There is only one report of a patient bearing a mutation in the heavy chain of NMII-B (*MYH10*). The mutation caused the deletion of the C-terminus from the beginning of the coiled coil domain. The patient displayed a severe neurologic phenotype (Tuzovic et al., 2013). *MYH9* mutations are the most common among non-muscle myosins and will be discussed in detail in the next section, since they are the focus of the second part of this thesis. In addition to the alterations at the genetic level, downregulation of *MYH9* expression levels has been described to contribute to squamous cell carcinoma progression, motivating the authors of that report to call *MYH9* a tumor suppressor gene (Schramek et al., 2014), which is a contested notion.

1.7 *MYH9*-related diseases.

Several mutations of the *MYH9* gene in humans result in a wide spectrum of autosomal dominant disorders, jointly termed *MYH9*-related diseases (*MYH9*-RD). The main feature of *MYH9*-RD is congenital thrombocytopenia, along with platelet macrocytosis and the appearance of protein inclusions containing MHCII-A in the cytoplasm of neutrophils (Althaus and Greinacher, 2010; Pecci et al., 2014). These mutations are located along different domains of MHCII-A heavy chain, yet they deliver similar clinical outcomes. They all feature macrothrombocytopenia from birth, characterized by low numbers of platelets of larger-than-normal size, which impairs clotting. However, patients may develop additional clinical manifestations later in life, including presenile cataracts, loss of hearing and glomerular nephropathy. The condition of many of these patients worsen over time. For example, patients that only display macrothrombocytopenia early in their lives may develop nephropathy in their later years. However, the initial symptoms are often mild, thus many young patients remain undiagnosed. This is the reason why these disorders, which are catalogued as rare diseases, may be more prevalent than officially diagnosed. Current prevalence is established at approximately 3:1.000.000 (Pecci et al., 2018, 2008; Savoia et al., 2017).

1.7.1 Clinical features of *MYH9*-RD patients

There are several factors that can determine the clinical outcomes of *MYH9*-RD and revealed some NMII-A paralog-specific functions. Differential NMII-A expression in tissues and cell types is the most straightforward. MHCII-A expression is ubiquitous, being detected in virtually every mammalian cell and tissue (Golomb et al., 2004), including every embryonic stage (Ma and Adelstein, 2014). In some cell types, MHCII-A is the only isoform expressed, for example in platelets and neutrophils (Marigo et al., 2004; Maupin et al., 1994). Even if it is co-expressed with other NMII paralogs, the relative amount of each of them could also give rise to paralog-specific effects. NMII-A is the most abundant NMII in mouse kidney or heart (97% and 96% of total NMII, respectively) (Pecci et al., 2018), whereas its levels are very low in mature neurons compared to NMII-B (Zhang et al., 2014).

Macrothrombocytopenia

This clinical manifestation is characterized by the presence of larger than usual platelets. *Per se*, a large size does not imply that the platelets are dysfunctional. However, patients stably display low numbers of these large platelets throughout their lives (Althaus and Greinacher, 2010). In most cases, decreased numbers of platelets correlate with mild bleeding. Only 28% of patients suffer menhorragia (severe menstrual bleeding), epistaxis (nasal bleeding), spontaneous mucosal bleeding and/or gum bleeding (Pecci et al., 2018) .

Platelets are generated in the bone marrow. They are excised from large, multinucleated precursors termed megakaryocytes (MKs). MKs differentiate from hematopoietic stem cells in the endosteal niche, that is, closer to the inner surface of the bone. Once MKs mature, they migrate to the sinusoid region of the bone marrow (the center of the medulla) in response to CXCL12 (a chemokine formerly known as stromal cell-derived factor (SDF)-1), and they extend protrusions into the sinusoids (Junt et al., 2007). These protrusions are excised to form mature platelets by a combination of shear stress (Dunois-Larde et al., 2009; Jiang et al., 2014) and NMII-driven constriction (Eckly et al., 2008; Spinler et al., 2015). While MKs express both NMII-A and NMII-B (Shin et al., 2014), only NMII-A seems involved in platelet scission. Reconstitution of some *MYH9*-RD mutations in mice has shown that MKs display chemotaxis defects that are related to their inability to properly activate NMII-A (Pal et al., 2020).

Non-syndromic sensorineural deafness

While most of the manifestations of *MYH9*-RD are hematological, *MYH9* mutations may also cause non-hematological manifestations, for example a specific type (DFNA17) of non-syndromic sensorineural autosomal dominant hearing loss (Lalwani et al., 2000). Loss of hearing is a common late-onset condition observed in *MYH9*-RD patients, with around 60% of subjects displaying impaired hearing (Canzi et al., 2016).

Nephritis

Nephritis appears in approximately 25% of *MYH9*-RD patients. It is usually very aggressive, and it initially features proteinuria, sometimes with microhematuria,

and rapid progression to chronic disease that often requires kidney transplantation (Pecci et al., 2014). The most severe cases of nephrotic failure have been described in patients bearing motor-domain mutations of MHCII-A (Furlano et al., 2019; Tabibzadeh et al., 2019).

Presenile cataracts

Early-onset cataracts are the rarest feature of *MYH9*-RD patients (Aoki et al., 2018). As such, the correlation between the precise mutation and the appearance of this manifestation is currently unknown, likely due to its low prevalence.

Other manifestations of *MYH9*-RD

Some *MYH9*-RD patients display alterations in liver enzymatic levels, mainly transaminases and γ-glutamyl transferase. This manifestation is quite benign, with few reported cases of liver failure (Pecci et al., 2012).

1.7.2 *MYH9*-RD diagnosis

MYH9 syndrome is initially suspected in cases of inherited macrothrombocytopenia. Suspicion becomes stronger if the patient displays other extra-hematological features, such as presenile cataracts, deafness, or glomerular nephropathy. However, automated platelet counting does not recognize giant platelets, often leading to misdiagnosis of these syndromes. For that, the first approach to identify those patients is to perform May-Grünwald Giemsa staining over peripheral blood smears. For the sake of clarity in this introduction, we selected two figures from an excellent review in the field (Pecci et al., 2018) and a primary article (Savoia et al., 2010), which best illustrate these phenomena and provide context to interpret our results. In a May-Grünwald Giemsa staining over peripheral blood smears, a *MYH9* patient would display platelet macrocytosis (**Figure 5A**) compared to control smears (**Figure 5B**). To distinguish *MYH9*-RD diagnosis from other platelet syndromes, hematologists search for faint, basophilic protein inclusions in the cytoplasm of granulocytes. These inclusions are termed "Döhle-like" bodies (**Figure 5C**). They are observed in a large percentage (42-84%) of *MYH9*-RD patients by May-Grünwald Giemsa staining (Savoia et al., 2017). Immunofluorescence staining of MHCII-A reveals that these inclusion bodies are positive for NMII-A heavy chain (**Figure**

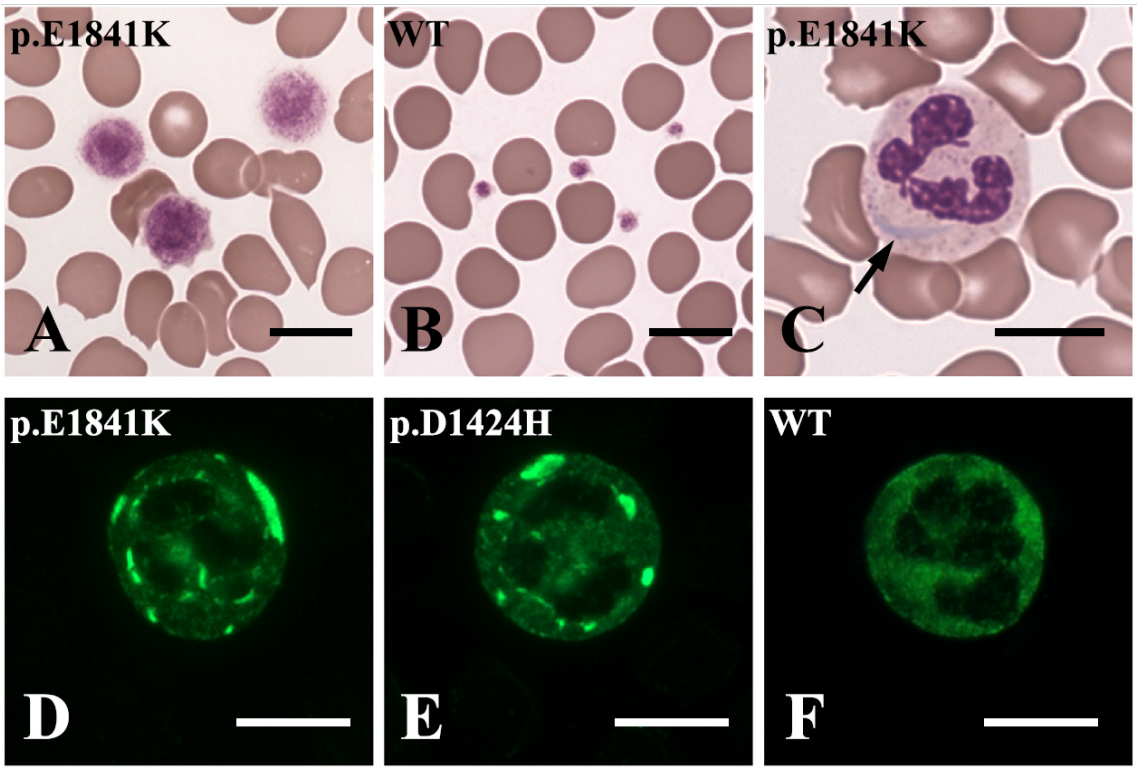

Figure 5: Summary of the abnormalities detected during the examination of peripheral blood smears of patients with *MYH9*-related disease (*MYH9*-RD). (A–C) Conventional May-Grünwald-Giemsa staining; **(D–F)** Immunofluorescence staining of MHCII-A. **(A)** Platelets of *MYH9*-RD patients are characterized by an extreme degree of macrocytosis (giant platelets); some platelets are even larger than erythrocytes. In **(B)**, platelets from a healthy subject are shown for comparison. **(C)** Aggregates of the MHCII-A in the cytoplasm of neutrophilic granulocytes may be identified after conventional staining of blood smears as faint basophilic (sky blue) inclusion bodies, called "Döhle-like" bodies (arrow). **(D–E)** Immunofluorescence staining with a specific antibody reveals the presence of MHCII-A in cytoplasmic aggregates. This constitutes a major indicator used to establish a definitive diagnosis of the disorder. In **(F)** the distribution of the MHCII-A in a granulocyte of a healthy individual is shown for comparison. The *MYH9* genotypes of each individual are indicated in each image. WT, wild type. Scale bars correspond to 10 µm. Figure and footnote extracted from (Pecci et al., 2018)

5D-E), compared to a diffuse MHCII-A staining in healthy donors (**Figure 5F**). These MHCII-A$^+$ inclusion bodies are detected in the neutrophils of every *MYH9* patient when cells are examined using immunofluorescence instead of May-Grünwald Giemsa staining (Pecci et al., 2018; Savoia et al., 2010).

The presence of these aggregates in the neutrophils of the patients is so consistent that MHCII-A immunostaining has been proposed and validated as a diagnostic tool to identify *MYH9* patients with 95% of specificity and 100% of sensitivity (Savoia et al., 2010). Interestingly, the size and number of these aggregates correlates with the location of the mutation in MHCII-A heavy chain (Kunishima et al., 2003;

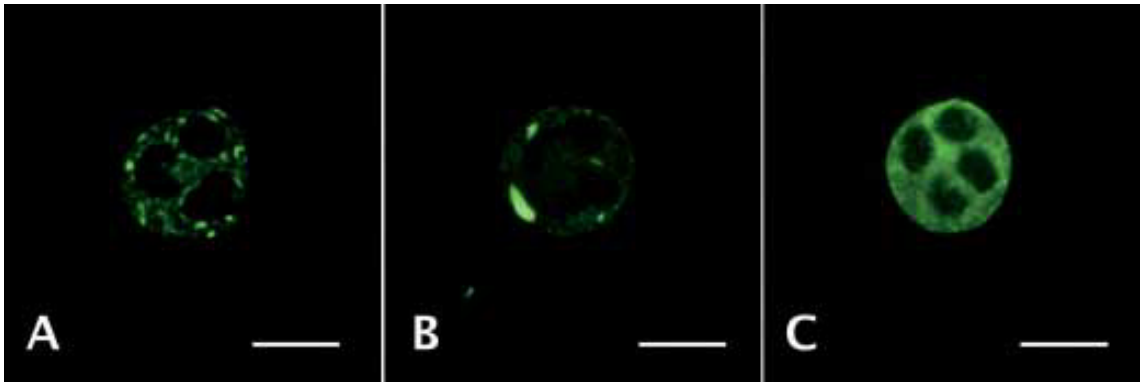

Figure 6: Morphological features of MHCII-A aggregates in neutrophils of patients with different *MYH9* mutations. (A) Patients with mutations in the motor domain of MHCII-A present a "speckled" pattern characterized by numerous aggregates of small size (<0.5 µm). **(B)** Patients with mutations in the rod-tail domain mainly display one to four main, large aggregates (2–7 µm) of different shapes, often together with additional, smaller aggregates. **(C)** Normal MHCII-A distribution pattern is shown for comparison. Scale bars correspond to 10 µm. Figure and footnote extracted from (Savoia et al., 2010).

Miyazaki et al., 2009; Savoia et al., 2010). The classification of these aggregates varies among groups (Kunishima and Saito, 2010; Savoia et al., 2010) but the consensus idea is that several but small aggregates, displaying a speckled pattern in the cytoplasm correlate with mutations in the head domain of MHCII-A (**Figure 6A**), whereas less abundant, but bigger, aggregates associate with mutations in the tail region of MHCII-A (**Figure 6B**). The identification of the causal *MYH9* mutation is not strictly required in the presence of typical MCHII-A neutrophil inclusions, however, it is important for providing a prognostic assessment (Pecci et al., 2018).

Originally, a syndrome with these features (leukocytic inclusions and the presence of giant platelets) was first described by May in 1909, and later by Hegglin in 1945. In 1972, Epstein et al. described a new syndrome characterized by hereditary nephritis, deafness and macrothrombocytopenia. This disease, severe in females, featured albuminuria (excess urine albumin) and microhematuria (erythrocytes in the urine) related to renal damage. Fetchner syndrome was described in 1985 as a new variant of hereditary nephritis that also featured early onset cataracts and leukocytic inclusions. Sebastian platelet syndrome was first described in 1990. This syndrome featured macrothrombocytopenia and different inclusions of smaller size. Finally, in 2000, two groups (Kelley et al., 2000; Seri et al., 2000) identified mutations in the *MYH9* gene as the underlying cause of these macrothrombocytopenias. May Hegglin Anomaly, Epstein Syndrome, Fetchner syndrome and Sebastian platelet

syndrome are now considered as subtypes of *MYH9*-related diseases.

1.7.3 Prevalent *MYH9*-RD mutations

MYH9-RD include 49 different alterations affecting 12 exons of the *MYH9* gene (De Rocco et al., 2013). Missense mutations are the most common, affecting at least 21 of the 1960 codons of the gene. A stop mutation has been detected in the last exon, generating a truncated, slightly smaller, MHCII-A protein. Duplications and in-frame deletions are the least frequent, and are usually due to the introduction of repeated sequences (Balduini et al., 2011). Despite all this, between 20-35% of *MYH9*-RD cases present *de novo* mutations. Somatic or germinal mosaicism is rare (Han et al., 2011).

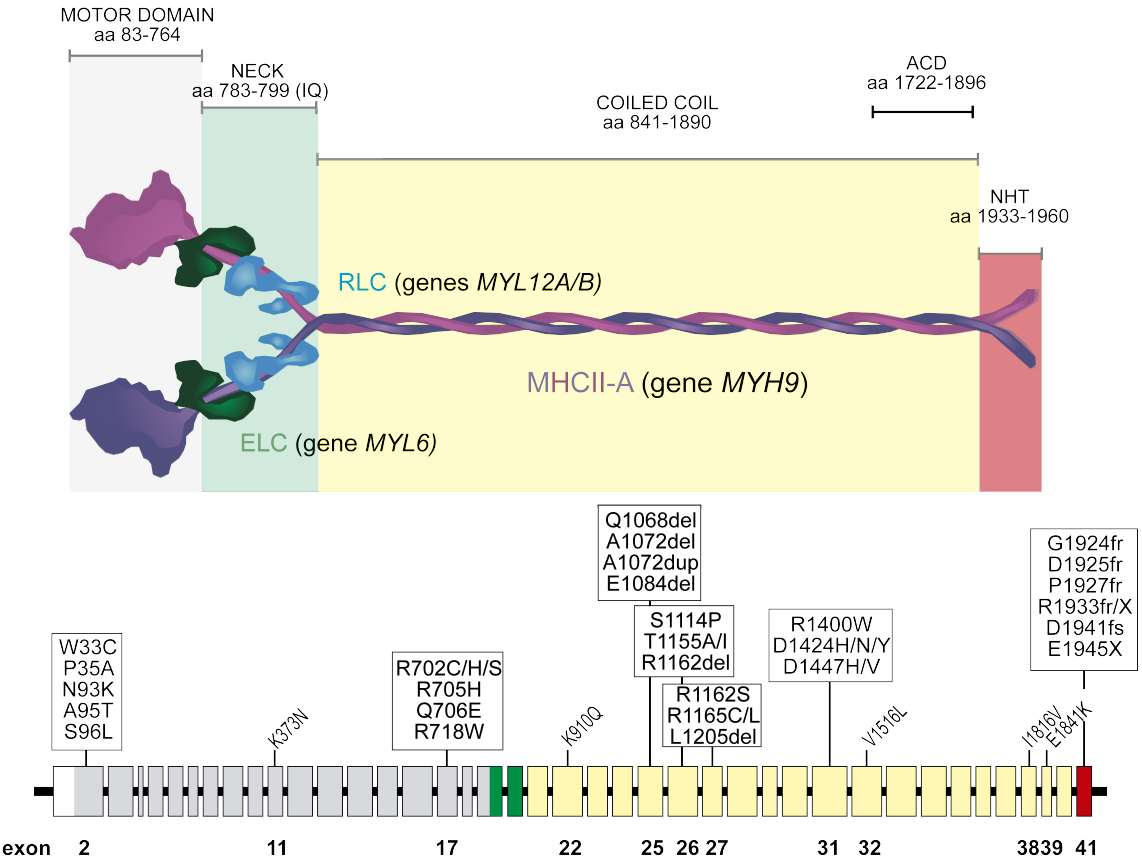

Figure 7: Schematic representation of *MYH9* mutations. Top, Color-coded organization of an extended NMII-A hexamer, including the domain organization of MHCII-A, and their binding to ELC (in dark green) and RLC (blue). ACD, assembly-competent domain. NHT, non-helical tailpiece. Bottom, exon organization of the *MYH9* gene and position of the most prevalent mutations found in *MYH9*-RD patients. Exon organization is color-coded: grey, motor domain; green, neck; yellow, coiled coil; red, NHT. Figure and footnote modified from (Asensio-Juárez et al., 2020).

In approximately 80% of the families, mutations are concentrated in codons for six specific amino acids: S96 (6%) and Arg702 (24%) located in the head domain, Arg1165 (9%), Asp1424 (20%), and Glu1841 (22%) in the coiled-coil, and Arg1933 (19%) in the non-helical tailpiece (**Figure 7**, bottom panel) (Balduini et al., 2011). In this manner, most *MYH9*-RD cases are associated with a limited number of genotypes. These major mutations have been located in 77 unrelated families, with 22 different genotypes of *MYH9*-RD. Therefore, despite the fact that the *MYH9*-RD present diverse symptoms, they sometime share common mutations (Seri et al., 2003).

Regarding the platelet phenotype, there is a consistent phenotype-genotype correlation in which mutations in the exons encoding the motor domain had more severe thrombocytopenia than patients with mutations affecting the tail domain or non-helical tailpiece (Pecci et al., 2018, 2008). In general, this correlation (motor domain substitutions displaying more severe phenotypes) also applies to the later-onset manifestations (Dong et al., 2005; Pecci et al., 2008; Saposnik et al., 2014), although there is more variability here and greater association with specific mutations.

The most frequent mutations in the motor domain affect the R702 codon. These mutations (to Cys, His or Ser) cause the most severe phenotype observed in *MYH9*-RD patients. Patients with R702 mutations are characterized by severe thrombocytopenia and are expected to display aggressive nephropathy and/or progressive deafness.

Mutations in codons for Arg1165 and Asp1424 also increase the risk of developing extra-hematological complications. Patients bearing the D1424H missense mutation are expected to develop proteinuria and deafness by the sixth decade of life and have a higher probability of developing cataracts. However, D1424N and E1841K missense substitutions, as well as the frameshift or nonsense alterations affecting the non-helical tailpiece (such as R1933X) are associated with a low risk of the extra-hematological features and usually macrothrombocytopenia remains the only feature of the disease, with only a mild late-onset hearing defect (Pecci et al., 2014; Verver et al., 2016).

For the second part of thesis, we selected several of the most prevalent *MYH9* variants affecting different domains of NMII-A heavy chain (MHCII-A -N93K, -R705H, -D1424H, -E1841K, -R1933X; **Figure 7**) to decipher how these alterations shape biochemical and dynamic behavior of NMII-A. We have also selected a mu-

tation (-R1162S) that is present in a family of patients routinely controlled at the HUSAL Hematology Department, thus granting us access to primary cells as discussed in the Methods and Results chapters.

2 Hypothesis and Objectives

The present thesis is divided in two major parts that address specific aspects of the cellular functions of NMII, from its regulation to its role in disease.
The first part describes a new mode of regulation of NMII. Starting from the detection, in the 1980s, of Y155 and Y142 phosphorylation on RLC in response to growth factors, the hypothesis of the present doctoral thesis work is that these residues have distinct regulatory functions on NMII.
In order to challenge our hypothesis, our aims were to:

1. Assess the individual role of Y155 and Y142 residues in RLC.
2. Determine the cellular effects of RLC phosphorylation on these residues.
3. Study the regulation of RLC through the phosphorylation of these residues

The second part focuses on the behavior of pathological variants of *MYH9* at the cellular level. We hypothesize that the clinical manifestations of *MYH9* patients can be ascribed to specific defects on NMII dynamics that can only be documented at the protein and cellular levels.
To challenge our second hypothesis, our aims were to:

1. Determine the role of mutations affecting different domains of NMII-A in the stability, interactome, enzymatic activity and assembly properties of NMII-A.
2. Characterize the behavior of NMII-A mutations at the cellular level, focusing on their role in cell adhesion and migration.
3. Characterize morphological and functional aspects of primary cells derived from a carrier of a specific *MYH9* mutation (c.3486G>T. R1162S).

3 Materials and Methods

3.1 Common Materials and Methods

3.1.1 Antibodies and reagents

The antibodies and reagents used in this thesis are listed in Tables 1 and 2, with a brief description including species, application, dilution/dosage, and the manufacturer.

Table 1: List of primary and secondary antibodies used in Western blot (WB), flow cytometry (FC) and immunofluorescence (IF). S, Host Species: H, human; M, mouse; R, rabbit; G, goat.

Antibody	S	Provider	Identifier	IF	WB	FC
MHCII-A, C-t (non-muscle)	R	Biolegend	909801	1:1000	1:20000	1:1000
MHCII-B, C-t (non-muscle)	R	Biolegend	909901	1:1000	1:20000	1:1000
Myo18A	R	Novus Biologicals	NB100-79839	-	1:2000	-
total RLC (RLC)	R	Rockland	600-401-938	-	-	1:1000
(MY21)	M	Merck	M4401	1:1000	1:2000	-
pS19 RLC	R	Cell Signaling Technologies	3675	-	1:500	-
EGFR	M	TFS[1]	AHR5072	-	1:1000	-
Phospho- MLC2 (Tyr155)-Antiserum 8471[2]	R	This paper, custom made by Pierce/ TFS	N/A	1:100	1:1000	-

[1]Thermo Fisher Scientific

[2]The 8471 antiserum was custom developed specifically for our laboratory in a rabbit host by TFS, using the following immunizing peptide conjugated to KLH: KGNFN(pY)VEFTRIC. Before use, the antibody was preincubated for 1h at room temperature with a tenfold excess of the non-

Antibody	**S**	**Provider**	**Identifier**	**IF**	**WB**	**FC**
Vinculin (hVinc-1)	M	Merck	V9131	1:1000	1:5000	-
α-Tubulin	M	Merck	T9026	-	1:5000	-
FLAG	M	Merck	F3165	1:1000	1:10000	-
GFP	M	Santa Cruz Biotechnology	9996	1:1000	1:10000	-
Mouse AlexaFluor568, highly cross-adsorbed	G	TFS	A11031	1:1000	-	1:1000
Mouse AlexaFluor647, highly cross-adsorbed	G	TFS	A32728	1:1000	-	1:1000
Rabbit AlexaFluor568, highly cross-adsorbed	G	TFS	A11036	1:1000	-	1:1000
Rabbit AlexaFluor647, highly cross-adsorbed	G	TFS	A21245	1:1000	-	1:1000
Mouse-HRP	G	TFS	A16078	-	1:10000	-
Rabbit-HRP	G	TFS	A16110	-	1:10000	-
CD49e - integrin α5 (FITC anti-human CD49e-integrin α5)	M	Biolegend	328007	-	-	1:100
CD11a - integrin αL (FITC anti-human CD11a-integrin αL)	M	Biolegend	350604	-	-	1:100
CD49d - integrin α4 (FITC anti-human CD49d -Integrin α4)	M	Biolegend	304315	-	-	1:100
CD18 - integrin β2 (FITC anti-human CD18 -integrin β2)	M	Biolegend	366305	-	-	1:100
CD29 - integrin β1 (AlexaFluor® 647 anti-human CD29-integrin β1)	M	Biolegend	303017	-	-	1:100
MHC Class II (Purified anti-human HLA-DR, DP, DQ)	M	Biolegend	361702	-	-	1:100

phosphorylated peptide, KGNFNYVEFTRIC, to prevent non-specific binding.

Antibody	S	Provider	Identifier	IF	WB	FC
CD11C (Alexa-Fluor® 647 anti-human CD11C)	M	Biolegend	301619	-	-	1:100
CD86 (PE Mouse Anti-Human CD86)	M	BD biosciences	557344	-	-	1:100

Table 2: List of reagents or resources.

Reagent or resource	Provider	Identifier
µ-Slide 8 Well	Ibidi	80826
µ-Slide Chemotaxis	Ibidi	80326
3-(N-Morpholino)propanesulfonic acid (MOPS)	Merck	RDD003
Acetonitrile	Merck	900667
Active human EGFR	Merck	SRP0239
Anti-FLAG M2 Magnetic Beads	Merck	M8823
Anti-GFP-conjugated magnetic beads (GFP-TRAP)	Chromotek	gtma-20
ATP	Merck	A7699
Bac-to-Bac™ Baculovirus Expression System	TFS[3]	10359016
BD BaculoGold Linearized Baculovirus DNA	BD Biosciences	554739
Beta-mercaptoethanol	Merck	M6250
BL21(DE3)pLysS	EMD Millipore	70236
Bovine serum albumin (BSA)	NZY Tech	MB04603
CCL19 (human recombinant CCL19)	Peprotech	300-29B
Cell Lytic B	Merck	B7435
CloneAmp	Takara Biotech	639298
Collagen I from rat tail (5 mg/ml)	Ibidi	50201
cOmplete, EDTA-free Protease Inhibitor Cocktail	Merck	11873580001

[3]Thermo Fisher Scientific

Reagent or resource	**Provider**	**Identifier**
DEXTRAN 500.000 MW (Alfa Aesar)	TFS	J63702
DRAQ5™ (5 mM)	TFS	62251
EGF (recombinant human)	TFS	PHG0311
Ethylene glycol-bis(β-aminoethyl ether)-N,N,N',N'-tetraacetic acid (EGTA)	Merck	3777
Ficoll-Paque PLUS	Merck	GE17-1440-02
Fixation Buffer eBioscience™	TFS	00-8222-49
γ-globulins from human blood	Merck	G4386
GeneTailor Kit	TFS	12397-014
Glutathione-agarose medium	ABT	4B-Glu-10
Granulocyte-Macrophage Colony Stimulating Factor (GM-CSF)	Peprotech	300-03
HEPES 1M	VWR	45000-690
IGF-1 (recombinant human)	TFS	PHG0071
Imidazole	Merck	792527
Interleukin-2 (IL-2)	Peprotech	200-02
Interleukin-4 (IL-4)	Peprotech	200-04
IPTG	NZY Tech	MB026
Janelia Fluor® HaloTag® Ligand-585 and -635	Luke Lavis (Janelia Farm)	-
Lipopolysaccharide from Escherichia coli O111:B4 (LPS)	Sigma	L3024
Lysozime	Merck	L6876
MagnaBind™ Goat Anti-Mouse IgG	TFS	21354
Magnesium chloride ($MgCl_2$)	Quality Biological	351-033-721
Manganese chloride ($MnCl_2$)	Merck	805930
MG-132	Merck	M7449
Mouse IgG-Agarose	Merck	A0919
N-Formyl-Met-Leu-Phe (fMLP)	Merck	F3506
Ni-NTA	QIAGEN	30230

Reagent or resource	**Provider**	**Identifier**
Permeabilization buffer eBioscience™	TFS	00-8333-56
Phalloidin-AlexaFluor 647	TFS	22287
Phorbol 12-myristate 13-acetate (PMA)	Merck	P8139
Phosphatase Inhibitor Cocktail 2	Merck	P5726
Phosphatase Inhibitor Cocktail 3	Merck	P0044
PhosSTOP	Roche	4906837001
phytohemagglutinin-L (PHA-L)	Merck	11249738001
Pierce 16% Formaldehyde (w/v), Methanol-free	TFS	28906
Pierce Recombinant Protein A, Peroxidase Conjugated	TFS	32400
Pierce Recombinant Protein G, Peroxidase Conjugated	TFS	31499
PreScission™ Protease	GE Healthcare	GE27-0843-01
Prolong Glass Antifade medium	TFS	P36984
Sf9 cells (from *Spodoptera frugiperda*)	TFS	12659017
Sodium azide	Merck	S2002
Sodium orthovanadate	Merck	S6508
SureBeads Protein A Magnetic Beads	BioRad	1614013
SYTOX™Green (5mM)	TFS	S7020
Tetraspeck™ fluorescent beads	TFS	T7282
Transwell® Permeable Supports (Costar)	Merck	CLS3472
Trifluoroacetic acid (TFA)	Merck	302031
Triton X-100	Merck	T8787
UltraCruz® PVDF Transfer membrane	Santa Cruz Biotech.	SC-3723
X-tremeGENE HP (Roche)	Merck	6366546001

3.1.2 Plasmids

- RLC-GFP: wild type myosin RLC coupled to GFP was a generous gift from Kathleen Kelly (NCI, Bethesda, MD). The gene encoded in this plasmid is chicken *Myl9* (NIH gene ID: 396215), which bears 97% protein homology with hamster non-muscle RLC, gene *Myl12B*). The Y142E/F and Y155E/F mutations were generated in the laboratory by site-directed mutagenesis using the GeneTailor kit using the primers indicated in Table 3.

- FLAG-tagged chicken RLC (*Myl9*) versions were also generated by the laboratory by routine subcloning into pCDNA3 with a built-in FLAG tag in the N-terminus (Zhang et al., 2003). The sequences for cloning are indicated in Table 3.

- His-tagged and tandem GST-FLAG-tagged RLC for *in vitro* kinase assays were obtained by in frame cloning of chicken RLC in pET302 or pGEX-6P1 (GE Healthcare). The cloning sequences are indicated in Table 3.

- pSUPER-RLC and pSUPER-c (control) plasmids were obtained by inserting the sequences GGGATGGCTTCATTGACAA, specific for RLC (mouse, genes *Myl12A* and *Myl12B*, hamster, gene *Myl12B*) but absent in chicken RLC, gene *Myl9* (2 mismatches, experimentally verified to be insensitive to the siRNA sequence) and CGTACGCGGAATACTTCGA in pSUPER vector (Oligoengine) according to the manufacturer's instructions.

- FLAG-tagged human MHCII-A subfragment-1 expression construct has been described previously (Kovacs et al., 2003).

- Lifeact-GFP was obtained from R. Wedlich-Soldner (Max Planck Institute, Martinsried) (Riedl et al., 2008).

- pEGFP-N1, from Clontech (currently Takara Biotech).

- GFP-MHCII-A wild type (originally provided by Bob Adelstein (NIH, Bethesda, MD, USA) were in frame, tandem (GFP, then MHCII-A) fusions of the corresponding human genes in the cytomegalovirus (CMV)- based pEGFP-C3 vector.

- FLAG- and mEOS2-MHCII-A wild type were generated by subcloning FLAG or mEOS2 into GFP-MHCII-A plasmid using AgeI /HindIII enzyme restriction sites

that flanked the GFP sequence (in brief, replacing GFP with FLAG or mEOS2 by in-frame cloning).

- GFP-MHCII-A N93K was previously generated in the laboratory by site directed mutagenesis on MHCII-A WT vector using the primers indicated in Table 3. For the MHCII-A mutagenesis experiments, the GeneTailor protocol was followed, but the kit's enzyme was substituted with CloneAmp (Takara Biotech), which is faster (5 s/kpb) and offers higher fidelity than the enzyme included in the kit.

- The rest of GFP-MHCII-A plasmids bearing mutations related to *MYH9*-RD were generated by site directed mutagenesis. These mutants include: GFP-MHCII-A R705H, GFP-MHCII-A R1162S, GFP-MHCII-A D1424H, GFP-MHCII-A E1841K and GFP-MHCII-A R1933X. Primers used are shown in Table 3.

- FLAG-/mEOS2-MHCII-A mutants were generated from the GFP-MHCII-A mutant counterparts. We used AgeI (which flanks the beginning of GFP) and BsiWI to exchange the GFP tag with the FLAG or mEOS2 tags. BsiWI is a unique restriction site at 575pb inside the MHCII-A sequence, therefore we used FLAG- or mEOS2-MHCII-A WT as the donor vector. We generated FLAG-/mEOS2-MHCII-A R705H, R1162S, D1424H, E1841K and R1933X mutants with this strategy, but not MHCII-A N93K because the mutation lies before the BsiWI restriction site. FLAG-/mEOS2-MHCII-A N93K were generated by site directed mutagenesis PCR from FLAG-MHCII-A WT and mEOS2-MHCII-A WT respectively, as described above and with the primers indicated in Table 3.

- mNeonGreen-MHCII-A wild type was generated by overlapping PCR using two sets of primers: set one contained the AgeI site 5' of mNeonGreen (F) and a reverse complement primer hybridizing with 22 nt of the 3' of mNeonGreen (minus the stop codon) and 22 nt of the in-frame linker between GFP and *Myh9* in the original GFP-containing plasmid. Set two included the forward version of the primer described above and the reverse complement primer containing the BsiWI site in *Myh9*. The first reaction (PCR1) yielded AgeI-mNeonGreen with a 3', 22 nt arm overlapping with the linker between GFP and *Myh9*; PCR2 yielded the 5' fragment of *Myh9* (including the 5' linker to GFP) up to the BsiWI site with a 5', 22 nt overhang overlapping the end of the mNeonGreen. The two PCR products were purified and combined in equimolar amounts, then used as a template for

another round of PCR (PCR3) using the AgeI – and BsiWI- containing primers of each set. The product (AgeI-mNeonGreen-linker-*Myh9*-BsiWI) was cloned into GFPMHCII-A using AgeI-BsiWI and validated by in-house sequencing.

- UNC45a-GFP was a kind gift from Prof. Pekka Lappalainen (University of Helsinki).

Table 3: List of primers sequences for mutagenesis and for cloning in the indicated vectors. Here (Fw) and (Rv) stand for forward and reverse, respectively.

Name		**Primers 5'-3'**
GFP-RLC Y142E	Fw	ACGAGGAGGTGGACGAGATGGAACGGGAGGCGCC
	Rv	CATCTCGTCCACCTCCTCGTCAGTGAACCT
GFP-RLC Y142F	Fw	ACGAGGAGGTGGACGAGATGTTCCGGGAGGCGCC
	Rv	CATCTCGTCCACCTCCTCGTCAGTGAACCT
GFP-RLC Y155E	Fw	ACAAGAAGGGCAACTTCAACGAAGTGGAGTTCAC
	Rv	GTTGAAGTTGCCCTTCTTGTCGATGGGCGC
GFP-RLC Y155F	Fw	ACAAGAAGGGCAACTTCAACTTTGTGGAGTTCAC
	Rv	GTTGAAGTTGCCCTTCTTGTCGATGGGCGC
GFP-MHCII-A N93K	Fw	TGGCAGAGCTCACGTGCCTCAAgGAAGCCTCGGT
	Rv	TTGAGGCACGTGAGCTCTGCCATGTCCTCC
GFP-MHCII-A R705H	Fw	TCGAGGGCATCCGTATCTGCCaCCAGGGCTTCCC
	Rv	GCAGATACGGATGCCCTCGAGAACACCGTT
GFP-MHCII-A R1162S	Fw	CAGCTGCCCAGCAGGAGCTCAGtTCAAAACGTGA
	Rv	GAGCTCCTGCTGGGCAGCTGTGGAATCCAG
GFP-MHCII-A D1424H	Fw	GGCTGCAGCAGGAGCTGGACcACCTGCTGGTGGA
	Rv	GTCCAGCTCCTGCTGCAGCCGCGTCTTGGT
GFP-MHCII-A E1841K	Fw	GCAAACAGGTGCGTCGGACCaAGAAGAAGCTGAA
	Rv	GGTCCGACGCACCTGTTTGCAGGCTGCCTG
GFP-MHCII-A R1933X	Fw	TGCCGTTTGTCGTGCCCCGCtGAATGGCCCGGAA
	Rv	GCGGGGCACGACAAACGGCAGGTCCCCGCG
primer to clone RLC mutants into pCDNA3-FLAG	Fw	CGAGCTCGGATCCATGTCCAGCAAACGTGCCAAA
	Rv	ATATCTGCAGAATTCCTAATCGTCCTTGTCCTTAGCTCC
primer to clone FLAG-RLC mutants into pGEX-6P1	Fw	AAAAAGAATTCATGGACTACAAGGACGACGATGACA
	Rv	TTTTTGCGGCCGCCTAATCGTCCTTGTCCTTAGCTCCGTGC
AgeI-mNeonGreen	Fw	AAAACCGGTCGCCACCATGGTGAGCAAGGGCGAGGAG

Name		Primers 5'-3'
mNeonGreen-*Myh9*	Fw	GCATGGACGAGCTGTACAAGTACTCAGATCTCGAGCTCAAG
	Rv	CTTGAGCTCGAGATCTGAGTACTTGTACAGCTCGTCCATGC
Myh9-BsiWI	Rv	ACGCCACGTACGCCAGATACTGG

3.2 Materials and Methods, part 1

3.2.1 Cell culture and transfection

CHO.K1 cells (ATCC #CCL-61) were cultured in low-glucose DMEM medium (Gibco) supplemented with 10% fetal bovine serum (FBS) from GE Healthcare HyClone (Pittsburgh, USA), 100 IU/ml penicillin and 100 µg/ml streptomycin (P/S, Gibco, Grand Island, NY, USA), 1% non-essential amino acids (NEAA, Gibco). Cells were maintained under normal culture conditions (37 ^{o}C in a humidified 5% CO_2 atmosphere).

The day before transfection, CHO.K1 cells were seeded at 10^4 cells per cm^2. On the day of transfection, cells were washed and incubated in penicillin/streptomycin-free medium until analysis. Cells were transfected overnight with 1µg DNA per 35-mm well using 2.5 µl per µg DNA of X-tremeGENE HP. Analysis was performed 24h (overexpression) or 96h (depletion and rescue) post-transfection. In co-transfection experiments, pSUPER plasmids containing the shRNA sequences were used in 10:1 excess to GFP-containing plasmids to ensure knockdown in fluorescence-positive cells. For immunofluorescence rescue experiments, cells were selected as follows: we first transfected cells with pSUPER-C or pSUPER-RLC and RLC-GFP (wild type). After four days, we performed flow cytometry on both populations, staining for RLC with Rockland's rabbit RLC antibody and a goat anti-rabbit antibody coupled to AlexaFluor647. We compared the intensity of the RLC channel in the GFP-transfected cells to the intensity of the RLC in non-transfected cells. We selected a population of cells within a comparable range of intensities, examined the GFP channel and used this population to create a flow cytometry gate. Another population of these cells was then sorted and adhered to fibronectin-coated coverslips, stained for RLC as indicated above and examined by confocal microscopy. These cells were used to establish the desired intensity in the GFP channel that corresponds to normal RLC levels. These conditions were saved and applied in all

subsequent experiments.

3.2.2 Cell plating and immunofluorescence

Cells were allowed to adhere to 2 µg/ml fibronectin-coated coverslips for 60 min, fixed using 4% of pre-warmed paraformaldehyde (PFA) in PBS, and permeabilized with 0.5% Triton X-100 for 5 min. Fibronectin was obtained by purification protocols from blood plasma (Akiyama, 2013). Coverslips were incubated with primary antibodies diluted and a species-appropriate, highly crosslinked, secondary antibody coupled to either Alexa Fluor 568/647 and/or phalloidin-AlexaFluor647 where indicated, rinsed and mounted in coverslips using Prolong Glass antifade medium.

3.2.3 Immunoprecipitation

CHO.K1 cells (3×100-mm dishes per condition) were lysed in 1 ml total ice-cold 50 mM Tris-HCl buffer pH7.4 containing 1% Triton X-100, 50 mM NaCl, 5 mM $MgCl_2$, 5 mM ATP, and protease and phosphatase inhibitor cocktails. Lysates were clarified by centrifugation (13000×g, 15 min at 4ºC) and incubated with 50 µl mouse IgG-agarose for 2 h at 4ºC under continuous stirring. Clarified lysates were incubated with 50 µl protein-A-conjugated magnetic beads pre-coupled to rabbit anti- MHCII-B; or anti-GFP-conjugated beads for 90 min at 4ºC under continuous stirring. The beads were rinsed four times with ice-cold TBS and immunoprecipitated proteins were removed from the beads using 80 µl 4×Laemmli buffer. Immunoprecipitates were then separated by PAGE/SDS, transferred to PVDF membranes, blocked with ovine serum albumin (BSA) and blotted with the antibodies indicated in each case.

3.2.4 Production of recombinant proteins and *in vitro* kinase assay

FLAG-MHCII-A subfragment-1 was expressed in the baculovirus/Sf9 system and purified by FLAG-affinity chromatography followed by size exclusion chromatography as described previously (Heissler et al., 2015), in collaboration with the group of Sarah Heissler (Ohio St. University, USA). For expression of recombinant RLC, pGEX-6P1 plasmids encoding tandem GST-FLAG-tagged RLC WT or mutants were introduced in BL21(DE3) pLysS competent cells, which were further allowed

to grow to plateau phase overnight in 40 ml LB medium at 37 ºC under constant shaking. Cultures were expanded to 400 ml and incubated for 2 more hours. 0.3 mM IPTG was added to the cultures, which were grown at 30ºC for 3h. Cells were collected, lysed using 1 mg/ml lysozyme in ice-cold TBS and sonicated five times for 30s. Lysates were clarified by centrifugation (11,000×g, 30 min at 4ºC) and incubated for 2 h with 300 µl glutathione-agarose beads. The beads were rinsed five times with ice-cold TBS and incubated with 20 U of Prescission protease in 200 µl Prescission buffer at 4ºC (to remove the GST tag, leaving the FLAG tag in) according to the manufacturer's instructions. His-tagged RLC was prepared as described (Kovacs et al., 2003). For IVK assays, 5 µg of recombinant RLC or 50 µl of MHCII-B immunoprecipitate were mixed with 0.5 µg of human active EGFR in 30 µl kinase buffer containing 5 mM MOPS, pH 7.2, 100 µM ATP, 2 mM β-glycerol-phosphate, 5mM $MgCl_2$, 2mM $MnCl_2$, 1mM EGTA, 0.5mM EDTA and incubated for 30 min at 30ºC. The reaction was stopped using 30 µl of 2× Laemmli buffer, separated using PAGE/SDS, transferred to PVDF membranes and blotted as indicated. For intact molecule mass spectrometry, 10 µM MHCII-A subfragment-1 or 10 µM His-RLC were incubated with 0.003 mg/ml EGFR in 10 mM MOPS pH 7.2, 50 mM NaCl, 5 mM $MgCl_2$, 0.1 mM EGTA, 2 mM $MnCl_2$, 1× phosphatase inhibitor cocktail PhosStop and 100 µM ATP for 2 h at room temperature (RT). For overnight incubation, samples were placed on ice after a 2 h incubation at room temperature. Kinase was omitted for the controls. Samples were mixed 1:1 with 5% acetonitrile+0.05% trifluoroacetic acid and subjected to HPLC-mass spectrometry as described previously (Vasquez et al., 2016).

3.2.5 Confocal microscopy

Images were obtained in a Leica SP8 confocal spectral microscope at 63× magnification. As source of illumination, the microscope was fitted with a pulsed white light (WL) laser (80 MHz). GFP was excited at 491 nm; whereas AlexaFluor568 and Alexa Fluor647 probes were excited with at 568 and 647 nm, respectively. Photon collection was set using internal standards of the microscope for each wavelength in sequential mode.

3.2.6 Migration assays

Cells were plated for 1 h on glass-bottomed dishes pre-incubated overnight with 2 µg/ml fibronectin in Live Cell Imaging Solution (140 mM NaCl, 2.5 mM KCl, 1.8 mM $CaCl_2$, 1 mM $MgCl_2$, 20 mM HEPES pH 7.4) supplemented with 10% FBS and maintained at 37°C. The transfected cells were identified using fluorescence for the first frame of the time-lapse video. The rest of the images were collected using very low levels of transmitted light, one image every 10 min for 16 h. Images were acquired on an inverted microscope (IX70; Olympus) equipped with a 60× Apochromat N objective (NA 1.45), a charge-coupled device (CCD) camera (Retiga EXi; QImaging) and MetaMorph software (Molecular Devices).

3.2.7 Polarity index and adhesion quantification

Polarity and focal adhesion number and size (represented as cellular adhesive area) were quantified as described elsewhere (Talayero and Vicente-Manzanares, 2021; Vicente-Manzanares et al., 2011). Briefly, to quantify cell polarity (axis ratio), cells were fixed, stained and images acquired in the Leica SP8 confocal microscope as indicated. For each individual cell, the axis ratio was calculated dividing the length of the long, migration-defined axis by the perpendicular axis crossing the nucleus of the cell. For adhesion analysis, we used ImageJ (Schneider et al., 2012) to subtract background, applied the CLAHE (Contrast Limited Adaptive Histogram Equalization) algorithm to create a high-contrast image that was subject to the threshold command of ImageJ and quantified using the Analyze Particles ImageJ built-in feature. % of adhesive area was obtained by dividing the adhesive area of the cell determined as described above divided by the total area of the cell determined manually.

For migration assays, the centroids of migrating cells were determined using the "Manual Tracking" plugin for ImageJ, transferred and plotted using Chemotaxis tool from Ibidi. Velocities were determined using the same software.

3.3 Materials and methods, part 2

3.3.1 Cell culture and transfection

Cell lines

African green monkey kidney fibroblast-like COS-7 cells (ATCC CRL-1651) were maintained in DMEM medium (Gibco). Human megakaryoblastic MEG-01 cells (ATCC CRL-2021) cells were maintained in RPMI1640 medium (Gibco). Human osteosarcoma U2OS cells (HTB-96; ATCC) were maintained in McCoy's medium (Gibco). All the mediums were supplemented 10% FBS (GE Healthcare HyClone), 100 IU/ml and 100 µg/ml P/S, respectively (Gibco) and 1% NEAA (Gibco). Cells were maintained under normal culture conditions (37 ºC in a humidified 5% CO_2 atmosphere).

Primary cells

Peripheral blood samples from *MYH9* patient and healthy donors were acquired in parallel in EDTA-blood collection tubes and processed immediately. Human peripheral blood mononuclear (PBMCs) and polymorphonuclear neutrophils (PMNs) were isolated by separation on a density gradient according to standard procedures. Initially, peripheral blood samples were diluted in two volumes of sterile PBS 1x Na+ K+ (PBS) and carefully layered onto 13 ml of Ficoll-Paque PLUS (GE Healthcare) in 50 ml tubes and centrifuged at 650×g for 45 minutes at RT without brakes.

PBMCs (located in the interphase between plasma and Ficoll-Paque PLUS) were collected and transferred to a new sterile 50 ml plastic tube. Tubes were filled with sterile PBS and washed three times, removing the supernatant and increasing the centrifugation speed: 200×g, 5 min; 250×g, 5 min and 300×g, 5 min. Finally, isolated PBMCs were resuspended in complete RPMI1640 medium: RPMI1640+L-Glutamine (Gibco, Paisley, UK) supplemented with 10% FBS (GE Healthcare HyClone), 100 IU/ml and 100 µg/ml P/S, respectively (Gibco), 1% NEAA (Gibco), HEPES Buffer 25 mM and 1% sodium pyruvate 100 mM (Gibco).

Monocytes were separated from PBMCs by adherence during one hour at 37°C, 5% CO_2 in 150mm-diameter tissue culture plates (Corning). PBMCs were cultured in RPMI1640 medium supplemented as before and in the presence of 1 µg/ml

phytohemagglutinin-L (PHA-L) for two days. Interleukin-2 (IL-2), used at 100 U/ml, was added two days after PHA-L stimulation to the medium and again every two days for a maximum time of seven days to obtain activated T cells.

To generate monocyte-derived dendritic cells (mDCs), a total of 10^5 PBMCs per cm^2 were set to adhere for one hour at 37°C, 5% CO_2 in tissue culture plates. Cells were washed three times with sterile PBS and cultured in the presence of 50 ng/ml of GM-CSF and 500 U/ml of IL-4. Medium was exchanged every two days for six to seven days to generate immature mDCs. To obtain mature mDCs, lipopolysaccharide (LPS) at 10 ng/ml was added for 24h at day six after isolation.

PMNs were isolated from the granulocyte-erythrocyte pellet fraction (Kuhns et al., 2015) and processed immediately given their brief lifespan in culture. The pellet was thoroughly resuspended in PBS up to 20 ml and mixed by inversion several times with 20 ml of sterile dextran (500.000 M_W) at 3% in PBS. The mix was incubated for 20 min at RT, to allow the sedimentation of erythrocytes. The resulting PMN-rich supernatant was collected in another 50 ml sterile tube and centrifuged for 5 mins at 450×g. To eliminate the remaining erythrocytes, three rounds of hypotonic shocks were performed: the pellet was resuspended in 10 ml of hypotonic lysis buffer (sterile PBS 0.2×) for 15 s followed by the immediate addition of 10 ml of re-equilibration buffer (sterile PBS 2.2×). The mix was further diluted with 30 ml of PBS 1×, and centrifuged 5 min at 450×g. This step was repeated until we obtained an off-white pellet (meaning the removal of most of the erythrocyte fraction) to a maximum of three times. Finally, PMNs were resuspended in complete RPMI1640 medium and immediately analyzed.

Transfection

The day before transfection, COS-7 and U2OS cells were seeded at 10^4 cells per cm^2 in 6-mm dishes. On the day of transfection, cells were washed and incubated in P/S-free medium until analysis. Cells were transfected overnight with 1 µg DNA per 35-mm well using 2.5 µl per µg DNA of X-tremeGENE HP. Medium was exchanged every 24h and analysis was performed 48h post transfection. Cells were transfected with a maximum of 500 ng of MHCII and up to 1 µg of total DNA with pBluescript empty vector to avoid over-expression side effects. For MEG-01 transfection, 15×10^6 cells were used per condition. Cell lines were pelleted and washed twice with room

temperature PBS. Centrifugation was always carried out at 300×g for 5 minutes at room temperature. Cells were washed again with OptiMem, a reduced serum medium with L-glutamine and HEPES (Gibco). Cells were resuspended in 400 µl of OptiMem, transferred to 0.4 cm gap cuvettes and mixed with 20-30 µg of plasmid. Transfection was performed using a Gene Pulser II System (Bio-Rad, Hercules, CA) using the following settings: 264 V, 975 mF, t∼20 ms. After electroporation, cells were cultured for 48h in complete RPMI1640 medium until analysis.

3.3.2 HaloTag labeling and kinetics assay

The protocol used here was derived from that described in (Merrill et al., 2019). Briefly, the day before transfection, COS-7 cells were seeded at 950 cells/cm^2 in 6-well dishes. Cells were transfected with HaloTag-MHCII-A WT or the mutants and incubated in P/S-free medium for 48 h. Two days after transfection, when the peak of MHCII-A expression occurs, cells were stained with HaloTag ligand JaneliaFluor®-585 (JF585) (50 nM) for 1 h at 37 ºC and 5% CO_2, washed, and maintained with DMEM medium supplemented with 5% FBS and NEAA for the rest of the experiment. JF585 has been shown to be stable *in vivo* over weeks, even in whole animals (Liang and Walczak, 2021). To monitor HaloTag degradation, a sample of the cells was fixed with Fixation buffer and stored at 4ºC protected from light, every day for the following eight days until acquisition on a FACSAria™ III.

3.3.3 Salt-dependent filamentation assay

Salt-dependent filamentation assays were performed as described in (Breckenridge et al., 2009). Briefly, 48h post-transfection, cells were lysed with 1 ml/150-mm dishes of cold Triton X-100 lysis buffer (50 mM Tris-HCl, pH 7.4, 5 mM NaCl, 0.6% Triton X-100, 1 mM EDTA, 1 mM EGTA, 5 mM DTT, 1 mM PMSF, 5mM $MgCl_2$, 5 mM ATP and protease and phosphatase inhibitor cocktails. Potassium acetate (CH_3CO_2K) was added at a final concentration of 560 mM. $MgCl_2$ and ATP promote non-muscle myosin II disassembly and increase NMII yield in the supernatant fraction after centrifugation. The lysate was separated by centrifugation at 7800×g for 15 min at 4°C and the supernatant was then divided in three (250 µl/salt concentration point) and mix with 750 µl of cold Triton X-100 lysis buffer + 50 mM, 145 mM, 215 mM of potassium acetate, to obtain 200, 250 and 300 mM

of final potassium acetate concentration respectively. The mix was incubated for 20 minutes at 4ºC and then centrifuged at 51,000×g for 20 min at 4°C. Pellets were then resuspended in 100 µl of cold Triton X-100 lysis buffer with potassium acetate at 560 mM, mixed 1:1 with 4× Laemmli buffer, separated using PAGE/SDS, transferred to PVDF membranes and blotted as indicated in each case. For dosimetry analyses, two 150-mm dishes were transfected per condition and 250 µl of pre-cleared lysates were mixed with 750 µl of cold Triton X-100 lysis buffer with 345, 280, 215, 145, 80 mM of potassium acetate or no potassium acetate, to obtain final concentrations of 400, 350, 300, 250, 200 and 140 mM of potassium acetate, respectively. In this case, supernatant fractions from the ultracentrifugation were precipitated with 70% acetone, the protein in the supernatant was separated by centrifugation at 7800×g for 15 min, and the pellet was suspended 1:1 in 4× Laemmli buffer. Equivalent portions of pellet and supernatants were subjected to WB analysis and probed for GFP.

3.3.4 Immunoprecipitation

48h post-transfection, cells were lysed with 350 µl/100-mm dish of cold NP-40 lysis buffer (50 mM Tris-HCl pH 7.4, 1% NP40, 150 mM NaCl, protease and phosphatase inhibitor cocktails, 5 mM $MgCl_2$ and 5 mM ATP). $MgCl_2$ and ATP promote non-muscle myosin II disassembly from actin filaments and thus increase NMII yield in the supernatant fraction after centrifugation. Cell lysates were disaggregated by ten passes through a 25G needle and centrifuged at 13000×g for 15 mins at 4ºC to remove the insoluble fraction (nucleus, cytoskeletal proteins, and plasma membrane). Before the pre-clearing step, a portion of the supernatant (50 µl) was extracted and mixed 1:1 with 4× Laemmlii buffer to obtain the lysate samples. Supernatant was then pre-cleared for 30 mins at 4ºC with MagnaBind™ Goat Anti-Mouse IgG (30 µl/100-mm dish) to reduce non-specific protein binding. After magnetic extraction of the pre-clearing beads, supernatants were incubated with either anti-FLAG or anti-GFP magnetic beads (8 µl/100-mm dish) for 2 h at 4ºC. The beads were then washed three times with lysis buffer (300 µl/100-mm dish) by magnetic isolation, resuspended in lysis buffer (60 µl/100-mm dish) and mixed 1:1 with 4× Laemmli buffer. Magnetic beads were washed and equilibrated with lysis buffer before use. The samples were separated using PAGE/SDS, transferred to PVDF membranes blocked with BSA and blotted with the antibodies indicated in each case.

3.3.5 ATPase activity determination and *in vitro* actin motility

Experiments were carried out as described in (Vasquez et al., 2016). The NADH-linked assay for ATPase determination was carried out using HMMII-A at 25°C in buffer containing 10 mM MOPS (pH 7.0), 50 mM NaCl, 2 mM $MgCl_2$, 2 mM ATP, 0.15 mM EGTA, 40 units/mL lactate dehydrogenase, 200 units/mL pyruvate kinase, 1 mM phosphoenolpyruvate, 0.2 mM NADH and varying concentrations of filamentous actin (0–100 mM). Myosin HMM was phosphorylated at room temperature for a minimum of 30 min prior to the assay by the addition of 0.2 mM ATP, 0.2 mM $CaCl_2$, 0.1 mM CaM, and 10 mg/mL MLCK.

In vitro actin motility assays were performed at 37 °C in a buffer comprising 50 mM KCl, 20 mM MOPS (pH 7.4), 5 mM $MgCl_2$, 0.1 mM EGTA, 1 mM ATP, 50 mM dithiothreitol, 0.7% methylcellulose, 2.5 mg/ml glucose, 0.1 mg/ml glucose oxidase, and 2 µg/ml catalase. Phosphorylated HMMII-A, either WT or N93K, were introduced at a protein concentration of 0.2 mg/ml into a flow chamber with a nitrocellulose-coated coverslip. The surface was subsequently blocked by 1 mg/ml bovine serum albumin and then incubated for 1 min at room temperature in a solution containing 5 µM unlabeled F-actin, 1 mM ATP, 0.2 mM $CaCl_2$, 1 µM calmodulin and 4 µg/ml MLCK. After wash-out, 30 nM F-actin labeled with rhodamine-phalloidin (Molecular Probes, Carlsbad, CA) in the above assay buffer was applied to the flow chamber. Sliding velocities of the actin filaments were analyzed at 37^{o}C using an Olympus IX70 inverted fluorescence microscope (Olympus, Hamburg, Germany), using a mercury lamp for illumination and standard rhodamine filters. Images were captured through a 100× MPlanApo, 1.4 NA objective every 2s for 3 min with an Orca Flash 4.0 CMOS camera (Hamamatsu Photonics Deutschland GmbH, Herrsching, Germany) controlled through xCellence RT software from Olympus. The velocity of actin filament movement over the myosin-coated surface was analyzed using the wrMTrck plugin for ImageJ.

3.3.6 Cell plating and immunofluorescence

Transfected cells were detached and allowed to adhere for 1h (for myosin segregation experiments) or 2 h (for adhesion assays) in 12 mm or 25 mm diameter glass

coverslips coated with 3 µg/ml fibronectin. Cells were fixed with pre-warmed PFA at 4% for 10 mins at 37 ºC, washed three times with TBS and permeabilized with 0.1% Triton X-100 in PHEM buffer, pH 6.9 (60 mM pipes, 25 mM HEPES, 10 mM EGTA, 2 mM $MgCl_2$, 2% BSA, 50 µg/ml human γ-globulins, 0.12 mM sucrose and 0.05% sodium azide) for 10 mins. Cells were blocked with PHEM Buffer for 30 mins and incubated with the indicated antibodies for 2 h followed by the appropriate Alexa Fluor- conjugated antibody and/or Alexa Fluor-conjugated phalloidin for 30 min. Incubations were performed at 37 ºC, with five rinses of 5 min with TBS between incubations before either mounting on glass slides using ProLong Glass antifade medium or storing in TBS-Azide (0.05%). Focal adhesion quantification was performed in images obtained using TIRF microscopy; therefore stained 25 mm coverslips were stored in TBS-Azide (0.05%) until imaged on Attofluor™ Cell Chambers (ThermoFisher).

For primary leukocytes, cells were allowed to adhere for 40-90 mins in 12 mm diameter glass coverslips coated with 20 µg/ml fibronectin, in the presence of 100 nM fMLP or 300 nM PMA for neutrophil adhesion assays. Cells were fixed with pre-warmed PFA at 4% for 10 mins at 37 ºC, washed three times with TBS and permeabilized with eBioscience™ Permeabilization Buffer. This buffer was also maintained during primary and secondary incubations and washes due to its reversible nature.

3.3.7 Fluorescence and confocal imaging

Imaging was performed using a confocal microscope (SP8; Leica). Images were obtained using a HC PL APO CS2 100×/1.40 OIL objective by illumination with light of the appropriate wavelength from a white laser: 499-nm for GFP or Alexa Fluor 488, 577-nm for HaloTag ligand JaneliaFluor®-585 and Alexa Fluor 568, and 653-nm for Alexa Fluor 647. Images were collected using spectral filtering and hybrid (HyD; Leica) detectors and Leica Application Suite X (LAS X) software (Leica). Images from neutrophil adhesion assays and MHCII-A staining in dendritic cells were processed using Lightning Deconvolution Image Processing software (Leica). For T cell staining of MHCII-A and adhesion assays using T lymphocytes or dendritic cells, images were acquired using a wide field fluorescence microscope (AF 6000LX DM6B-Z; Leica) fitted with a Leica DFC9000 GT VSC-12287 camera and LAS X

software (Leica). Images were obtained using a HC PL APO 100×/1.44 OIL and HC PL APO 63×/1.40 OIL objectives.

For T cells, the polarity index is calculated as the result of dividing the length of the main migration axis or major axis (which denotes the direction of migration) by the length of the perpendicular axis that passes through the centre of the nucleus (minor axis) (Vicente-Manzanares et al., 2007).

Stimulated emission depletion (STED) imaging

All the images acquired using STED were collected from cells adhered on #1.5H thickness coverslips. To remove impurities from the glass, coverslips were washed for 10 mins in MilliQ water, incubated overnight in 20% H_2SO_4, washed 3 times in MilliQ water for 10 mins and left at 37 ºC until dried ("squeaky clean" method). MEG-01 cells co-transfected with mNeonGreen-MHCII-A wild type and Halotag-MHCII-A mutants were incubated for 1h with JaneliaFluor®-635 at 50 nM (to illuminate the Halotag construct), adhered for 30 min to surfaces coated with 20 µg/ml fibronectin in the presence of 100 ng/ml PMA, then fixed as for immunofluorescence. Coverslips were then mounted using Prolong Glass and examined in a Leica SP8 STED 3× microscope. The imaging routine included the acquisition of a confocal image; sequential (635nm-491nm) acquisition with active depletion; then, acquisition of another confocal image to verify complete depletion. STED acquisition using a multi-line WLL laser with one illumination line at 635 nm depleted with 75% of a 775nm laser (for JaneliaFluor®-635 imaging) and another at 491 nm depleted with 40-50% of a 592nm laser (for mNeonGreen imaging). Laser power was 7% for both acquisition lines and HyD gain at around 100%. Images were captured through a HC PL APO, 100×/1.4 NA, Oil STED White, WD 0.13 mm objective and two parallel HyD detectors. Images were captured at 1024×1024 pixels for a pixel size of around 25nm and exported as LIF files using LAS X software. Image processing was performed using ImageJ.

3.3.8 Total internal reflection (TIRF) microscopy

All experiments acquired with TIRF microscopy were performed on #1.5H thickness coverslips prepared as indicated for the STED experiments.

Focal adhesion imaging and quantification

Stained 25 mm coverslips of #1.5H thickness were stored in TBS-Azide 0.05% until imaged, when they were mounted in Attofluor™ Cell Chambers (ThermoFisher) and maintained in Live Cell Imaging Solution (140 mM NaCl, 2.5 mM KCl, 1.8 mM $CaCl_2$, 1.0 mM $MgCl_2$, 20 mM HEPES pH 7.4). Images for adhesion assays were acquired by TIRF microscopy on an inverted microscope (AF 6000LX DMI8, Leica) equipped with a HC PL APO 63×/1.47 OIL objective, Leica DFC9000 GTC VSC-13208 camera and LAS X software (Leica). Focal adhesion quantification was performed as described in Section 3.2.7 of the Materials and Methods. At least 45 cells were analyzed per condition in three independent experiments.

In vivo high speed, simultaneous TIRF imaging

For *in vivo* experiments, GFP/HaloTag-tagged probes were acquired at 100 nm penetration depth (as selected via TIRF expert mode) with the HC PL APO 100x/1.47 OIL objective and the Hamamatsu W-View Gemini system. This system is an image splitting optics that allows the simultaneous acquisition of dual wavelength images onto the same camera at a high speed. The W-View Gemini device was aligned using 1 µm-wide Tetraspeck™ fluorescent beads. Cells were stained for 1h in P/S-free medium with HaloTag ligand JaneliaFluor®-585 (50 nM) and imaged 5-10 mins after plating on coverslips coated with fibronectin at 3µg/ml. Images were acquired every 1s for 10 minutes with a Photometrics Prime95B-A21B203015 camera. Cells were kept with Live Cell Imaging Solution supplemented with 10% FBS in temperature-controlled incubators at 5% CO_2 and 37 ºC.

3.3.9 Image Correlation Spectroscopy (ICS) analyses

Preprocessing

The preprocessing of TIRF image stacks was performed with FIJI image processing software (Petersen et al., 1993; Schindelin et al., 2012). First, the mean intensity

value of pixels within the selected background ROI for each frame was calculated and then subtracted from every pixel in the image to perform background subtraction. Next, the Trainable Weka Segmentation plugin was used to obtain the probability of each image pixel belonging to each of the following classes: minifilaments, cell body, or background (Arganda-Carreras et al., 2017). With this plugin, Random Forest segmentation models were trained on 5-10 manually segmented frames of each stack, followed by application to each frame of the stack. Thresholding was performed on the resulting probability maps to obtain binary masks with pixels that were assessed as most likely to belong to the minifilaments class. Manual mask correction was performed to fix glaring classification errors. After the binary mask was obtained for each of the two image channels, their AND mask was calculated and applied to each channel and frame of the background-corrected image stacks.

Image Correlation Analysis

The pixel intensity values contained in the segmented TIRF image stacks were used to extract information about the WT and mutant myosin IIA populations in minifilaments. The mean fluorescence intensity of the image pixels $\langle N_s \rangle$ is directly proportional to the mean number of fluorophores detected in a focal volume (Wiseman and Petersen, 1999):

$$\langle I \rangle = \frac{1}{2} \rho I_0 \varepsilon Q \langle N_s \rangle \tag{3.1}$$

Where ρ is the microscopy system's collection and detection efficiency, I_0 is the intensity of incident excitation light at the center of the focal spot, ε is the fluorophore's extinction coefficient, and Q is the fluorophore's quantum yield. Since the same optical setup was used for the acquisition of images in both detection channels, the intensity correction was performed under the assumption that the collection efficiency and incident intensity remain approximately constant for both channels (Grimm et al., 2017; Patterson et al., 1997)

$$\frac{\langle I \rangle_{JF585}}{\langle I \rangle_{eGFP}} = \frac{\varepsilon_{JF585} Q_{JF585} \langle N_{JF585} \rangle}{\varepsilon_{eGFP} Q_{eGFP} \langle N_{eGFP} \rangle} \tag{3.2}$$

Next, we used spatial image correlation spectroscopy analysis to measure the mean number $\langle N \rangle$ of independent fluorescent units of the labeled myosin IIA within the focal region in the images of minifilaments obtained with TIRF microscopy. For any

given region of interest (ROI) in an image, the fluctuations in fluorescence intensity can be defined as (Petersen et al., 1993):

$$\delta I(x,y) = I(x,y) - \langle I \rangle \tag{3.3}$$

where $I(x,y)$ and $\langle I \rangle$ are the intensity at pixel position (x,y) and the spatial average intensity of the pixels in the selected ROI, respectively. The squared relative intensity fluctuation for an image ROI (the image intensity variance divided by the mean intensity squared) is equal to the average number of independent fluorescent particles (i.e. oligomers) in the beam focal spot, $\langle N \rangle$, for ideal particles:

$$\langle N \rangle^{-1} = \frac{\langle \delta I \rangle^2}{\langle I \rangle^2} = g(0,0) \tag{3.4}$$

$\langle N \rangle$ is obtained in practice from the zero spatial lags amplitude, $g(0,0)$, of the normalized spatial intensity fluctuation autocorrelation function due the presence of white noise in the images. We defined ξ and η as spatial lags (pixel shifts), respectively, to calculate spatial autocorrelation functions for each channel in each image frame:

$$g(\xi,\eta) = \frac{\langle \delta I(x,y)\delta I(x+\xi, y+\eta)\rangle}{\langle N \rangle^2} \tag{3.5}$$

Evaluating (3.5) at zero spatial lags gives the zero lags amplitude of the correlation function $g(0,0)$ and is identical to (3.4) in this limit, thus yielding the inverse of the particle density in the image channel. However, direct calculation of accurate particle densities from correlation functions is not possible due to the omnipresent white noise and various random short-range correlations in cellular images acquired with fluorescence microscopy. Hence, autocorrelation functions were corrected by setting four values neighboring zero lags to zero weight in the amplitude fitting.

Next, $g(0,0)$ was estimated by fitting (3.5) as the 2D Gaussian function to extract the white noise-corrected zero lags amplitude via fit extrapolation:

$$g(\xi,\eta) = g(0,0)\exp\left[-\frac{(\xi-u)^2 + (\eta-\nu)^2)}{\omega_0^2}\right] + r_\infty, \tag{3.6}$$

where ω_0 is the e^{-2} correlation radius, (u,v) is the position of the Gaussian peak amplitude maximum, and r_∞ is the offset parameter to account for the long-range spatial correlations. The resulting correlation function fit was then used to estimate

the white noise corrected zero-lags amplitude of the normalized spatial intensity fluctuation correlation function.

Finally, the ratio between the mean population density of all fluorescent subunits in the ROI to the mean population density of independent fluorescent entities in the ROI was used to calculate a parameter called the degree of aggregation for the protein tagged with the fluorophore (Wiseman and Petersen, 1999):

$$\langle DA \rangle = \frac{\langle I \rangle}{\langle N \rangle} \tag{3.7}$$

Overall, parameters $\langle I \rangle$, $\langle N \rangle$, and $\langle DA \rangle$ were calculated for each frame of the 600x600 pixel 600-frame TIRF image stacks, separate for each imaging channel. All intensity and ICS analysis was performed with custom Python and MATLAB code.

3.3.10 Fluorescence Recovery After Photo-bleaching (FRAP)

For photo-manipulation experiments, transfected cells were allowed to adhere for 2h on 25-mm coverslips coated with fibronectin (8 µg/ml) and then kept in Live Cell Imaging Solution supplemented with 10% FBS at 5% CO_2 and 37 ºC in temperature-controlled incubators. A representative FRAP sequence is shown in **Figure 8**. Confocal images for photo-manipulation experiments were acquired using a confocal microscope (SP5; Leica). Images were obtained using a HCX PL APO CS 63.0× 1.40 OIL UV objective by illumination with light of the appropriate wavelength from UV-laser (for mEOS2 photo-conversion), 488-nm Ar laser (for GFP and not-photo-converted mEOS2 detection) and 561-nm diode-pumped solid-state laser (for photo-converted mEOS2 detection). Images were acquired using spectral filtering and hybrid (HyD; Leica) detectors and collected using LAS X software (Leica).

For FRAP analysis, a selected cellular area of 950 µm^2 that contained GFP-fusion proteins decorating actomyosin filaments was scanned two times and then a region of interest (6-7 µm^2) was bleached using 20 scans at 100% laser power. To image the recovery of fluorescence intensity after photo-bleaching, we recorded 5 scans at 0.526s, 15 scans at 1s and 30 scans at 4s. The bleaching effect due to image acquisition was either corrected or absent in these conditions and was verified on cells previously fixed with PFA 4%, and then imaged with the same *in vivo* experimental conditions. Background subtraction and normalization was calculated using built-

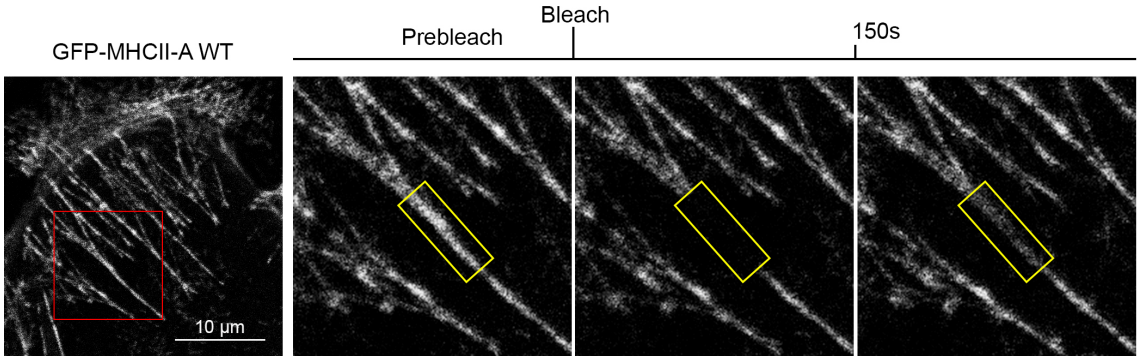

Figure 8: Representative FRAP sequence. Snapshots of a confocal time-lapse video of a COS-7 cell transfected with GFP-MHCII-A wild type. Yellow box indicates the region of interest that contains the bleached fluorescent myosin bundle. The first and second snapshot shows the cell before photo-bleaching (pre-bleach). The third snapshot corresponds to a time point captured immediately after photo-bleaching. The fourth snapshot represents the last scan after photo-bleaching.

in algorithms, and normalized intensities versus time (seconds) were represented. FRAP data were always represented as the means ± SEM of at least 40 individual measurements per condition in three independent experiments. Normalized FRAP data was fitted to a one phase exponential model following the expression

$$I(t) = P(1 - e^{-Kt})$$

to obtain the exponential rate of recovery K and the Plateau P. We verified that a one phase exponential model interpolates the data with great accuracy, as is to be expected in the reaction dominant FRAP setting, since diffusion effects were irrelevant in this case.

In the reaction-dominant model, exponential recovery rate is identical to the dissociation constant K_{off} (Brunet et al., 2006; Bulinski et al., 2001; Mii et al., 2021; Sprague et al., 2004) and it is independent of the association constant K_{on}. In fact, K_{on} cannot be obtained from the FRAP data in a direct way, since K_{on} only affects indirectly the size of the plateau through the formula

$$SK_{on} = \frac{PK_{off}}{F_{eq}}$$

where S is the concentration of free binding sites on the filament and F_{eq} is the concentration of free binding molecules (F is constant since diffusion effects are assumed to reach equilibrium instantly in this model). Thus, we could only obtain the esti-

mated $K^*_{on} = SK_{on}$ from the data and the previous formula(Sprague et al., 2004). In order to obtain an estimate of the variation of K^*_{on} between our experimental conditions, we assumed that the average of the concentration of free binding sites (S) on the filament is independent of the experimental conditions. The values of K_{off}, K^*_{on} and plateaus were obtained by fitting FRAP values to a one phase association model in GraphPad Prism with the constraint $I(0) > 0$, to remove non-physical fittings that assume negative initial values of fluorescence after photobleaching

3.3.11 Photo-conversion

Cell plating and image acquisition was performed as described in the FRAP section above. Initially, a cellular area of 950 μ^2 that contained mEOS2-MHCII-A decorated actomyosin filaments was scanned two times and a region of interest (6-7 μ^2) was photo-converted using 15 scans at 5% UV power with the 405-nm diode laser. A fraction of total mEOS2-decorated actomyosin filaments irreversibly switched its excitation/emission from green (506/516 nm) to red (571/581 nm) and the selected cellular area was imaged with the 561-nm diode- pumped solid-state laser 10 scans

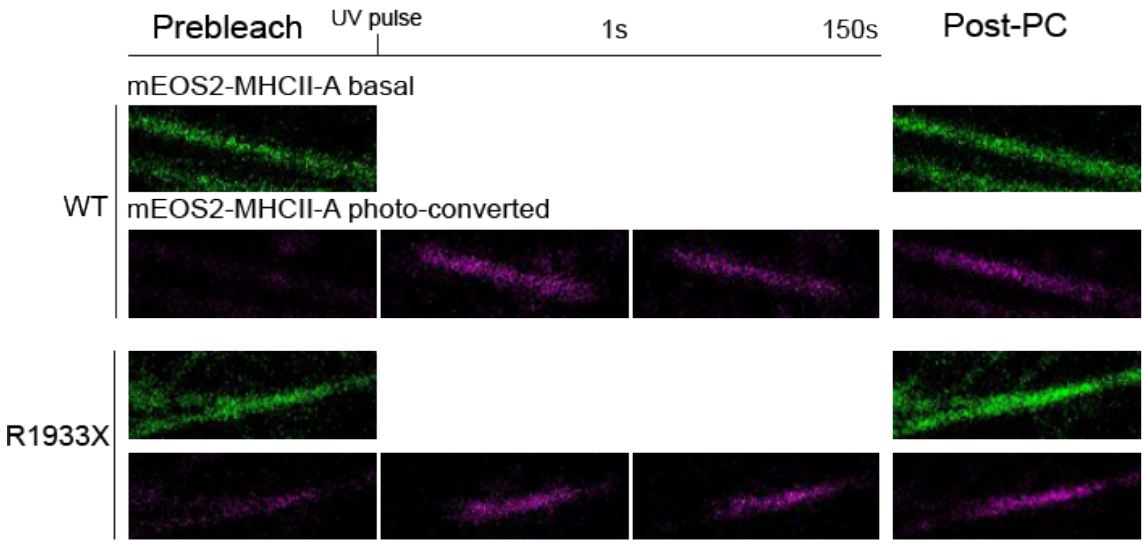

Figure 9: Representative photo-conversion sequence. Snapshot magnification of a confocal time-lapse video of a COS-7 cell transfected with mEOS2-MHCII-A wild type (top rows) or mEOS2-MHCII-A R1933X (bottom rows). The first column shows the filament before photo-conversion acquired in both channels, green and red (pre-bleach). The second column corresponds to a time point captured 1s after photo-conversion. At this point the green channel was not acquired. The fourth column represents the photo-converted bundle 150s after the UV pulse. The last column shows the imaged acquired in both channels after photo-conversion (post-PC) to verify the focal plane. Total image length=8µm.

every 0.265s, 10 scans every 1s and 30 scans every 4s (**Figure 9**). In our experimental conditions, dual acquisition of photo-converted and non-photo-converted mEOS2 produced substantial bleaching. Therefore, we only acquired the photo-converted mEOS2 molecules with the 561-nm diode- pumped solid-state laser and acquired another image at the end of the experiment to validate the focal plane position and rule out any decrease in fluorescence intensity due to a loss of the focal plane during the experiment. Bleaching effect, background subtraction and normalization of the data were assessed as described above.

Normalized photo-conversion data also adjusts to a one phase exponential model, in this case the equation

$$I(t) = P + (1 - P)e^{-Kt}$$

yields the exponential decay rate K and the Plateau P.

3.3.12 Flow Cytometry

Cells were stained for flow cytometry using PBS staining buffer (PBSst). PBSst contains 0.5% FBS, 0.5% BSA, 2.5 mM EDTA and 0.01% sodium azide. Non-sterile 5 mL polypropylene round-botton tubes (12×75 mm style) from Falcon were used to stain the cells. In some cases, cells were fixed beforehand using Fixation Buffer.

Before blood sample staining, Fc receptors on the surface of dendritic cells were blocked with 0.1 mg/ml of human γ-globulins for 30 minutes.

Extracellular staining

Cells were incubated with labelled antibodies (diluted in PBSst) against cell surface antigens for 30 minutes, washed by addition of three volumes of PBSst, centrifuged at 650×g for 3 minutes at RT and resuspended in PBSst.

For unlabelled antibodies, cells were incubated with a primary antibody against the antigen of interest for 30 minutes, washed by adding three volumes of PBSst and centrifuged at 650×g for 3 minutes at RT. Cells were then incubated with a labelled secondary antibody, which recognizes the Fc portion of the primary antibody, for 30 minutes. Finally, cells were washed again with PBSst, centrifuged at 650×g for 3 minutes at RT and resuspended in PBSst. Cell staining was performed at 4 ^{o}C.

Intracellular staining

In order to detect molecules which are not present on the cell surface, cells were fixed with Fixation Buffer, then permeabilized using 1× Permeabilization buffer, diluted in PBSst. Antibodies were diluted and washed in 1× Permeabilization buffer to preserve membrane permeability throughout the protocol.

3.3.13 Leukocyte migration

3D collagen migration and quantification

On day six, immature monocyte-derived dendritic cells were stimulated with 10 ng/ml lipopolysaccharide (LPS) for 24h to induce mDCs maturation (de la Fuente et al., 2005). 3D collagen gels were performed in Ibidi µ-Slide Chemotaxis devices, following the manufacturer's instructions.

Briefly, cells were harvested, centrifuged, and resuspended in complete RPMI medium at 18×10^6 cells/ml, to obtain a final cell suspension at 3×10^6 cells/ml when mixed with the collagen mixture. The collagen mixture was prepared on ice by adding the components as indicated in Table 4. The final addition of collagen and the cell suspension was mixed thoroughly and carefully to avoid the formation of bubbles. Immediately afterwards, 6 µl of the mixture were added to the Ibidi µ-channels and set to polymerize at 37 ºC for 15 minutes. Once polymerization was complete (the gel mixture becomes turbid and mDCs were suspended in different planes upon inspection in a conventional wide field microscope), the additional chambers were filled with complete pre-warmed RPMI1640 medium alone or in the presence of CCL19 at a final concentration of 200 ng/ml (Anderson et al., 2009).

Table 4: Composition of a 1.5 mg/ml rat collagen I gel.

Component	Volume
10x MEM	2 µl
H_2O	7,3 µl
$NaHCO_3$ 7.5%	7 µl
1x RPMI 1640	5 µl
Collagen I from rat tail (5 mg/ml)	10 µl
Cell suspension	5 µl

Cells were imaged in temperature-controlled incubators (5% CO_2 and 37 ºC) every 5 mins for the next 12h using Nikon Eclipse TE2000-E with Plan Fluor 10x (N/A 0.3) Ph1 DLL and Metamorph software.

For migration assays, the centroids of migrating cells were determined using the "Manual Tracking" plugin for ImageJ, transferred and plotted using Chemotaxis tool from Ibidi. Velocities, directness and rose plots were determined using the same software. Directness indicates the straightness of migration of a cell trajectory, and it represents the ratio between the Euclidian vs. accumulated distance of a given trajectory.

Transmigration assays

Neutrophil migration assays were carried out in Transwell® Permeable Supports, with 6.5mm-inserts in 24 well plates and 5.0 µm-pore size polycarbonate membranes. The day before the experiment was performed, cells were starved for at least 12 hours: cells were washed with PBS and resuspended in FBS-free RPMI1640, containing 0.1% BSA. On the day of the migration assay, cells were divided in three conditions:

- Control, where only cells are added in the absence of the Transwell membrane directly into the well. This condition was used for setting cell input (100%).
- Non-stimulated (basal) migration in the absence of chemoattractant.
- Stimulated migration, by adding 100 nM of fMLP at the bottom chamber of the system.

The setup was prepared adding 600 µl of medium ± fMLP to the bottom chamber of the Transwell and the cells, 1×10^6 cells per condition, in 100 µl of medium to the upper chamber of the Transwell. The Transwell filters were laid on the bottom chambers carefully and making sure no bubbles appeared during overlay. After 4 h of incubation at 37 ºC and 5% CO_2, we harvested the cells in the lower chamber and determine their number by flow cytometry. Data acquisition was carried out on a FACSAria™ III. Results for Transwell assays were reported as chemotactic index, fold increase over baseline, measured as induced migration towards N-Formyl-Met-Leu-Phe (fMLP) over basal migration without stimuli, with respect to the 100% condition.

3.3.14 *In vitro* quantification of NET formation

100 µl of PMNs at 2.5×10^6 cells/ml were seeded in 96-well assay plate (Corning #3603, Sigma Aldrich). 100 µl of control (DMSO) or PMA at a final concentration of 300 nM were added in triplicates. The experiment was performed with complete RPMI1640 medium without phenol red (Gibco) in the presence of 1 µM SYTOX Green. SYTOX green stain measurement was performed using a Tecan Infinity M200 Pro plate reader (ex:444±5 nm/ em:480±10 nm) every 10 mins for 12h at 37 ^{o}C. For time-lapse imaging, 2.5×10^5 PMNs were seeded per well in µ-Slide 8 well chambers (Ibidi) in complete RPMI1640 medium without phenol red (Gibco) in the presence of 0.25 µM SYTOX Green. Cells were stimulated with 300 nM PMA or DMSO (control) and imaged at 5 mins intervals for 5.5h in temperature-controlled incubators. Widefield and fluorescent images were acquired using AF 6000LX DMI8 (Leica) microscope equipped with HC PL APO 40×/0.95 DRY (NA: 0.95) objective, with the appropriate lasers and filters and LAS X Software (Leica). The quantification of NET formation was performed by counting the number of SYTOX green-positive cells in each time point imaged, divided by the total number of cells in the analyzed field.

3.4 Statistics

Statistical significance between two groups was calculated using two-tailed Student's t test for parametric variables, Mann-Whitney's U test for nonparametric variables and Wilcoxon matched-pairs signed rank test for paired and nonparametric variables. Shapiro-Wilk normality test was performed to determine if the data displayed a normal or non-normal distribution. Ranges of significance were represented with the p value. (*) $p < 0.05$; (**) $p < 0.01$; (***) $p < 0.001$; and (****) $p < 0.001$. All statistical analyses and graphic representations were performed using GraphPad Prism 8.

3.5 Ethics statement

This study was performed according to the principles of the Declaration of Helsinki and approved by the local Ethics Committee for Basic Research at the "Hospital Universitario de Salamanca" for blood sample collection; informed consent was obtained from all human volunteers.

4 Results

4.1 Results: part 1

4.1.1 Preliminary data

In this section, we summarize data from the work that was developed by previous members of the group. Their inclusion here is necessary for a complete understanding of the results presented later in this chapter.

Tyrosine phosphorylation of the RLC on residues 142 (Y142) and 155 (Y155) was originally described back in the 1980s (Gallis et al., 1983). Since then, their occurrence has been confirmed in several phospho-proteomics studies, aggregated in Phosphosite Plus (https://www.phosphosite.org/, genes *Myl9* and *Myl12*), but its biological significance remained unaddressed. To investigate their role in a cellular context, our laboratory reassessed the occurrence of phosphorylation of these tyrosine residues by mass spectrometry. These experiments confirmed the presence of mono-phosphorylated peptides of Y142 and Y155. Less than 10% of the total immunoprecipitated RLC was phosphorylated in these residues. Also, we detected S19 phosphorylation on approximately 70% of total immunoprecipitated RLC, as expected. Finally, mass spectrometry revealed that a very small percentage of cellular RLC was bis-phosphorylated on T18+S19 and/or Y142+Y155 (**Figure 10**).

Our group also developed plasmid constructions of RLC carrying phospho-mimetic (Tyrosine to Glutamic acid) and non-phosphorylatable (Tyrosine to Phenylalanine) mutants of Y142 and Y155 residues, coupled to EGFP or FLAG tags. The study of their effect on NMII filamentation was subsequently performed by expressing mutant RLCs in CHO.K1 cells to levels comparable to those of endogenous RLC (Vicente-Manzanares et al., 2008). The cells were then allowed to spread on fibronectin. None of the mutants had an effect on the expression levels or localization

SITE [a]	Phosphopeptide	Digest [b]	% rel. phos [c]
T18+S19 [d]	^{12}RPQRA**TS**NVFAMFDQSQIQE^{32}	Sub Lys-C	3
S19	^{12}RPQRAT**S**NVFAMFDQSQIQE^{32}	Sub Lys-C	70
Y142	^{141}M**Y**REAPIDKKGNFNYVE^{157}	Glu-C	6
Y155	^{141}MYREAPIDKKGNFN**Y**VE^{157}	Glu-C	8
Y142+Y155 [d]	^{141}M**Y**REAPIDKKGNFN**Y**VE^{157}	Glu-C	1

Figure 10: Identification of RLC tyrosine phosphorylation sites by mass spectrometry. Results of mass spectrometry analysis of immunoprecipitated FLAG-RLC from HEK-293 cells treated with peroxovanadate and calyculin A to inhibit Tyr and S/T phosphatases. Phosphorylated residues are in underlined bold within the sequence. See (Aguilar-Cuenca et al., 2020) for additional details.

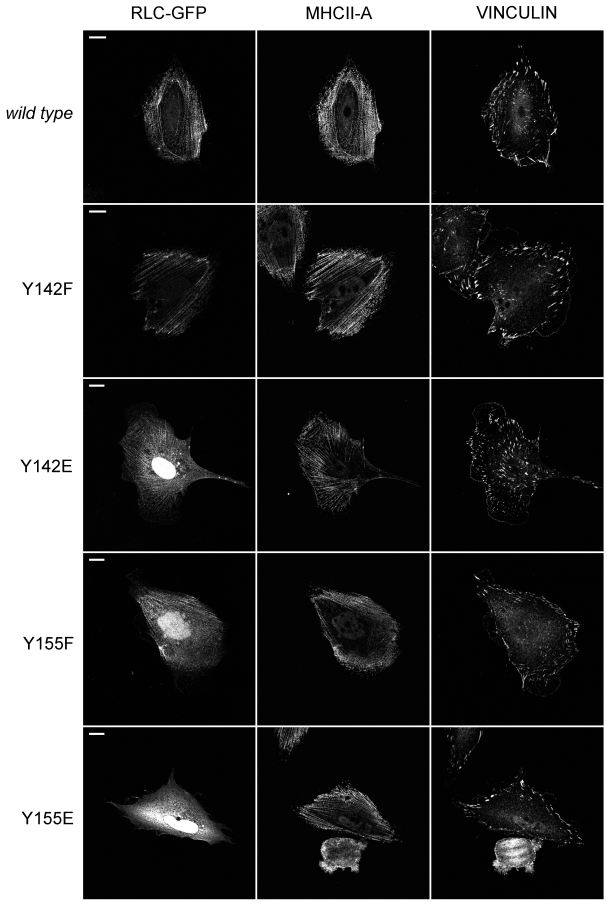

Figure 11: Y155 is required for the correct localization of RLC to actomyosin filaments. Confocal images of fibronectin-bound, CHO.K1 cells transfected with the indicated EGFP-tagged versions of RLC. After 2h of adhesion, cells were fixed, permeabilized and stained for endogenous vinculin and MHCII-A. Bars=10 µm. Pictures are representative of $>$ 500 cells examined in three independent experiments.

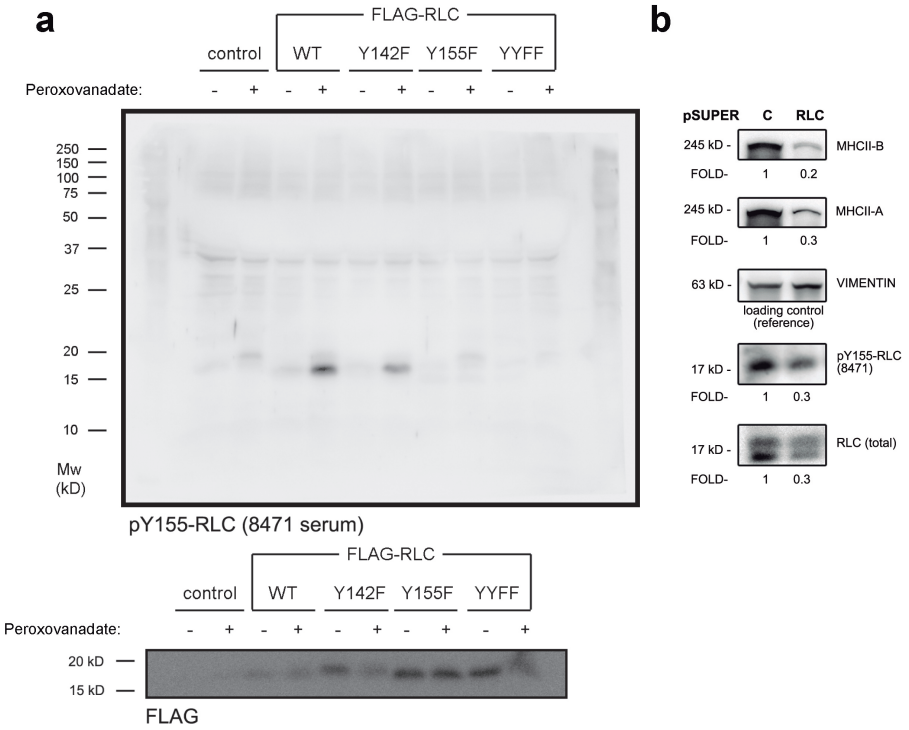

Figure 12: The 8471 antiserum recognizes RLC phosphorylated on Y155 by Western blot. (a) CHO.K1 cells were transfected, or not (control), with the indicated FLAG-RLC mutant and treated (+) or not (-) with 1 µM sodium peroxovanadate for 30 min. Cells were lysed and extracts blotted using the 8471 antiserum (1:1000 dilution, top panel) or anti-FLAG antibody (loading control, bottom panel). **(b)** CHO.K1 cells were transfected with pSUPER-RLC or a control sequence (pSUPER-C), cultured for 96h and lysed. Lysates were separated by PAGE/SDS and blotted against pY155-RLC, MHCII-A and MHCII-B. Vimentin is shown as a loading control. Experiment is representative of five performed.

of MHCII-A (**Figure 11**) or MHCII-B. The images revealed that RLC Y142F localized to myosin filaments with similar frequency to that of endogenous, wild type RLC, whereas RLC Y142E localized less frequently to myosin filaments and displayed increased nuclear localization (**Figure 11**, third row). The behavior of RLC Y155F was similar to that of RLC Y142E, displaying less frequent localization to myosin filaments, mostly appearing instead in a diffuse fashion in the cytoplasm and the nucleus. On the other hand, RLC Y155E almost never appeared in myosin filaments (**Figure 11**, bottom row). The experiments indicated a decreased capability of Y142E, Y155F and specially Y155E to compete with endogenous RLC on pre-assembled actomyosin filaments.

We also generated and confirmed the specificity of a polyclonal antibody (8471) for the recognition of RLC epitope around Y155 only when Y155 is phosphorylated. The antibody was used to demonstrate RLC phosphorylation on Y155 upon stim-

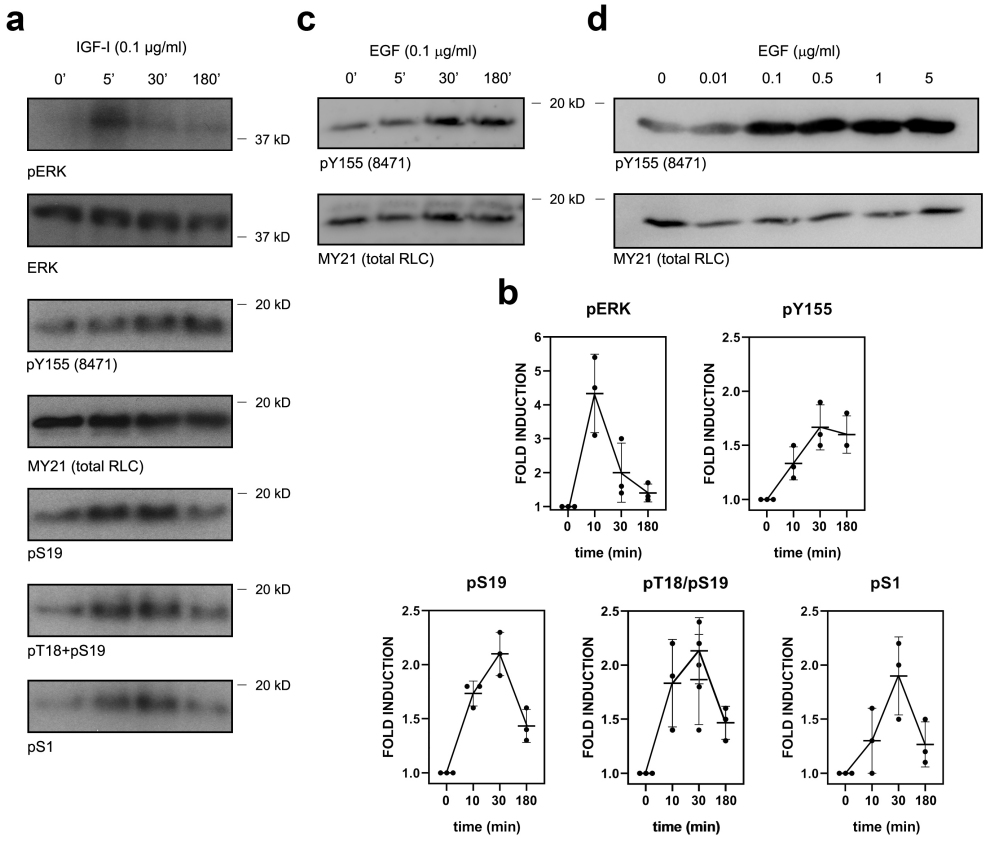

Figure 13: Growth factor-dependent phosphorylation of RLC on Y155 is kinetically different from its phosphorylation on S1, S19 and T18/S19. **(a)** CHO.K1 cells were serum-starved for 16h, then treated with IGF-I (0.1 µg/ml) for the indicated times, lysed with Laemmli buffer and blotted for ERK, phosphorylated and total; and RLC, phosphorylated in the indicated residues and total. Experiment is representative of three performed. **(b)** Quantification of the densitometric profiles of the blots shown in (a) and its biological replicates. **(c)** Serum-starved A549 cells were treated for the indicated times with 0.1 µg/ml EGF and treated as in (a). Experiment is representative of three performed. **(d)** Serum-starved HEK-293 cells were treated for 30 min with the indicated dose of EGF. Experiment is representative of three performed.

ulation with peroxovanadate in serum-starved CHO.K1 cells (**Figure 12a**). The specificity for RLC was also confirmed in RLC knockdown experiments the same cell line (**Figure 12b**).

Since growth factors promote Y155 phosphorylation in carcinoma cells (Gallis et al., 1983), we previously characterized the role of phosphorylation of RLC on Y155 as a regulator of NMII assembly in the context of growth factor-driven protrusion. Several cell lines were used that respond to IGF or EGF. CHO.K1 cells do not respond to EGF (Jo et al., 2003), but they strongly do to IGF-I (Sunstrom et al., 1998), eliciting many common downstream signals (Voudouri et al., 2015). In these cells, the 8471 antibody revealed a modest and sustained increase (up to 3h) in the

levels of RLC phosphorylated on Y155 in response to IGF-I (**Figure 13A-B**). Y155 phosphorylation kinetics was markedly different from those of RLC phosphorylation on S19, T18/S19 and S1 in response to the same stimulus, which reached a maximum after 30 min, declining sharply thereafter (**Figure 13A-B**). Similar observations were made in A549 cells (**Figure 13C**) and in HEK-293 cells in a dose-dependent manner in response to EGF (**Figure 13D**), as both cell lines respond robustly to this growth factor (Diaz et al., 2010; Thebault et al., 2009). These experiments indicated that growth factors of the EGF/IGF-I family trigger phosphorylation of RLC on Y155 in live cells. However, the global increase in Y155 phosphorylation was modest.

All these data are direct precedents that lead into the first part of this thesis, that is, the characterization of the role of Y142 and Y155 and their phosphorylation on RLC function.

4.1.2 Phospho-mimetic and non-phosphorylatable mutants of RLC Y142 and Y155 differentially affect the ability of NMII to promote adhesion maturation, front-back polarity and cell migration.

To address whether modification of Y142 and Y155 residues of RLC has an effect on NMII function, we silenced RLC in CHO.K1 cells, followed by rescue with an EGFP-coupled, silencing-insensitive form of RLC in which Y142/155 had been mutated to Glu (phospho-mimetic) or Phe (non-phosphorylatable). Efficient silencing of endogenous RLC using a specific short hairpin RNA (shRNA) also decreased the levels of endogenous MHCII-A and MHCII-B (**Figure 14A**), consistent with a previous report (Park et al., 2011). At a cellular level, RLC silencing induced a spiky, round phenotype (**Figure 14B**).

We found that expression of wild type RLC and the Y142F, Y142E and Y155F mutants to levels comparable to those of endogenous RLC efficiently restored expression of MHCII-A (**Figure 14B-C**) and MHCII-B (**Figure 14C**). However, Y155E did not (**Figure 14B-C**). On the other hand, RLC depletion did not significantly affect the expression of Myo18A, another myosin variant that also interacts with RLC (Guzik-Lendrum et al., 2013; Tan et al., 2008) (**Figure 14C**). We next examined

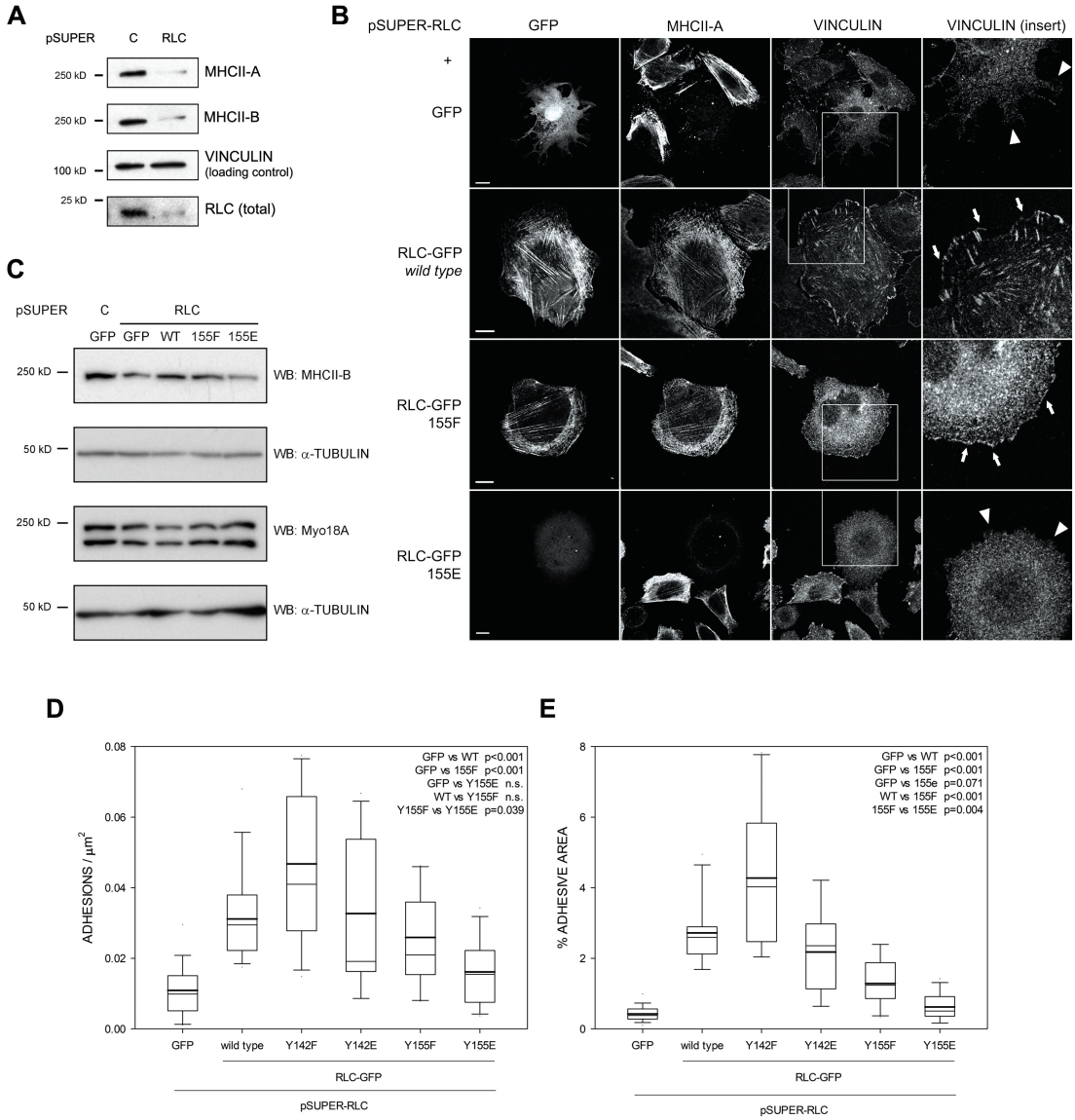

Figure 14: Replacement of endogenous RLC with phosphomimetic/non-phosphorylatable mutants reveals a key role for Y155 in NMII assembly and adhesion maturation. **(A)** CHO.K1 cells were transfected with pSUPER-RLC or a control sequence (pSUPER-C), cultured for 96h and lysed. Lysates were separated by PAGE/SDS and blotted against RLC, MHCII-A and MHCII-B. Vinculin is shown as a loading control. Experiment is representative of eight performed. **(B)** CHO.K1 cells were co-transfected with pSUPER-RLC together with EGFP or RLC-EGFP, wild type, Y155F or Y155E (first column). After 96h, cells were allowed to spread on fibronectin for 2h, fixed, permeabilized and stained as indicated. Bars=10 µm. Fourth column, magnification of the boxed regions in the vinculin column. Arrows point to adhesions. Arrowheads indicate the lack of adhesions in comparable regions. **(C)** CHO.K1 cells were co-transfected with a control sequence (pSUPER-C) or pSUPER-RLC and EGFP or the indicated RLC-EGFP mutants, cultured for 96h and lysed. Lysates were separated by PAGE/SDS and blotted against MHCII-B or Myo18A. Alpha (α)-tubulin is shown as a loading control. Note the decrease in the levels of MHCII-B in the pSUPER-RLC+EGFP and the pSUPER-RLC+Y155E lanes, but the restoration in the wild type and Y155F lanes. Conversely, the levels of Myo18A are not altered significantly. Experiment is representative of three performed. **(D-E)** Quantification of the number of adhesions per µm^2 **(D)** and adhesive area **(E)** in the conditions represented in (B). n $\geq$ 20 cells from three independent experiments ($>$ 2000 adhesions per condition). Significances were determined using Mann Whitney's U test and are shown in the figures.

focal adhesion formation, size and distribution, and found that RLC depletion abrogated focal adhesion formation (**Figure 14D**). Surprisingly, this effect extended to nascent adhesions that assemble in protruding lamellipodia (**Figure 14B**, arrowheads in top right panel). Wild type RLC and both Y142 mutants restored adhesion elongation and distribution (**Figure 14B**, arrows in second row, fourth panel). Y142F RLC had a stronger effect on focal adhesions than that of wild type RLC (**Figure 14D-E**). On the other hand, the Y155E mutant did not rescue at all the effects caused by the loss of endogenous RLC (**Figure 14B, D-E**). Y155E-expressing, endogenous RLC-depleted cells remained devoid of elongated adhesions in the lamellum and cell body, and nascent adhesions in the lamellipodium (**Figure 14B**, arrowheads in bottom right panel). Interestingly, the Y155F RLC mutant efficiently restored the number of adhesions (**Figure 14D**), but it poorly rescued adhesion elongation in the lamellum and cell body (**Figure 14B, D**). Conversely, it did restore the formation of nascent adhesions in lamellipodia (**Figure 14B**, arrows in third row, fourth panel). When we examined the organization of NMII filaments, we observed that depletion of endogenous RLC enhanced the localization of RLC Y142E and RLC Y155F to myosin filaments (**Figure 15A**), but not the Y155E mutant, which did not support myosin filament formation even when endogenous RLC was removed (**Figure 14B** and **Figure 15A**).

Consistent with previous data in which we had depleted the levels of MHCII-A and II-B (Choi et al., 2008; Vicente-Manzanares et al., 2008), RLC depletion also increased cellular spreading and produced a significant loss of front-back polarity (**Figure 15A-B**). Expression of near-endogenous levels of wild type RLC and both Y142 mutants also reversed this effect, but RLC Y155E did not. Interestingly, RLC Y155F did not restore polarity, despite having the ability to partially support NMII focal adhesion assembly and actomyosin filament formation as described above (**Figure 14D** and **Figure 15A**). Importantly, RLC Y155F also displayed defective phosphorylation on S19 and T18+S19 in response to adhesion (**Figure 15C**). Loss of front-rear polarity resulted in the inability of the cells to migrate properly on bi-dimensional substrates, which was restored by expression of wild type RLC, but not RLC Y155E (**Figure 15D-E**). On the other hand, RLC Y155F partially restored cell migration, but to a reduced extent compared to wild type RLC (**Figure 15E**).

Together, these data delineate a key role for Y155 modifications in the control of the cellular functions of NMII. Our data establish that mutation of Y155 to E (Glu)

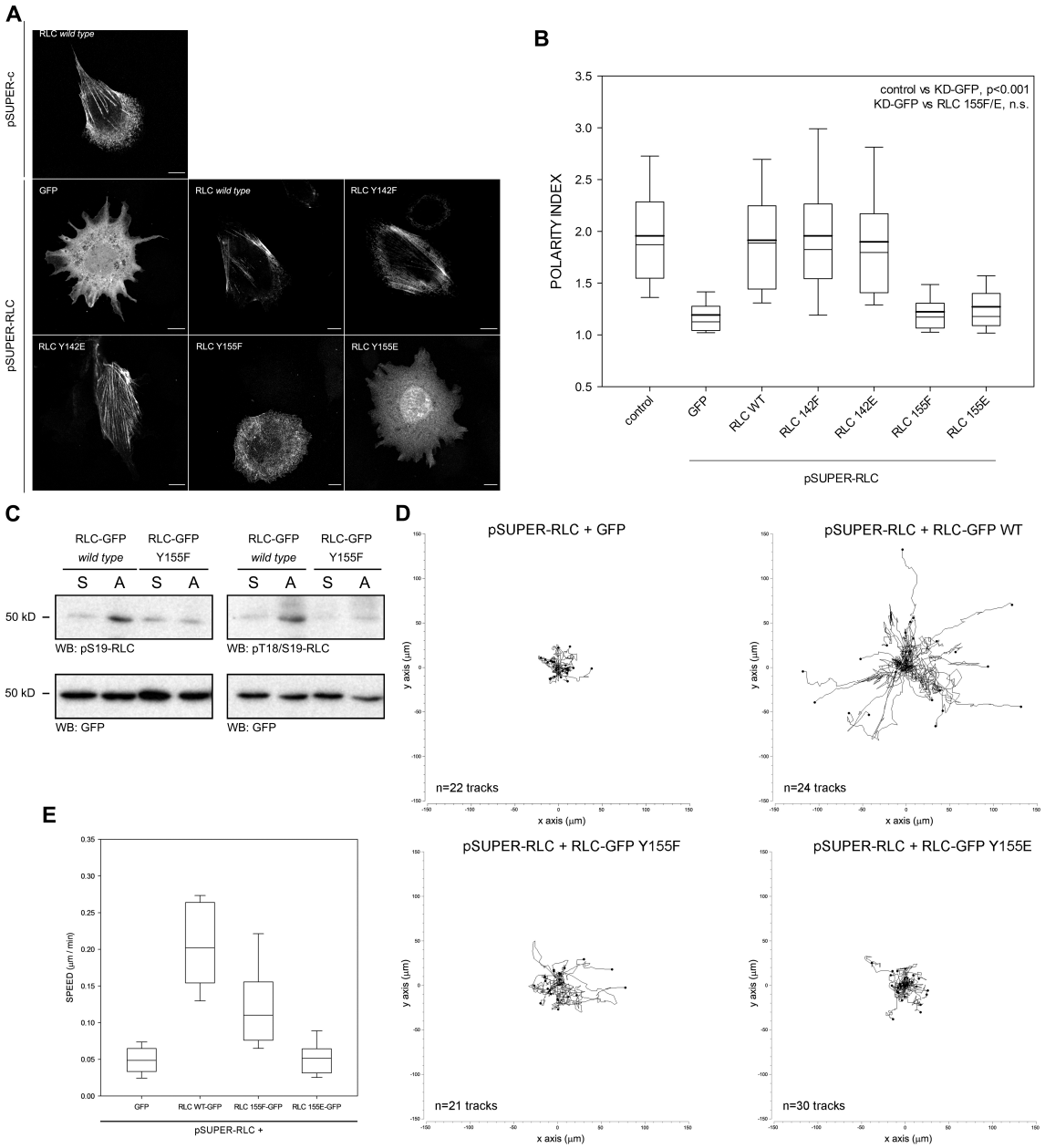

Figure 15: Y155 is required to generate NMII-dependent front-back polarity and enable cell migration. **(A)** CHO.K1 cells were co-transfected with pSUPER-C and pSUPER-RLC and EGFP or the indicated EGFP-coupled RLC mutants. After 96h, cells were allowed to adhere to fibronectin for 2h and fixed. Bars=10 µm. Representative confocal images of > 500 examined per condition in three representative experiments. **(B)** Quantification of the polarity index as indicated in Section 3.2.7 of the Materials and Methods chapter from three independent experiments. Relevant significances are indicated in the figure. **(C)** CHO.K1 cells expressing EGFP-tagged RLC or the Y155F mutant were either kept in suspension (S) or allowed to adhere to fibronectin for 1h (A) and lysed. Lysates were separated by PAGE/SDS, transferred to PVDF membranes and blotted as indicated. Experiment is representative of three performed. **(D)** CHO.K1 cells were transfected with pSUPER-RLC and co-transfected with EGFP (control) or EGFP-coupled wild type (WT) RLC, Y155F or Y155E mutant as indicated. After 96h, cells were sorted by flow cytometry, adhered to fibronectin-coated coverslips and filmed as they migrate freely for sixteen hours. Data represent the indicated number of tracks from a representative experiment out of three performed. **(E)** Speed measurements from the analysis of migratory tracks as shown in (C). All the conditions are significantly different with respect to each other except EGFP vs. Y155E.

completely abrogates the ability of RLC to enable the cellular function of NMII, whereas its substitution with F (Phe) allows NMII to form filaments and assemble nascent adhesions. However, NMII filaments containing RLC Y155F do not support proper adhesion maturation outside lamellipodia, enable front-back cell polarization or efficient bi-dimensional cell migration.

4.1.3 Phosphorylation of the RLC on Y155 impairs its association to the myosin heavy chain to form functional NMII hexamers

The experiments described in Section 4.1.2 suggested that Y155 of the RLC acts as a dial that controls the ability of NMII to perform its cellular functions to a different degree when it is Tyr (Y, wild type), Phe (F, non-phosphorylatable) or Glu (E, phospho-mimetic). However, these experiments did not provide mechanistic insight into the actual control mechanism. Based on the structure of RLC on smooth muscle myosin II (SMMII) and assuming a reasonable degree of similarity between the interactive surfaces of SMMII and NMII with RLC due to their sequence homology, it would appear that the C-terminal domain of RLC (where Y155 lies) adopts a clamp-like conformation that stabilizes the interaction with part of the lever arm of MHCII in the folded conformation, suggesting a role in the formation and stabilization of the 10S structure (Heissler et al., 2021). Due to the ability of Glu (E) substitutions to mimic Tyr (Y) phosphorylation in some contexts (Atilgan et al., 2006), the two most likely possibilities are that: (i) Y155 phosphorylation controls the conformation of NMII; or (ii) that it regulates the interaction of the RLC with the heavy chain to form the NMII hexamer in an allosteric manner. In (i), RLC would interact normally with MHCII; in (ii), the interaction of RLC with MHCII would be affected. To distinguish between these two possibilities, we first examined the interaction of the RLC Y155 mutants with MHCII in control, live cells by co-immunoprecipitation. Although MHCII-B was preferentially analyzed in these experiments because the MHCII-B antibody provided a better yield in immunoprecipitation, similar data were obtained when an antibody against MHCII-A was used. We found that immunoprecipitation of MHCII-B pulled down a reduced amount of RLC Y155F and a negligible amount of RLC Y155E compared to wild type RLC (**Figure 16A**, second row). Reciprocal immunoprecipitation of

RLC-EGFP mutants showed a reduced capability of RLC Y155F to interact with MHCII-B. Also, MHCII-B was almost undetectable in RLC Y155E immunoprecipitates (**Figure 16B**, first row). These results suggested that Y155 phosphorylation negatively regulates the interaction of MHCII with RLC during the formation or turnover of the NMII hexamer. They also suggested that phospho-Y155 RLC does not interact properly with MHCII. However, Y155E RLC is a proxy of phosphorylation, but it may not replicate all the changes caused by actual phosphorylation. To formally address this, we used the polyclonal antibody (8471) that recognized the RLC epitope around Y155 only when Y155 is phosphorylated (**Figure 12**). We aimed at identifying the kinase(s) that could mediate Y155 phosphorylation. The Scansite algorithm (Obenauer et al., 2003) predicted that RTK receptors (PDGFR, EGFR) could phosphorylate RLC directly on Y155. To test this, we produced recombinant, FLAG-tagged RLC (**Figure 16C**, third row) and used it as a substrate for a GST-fusion protein containing the active kinase domain of EGFR (**Figure 16C**, first row). The kinase domain of EGFR robustly phosphorylated wild type, recombinant RLC on Y155 as detected by the 8471 antibody. Also, the Y142F mutant RLC was also phosphorylated on Y155. However, the antibody did not recognize the Y155F mutant (**Figure 16C**, second row). This experiment indicated that RLC can be phosphorylated *in vitro* by EGFR on Y155, and the 8471 antibody enabled its detection.

We next immunoprecipitated MHCII-B and examined the phosphorylation status of the associated RLC on Y155 and S19. To boost RLC phosphorylation on Y155, we treated the cells with peroxovanadate. As expected, we detected RLC phosphorylated on S19 in MHCII immunoprecipitates, consistent with the canonical activation mechanism of NMII by phosphorylation of this residue (**Figure 16D**, third row). However, we did not detect phospho-Y155 RLC in MHCII immunoprecipitates (**Figure 16D**, second row, last lane), despite the presence of abundant phospho-Y155 RLC in peroxovanadate-treated cell lysates (**Figure 16D**, second row, second lane). Together with the co-immunoprecipitation assays using the Y155E mutant, these experiments strongly suggested that, when phosphorylated on Y155, RLC interacts poorly with MHCII. To confirm this, we pulled down endogenous MHCII-B and incubated the immunoprecipitates with increasing amounts of FLAG-tagged RLC, non-phosphorylated or phosphorylated in Y155 by pre-incubation with active EGFR kinase and ATP. We used wild type RLC and the Y142F mutant to pre-

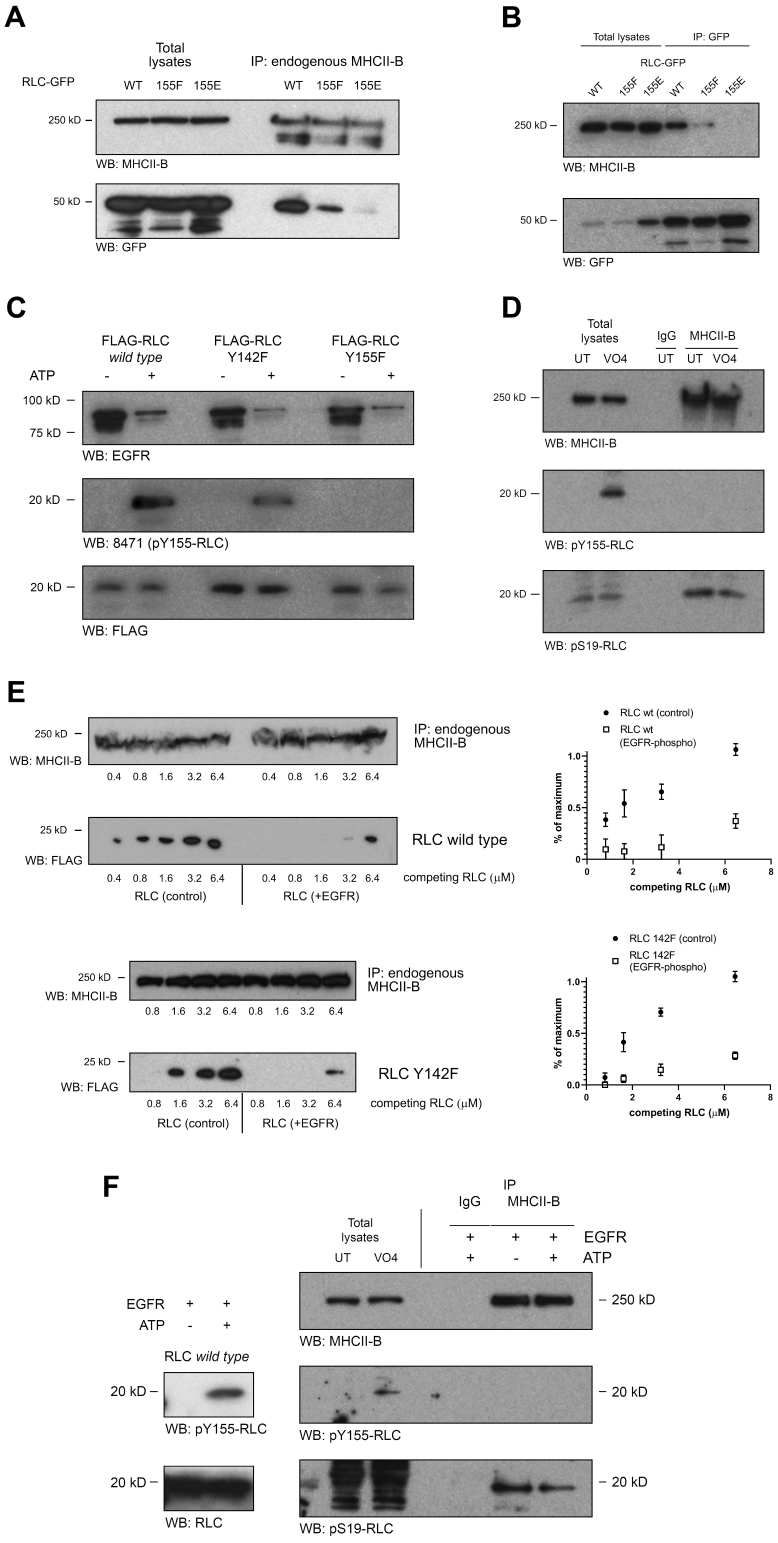

Figure 16: Y155 phosphorylation abrogates the association of RLC to NMII hexamers and filaments. **(A)** Cells were transfected with wild type (WT throughout the figure) RLC-EGFP or the indicated mutants. After 24h, cells were lysed and endogenous MHCII-B was immunoprecipitated with a specific antibody. Immunoprecipitated proteins were separated by PAGE-SDS and blotted for MHCII-B (immunoprecipitation yield, top) and EGFP (bottom). A representative experiment of three performed is shown.(Continues in the next page).

(B) Cells were transfected and lysed as in (A). RLC-EGFP variants were then immunoprecipitated with GFP-TRAP magnetic agarose. Immunoprecipitated proteins were separated by PAGE-SDS and blotted for MHCII-B (top) and EGFP (immunoprecipitation yield, bottom). A representative experiment of three performed is shown. **(C)** *In vitro* kinase assay of recombinant FLAG-RLC, wild type or the indicated mutants (substrates) and recombinant active GST-EGFR (kinase). The *in vitro* kinase assay was carried out for 30 min at 30^{o}C in the presence (+) or absence (-) of ATP, stopped with Laemmli buffer, separated by PAGE/SDS, transferred to PVDF membranes and blotted using antibodies against EGFR (top), pY155 (middle) and FLAG (bottom). A representative experiment out of five performed is shown. **(D)** CHO.K1 cells were treated (VO_4) or not (UT) with 1µM sodium peroxovanadate for 30 min, lysed and endogenous MHCII-B was immunoprecipitated with a specific antibody. Immunoprecipitated proteins were separated by PAGE-SDS and blotted for MHCII-B (immunoprecipitation yield, top), or its associated RLC, phosphorylated in pY155 (middle) or pS19 (bottom). A representative experiment of three performed is shown. **(E)** MHCII-B was immunoprecipitated from untreated CHO.K1 cells as in (D). Equal amounts of the immunoprecipitates were separated and incubated with increasing amounts of competing FLAG-tagged RLC, wild type (top) or Y142F, non-phosphorylated (left) or phosphorylated for 30 min with recombinant active GST- EGFR kinase in the presence of ATP (right). First and third box depict blotted MHCII-B (immunoprecipitation yield); second and fourth box depict blotted FLAG. A representative experiment of three performed is shown. Right panels represent the quantification of the densitometric analysis of three independent experiments as in left. **(F)** *In vitro* kinase assay of recombinant RLC (left) or endogenous RLC assembled into NMII (right). Blots on right represent endogenous MHCII-B immunoprecipitated as in (A). Immunoprecipitated material was incubated with EGFR kinase (rEGFR) fragment in the presence (+) or absence (-) of ATP as indicated before. Lysates of untreated and peroxovanadate-treated cells are also shown as reference. Samples were blotted with anti-MHCII-B (immunoprecipitation yield, top); anti-pY155 RLC (middle boxes) or pS19 RLC (bottom boxes). Panels in left depict an *in vitro* kinase assay done in parallel to the one shown in the panels on right, using the same reagents and conditions except the phosphorylation substrate, which in this case was 1 µg of recombinant, wild type FLAG-RLC. A representative experiment of three performed is shown.

vent interferences from the potential phosphorylation of Y142 by EGFR. In both cases, we observed that, while non-phosphorylated RLC readily displaced endogenous RLC from immunoprecipitated MHCII-B, Y155-phosphorylated RLC did it only at a much higher concentration (**Figure 16E**, second and fourth rows). This clearly indicates that Y155-phosphorylated RLC has a decreased affinity for MHCII-B compared to the non-phosphorylated form.

These experiments prompted us to probe whether RLC could actually become phosphorylated on Y155 while in the context of the NMII hexamer. We performed *in vitro* phosphorylation experiments, in which we used the entire NMII hexamer (immunoprecipitated with an antibody against MHCII-B) as a substrate for recombinant EGFR kinase. We found that, when in the context of the NMII hexamer, RLC did not become phosphorylated on Y155 (**Figure 16F**, second row, last lane), whereas it was readily phosphorylated in the NMII-unbound, free form (**Figure 16F**, left boxes). Also, experiments done in collaboration with the group of Sarah

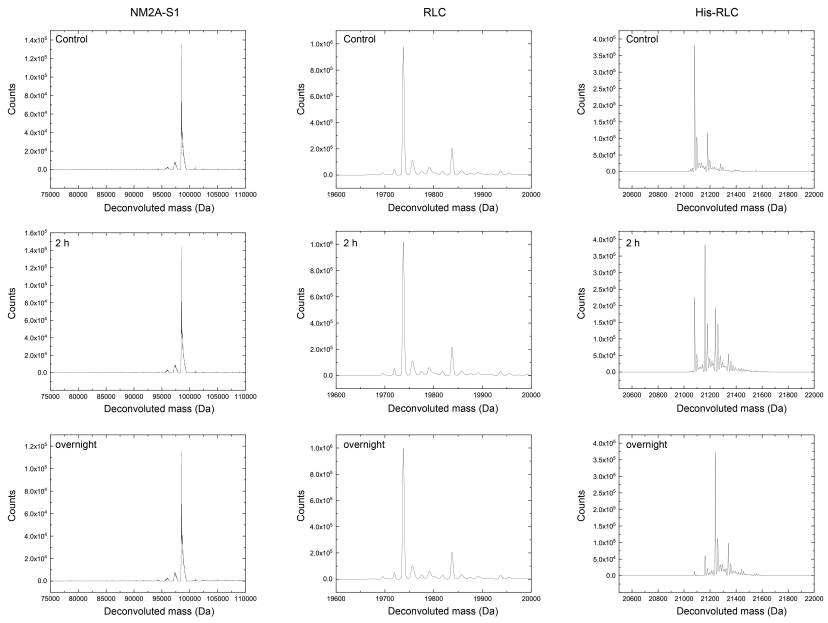

Figure 17: Phosphorylation of free, but not S1-associated RLC determined by intact protein mass spectrometry. Intact protein mass spectrometry of MHCII-A subfragment-1 and His-RLC after phosphorylation with EGFR. Deconvoluted mass spectra of the MHCII-A motor domain (left), the subfragment-1-bound RLC (center) and His-RLC (right) are shown after 2h and overnight incubation with EGFR as well as non-phosphorylated controls. Note that EGFR neither phosphorylated the MHCII-A motor domain nor the subfragment-1 bound RLC. 55.2% of the His-RLC was single phosphorylated and 23.2% double phosphorylated by EGFR after 2 hrs. Overnight incubation resulted in 11.3% single phosphorylated and 86.5% double phosphorylated His-RLC.

Heissler (Ohio State University) using recombinant subfragment-1 NMII-A produced in baculovirus transduced-Sf9 cells, or free recombinant His-tagged RLC, followed by *in vitro* phosphorylation with recombinant EGFR kinase and mass spectrometry analysis yielded a similar conclusion (**Figure 17**). These data show that RLC becomes phosphorylated in Y155 when free, that is, outside of the context of the NMII hexamer, and that Y155 phosphorylation effectively prevents RLC incorporation to the hexamer.

4.1.4 Preferential phosphorylation of the RLC on Y155 at the leading edge contributes to the inhibition of local NMII assembly in protrusions

Growth factors induce actin polymerization-driven protrusion. Others and our group have shown that NMII is not actively assembling in the protruding region; if it does, protrusion stops (Burnette et al., 2011; Vicente-Manzanares et al., 2011).

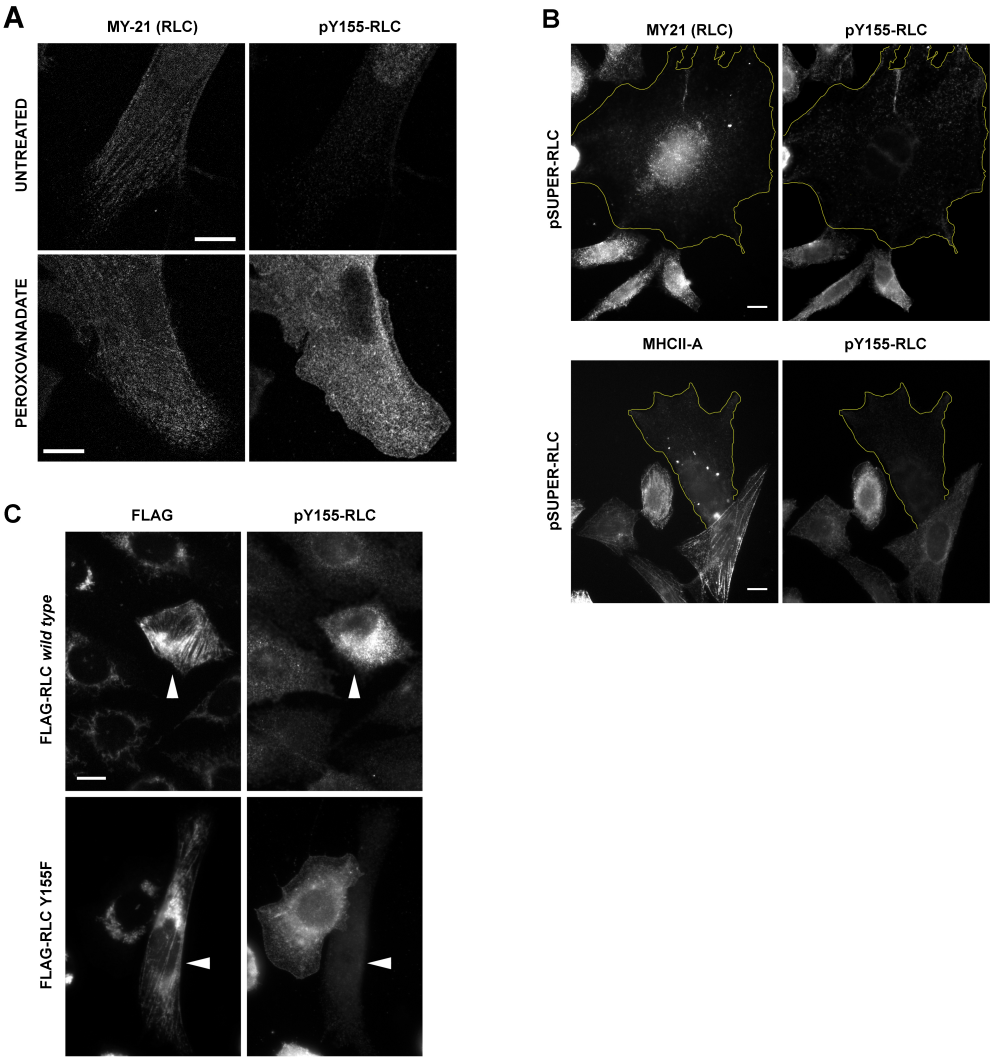

Figure 18: The 8471 antiserum recognizes RLC phosphorylated on Y155 in indirect immunofluorescence assays. (A) CHO.K1 cells were allowed to spread on fibronectin, either left untreated (top row) or treated with 1 µM peroxovanadate for 30 min (bottom row). Cells were subsequently fixed and stained for RLC (MY21, left column) or pY155 RLC (right column). Bars= 10µm. Images were collected and are shown using the same acquisition and representation settings, respectively. **(B)** Representative immunofluorescence images of a RLC-depleted cell (outlined in yellow), stained for endogenous, total RLC (MY21, left) and pY155 RLC (right). Note the much bigger size of the RLC-depleted cell and decreased MY21 signal compared to the non-depleted cells at the bottom. Bars=10 µm. Images represent $>$ 200 cells examined in three independent experiments. **(C)** Representative immunofluorescence images of RLC-depleted cells rescued with FLAG-tagged RLC, wild type (top row) or Y155F (bottom row). Cells were stained for FLAG (left column) and pY155 RLC (right column). Bar=10 µm. Arrowheads point to transfected cells. Note the increased signal in the wild type RLC-transfected cell compared to the Y155F-expressing cell. Images represent $>$ 100 cells examined in three independent experiments.

The group previously studied the phosphorylation of RLC on Y155 as a regulator of NMII assembly in the context of growth factor-driven protrusion (see preliminary data, **Figure 13**). These experiments indicated that growth factors of the EGF/IGF-I family trigger phosphorylation of RLC on Y155 in live cells. However, it is important to highlight that the global increase in Y155 phosphorylation was modest. This suggested that this phosphorylation could be important regionally to control NMII assembly. To investigate whether the increase in Y155 phosphorylation was spatially restricted, we examined the localization of phospho-Y155 RLC in CHO.K1 cells treated with IGF-I. Since the antibody that detects phospho-Y155 had not been previously used for immunofluorescence, we set up a series of specificity controls (shown in **Figure 18**), which needed to satisfy several validation criteria. Specifically, we observed a clear signal increase in response to peroxovanadate (**Figure 18A**) that decreased in RLC-depleted cells (**Figure 18B**). Also, staining intensity increased in cells overexpressing wild type, FLAG-tagged RLC (**Figure 18C**) but not in cells expressing the Y155F mutant (**Figure 18C**).

Then, we probed the localization of phospho-Y155 RLC in migrating cells. We observed that, in cells treated (10 min) with IGF-I or the phorbol-myristate acetate (PMA), phospho-Y155 RLC appeared in protruding edges consistent with lamellipodial localization, whereas it was largely absent from the lamellum (**Figure 19**). These data indicate that phospho-Y155 RLC, which is unable to associate to NMII filaments, accumulates at protrusive regions of the cell. Together with the fact that

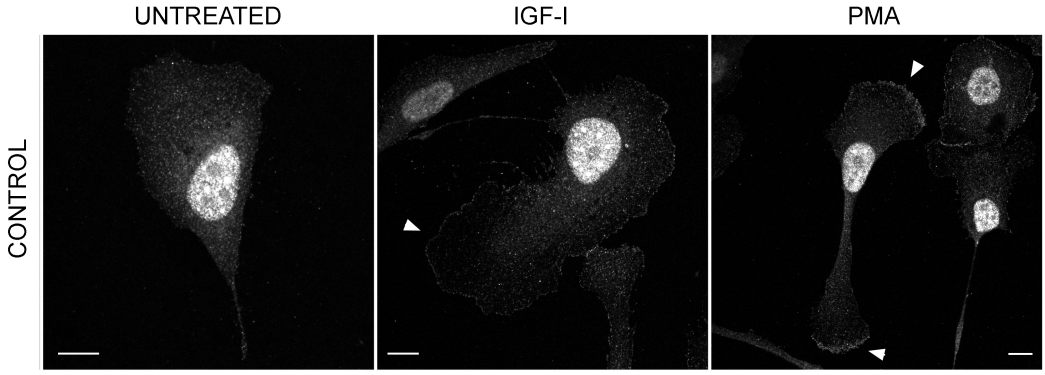

Figure 19: Y155-phosphorylated RLC and the phospho-mimetic mutant Y155E preferentially localizes to the leading edge of polarized cells. Representative confocal images of CHO.K1 cells spread on fibronectin, serum-starved for 16h, then treated with IGF-I (100 ng/ml) or PMA (20 ng/ml) for 10 min, fixed and stained with the pY155 antibody. Bars=10 µm.

RLC exchanges rapidly in and out of NMII filaments as shown by FRAP (up to 80% in 60s (Watanabe et al., 2007), which is higher than that of MHCII-A (Vicente-Manzanares et al., 2007)), these experiments are consistent with a model in which growth factor-driven phosphorylation of RLC on Y155 at the leading edge locally abrogates the exchange of RLC in and out of NMII filaments, thereby preventing filament stabilization and assembly, and maintaining the edge of the protrusion free of assembled NMII.

4.2 Results, part 2*A*: the cellular alterations of *MYH9* mutations

4.2.1 A mutant of MHCII-A (N93K), previously described as non-contractile, actually displays significant contractile capacity in its motor domain

One of the first studied *MYH9* mutations was N93K, which resides in the motor domain of MHCII-A (Hu et al., 2002). An early biochemical study using HMM produced in Sf9 cells reported that the mutant protein displayed negligible ATPase activity (measured by phosphate release rate, s^{-1}) and no *in vitro* sliding of actin filaments compared to wild type (Hu et al., 2002). Since the mutant protein does bind actin filaments, it was postulated that the mutant had indeed the ability to hydrolyze ATP, but not to release the inorganic phosphate, which explained the observed phenotype, i.e. binding to actin filaments but an inability to contract them. This was the rationale to use this mutant as a NMII-A variant devoid of contractile activity, thus theoretically enabling the separation between the contraction and

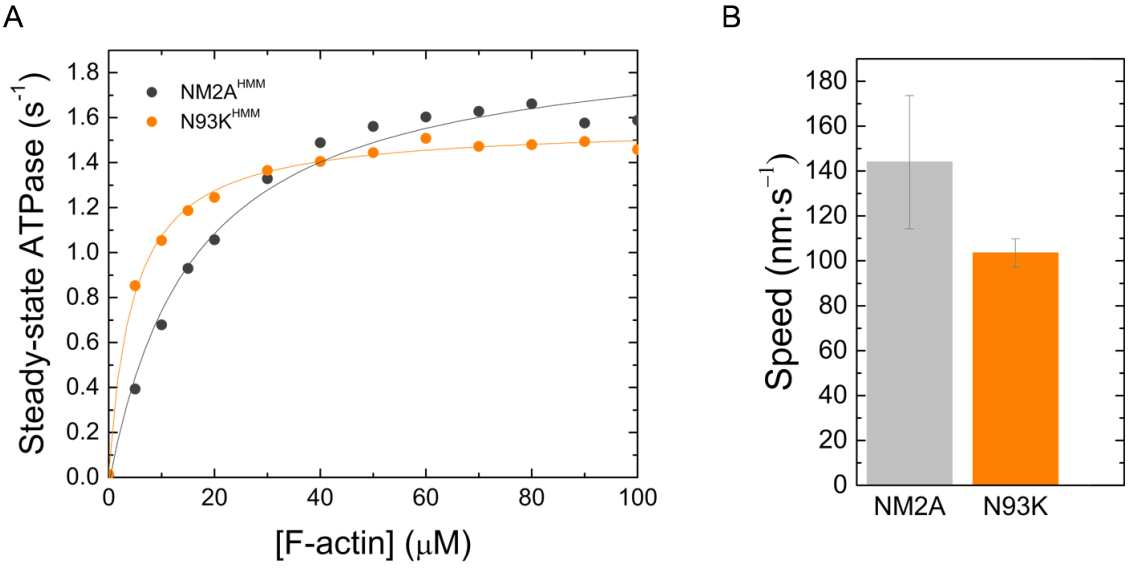

Figure 20: NMII-A N93K has contractile activity. **(A)** ATPase activity of MHCII-A WT and N93K mutant HMM fragments. The activity was measured indirectly in a coupled assay to NAPDH oxidation (see Materials and Methods). Experiment representative of three performed. **(B)** Distribution of the *in vitro* sliding velocities of MHCII-A WT and N93K mutant HMM fragments. Error bars indicate the sample standard deviation of three independent experiments.

cross-linking functions of NMII-A (Alieva et al., 2019; Choi et al., 2008; Taneja and Burnette, 2019). However, new experiments done in collaboration with Sarah Heissler using HMMII-A (see **Figure 1** for details on the size and structure of this fragment) expressed in baculovirus-transduced Sf9 cells demonstrated that these truncated versions bearing the N93K mutation displayed significant ATPase (i.e. contractile) activity (**Figure 20A**) and actin filament sliding speed (**Figure 20B**), to levels up to 80% capacity of the wild type form).

4.2.2 N93K displays a subcellular localization consistent with its contractile ability

The distribution of the NMII paralogs in adherent cells follows a conserved pattern. In general, the two major ones (II-A and II-B) overlap in some regions, whereas they are overrepresented in other areas. NMII-B is more abundant in central and posterior regions than NMII-A. Conversely, NMII-A is enriched near protrusive regions **Figure 4**) (Kolega, 2003; Maupin et al., 1994). In this context, the C-terminus region of the heavy chain of NMII is sufficient to define the paralog-specific subcellular localization, as shown in experiments using NMII chimeras (Sandquist and Means, 2008; Vicente-Manzanares et al., 2008). NMII chimeras bearing the head of MHCII-B and the coiled-coil and C-terminal region of MHCII-A (MHCII-B/A, **Figure 21A**) localized in a similar manner to wild type NMII-A (**Figure 21B-C**, upper panels). Conversely, the head of MHCII-A attached to the tail of MHCII-B localized as wild type NMII-B (Vicente-Manzanares et al., 2008). However, it is important to note that these chimeras retain contractile activity that, based on biochemical evidence using motor domains and HMM fragments (Kim et al., 2005), was lower for the NMII-B/A than the NMII-A/B chimera. In other words, while the C-terminus region of the protein directs the localization of the chimeras, the head domain alone determines the actin binding, ATPase kinetics and duty ratio of the entire molecule (Kovacs et al., 2003).

A previous study from Adelstein's group defined the R709C mutation of the catalytic domain of MHCII-B as a non-contractile form of NMII-B (Kim et al., 2005). Unlike N93K MHCII-A, which efficiently rescues most of the cellular phenomena associated to endogenous NMII-A silencing (Choi et al., 2008), R709 MHCII-B did not restore the wild type phenotype upon deletion of endogenous NMII-B, at both

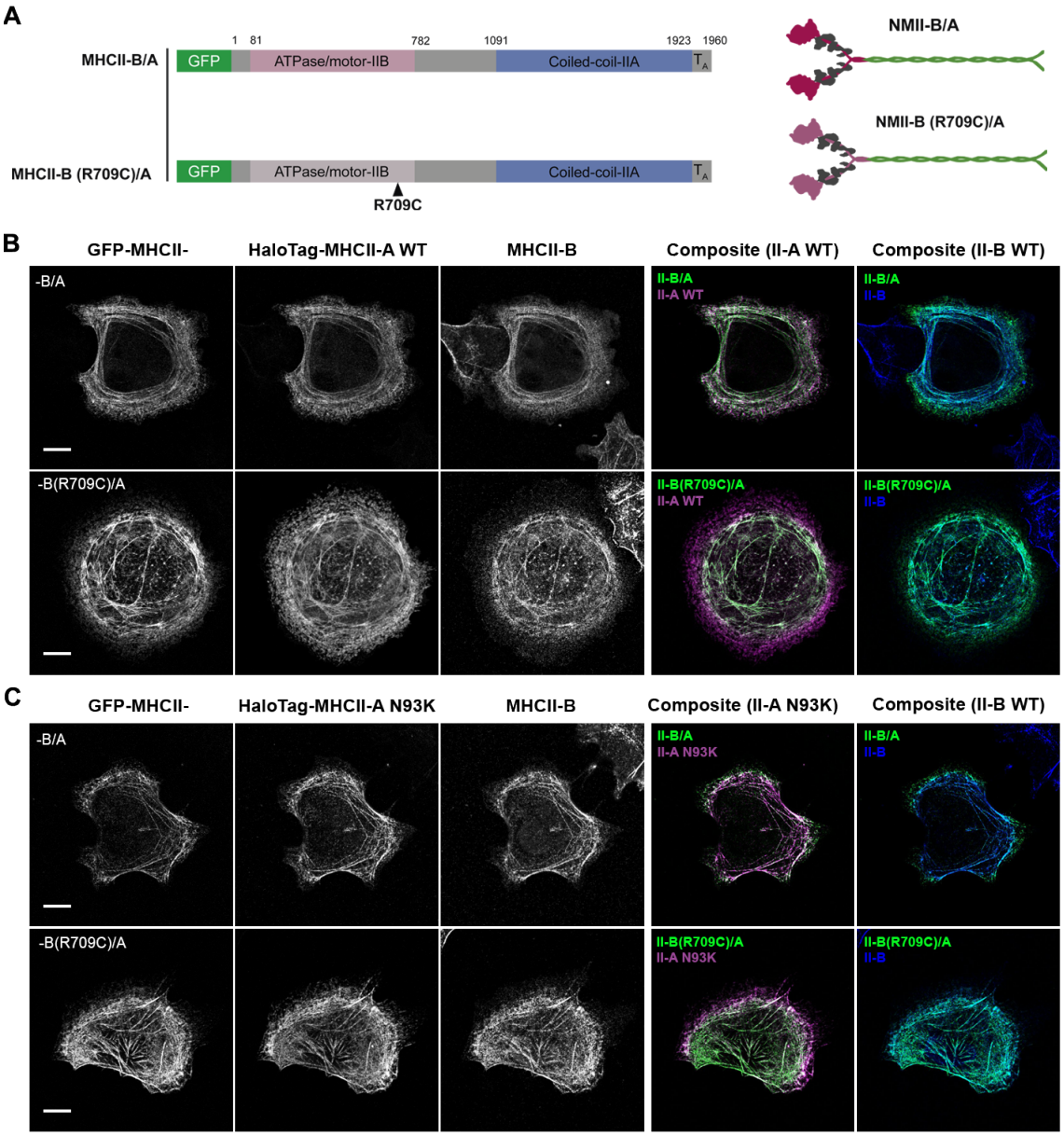

Figure 21: NMII-A N93K displays a subcellular localization consistent with some retention contractile activity in the motor domain. **(A)** Schematic representation of NMII chimeras. **(B)** Representative confocal images of COS-7 cells co-transfected with HaloTag-MHCII-A WT and the chimeric constructs coupled to EGFP as indicated. Cells were stained with JaneliaFluor®-585 for 1h (50 nM), allowed to spread on fibronectin substrates (3 µg/ml) for 90 minutes, fixed and stained for endogenous MHCII-B. **(C)** Same as in (B). This time, the chimeras were co-transfected with HaloTag-MHCII-A N93K. Note that while N93K mutant lied behind the EGFP-MHCII- B/A chimera, it localized anterior to the non-contractile chimera the EGFP-MHCII- II-B(R709C)/A. Scale bar = 10 µm.

cellular and organism levels (Takeda et al., 2003; Ma et al., 2007, 2004). We thus reasoned that a II-B/A chimera carrying the R709C mutation would result in a non-contractile form of NMII whose localization determinants (as dictated by its unmodified tail domain) would be the same as wild type NMII-A, enabling us to use it as a *bona fide*, non-contractile, "NMII-A-like" variant (**Figure 21A**). Immunofluorescence experiments in COS-7 cells (which are naturally devoid of MHCII-A, (Pecci et al., 2018) revealed that the chimera NMII-B(R709C)/A did not co-localize with wild type NMII-A or the chimera NMII-B/A. Instead, it was distributed in more central regions of the cell (**Figure 21B-C**, lower panels), indicating that some contractile activity, while not sufficient to dictate its positioning, is needed for NMII-A to appear in more anterior localizations. Based on this new evidence and enabled by access to high-end microscopy, we decided to use the specific position of NMII-A N93K as a proxy to evaluate its contractile capacity compared to the known distribution and behavior of the non-mutated (NMII-B/A), and non-contractile (NMII-B(R709C)/A) chimeras. We found that, despite a high degree of overlap, NMII-A N93K mainly localized behind the NMII-B/A chimera (which localizes as NMII-A) with respect to the leading edge in the most protrusive regions (**Figure 21C**, upper panel). However, NMII-A N93K appears closer to the leading edge than the non-contractile chimera MHCII-B(R709C)/A. In this scenario, NMII-A N93K localized in an anterior manner compared to the motor-dead chimera (**Figure 21C**, lower panel), supporting the *in vitro* data that N93K preserves some of the contractile activity of NMII-A in a cellular context. However, the fact that its localization is not completely overlapping with that of wild type NMII-A or the NMII-B/A chimera indicate the existence of a defect that cannot be attributed to reduced ATPase activity or its *in vitro* ability to move actin filaments.

4.2.3 NMII-A mutants display no apparent lifetime differences when expressed in COS-7 cells

Analysis of the morphology and distribution of mutant variants of MHCII-A in the cytoplasm of neutrophils of *MYH9* patients (Kunishima et al., 2001; Seri et al., 2003) suggests that mutant proteins have a tendency to form aggregates. Protein aggregation can have various origins, including a defect in the degradative process of the NMII-A variants bearing these mutations. To test this hypothesis, we performed

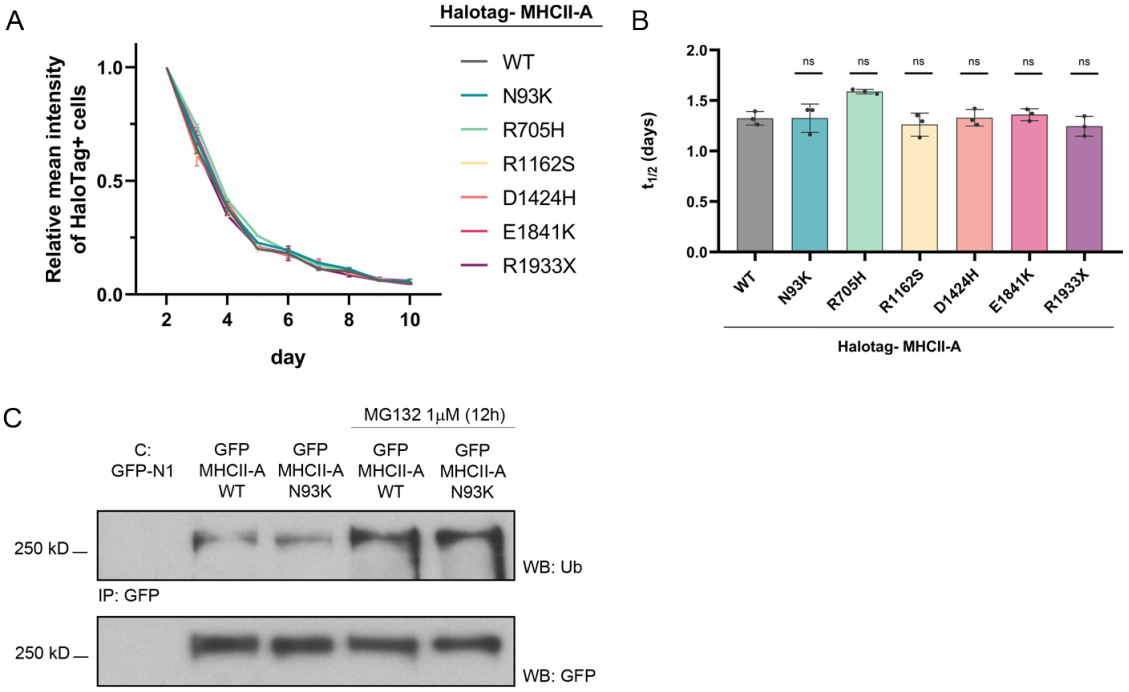

Figure 22: NMII-A mutants show no differences in degradation rates or alterations via the ubiquitin-proteasome pathway. (A) Relative mean fluorescence intensity (± SEM) of HaloTag$^+$ cells from three independent experiments. Mean fluorescence intensity was normalized to initial intensity levels to correct for differences in the expression levels among conditions. **(B)** Half-life (± SEM) of HaloTag-MHCII-A WT or the mutant constructions. Data were adjusted to a one phase exponential decay model. There were no differences in the fluorescence decay rate between WT or the indicated mutants. Nonparametric Mann-Whitney U test was used to evaluate statistical significance of the half-life of MHCII-A WT vs. mutants. n.s., non significant. **(C)** Ubiquitin levels of immunoprecipitated EGFP-MHCII-A WT or N93K in COS-7 cells. 48h post-transfection, the heavy chain was isolated with EGFP-Dynabeads and subjected to WB analysis with anti-ubiquitin antibody (Ub), upper panel. Total EGFP-MHCII-A levels were assessed after membrane stripping, lower panel. Image is representative of three experiments performed.

"dye and chase" experiments in COS-7 cells using a fluorescent label on Halotag-tagged versions of MHCII-A. HaloTag-MHCII-A WT, or mutant, pools were stained with the HaloTag ligand JaneliaFluor®-585 two days post-transfection, then excess dye was washed out. In this manner, only the pool of protein present at the time of the labeling becomes fluorescent; and cellular protein produced post-labeling does not become labeled. This provides a strategic advantage over fluorescent proteins (e.g. EGFP) that enables execution of this experiment. The stained pool was gated by flow cytometry and the mean fluorescence of the HaloTag$^+$ cell population was monitored every day for the following eight days. Alterations in the degradative process would show as accelerated, or delayed, decay of the signal as analyzed by flow cytometry. We found no differences in the fluorescence mean decay of HaloTag$^+$

population between the wild type form and the mutants in the course of this experiment, with a t1/2 of approximately 4 days (**Figure 22A-B**).

We also evaluated NMII degradation through the ubiquitin-proteasome pathway. COS-7 cells were transfected with EGFP-MHCII-A WT or the N93K mutant and the heavy chain was immunoprecipitated by magnetic isolation with EGFP-Dynabeads (**Figure 22C**, lower panel). As a positive control for ubiquitin staining, we used MG-132, an inhibitor of the 26S-proteasome, reported to mediate myosin degradation (Henderson et al., 2005; Landsverk et al., 2007; Lee and Goldberg, 1998). We found no differences in the ubiquitin levels of MHCII-A WT and N93K mutant (**Figure 22C**, upper panel), suggesting that the accumulation of the later is not due to alterations to the proteasome-dependent degradation pathway.

4.2.4 N93K NMII-A filaments display similar salt-dependent stability compared to wild type NMII-A filaments

To test the biochemical properties of the myosin II filaments made of the N93K mutant, we evaluated their behavior using a salt-dependent filamentation assay. High salt concentrations (i.e. 500 mM potassium acetate (CH_3CO_2K)) render non-muscle myosin II in a monomeric but extended conformation (6S) by destabilizing both NMII assembly into filaments and impairing the ability to return to the 10S, folded conformation (Breckenridge et al., 2009). In this scenario, lowering the salt concentration would drive NMII to either go back to the folded state, or to assemble into mini-filaments in an actin-independent manner (**Figure 23A**). We can distinguish the two species by ultracentrifugation, where the pellet fraction will contain the mini-filaments (**Figure 23A**) and the supernatant the folded (10S) form.

To determine optimal salt concentrations for this study, we first evaluated the assembly capacity of the wild type form of NMII-A. Briefly, we transfected COS-7 cells with the heavy chain of NMII-A coupled to EGFP, which does not affect assembly (Breckenridge et al., 2009). After 48h, we lysed the cells in buffer containing a high concentration of potassium acetate; then precleared the insoluble fraction (plasma membrane and actin filaments among others) by centrifugation. The lysate was then divided into a set of lower concentrations of potassium acetate and then the two fractions (insoluble, filamentous fraction and soluble fraction) were separated by ultracentrifugation. The insoluble fraction was resuspended in 2× Laemmli buffer.

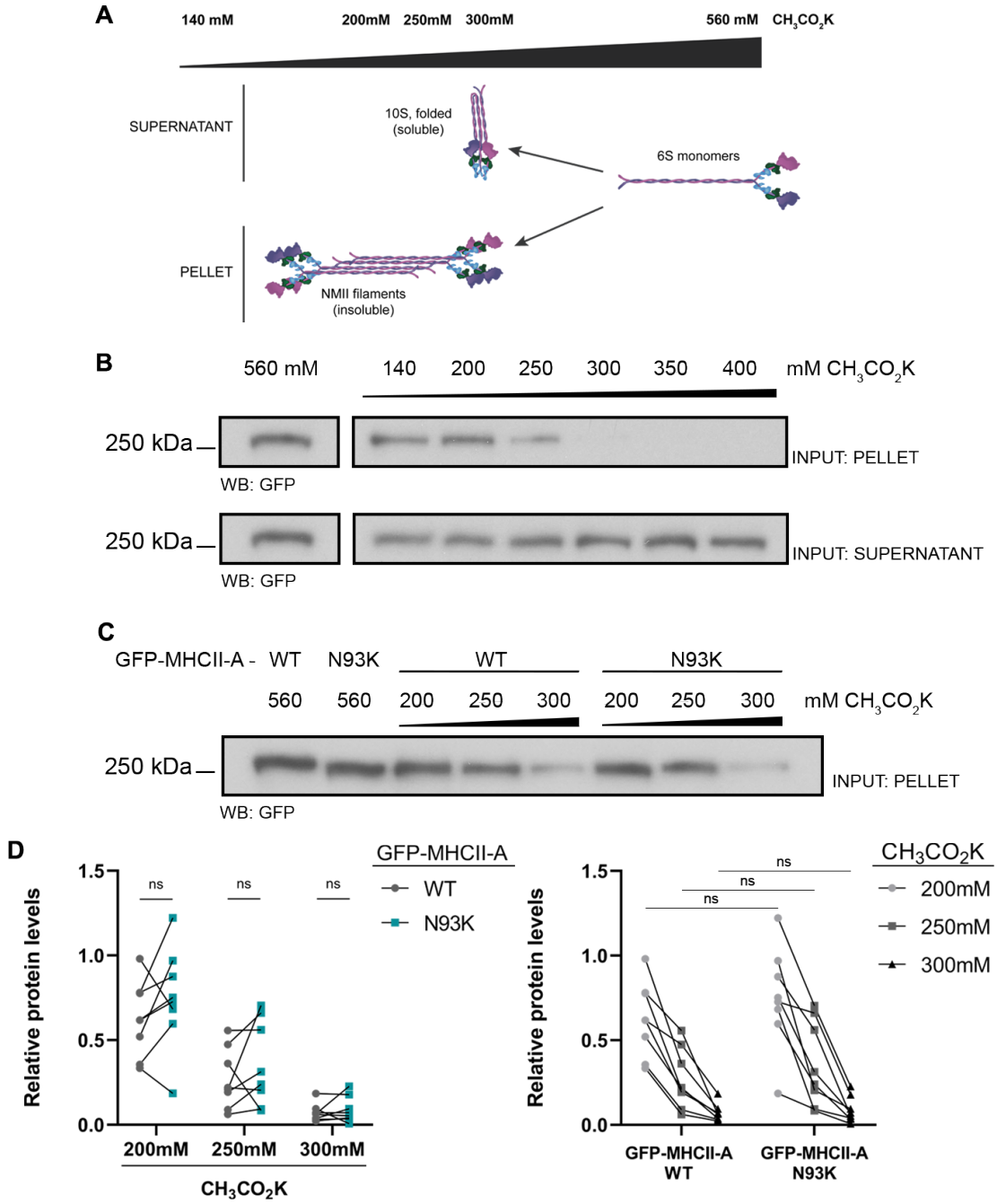

Figure 23: NMII-A N93K mutant display no differences in assembly behavior compared to NMII-A WT. (A) Schematic drawing of the assembly state of NMII on different salt concentrations. While high salt concentrations force NMII into a 6S monomeric form, lower salt concentrations displace this equilibrium towards the folded, soluble 10S conformation or the assembled, insoluble form. Both populations can be distinguished by ultracentrifugation. **(B)** Pellet and supernatant fractions of NMII-A on a salt dosimetry. A range of 200 to 300 mM of potassium acetate was selected to further test NMII-A filamentation of WT vs. mutant form. **(C)** NMII-A mini-filaments were solubilized at 560 mM of potassium acetate and a sample was taken as a loading control to verify NMII-A expression levels. After incubation with 200-300 mM of potassium acetate and ultracentrifugation, we evaluated the presence of MHCII-A in the pellet fraction by Western blot. (Continues in the next page).

(D) Relative protein levels in the pellet fraction. MHCII-A pellet fraction was normalized to MHCII-A expression levels on the lysate at 560 mM (all soluble). N93K filamentation capacity is similar to that of NMII-A WT (left panel). Both increase its pellet fraction to similar levels at increasingly lower salt concentrations (right panel). Wilcoxon matched-pairs signed rank test was used to evaluate statistical significance of relative levels of MHCII-A WT vs. N93K in the pellet fraction of eight independent experiments. n.s., not significant.

The soluble fraction was then precipitated with acetone and resuspended also in 2× Laemmli buffer. Based on preliminary experiments using a wide range of concentrations (**Figure 23B**), we performed the definitive experiments using 200, 250 and 350 mM potassium acetate. The evaluation of the assembly behavior of N93K mutant in these experimental salt conditions revealed no differences in the filamentous fraction (pellet) compared to the wild type form at any of the salt concentrations selected (**Figure 23C-D**, left panel). Both fusion proteins behave similarly, becoming more filamentous when incubated at lower salt concentrations (**Figure 23D**, right panel).

4.2.5 N93K NMII-A shows an increased cellular association to the chaperone UNC45a

UNC45a participates in the folding and organization of stress fiber assembly of class II non-muscle myosin. U2OS cells in which UNC45a was deleted via CRISPR/Cas9 displayed decreased NMII protein expression levels and an alteration of the organization and function of stress fibers. UNC45a seems to prevent NMII-A misfolding, aggregation and proteosomal degradation (Lehtimaki et al., 2017b). We observed increased levels of UNC45a interacting with the N93K variant as compared with the wild type form in an immunoprecipitation-based proteomic screening using HEK-293T cells. This screening was designed to determine whether N93K induced alterations in the NMII-A interactome in live cells. These data were confirmed by co-immunoprecipitation, which showed that the N93K mutant displayed an enhanced interaction with UNC45a compared to the wild type form of NMII-A in COS-7 cells (**Figure 24**).

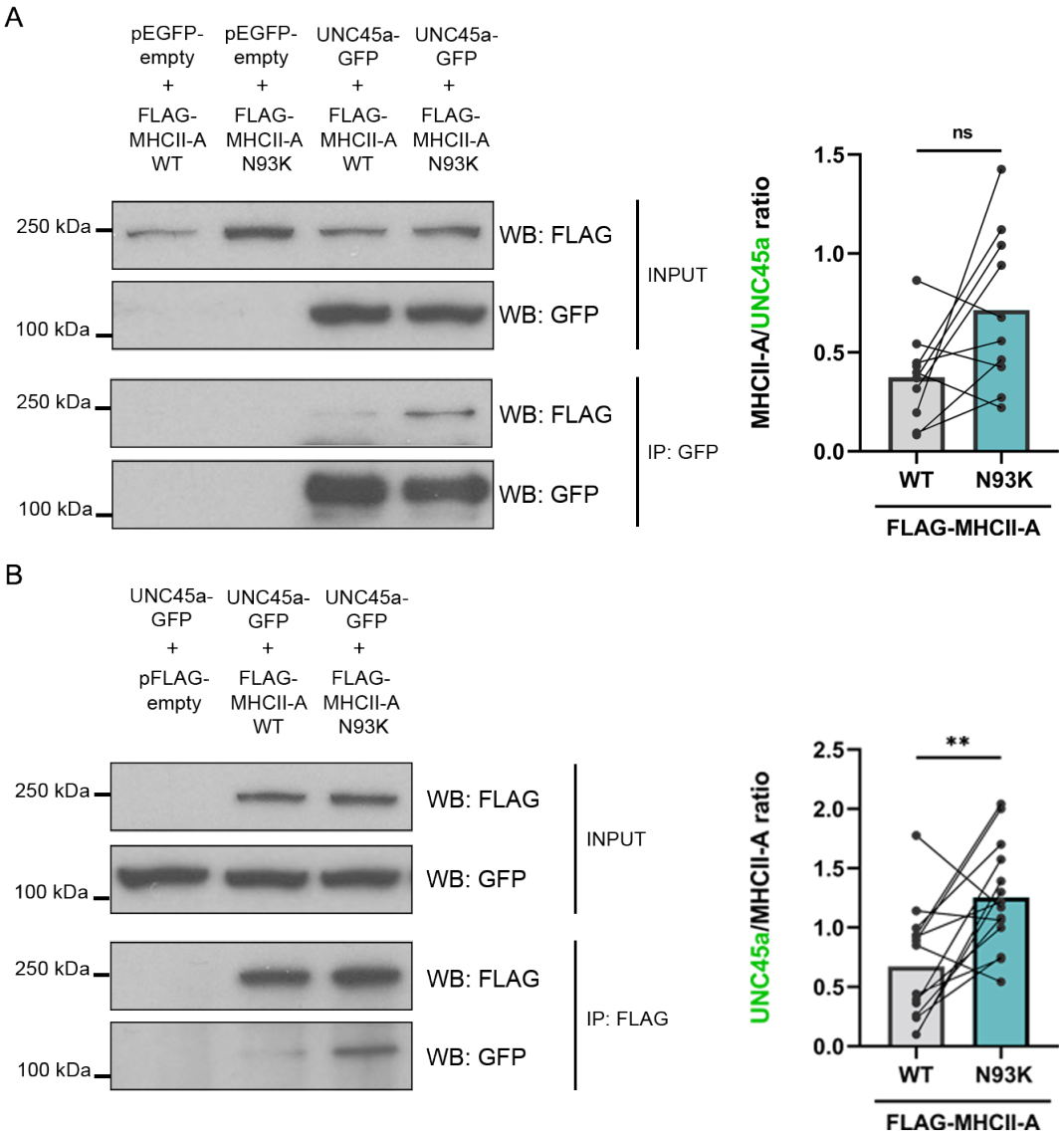

Figure 24: UNC45a displays an increased association with the mutant variant NMII-A N93K in cells. (A) Left, representative immunoblots of UNC45a-EGFP immunoprecipitation in COS-7 cells, transfected as indicated and equally loaded for separation by SDS-PAGE. Figure shows co-immunoprecipitation of FLAG-MHCII-A, enriched in the case of the N93K mutant. Right, densitometric quantification of MHCII-A co-immunoprecipitation, corrected by the amount of UNC45-a in the immunoprecipitate. MHCII-A N93K increased association with UNC45a was also observed when immunoprecipitating FLAG-MHCII-A, as shown in (B). Data from ten independent experiments. **(B)** Left, representative immunoblots of MHCII-A immunoprecipitation, the lowest panel shows UNC45-a co-immunoprecipitation, increased in FLAG-MHCII-A N93K immunoprecipitate. Right, densitometric quantification of UNC45a co-immunoprecipitation, corrected by the amount of immunoprecipitated FLAG-MHCII-A. Wilcoxon matched-pairs signed rank test was used to evaluate statistical significance of relative levels co-immunoprecipitation levels in WT vs. N93K condition. Data from at least ten independent experiments. ** $p < 0.01$; n.s., not significant.

4.2.6 *MYH9* mutations spatially segregate the variant NMII-A from the wild type

To extend our analysis beyond the N93K mutation, we first selected and then constructed a collection of representative *MYH9* mutations affecting different regions of the protein (see the Section 1.7 of the Introduction for details). The selected mutations included N93K, R705H (also in the head domain), R1162S (coiled-coil domain), D1424H (coiled-coil domain), E1841K (end of the coiled-coil domain) and R1933X, which generates a mutant form that lacks the non-helical tail domain.

We then expressed these mutants in U2OS osteosarcoma cells, which are a well-characterized model to study NMII paralog-specific segregation (Juanes-Garcia et al., 2015; Weissenbruch et al., 2022). In these cells, NMII-A is enriched in actomyosin structures closer to the leading edge (lamellae), whereas NMII-B decorates more central and posterior actomyosin bundles (Juanes-Garcia et al., 2015). We co-transfected U2OS with wild type MHCII-A coupled to EGFP and MHCII-A mutants coupled to HaloTag. Two days post-transfection, we evaluated their localization by immunofluorescence on cells adhered on fibronectin substrates for 90 minutes. While the mutants partially co-localized with wild type MHCII-A, they all were underrepresented in protrusive regions compared to the wild type form. Instead, they occupied an intermediate localization, behind wild type NMII-A but in front of NMII-B-rich filaments. Interestingly, every NMII-A mutant tested displayed this intermediate localization (**Figure 25**). This observation suggested that alterations in NMII-A structure translate into a more stable (or less dynamic) behavior of NMII-A independently of the affected domain (motor, tail or non-helical tail). These observations were also recapitulated in COS-7 cells (**Figure 26**). We also verified that the effects were not spurious and created by the use of Halotag or EGFP by performing the same experiments using reciprocal tagging, that is, EGFP-MHCII-A mutants and Halotag-MHCII-A wild type (**Figure 26**).

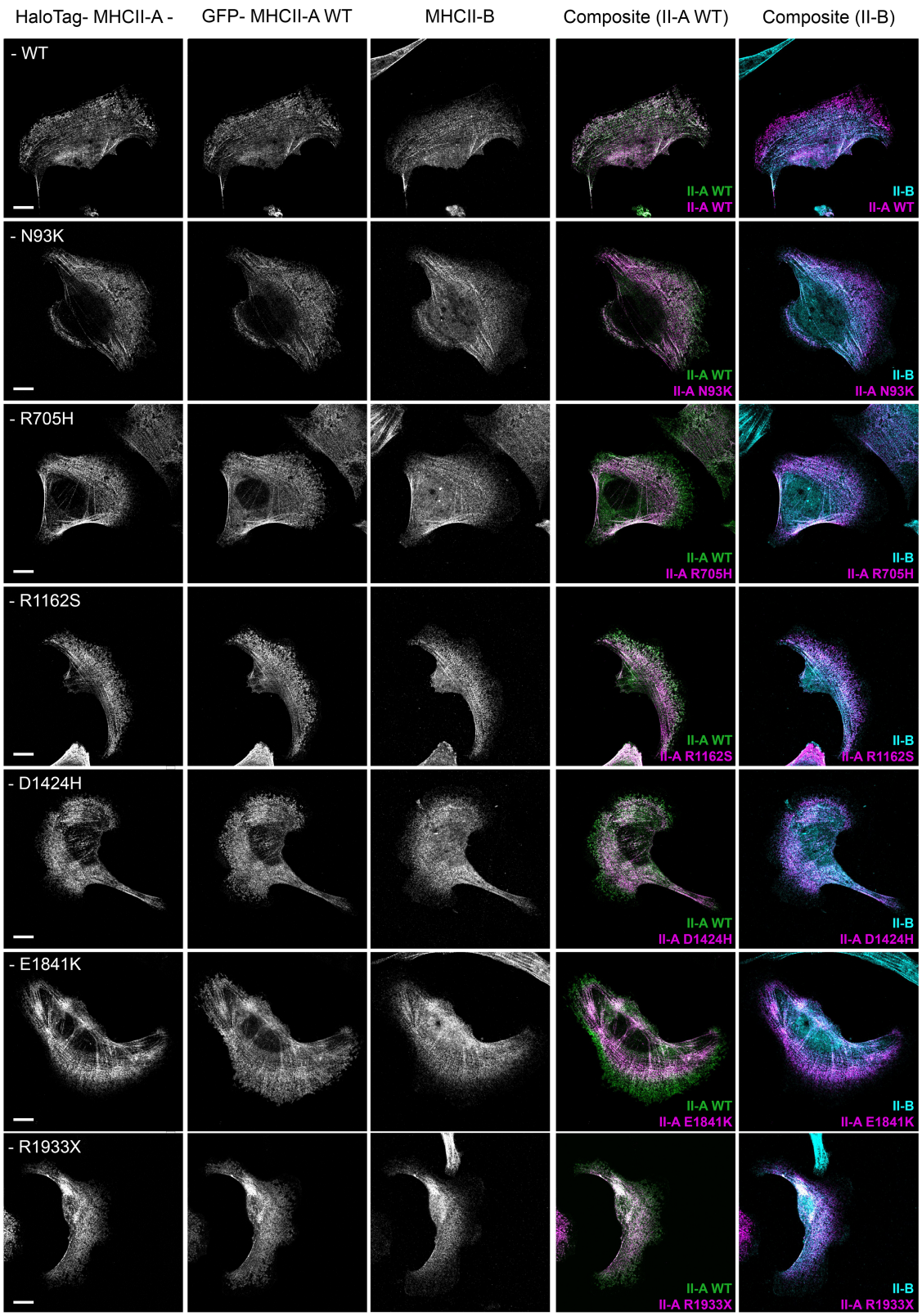

Figure 25: NMII-A mutants decorate more central and stable actomyosin structures in U2OS cells. (See caption at page 89).

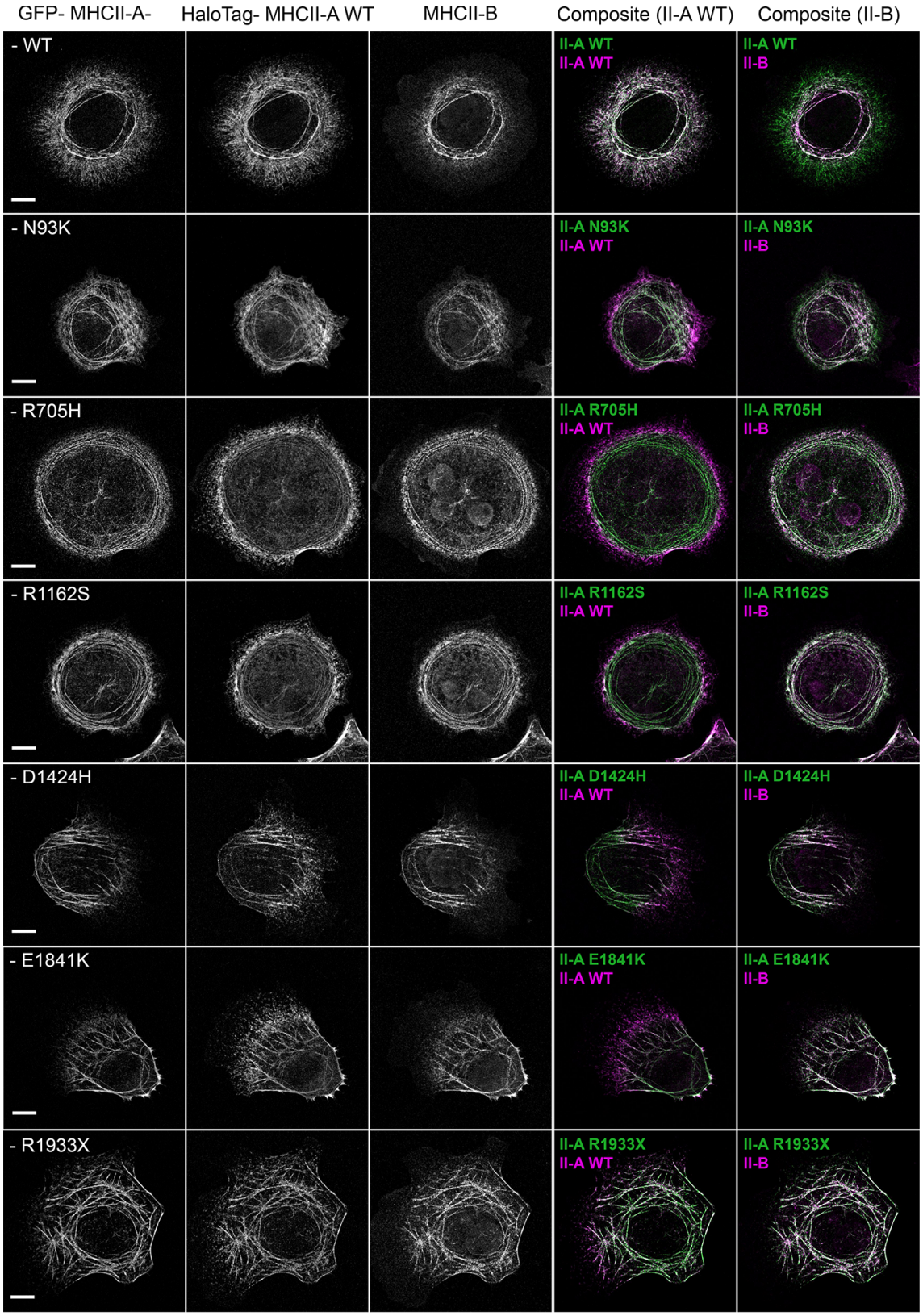

Figure 26: NMII-A mutants localize to more central actomyosin structures in COS-7 cells. (See caption at page 89).

Figure 25 (page 87): **NMII-A mutants decorate more central and stable actomyosin structures in U2OS cells.** Representative confocal images of U2OS cells co-transfected with EGFP-MHCII-A wild type and the different MHCII-A mutants coupled to HaloTag. Cells were stained with HaloTag ligand Janelia Fluor®-585 (50 nM) for 1h and then allowed to spread on fibronectin substrates (3 µg/ml) for 90 minutes, fixed and stained for endogenous MHCII-B. Unlike NMII-A WT, NMII-A mutants are not enriched in the protrusive regions. All display an intermediate localization between NMII-A and NMII-B, that is independent of the affected domain of MHCII-A. Scale bar= 10µm.

Figure 26 (page 88): **NMII-A mutants localize to more central actomyosin structures in COS-7 cells.** Representative confocal images of COS-7 cells co-transfected with HaloTag-MHCII-A WT and the different MHCII-A mutants coupled to EGFP. Cells were stained with HaloTag ligand Janelia Fluor®-585 (50 nM) for 1h and then allowed to spread on fibronectin substrates (3 µg/ml) for 90 minutes, fixed and stained for endogenous MHCII-B. Note that for the shake of clarity, we use the same pseudo-colors to compare the EGFP-MHCII-A mutants both with the HaloTag-MHCII-A WT form and MHCII-B. In COS-7 cells, all mutants localized behind MHCII-A WT and similar to MHCII-B. Scale bar= 10µm.

4.2.7 NMII-A mutants preserve some of NMII-A ability to initiate adhesion assembly

The contractile activity of NMII-A and its specific ability to generate intracellular force are required in the initial steps of adhesion formation and growth (Dumbauld et al., 2010; Vicente-Manzanares et al., 2007). We used this paralog-specific function to evaluate the contractile behavior of NMII-A mutants in the COS-7 cell model. To assess this, COS-7 cells were transfected with EGFP-coupled MHCII-A, wild type or the mutant variants. After 48h, cells were allowed to adhere on fibronectin substrates for 150 minutes, fixed and stained for endogenous vinculin, a component of focal adhesion complexes at every stage (Choi et al., 2008). The determination of the adhesive area was performed by TIRF microscopy as described in Section 3.3.8 of the Materials and Methods chapter of this thesis. As expected, COS-7 transfected with a plasmid carrying EGFP alone displayed a low number of small adhesions, since endogenous NMII-B alone does not efficiently support adhesion growth (**Figure 27A**, first row; B-C). Expression of EGFP-MHCII-A WT increased the number of adhesions and the adhesive area drastically (adhesive area is a proxy for adhesion size if the cell area is not affected, see Section 3.2.7 for details on its quantification) (**Figure 27A**, second row; B-C). Quantification of focal adhesions in COS-7 cells transfected with EGFP-MHCII-A mutants revealed that, in general, most mutants

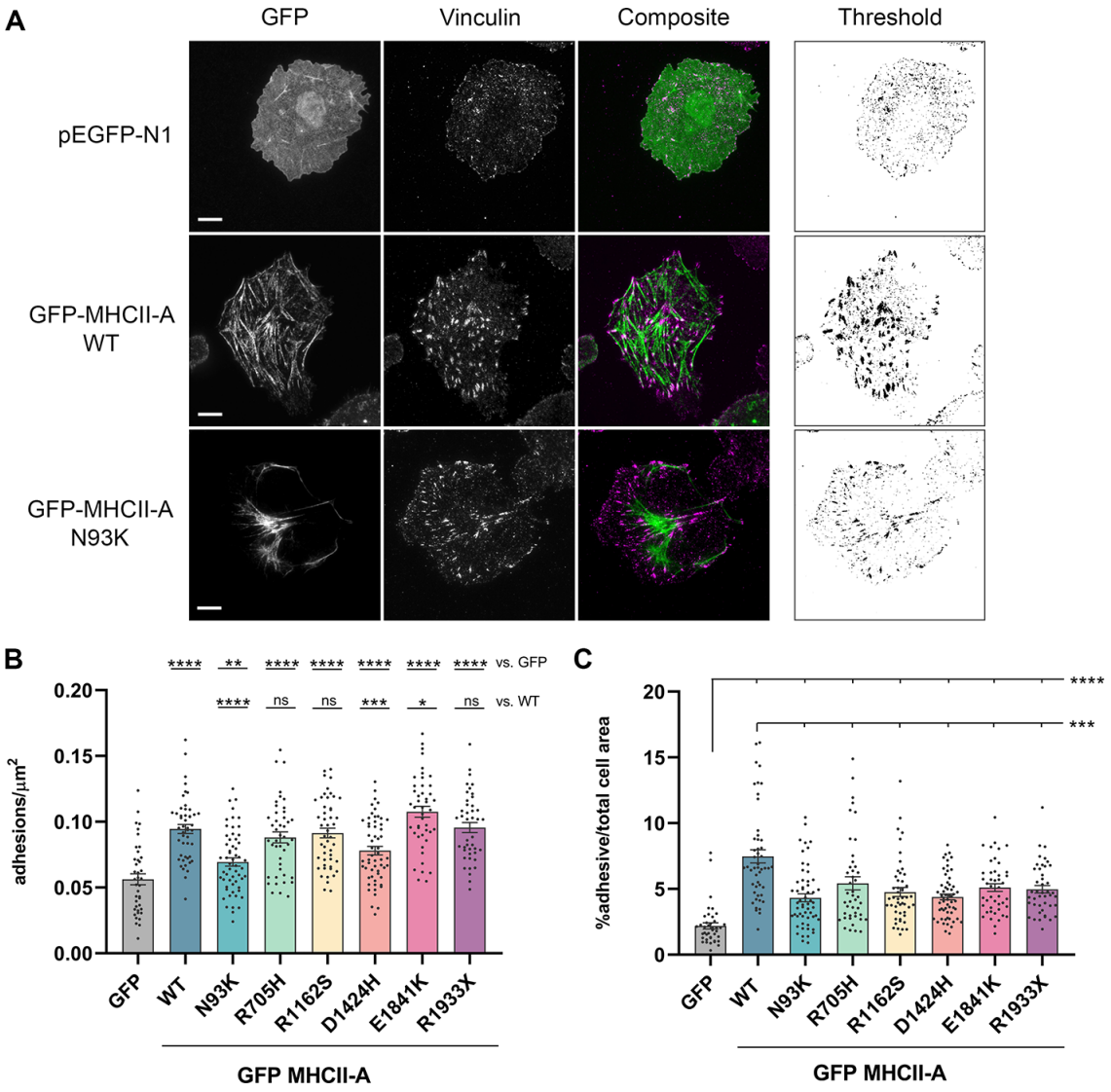

Figure 27: Most NMII-A mutants support adhesion assembly but do not enable efficient adhesion growth. (A) Representative TIRF images of COS-7 cells transfected with EGFP alone, EGFP-MHCII-A WT or the mutants, only N93K mutant is depicted here for illustration. 48h post-transfection, cells were allowed to adhere on fibronectin substrates (3 µg/ml) for 150 minutes, fixed and stained for vinculin. Right column shows an example of the threshold used to calculate adhesive area. Scale bar= 10 µm. **(B)** Quantification of the number of adhesions per μm^2 and **(C)** the adhesive area of COS-7 cells transfected as in (A). Data are the mean ± SEM of approximately 40 cells/condition from three independent experiments. Statistical significance of EGFP-MHCII-A vs. EGFP and EGFP-MHCII-A WT vs EGFP-MHCII-A mutants was addressed with unpaired t test for the adhesion/μm^2 data, and Mann-Whitney U test for the adhesive area. * $p < 0.05$; ** $p < 0.01$; *** $p < 0.001$, **** $p < 0.0001$, n.s., not significant.

were able to support initial adhesion assembly (measured as number of adhesions) significantly better than control cells transfected with EGFP alone, and to a similar extent to that of the wild type form. However, the expression of MHCII-A mutants instead of the wild type form resulted in smaller adhesive areas (meaning individual adhesion size) compared to MHCII-A WT, suggesting that, although mutant NMII-A can initiate adhesion assembly, adhesions do not elongate and undergo maturation as efficiently as in cells expressing wild type MHCII-A. Strikingly, MHCII-A variants carrying the N93K or D1424H mutations were not able to support adhesion assembly as efficiently as the wild type form or the other mutants in the first place (**Figure 27B**).

4.2.8 NMII-A mutants have similar filament association/dissociation rates but differ in stability within filaments

Together, the above data prompted us to characterize the dynamic properties of filaments made of the diverse mutants under study. Based on our previous work, the ability of actomyosin filaments decorated with diverse variants of NMII-A (or NMII-B) to promote adhesion formation and/or elongation more or less efficiently is related to the stability of the actomyosin filaments themselves (Vicente-Manzanares et al., 2011). FRAP and photo-conversion analyses are ideal techniques to explore this end. As explained in more detail in Section 3.3.10 of the Material and Methods, we selected COS-7 cells with either EGFP-MHCII-A WT or EGFP-MHCII-A mutants decorating actomyosin bundles at comparable intensities (**Figure 8**). The region was bleached and imaged over a defined period to evaluate the dynamic recovery. The resulting FRAP curve for each individual filament was adjusted to a one-phase exponential recovery model to obtain the exponential constant rate (K), which was identical to the dissociation constant k_{off} in FRAP and photo-conversion experiments (Brunet et al., 2006; Bulinski et al., 2001; Mii et al., 2021; Sprague et al., 2004), and the maximum recovery value (plateau) of each filament (**Figure 28A**). The analysis of the FRAP curves (**Figure 28B**) revealed that NMII-A mutants display slower recovery rates than those of wild type NMII-A, but that all mutants had the same rates of recovery independent of the localization of the mutation in the heavy chain of NMII-A (**Figure 28C**). Strikingly, although they recovered at the same rate, NMII-A mutants reached different maximum recovery values (**Figure**

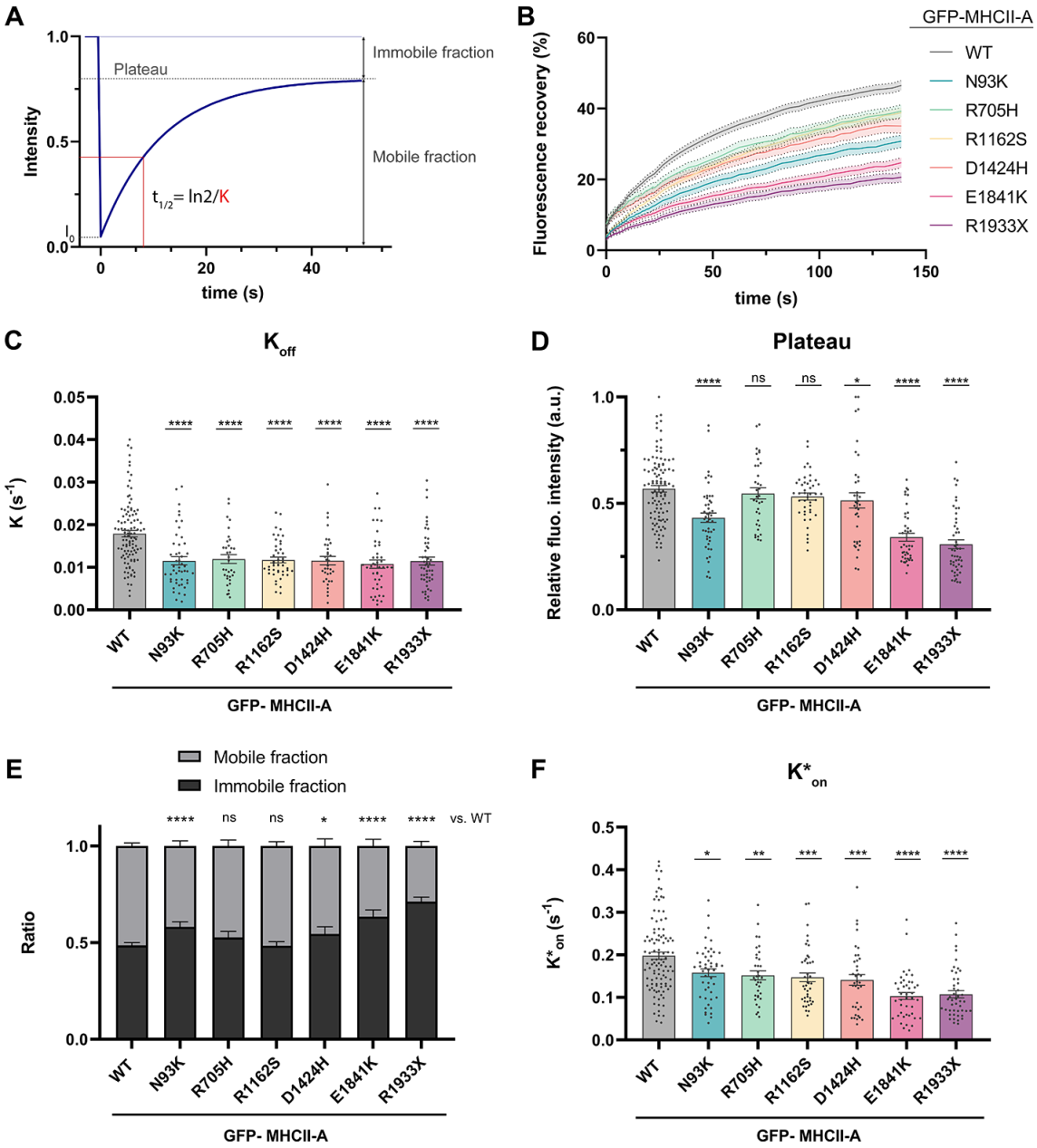

Figure 28: Every NMII-A mutant displays a decreased k_{off} compared to that of the wild type form, but different stability within actomyosin filaments. (A) Schematic representation of a one-phase exponential recovery model. In red, the exponential recovery rate, which associates directly with k_{off}. **(B)** FRAP curves of EGFP-MHCII-A decorated actomyosin filaments. COS-7 cells, transfected with either EGFP-MHCII-A WT or EGFP-MHCII-A bearing the selected mutations were allowed to adhere on fibronectin-coated (8 µg/ml) coverslips for 2h and then imaged. Data is the average of >50 filaments from three independent experiments. **(C)** Exponential recovery rates (K) for the resulting fitting curves. Mean ± SEM. **(D)** Plateau values for the resulting fitting curves. The recovery intensity values were normalized to pre-bleach images. Data are the mean ± SEM. **(E)** Mobile and immobile fractions for the filaments subjected to the FRAP assay. Data are the mean ± SEM. Statistical significance was assessed over the immobile fraction. **(F)** Estimated k^*_{on}, derived from K and plateau values (see Section 3.3.10 of the Materials and Methods). Data are the mean ± SEM. Nonparametric Mann-Whitney U test was used to evaluate statistical significance of MHCII-A WT vs MHCII-A mutants. * $p < 0.05$; ** $p < 0.01$; *** $p < 0.001$, **** $p < 0.0001$, n.s., not significant.

28D) suggesting that the stability of each mutant within the actomyosin filament is different. NMII-A mutants bearing the motor domain substitution R705H and the coiled-coil substitutions R1162S and D1424H displayed no significant difference in their plateaus compared to that of the wild type form. However, the motor domain substitution N93K and both mutations affecting the end of the coiled-coil region (E1841K) and the non-helical tail (R1933X) exhibited lower plateau values compared to the wild type form, consistent with higher immobile fractions (**Figure 28D-E**) and a more stable behavior of these mutants within actomyosin filaments. From the plateau and K values on FRAP experiments we could obtain an estimate of the association constant (k^*_{on}) (Sprague et al., 2004), which displayed decreased values for every NMII-A mutant (**Figure 28D**), particularly those localizing their mutation in the tail domain. Overall, our data indicated that mutations within the end of the coiled-coil domain and the non-helical tail had, on average, a lower estimated k^*_{on} than those within the head domain.

The same behavior was observed when we evaluated the dynamic properties of NMII-A mutants by photo-conversion, which rules out potential side effects related to the biochemical nature of the tag affecting the dynamics of MHCII-A. mEOS2 is a photo-switchable, green-emitting fluorescent protein that shifts to red emission upon UV light-triggered photo-conversion (**Figure 9**) (Wiedenmann et al., 2004). In this case, the decay in red emission fluorescence upon UV photoconversion of mEOS2–MHCII-A WT/mutants-decorated actomyosin filaments adjusted to a one-phase exponential decay model (**Figure 29A-B**). Analysis of the exponential decay rates (K), and the minimum recovery values (plateaus) revealed that all the mutants display slower decay rates than those of the wild type form. Every mutant displayed a similar decay rate (**Figure 29C**). However, analysis of the plateaus revealed similar values to the wild type form, except for E1841K (located at the end of the coiled coil region of MHCII-A) and R1933X (located at the non-helical tail domain). The values corresponding to these mutants were significantly higher, clearly reflecting their increased stability in filaments and confirming the information extracted from the FRAP data using an independent technique (**Figure 29D**).

The relative variations observed in some mutants by photo-conversion and by FRAP (the most notable was the decay rate of the E1841K, which was quite similar to that of the wild type form) could be due to a limited acquisition window in the photo-conversion experiments, that could have affected the modeling and values of

the fitting curve. Another possibility is that, while photo-conversion formally measures a similar parameter to that of FRAP, the biological interpretation of the data actually refers to the exchange out of the filament (not into the filament, as FRAP), which could be slightly different than what is measured by FRAP, particularly in light of possible effects on the stability of the myosin bipolar/multipolar assemblies (see the Discussion section).

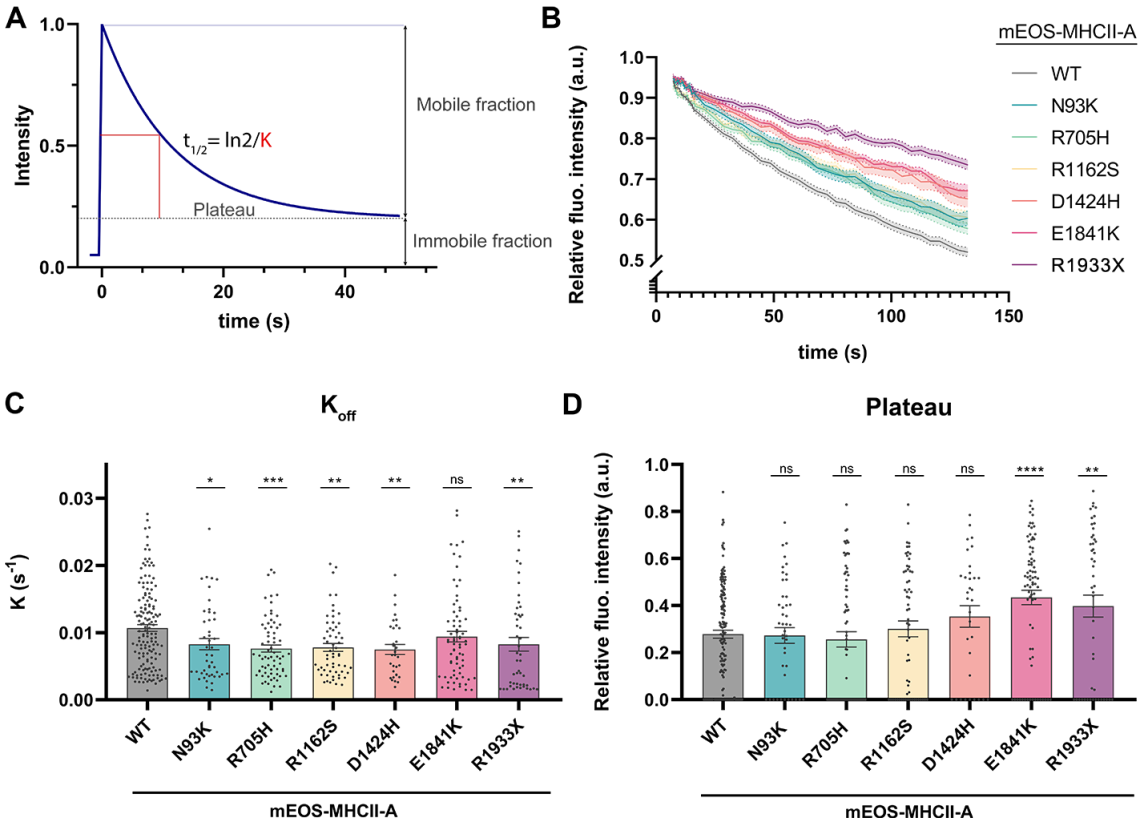

Figure 29: Photo-conversion of mEOS2-coupled NMII-A mutants reveals decreased decay rates compared to the wild type form and different stability within the actomyosin filaments, consistent with the FRAP data. **(A)** Schematic representation a one-phase exponential decay model. The exponential decay rate, in red, associates directly with k_{off}. **(B)** Photo-conversion curves of mEOS2- MHCII-A wild type and the mutants N93K, R705H, D1424H, E14841K and R1933X. Transfected COS-7 cells were allowed to adhere on fibronectin-coated (8 µg/ml) coverslips for 2h and then imaged. Data is the average of >40 filaments from three independent experiments. **(C)** Exponential decay rates (K) for the resulting fitting curves. Data are the means ±SEM. **(D)** Plateau values for the resulting fitting curves. Data are the means ±SEM. Nonparametric Mann-Whitney U test was used to evaluate statistical significance of mEOS2-MHCII-A WT vs MHCII-A mutants. * $p < 0.05$; ** $p < 0.01$; *** $p < 0.001$, **** $p < 0.0001$, n.s., not significant.

4.2.9 Wild type NMII-A dynamics are affected by co-polymerization with NMII-A mutants

The geometry, mechanical properties and thus the function of actomyosin bundles are tightly regulated and partially dependent on their specific composition, particularly in terms of NMII paralog content. Although the NMII paralogs exert redundant functions in some cellular processes, others require finely tuned actomyosin filaments endowed with specific mechanical properties, which heavily rely on the specific paralog composition of the bundle (Baird et al., 2017). For example, actomyosin filaments enriched in NMII-A are best suited for force generation processes, e.g. ECM remodeling (Liu et al., 2014), whereas NMII-B decorated filaments are associated with tension buildup and load bearing processes, for example those needed for axon elongation, migratory polarity maintenance, or nucleus translocation (Bridgman et al., 2001; Thomas et al., 2015; Vicente-Manzanares et al., 2008). Between these two extreme scenarios, the relative abundance of NMII-A and NMII-B provides a whole range of actomyosin bundles with different dynamic properties. In fact, co-assembly of NMII-A and NMII-B seems to influence the dynamic behavior of each other, including the role of NMII-A-only filaments as scaffolds for the assembly of NMII-B-containing bundles (Vicente-Manzanares et al., 2011).

The increased stability of some NMII-A mutants shown by FRAP and photoconversion prompted us to evaluate whether the co-assembly of NMII-A mutants with the wild type form could also be modifying the dynamics of the latter. This is important in a translational scenario since *MYH9* patients rarely display mosaicism, i.e. they always carry one wild type and one mutant allele of *MYH9*, resulting in co-expression of the wild type and the mutant variant of MHCII-A (Deutsch et al., 2003). To address this possibility, we co-transfected COS-7 cells with MHCII-A WT coupled to EGFP and a selection of MHCII-A mutants with different filament stability coupled to HaloTag. In this context, we evaluated the dynamics of the wild type form when it was co-assembling with a given NMII-A mutant by FRAP. As a control, we co-expressed EGFP- and Halotag-coupled wild type MHCII-A. The resulting fluorescence recovery curves (**Figure 30A**) displayed no significant difference on NMII-A WT recovery rates in the different co-assembling conditions (**Figure 30B**).

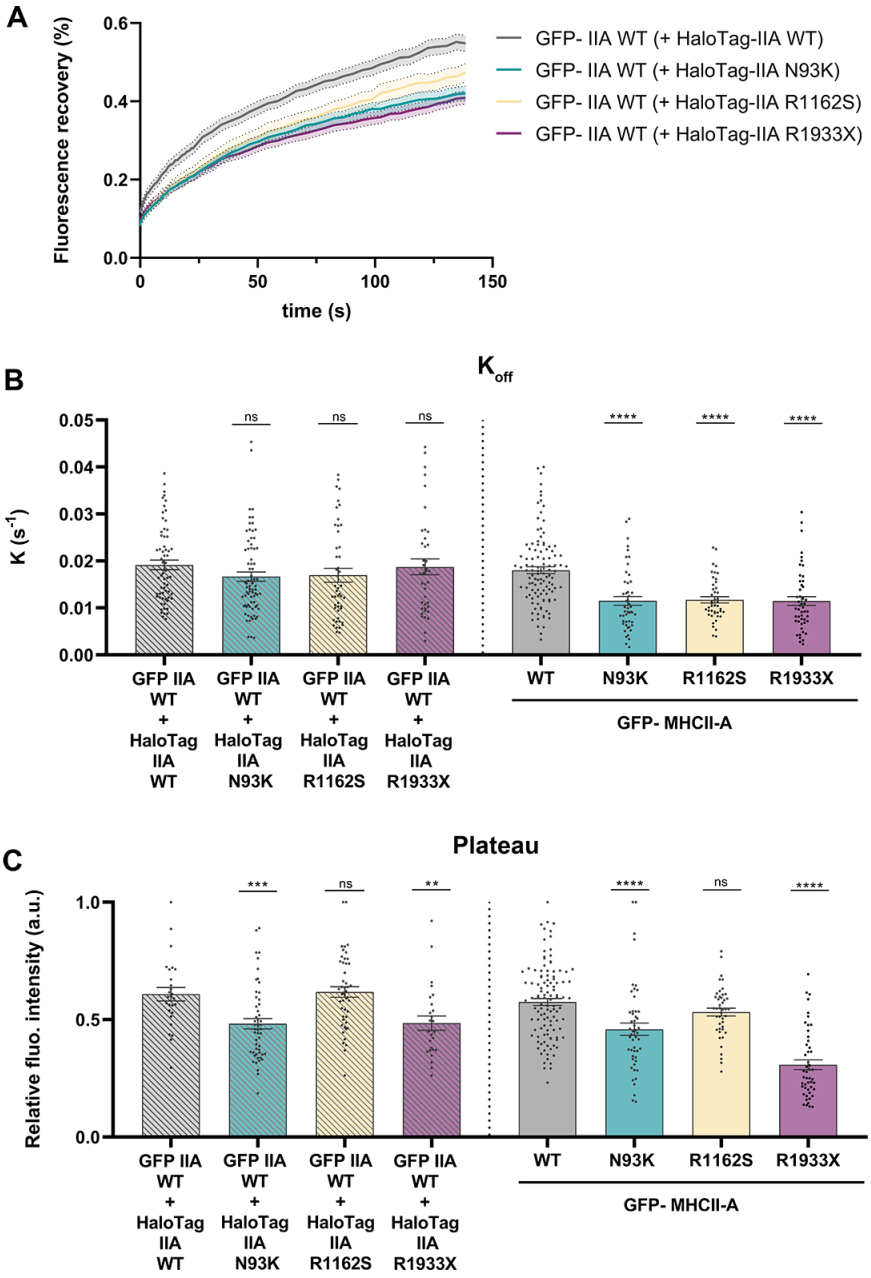

Figure 30: Co-polymerization of wild type NMII-A with selected *MYH9* mutants increases its stability in actomyosin filaments. **(A)** FRAP curves of EGFP-MHCII-A WT in the presence of HaloTag-MHCII-A WT or the mutants N93K, R1162S and R1933X. Transfected COS-7 cells were allowed to adhere on fibronectin-coated (8 µg/ml) coverslips for 2h and then imaged. Data is the average of >40 filaments (±SEM) from three independent experiments. **(B)** Left, mean exponential recovery rates (±SEM) for EGFP-MHCII-A WT when co-polymerizing with the indicated HaloTag-MHCII-A. On the right, the mean recovery rates for the individual mutants are also shown, obtained from **Figure 28C** for easier comparison. **(C)** Left, mean plateau values (±SEM) for the resulting fitting curves, adjusted to a one-phase exponential association model. On the right, the plateau values of the individual mutants obtained from **Figure 28D**. Nonparametric Mann-Whitney U test was used to evaluate statistical significance of EGFP-MHCII-A WT copolymerizing with HaloTag- MHCII-A WT vs. HaloTag- MHCII-A mutants. ** $p < 0.01$; *** $p < 0.001$, **** $p < 0.0001$, n.s., not significant.

Remarkably, wild type NMII-A displayed lower plateau values when co-assembling with NMII-A mutants with the highest immobile fraction (**Figure 28E**) such as NMII-A N93K and R1933X, suggesting that wild type NMII-A stability is increased by copolymerization with more stable NMII-A mutants (**Figure 30C**).

4.2.10 Spatial segregation of *MYH9* mutations begins during initial assembly of NMII-A filaments in the initial phase of isometric spreading

Actomyosin structures assemble *de novo* in post-lamellipodial regions. In these regions, all NMII-A mutants localized further away from the leading edge than the wild type form (**Figure 25**, **Figure 26**). This phenotype could be the result of an increased stability on actomyosin filaments, which accumulates the most stable myosin on the actomyosin structures that grow and evolve inwards, not unlike the segregation effect observed for NMII-B, and consistent with the FRAP and photoconversion data of the NMII-A mutants (**Figure 28**, **Figure 29**). However, it could also be due to a defect in the initial steps of myosin II mini-filament formation. The generation of a nucleation point from which NMII mini-filaments grow requires efficient binding of NMII heads to actin filaments and the stability of the extended, bipolar structure as determined by coiled-coil interactions. Alterations in this equilibrium, either by coiled-coil mutations that could, for example, destabilize tail interactions between hexamers; or motor domain substitutions that could affect either the actin binding or the ATPase domain; may reduce the ability of the mutants to nucleate and to act as nucleation points for other monomers. In this scenario, NMII-A mutants would better incorporate into fully formed wild type NMII-A minifilaments, which would also be consistent with a more posterior localization observed in **Figure 25** and **Figure 26**.

To address this, we evaluated NMII-A nucleation in the initial steps of COS-7 spreading on fibronectin substrates. We transfected COS-7 cells with EGFP-MHCII-A wild type and HaloTag- MHCII-A mutants. Two days post-transfection, cells were incubated for one hour with the HaloTag ligand Janelia Fluor®-585 to illuminate the mutant, seeded on fibronectin substrates and immediately imaged by TIRF microscopy.

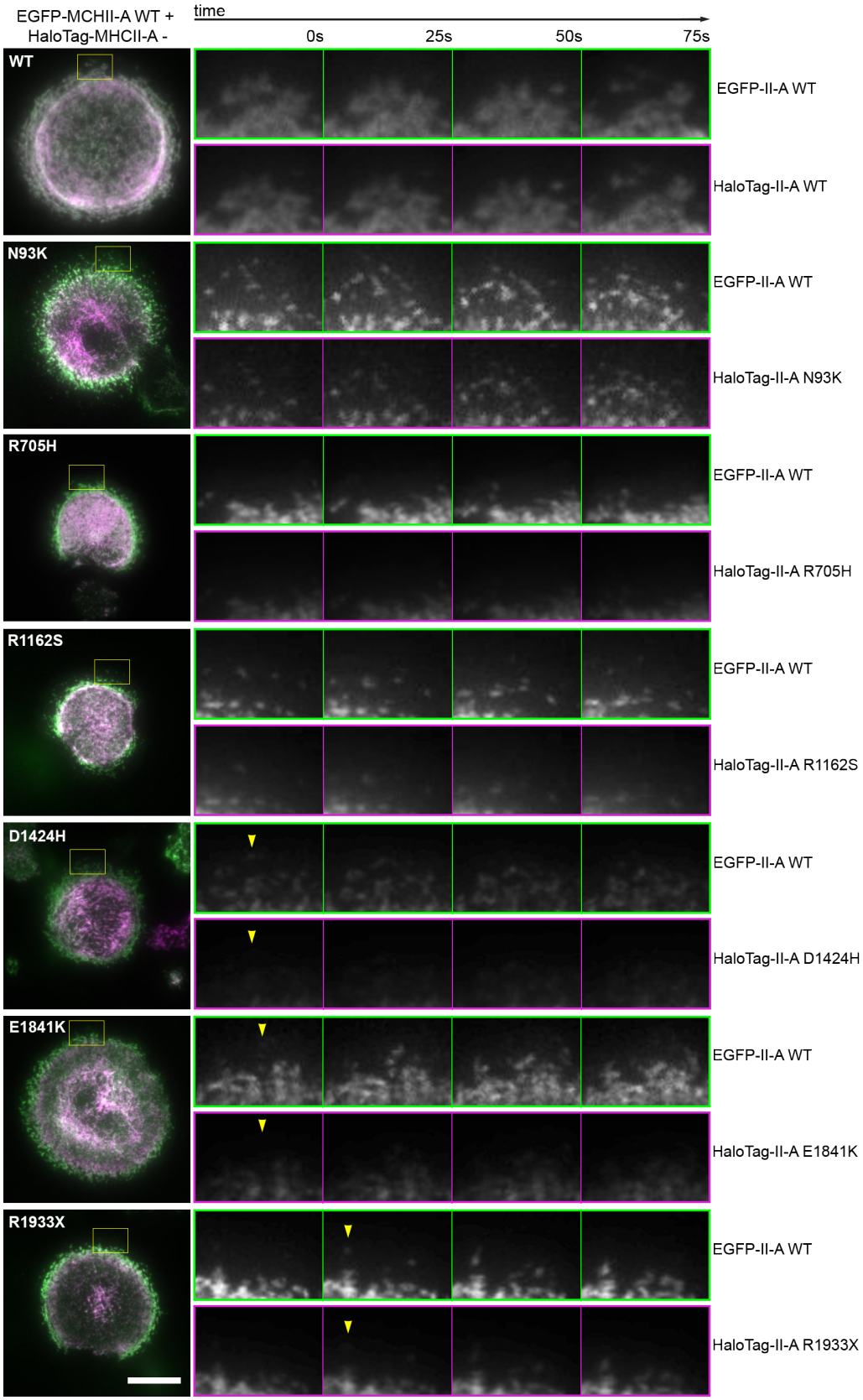

Figure 31: Nucleation of NMII-A and *MYH9* mutants in post lamellipodial regions. (See caption next page).

Figure 31 (page 98): TIRF images from time-lapse videos of COS-7 cells transfected with EGFP-MHCII-A WT and HaloTag-MHCII-A mutants, stained with Janelia Fluor®-585 (50 nM) for 1 h and imaged immediately after seeded. Note that all NMII-A mutants are underrepresented to a variable degree in the nucleating events of NMII compared to the wild type form. Some nucleating spots (yellow arrowheads) initially only contained the wild type form. Scale bar = 10 µm. Magnification yellow box total length = 7 µm.

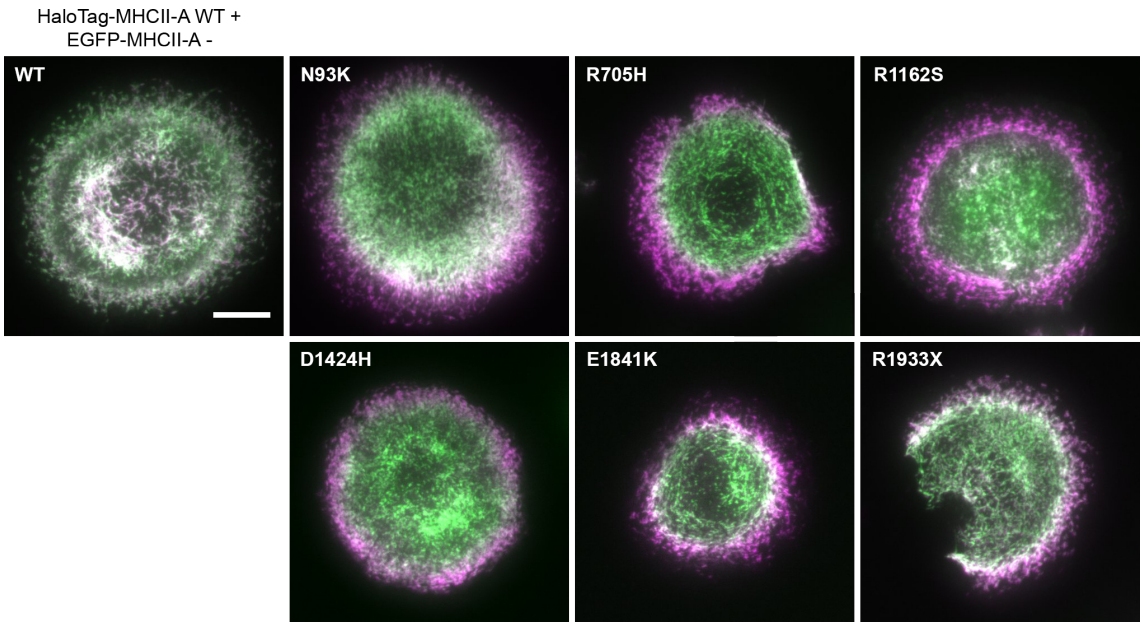

Figure 32: Localization of NMII-A mutants in spreading COS-7 cells. Representative TIRF images of COS-7 cells transfected with HaloTag-MHCII-A wild type and EGFP-MHCII-A mutants, stained with Janelia Fluor®-585 (50 nM) for 1 h, and imaged immediately after seeded in fibronectin-coated coverslips (3 µm/ml). Scale bar = 10 µm.

Image acquisition was performed using a Hamamatsu W-View Gemini system coupled to the camera outlet of the microscope, which allows fast acquisition of two channels simultaneously.

Time-lapse videos revealed the segregation between NMII-A WT and NMII-A mutants even in the initial steps of isometric spreading (**Figure 31**). The NMII-A-rich, nucleating regions closer the cell membrane (**Figure 31**, yellow boxes) still contained the mutant variants, but always to a lesser extent independent of the expression levels or the tag used (**Figure 32**). We could observe events of incorporation of the mutant into pre-formed wild type NMII-A minifilaments (**Figure 31**, yellow arrows).

To improve our analysis of the degree of aggregation and dynamic behavior of the NMII-A mutants, we began collaborating with Prof. Paul Wiseman (McGill University, Montreal, Canada). His group performed Image Correlation Spectroscopy

(ICS) analysis on the TIRF time-lapse videos generated in our lab as part of this work. ICS reveals information about the aggregation state of fluorescent-tagged molecules (Wiseman and Petersen, 1999). In the context of NMII filaments, it potentially provides information of the dynamics of filaments made of EGFP-NMII-A WT, HaloTag-NMII-A mutants or mixed filaments.

So far, we have focused on the post-lamellipodial edges of the cell, where individual NMII minifilaments could be distinguished as discrete dots. As cells continue protrusion, these dots move inwards and fuse into bigger actomyosin structures, thus making it impossible to track them individually. To specifically address the isolated population of minifilaments in post-lamellipodial edges, we isolated these regions using a machine learning-based initial segmentation step to identify post-lamellipodial regions in a semi-automated (automated identification and manual curation) manner (**Figure 33A**), and we performed ICS of the segmented region. From the ICS analysis we obtained the average density of filaments (number of independent clusters detected by ICS) and the average intensity of these regions, from the ratio between them we established an average "degree of aggregation" (DA) of the clusters (Wiseman and Petersen, 1999). Heuristically, the degree of aggregation measures the average quantity of molecules in a cluster.

The analysis of cells co-expressing the wild type form coupled to EGFP or HaloTag showed that ICS technique yielded similar densities of the wild type form coupled to either of the tags, as expected (**Figure 33B**). However, there were considerable differences in the intensities in both channels, which artificially skewed the values of the degree of aggregation (**Figure 33B**). This part is still a work in progress, and up to this point, these analyses have yet to yield usable biological data. However, these experiments open up exciting avenues that may allow us to make novel observations not attainable by other means, hence they are included here. The analysis performed to the rest of the mutants is attached in the Appendix, and steps to improve these experiments so they provide usable biological data are described in Section 5.2.3 of the Discussion chapter.

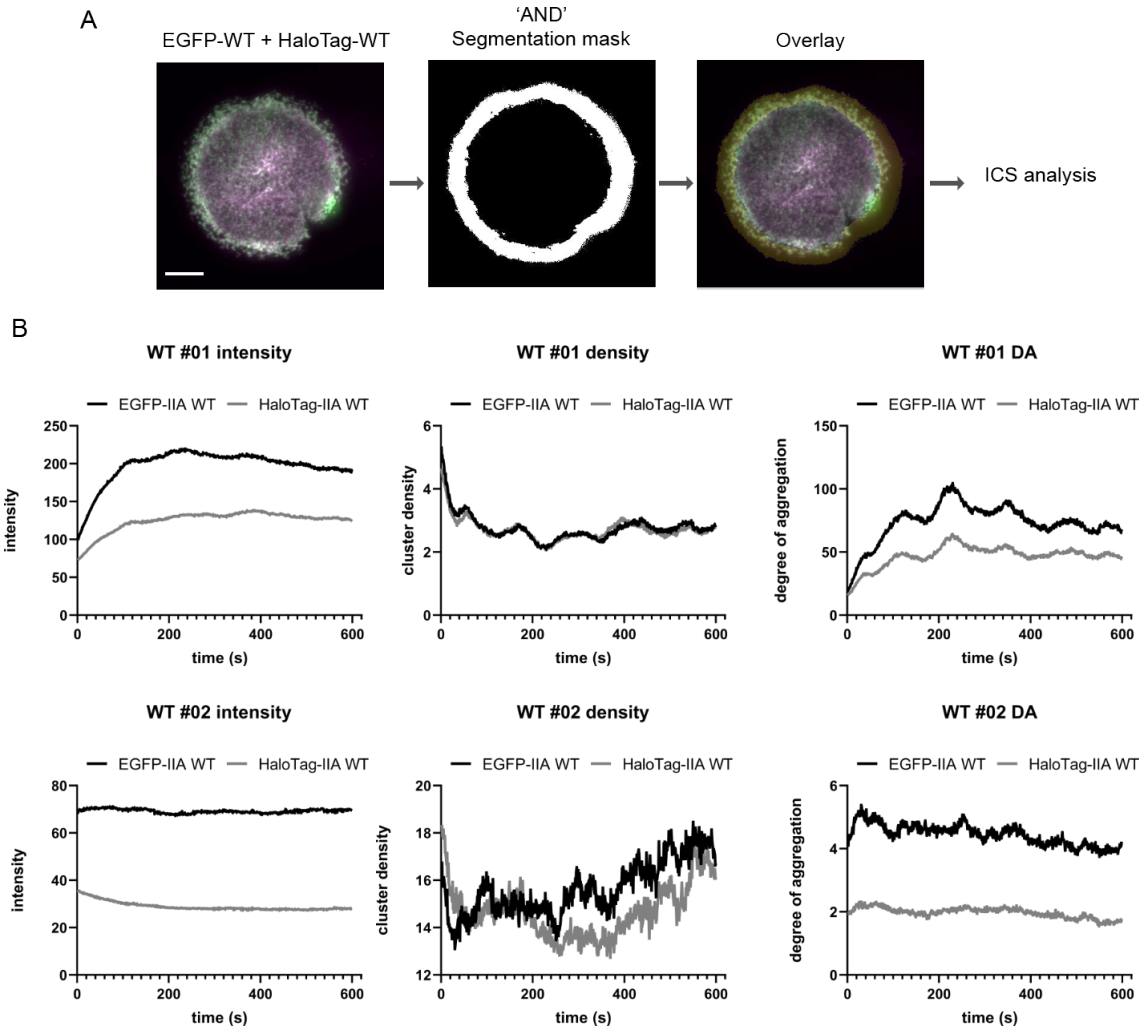

Figure 33: ICS analysis on time-lapse TIRF videos. (A) Schematic representation on the segmentation step for the time-lapse videos. Scale bar = 10 µm. **(B)** ICS analysis of two COS-7 cells (one is shown in (A); the other is not shown) co-transfected with MHCII-A WT coupled to HaloTag and EGFP. The density of individual clusters is similar between tags, meaning the analysis identified NMII clusters correctly. The differences in the intensity biased the data for the degree of aggregation, indicating a higher degree of aggregation for the MHCII-A WT coupled to EGFP.

4.2.11 The phenotypic manifestations of NMII-A mutations are cell-lineage dependent

So far, the study of NMII-A mutants was performed in classically adherent cell lines from epithelial or mesenchymal origins that grow adhered to a substrate. The dynamics of NMII in this context have been widely studied by our laboratory, making them a tractable model for us to assess the dynamic behavior of NMII-A mutants. However, most of the pathological phenotypes of these mutations manifest themselves in cell types that do not display NMII-A localized in fibers (hematopoietic cells, e.g. megakaryocytes, platelets or neutrophils, which do not display focal adhesions in bi-dimensional substrates, yet become adhesive in an integrin-dependent fashion). We then selected N93K and E1841K as representative mutations of the head and assembly domain, respectively, and expressed them in the megakaryocyte cell line MEG-01. MEG-01 cells were transfected with mNeonGreen-MHCII-A wild type and HaloTag-MHCII-A mutants, stained with Janelia Fluor®-635 for 1h before their adherence in fibronectin substrates under PMA stimulation (to promote adhesion and protrusion). As a control, we co-expressed mNeonGreen- and Halotag-coupled wild type MHCII-A. STED images revealed a diffuse pattern for NMII-A WT consistent with a lack of organization in large filaments or bundles.

Strikingly, the localization of the NMII-A mutants with respect to the wild type form of NMII-A adopted a different pattern compared to those seen in COS-7 and U2OS cell line. First, the NMII-A mutants were further from the leading edge than NMII-A wild type, following a pattern similar to that seen in adherent cells. In the case of E1841K, a small segment behind the edge of the cell displayed mainly wild type, but this difference was tenuous compared to U2OS cells. In addition, NMII-A N93K distributed diffusely, but it displayed a visually higher degree of aggregation than cells expressing both wild type tagged forms (**Figure 34**, middle row). Interestingly, N93K aggregates also contained wild type NMII-A, shown as co-localization. Conversely, NMII-A E1841K mutant formed conspicuous filament-like structures that did not contain the wild type form (**Figure 34**, bottom row). Together, this data indicates that in a non-filamentous cellular context, the motor domain mutation N93K segregates better with the wild type form, likely modifying the behavior of the latter. Additionally, it reveals a phenotype of over-assembly for the tail domain that does not affect the localization of the wild type form.

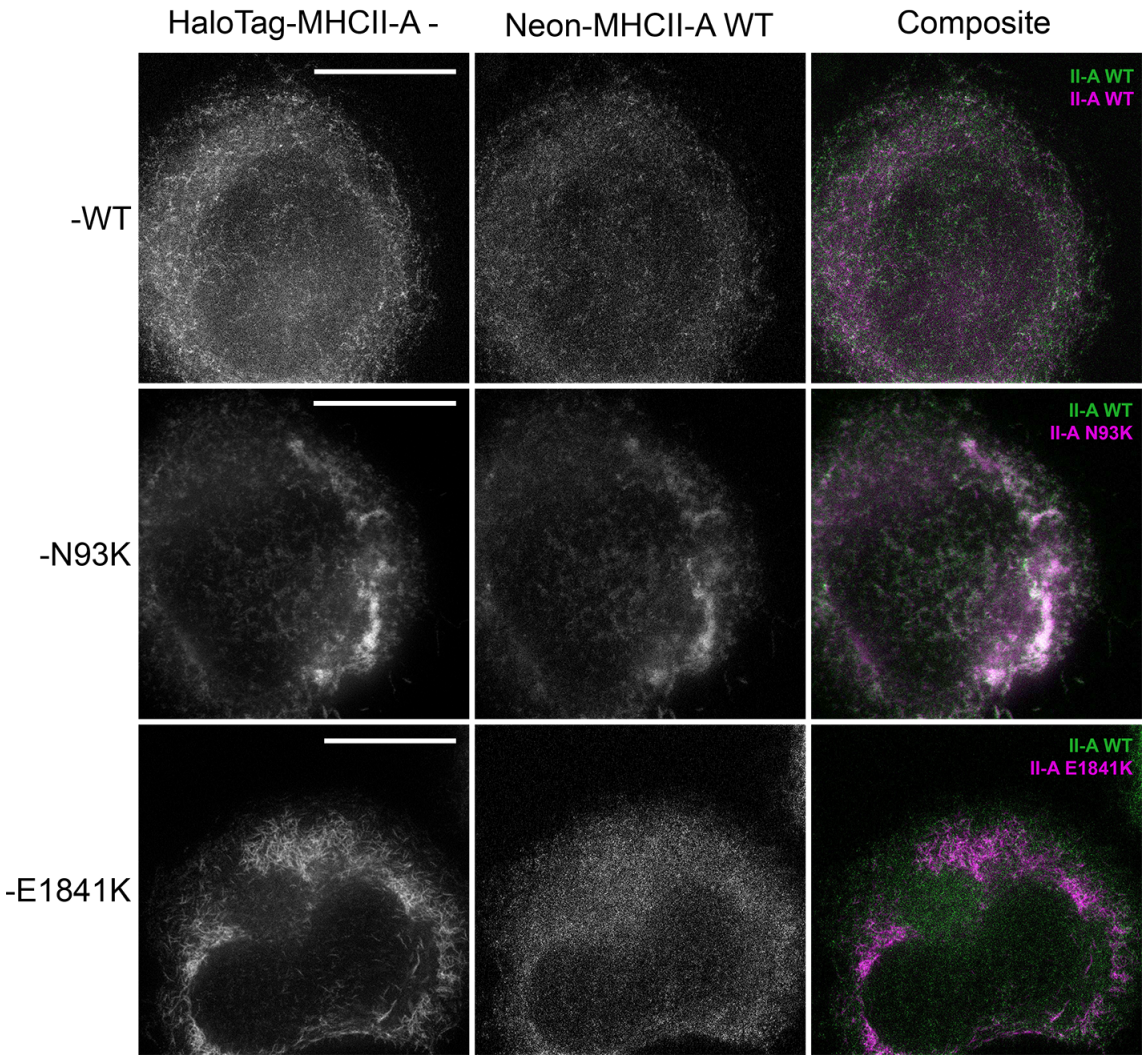

Figure 34: NMII-A N93K forms aggregates that also contain the wild type form while E1841K over-assembles in filaments that do not contain NMII-A in MEG-01 cells. Representative STED images of MEG-01 cells transfected with mNeonGreen-MHCII-A WT and HaloTag-MHCII-A WT. After 48h, cells were stained with HaloTag ligand JaneliaFluor®-635 (50 nM) for 1h, stimulated with PMA (100 ng/ml) and allowed to adhere on fibronectin substrates (20 µg/ml) for 30 min. Scale bar = 10µm.

4.3 Results, part 2*B*: The leukocyte alterations of a *MYH9* patient

MHCII-A R1162S (*MYH9* variant c.3486G>T) is a specific MHCII-A mutation located in the coiled coil region of MHCII-A and originally identify by the group of Dr. José María Bastida (Hospital Universitario de Salamanca) in a cohort of patients with inherited platelet disorders (Bastida et al., 2018). The patient was initially suspected to suffer from *MYH9*-RD since several family members displayed lifelong macrothrombocytopenia, sensorineural hearing loss and neutrophil inclusion bodies in blood smears. The mutation was confirmed by high throughput sequencing (Bastida et al., 2018). A detailed characterization of the clinical features of *MYH9*-RD family bearing the R1162S mutation is summarized in Table 5.

Table 5: Clinical features of *MYH9*-RD phenotype caused by R1162S mutation. P: Platelet count. Y: years.

Patient	**Age**	**Macro-thrombo-cytopenia**	**Deafness**	**Renal failure**	**Cataract**	**Other**
Index	62	X (P=30×10^9/L)	X (< 30 y)	-	-	Rheumatic fever and tonsillec-tomy due to repeated infections
Father	exi-tus	X	X (< 30 y)	X (< 70y)	X (< 70y)	Unknown
Brother	65	X (P=73×10^9/L)	X (< 30 y)	X	-	Unknown
Daughter	35	X (P=83×10^9/L)	X (< 30 y)	-	-	Tonsillectomy due to re-peated infections
Niece	32	X (P=75×10^9/L)	X (new di-agnosis)	-	-	Tonsillectomy due to re-peated infections

In addition to macrothrombocytopenia, several family members displayed some extra-hematological features of the disease, including some degree of early onset hearing impairment developed at young age. One individual displayed early onset

cataracts, and the two older family members suffered from renal failure. Strikingly, three out of the five family members required a tonsillectomy due to the appearance of recurrent infections.

In collaboration with the group of Dr. Jose María Bastida, we addressed whether MHCII-A R1162S mutation affects the morphology and cellular function in leukocyte populations where the NMII-A paralog is predominant, or the only one expressed (Marigo et al., 2004; Maupin et al., 1994). We focused on the morphology and cellular function of functional activated T cells, monocyte-derived dendritic cells (mDCs), and neutrophils. All the experiments were carried out in parallel with peripheral blood samples from healthy donors extracted the same day as the patient's.

4.3.1 Activated T cells

T cells were isolated on a Ficoll gradient and stimulated with PHA and IL-2 for six days, as described in more detail in the Material and Methods section.

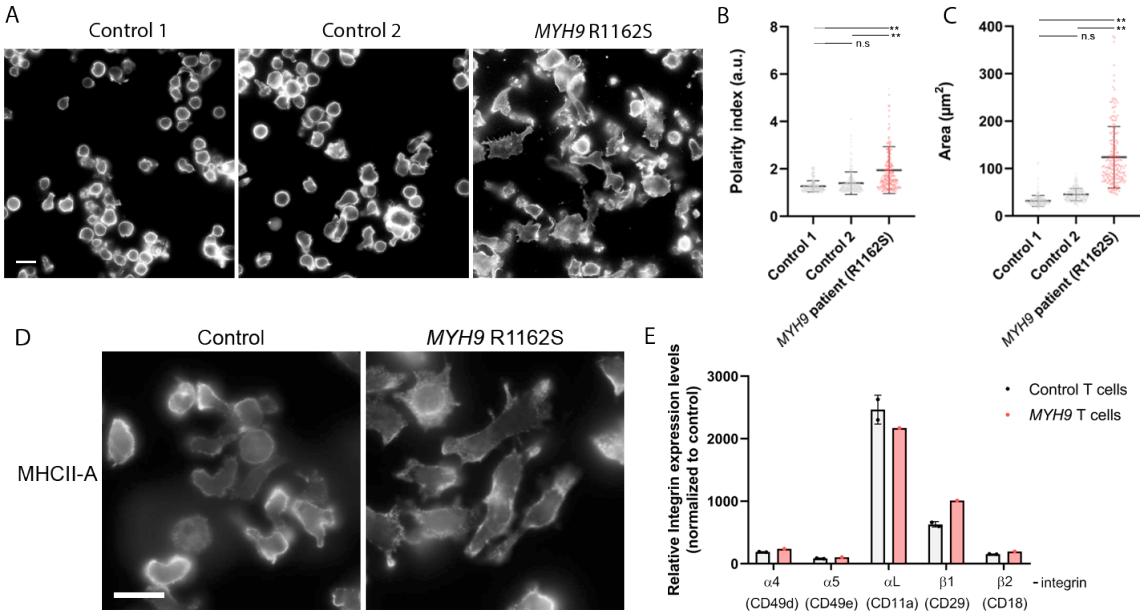

Figure 35: T cells show exacerbated polarization and area of spreading on fibronectin surfaces. **(A)** Representative fluorescent images of activated T cells that were allowed to adhere on fibronectin substrates (20 µg/ml) for 40 mins, fixed and stained with phalloidin. Cell shape was manually determined from the phalloidin staining. Bar=10µm **(B)** Quantification of cell area and **(C)** polarity index was assessed using ImageJ built-in algorithms. N = 100 cells per condition in two independent experiments. **(D)** MHCII-A localization from experiments described in (A). **(E)** Relative surface expression levels of the indicated integrins by flow cytometry. Fluorescence levels were normalized to the fluorescent levels of unstained control samples. Nonparametric Mann-Whitney U test was used to evaluate statistical significance of control vs *MYH9* R1162S activated T cells. ** $p < 0.01$; n.s., not significant. In (E), there were no significant differences.

At day six after isolation, functional activated T cells were allowed to adhere on fibronectin substrates and cell morphology was assessed by phalloidin staining. T cells carrying the MHCII-A R1162S variant displayed an exacerbated polarization (**Figure 35A-B**) and area of spreading (**Figure 35A-C**) upon adhesion on fibronectin, compared to the more round-like morphology of activated T cells derived from healthy donors. Additionally, MHCII-A staining revealed no significant differences in NMII-A localization (**Figure 35D**). Finally, assessment of the surface expression levels of several integrins, including α4β1 and α5β1, which are the major fibronectin receptors in these cells revealed no differences that could account for the alterations observed on fibronectin substrates (**Figure 35E**).

4.3.2 Monocyte-derived dendritic cells

Monocytes were isolated from a Ficoll gradient and stimulated with GM-CSF and IL-4 for six days to obtain immature mDCs.

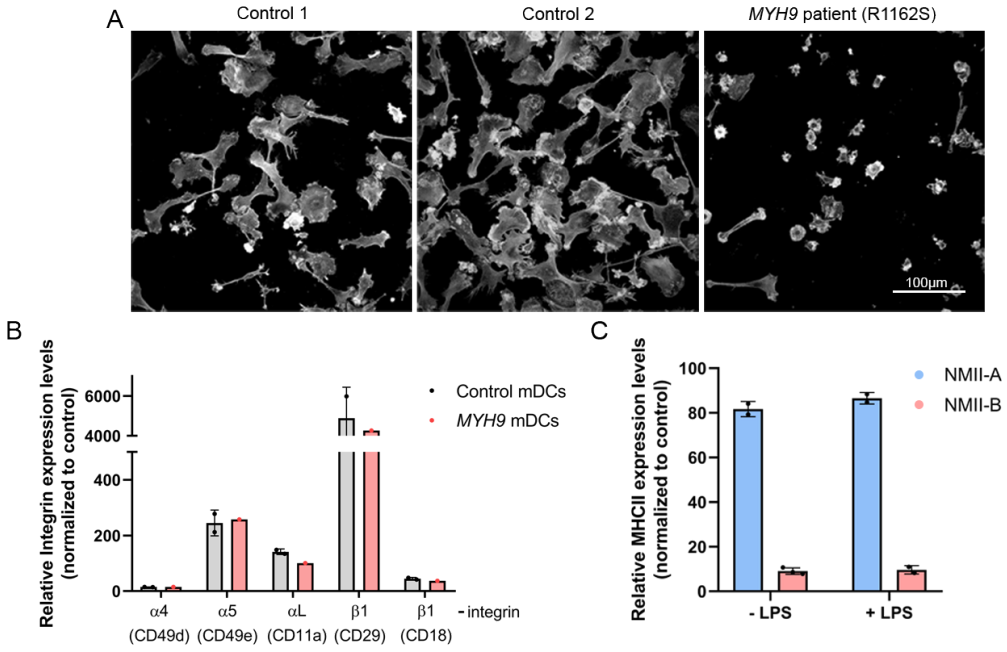

Figure 36: *MYH9*-R1162S dendritic cells exhibit deficient adhesion on fibronectin. **(A)** Representative fluorescent images of mDCs allowed to adhere for 40 mins on fibronectin-coated coverslips, fixed, and stained with phalloidin. mDCs carrying R1162S variant adhered less to fibronectin than control mDCs. Bar = 100 µm. **(B)** Relative surface expression levels of the indicated integrins by flow cytometry. Fluorescence levels were normalized to the fluorescent levels of unstained control samples. **(C)** Relative expression levels of of MHCII-A (blue) and MHCII-B (red) in immature and mature mDCs. MHCII fluorescence levels were normalized using the fluorescent levels of control samples incubated only with secondary antibody. Quantification of at least two independent experiments.

Assessment of the cellular morphology revealed that mDCs bearing the R1162S mutation underwent reduced spreading on fibronectin substrates (**Figure 36A**). The evaluation of surface expression levels of integrin αL, α4, α5, β1 and β2 showed no differences that could account for the adhesion and/or spreading deficiency (**Figure 36B**). R1162S mDCs displayed lower surface expression levels of integrin αL, although this reduction cannot account for the adhesion deficiency on fibronectin substrates, since fibronectin-dependent adhesion is mediated by integrin complex α4β1 and α5β1, which are not altered in cells carrying the mutant protein. NMI-A staining revealed that mDCs displayed a sarcomeric-like organization along actin fibers and a disordered distribution around actin-rich vinculin-positive podosomes (**Figure 37**). Additionally, similar to blood peripheral monocytes (Marigo et al., 2004) mDCs expressed predominantly NMII-A but also NMII-B, and the relative

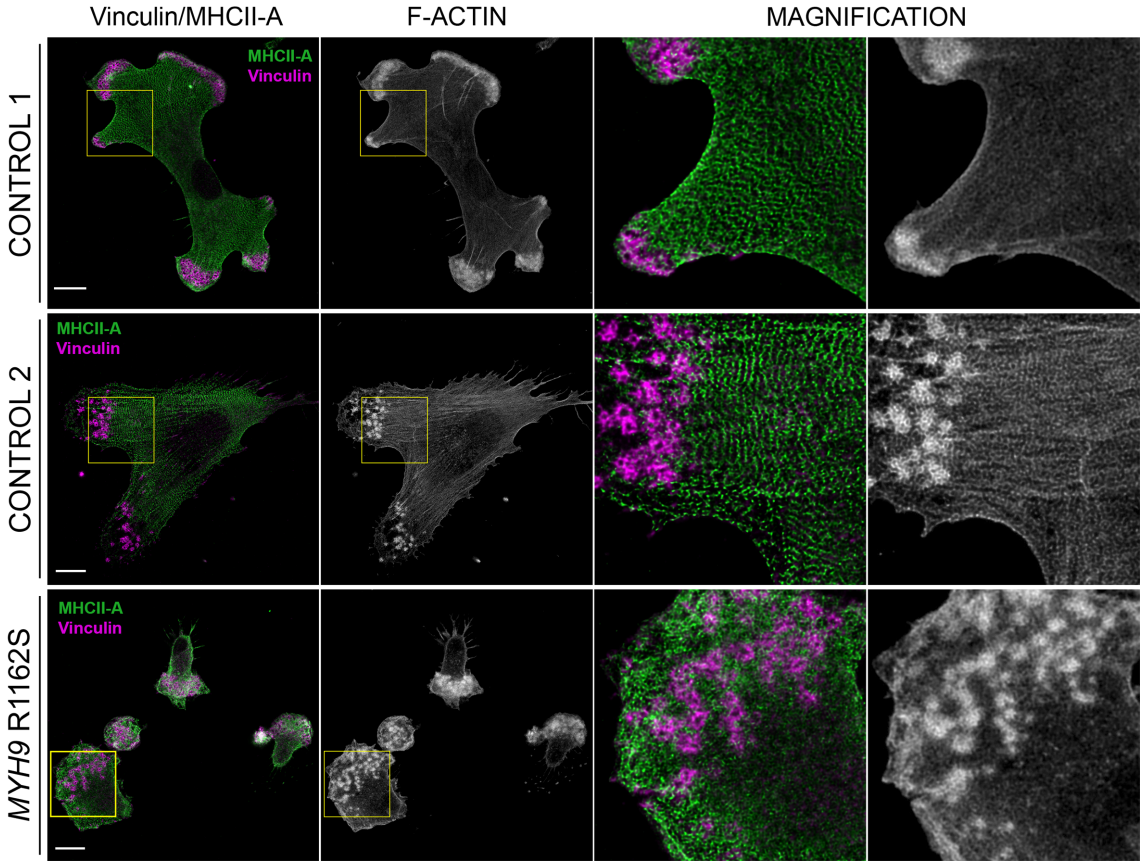

Figure 37: NMII-A organizes in sarcomeric-like stacks in mDCs adhered on fibronectin substrates. Representative confocal images of mDCs adhered for 90 mins on fibronectin-coated (20 µg/ml) coverslips, fixed and stained for MHCII-A, vinculin and phalloidin. *MYH9* mDCs displayed a decreased area of spreading and were enriched in podosome structures. Scale bar = 10 µm. Magnification box total length = 22 µm.

expression levels did not change upon LPS maturation (**Figure 36C**).

Since NMII function is essential for the 3D migration of diverse cell types (Agarwal and Zaidel-Bar, 2019; Moreno-Arotzena et al., 2015; Thomas et al., 2015), we next evaluated the migratory behavior of mDCs embedded in 3D collagen gels. At day 5, immature mDCs were stimulated with LPS (10 ng/ml) for 24h to obtain mature, migratory mDCs determined by the upregulation of specific markers (**Figure 38A**). Dendritic cells were then embedded on collagen gels and allowed to migrate for 12 h on a CCL19 chemotactic gradient using Ibidi® µ-Slide Chemotaxis chambers (**Figure 38B**). Both mDCs migrate towards CCL19 (**Figure 38B-E**),

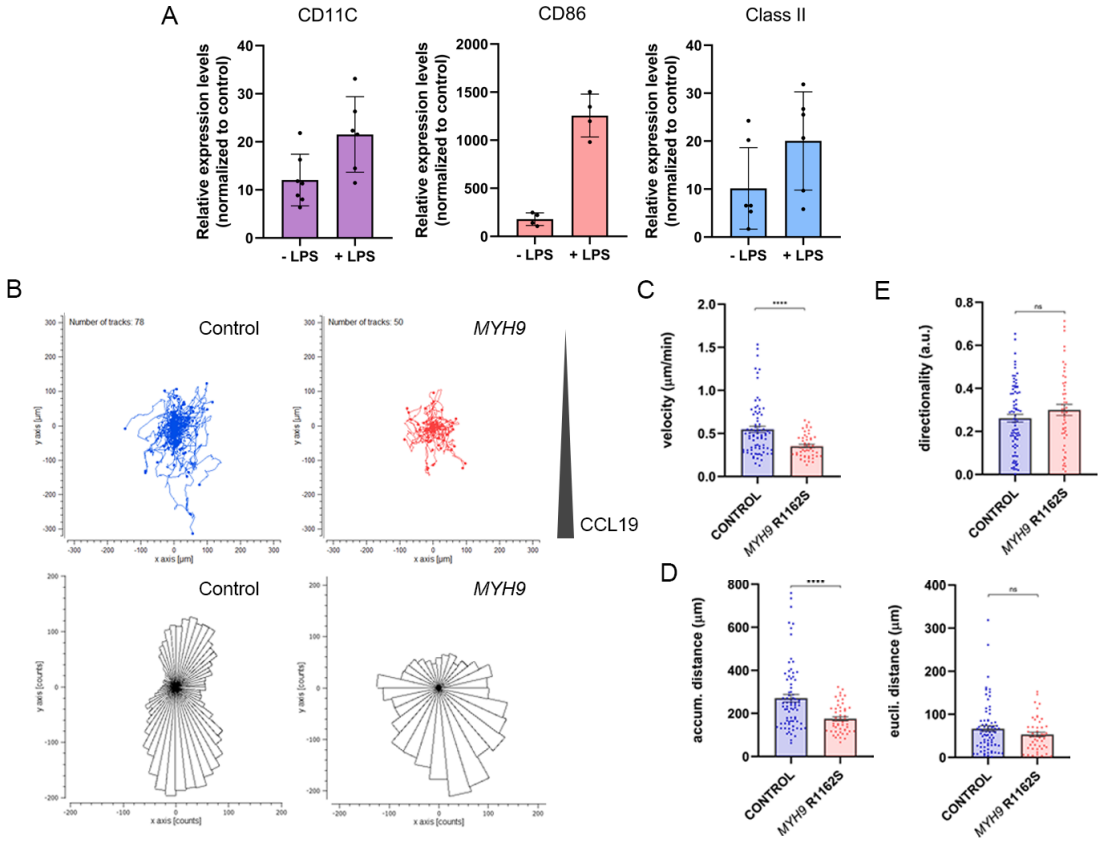

Figure 38: *MYH9*-R1162S decreases dendritic cell migration speed in 3D collagen gels. **(A)** Relative surface expression levels of class marker CD11c and maturation markers CD86 and Class II in control mDCs with or without LPS stimulation. Quantification of four independent experiments. **(B)** Top, data represent the indicated number of tracks and cells' trajectories from each condition. Bottom, rose-plot diagrams of mDCs migration on a CCL19 gradient. N= 78 cells (control) and 50 cells (*MYH9*) **(C)** Average migratory velocity, **(D)** accumulated distance (left panel) and Euclidean distance (right panel), and **(E)** directionality were calculated using Ibidi's Chemotaxis and Migration Tool from the migratory tracks. Data are the mean ±SEM. Both mDCs migrate towards CCL19, but *MYH9* R1162S mDCs migrate slower, and slightly more persistently. Nonparametric Mann-Whitney U test was used to evaluate statistical significance of control vs *MYH9* R1162S-mDCs. **** $p < 0.0001$; n.s., not significant.

although *MYH9*-mDCs were slower (**Figure 38C**). They also displayed decreased accumulated distances compared to Control-mDCs, given similar Euclidian distances among them (**Figure 38D**), which suggested that mDCs bearing R1162S mutation migrate more persistently. However, this effect was mild since the directionality, which reflects the ability to migrate persistently along a direction, is not significantly different between the two conditions (**Figure 38E**). Strikingly, we also observed a significantly higher number of membrane rupture and cytoplast shedding events on *MYH9*-mDCs upon migration through collagen pores (**Figure 39**). This effect was also observed in mDCs derived from healthy donors, but not as frequent (**Figure 39B**), even in very stretched cells (**Figure 39A**).

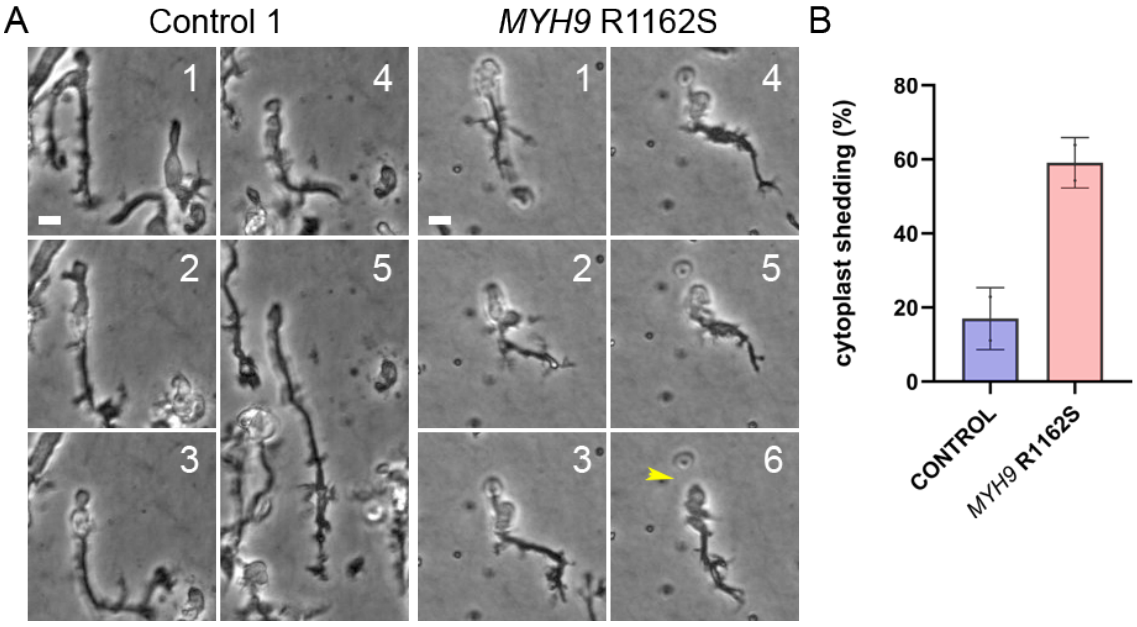

Figure 39: ***MYH9*-R1162S dendritic cells exhibit cellular scissions upon migration on 3D collagen gels. (A)** Illustrative images of R1162S mDCs showing a compromised cellular integrity, breakages (yellow arrow) were observed upon migration through collagen pores **(B)** Percentage of mDCs displaying cytoplast shedding in two different microscopic fields of the collagen gel. N = 93 cells (Control) and 71 cells (*MYH9* R1162S). Time frame = 25 mins. Bar = 10µm.

4.3.3 Neutrophils

Neutrophils were isolated from the pellet fraction of a Ficoll gradient, enriched by hypotonic shocks to remove erythrocytes and processed immediately. Cells were stimulated with fMLP (100 nM), allowed to adhere for 30 mins on fibronectin substrates and their morphology was evaluated by immunofluorescence. In neutrophils obtained from healthy donors, MHCII-A shows a diffuse pattern, displaying an even

distribution throughout the cell in non-polarized cells or, in polarized cells, concentrated at the back, in opposition to actin-rich protrusive structures at the front (**Figure 40A-B**, upper panels). Most strikingly, neutrophils bearing *MYH9*-R1162S mutation do not display the MHCII-A aggregates characteristic of *MYH9* patients and featured in blood smears. Instead, we found highly organized, stack-like structures that are distributed across the cytoplasm in a punctuated fashion in non-polarized cells or concentrated at the back of polarized neutrophils (**Figure 40C**). However, even though neutrophils bearing MHCII-A R1162S mutation still display actin-myosin front-back polarity, they show reduced fMLP-dependent chemotaxis in Boyden chambers (**Figure 41**).

Finally, we studied the ability of these neutrophils to form Neutrophil Extracellular Traps (NETs). NETs are web-like DNA structures released as the last response of activated neutrophils and are designed to trap and neutralize pathogens during the innate immune response. This multi-step, highly orchestrated process involves actin disassembly, chromatin decondensation and nuclear rounding, progressive plasma membrane and nuclear envelope (NE) permeabilization, NE rupture to release DNA into the cytoplasm, and finally plasma membrane rupture and the expel of extracellular DNA. The first step of the NETosis program involves the onset of a signaling and enzymatic cascade that includes biochemical modifications such as histone citrullination and cleavage (Wang et al., 2009) and phosphorylation of lamins and their subsequent disassembly (Li et al., 2020). It also involves the disassembly of the actin and microtubule cytoskeleton, which ensures the mechanical instability necessary for membrane rupture and DNA expulsion upon chromatin decondensation and swelling (Neubert et al., 2018; Thiam et al., 2020).

We used PMA as an activation signal via PKC, which drives ROS induction and the onset of the NETosis program (Remijsen et al., 2011; Takei et al., 1996). After 90 minutes of PMA stimulation, we observed a clear induction of actin disassembly (**Figure 42**, right panels). In accordance, NMII-A was equally affected, failing to distribute evenly throughout the cell body and either disassembling or becoming accumulated around the nucleus (**Figure 42**, right upper and middle panels). However, in *MYH9*-R1162S neutrophils, even with a profound disassembly of the actin cytoskeleton, we could still observe NMII-A hyper-stacks, suggesting that these myosin structures were more resistant to disorganization and disassembly (**Figure 42**, right bottom panel).

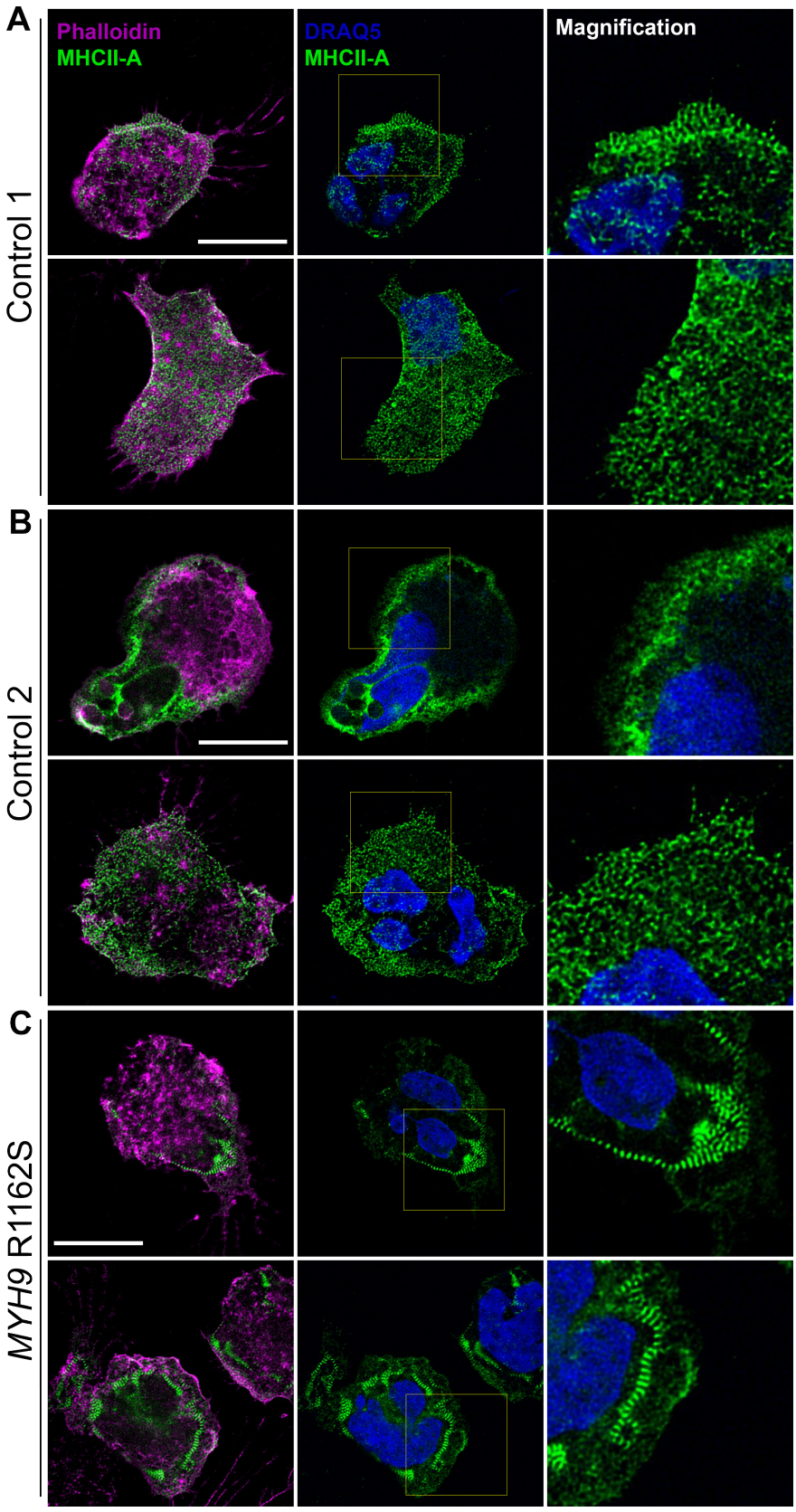

Figure 40: *MYH9*-R1162S neutrophils showed altered myosin II distribution. (Continues in the next page)

Figure 40 (page 111): ***MYH9*-R1162S neutrophils showed altered myosin II distribution.** Representative confocal images of MHCII-A localization in neutrophils derived from two **(A)** and **(B)** healthy donors, or **(C)** the *MYH9* R116S patient. Upper panels show cells with a polarized morphology. Lower panels show unpolarized cells within the same coverslip. Note the stacked MHCII-A structures in *MYH9* R1162S neutrophils, absent from healthy controls, adhered on fibronectin (20 µg/ml). Bar=10 µm. Magnification box size = 11 µm.

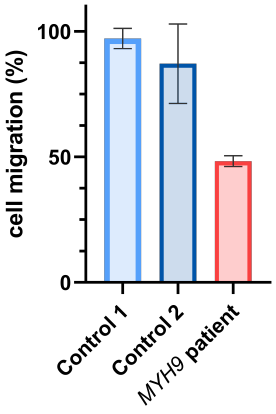

Figure 41: *MYH9*-R1162S neutrophils migrate deficiently towards fMLP. fMLP-dependent (100 nM) neutrophil migration on Boyden chambers (pore size = 5 µm) shown as the difference in percentage of migration between unstimulated vs. fMLP-stimulated conditions. Data are the mean ±SD of three experimental replicates.

We hypothesized that the uneven and punctuated accumulation of myosin structures of high stability (**Figure 42**) may jeopardize cortical integrity, compromising the ability of neutrophils derived from the *MYH9* patient to perform NETosis. To evaluate NETosis in a semi-quantitative manner, we used the cell impermeable SYTOX green dye, which binds to extracellular DNA, and monitored NET formation over time by quantifying total increase in fluorescence using a plate reader (**Figure 43A**) and by time-lapse imaging (**Figure 43B-C**). In time-lapse imaging, NETosis were quantified as the percentage of NETosis events/total number of cells in the microscopic field. As a control, neutrophils were treated with DMSO (vehicle). Control conditions showed no significant increase in overall SYTOX green fluorescence (**Figure 43A**) or SYTOX-positive cells (**Figure 43B**) over the course of the experiments, indicating that the experimental setup did not affect neutrophils' cellular integrity and that there were no effects of necrosis (which would also translate in an increase in total fluorescence as the membrane becomes compromised, or give positive cells in the time-lapse imaging videos). The increase in SYTOX green fluorescence followed a sigmoidal curve that plateaued at 6 hours after PMA stimulation (300 nM) (**Figure 43A**). Strikingly, neutrophils derived from *MYH9* patient showed an earlier onset of NETosis, although the NETosis plateau was comparable. Accelerated NETosis onset was also observed on the time-lapse videos (**Figure 43B**).

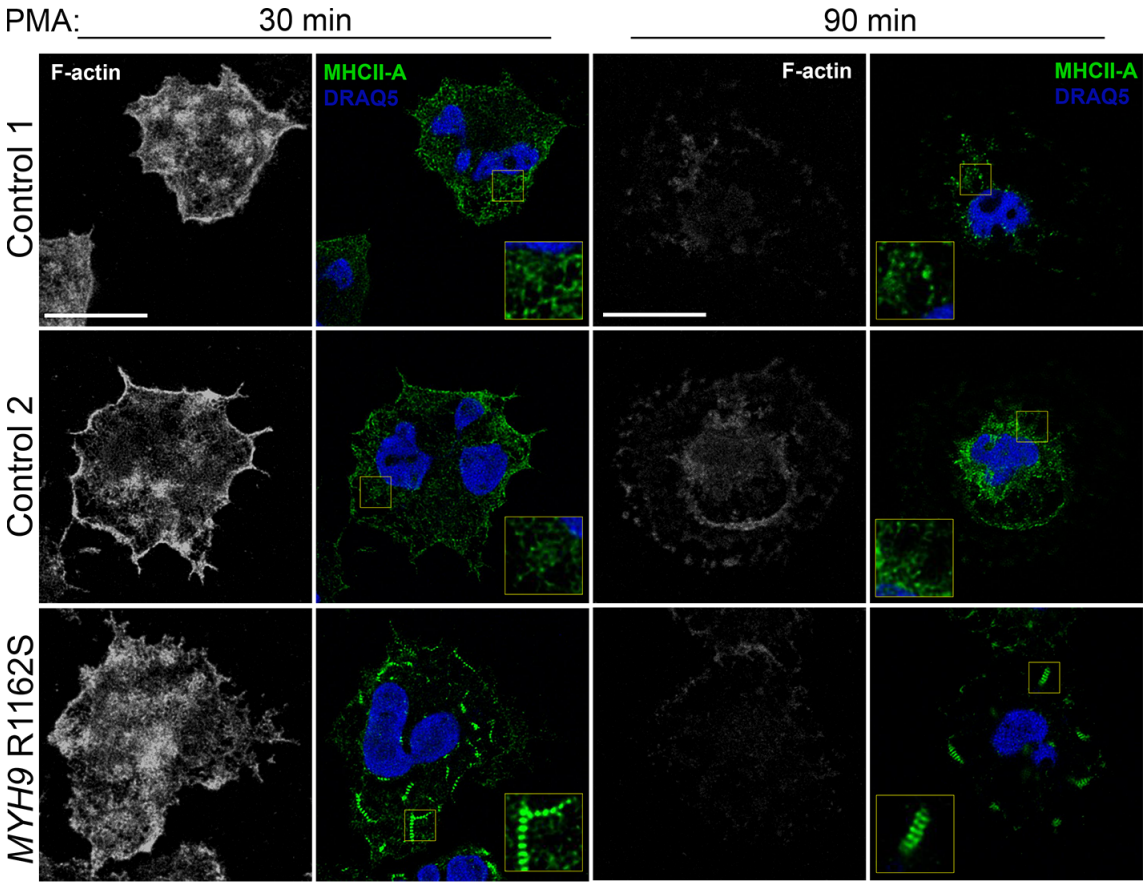

Figure 42: *MYH9*-R1162S structures are resistant to PMA-induced actin turnover. Representative confocal images of MHCII-A localization in neutrophils derived from two healthy donors or the *MYH9* R1162S patient. Neutrophils were stimulated with PMA (300 nM), adhered on fibronectin-coated coverslips, fixed at the indicated time points, and stained for filamentous actin (F-actin) and MHCII-A. DNA was marked with the fluorescent probe DRAQ5 (1 µM). PMA stimulation induced a decrease in F-actin content with consequent loss of MHCII-A localization and assembly in control conditions, while *MYH9* R1162S neutrophils preserved MHCII-A stack-like structures even after overall actin disassembly occurs. Bar=10 µm. Magnification box size=3 µm.

Interestingly, their control conditions also displayed more SYTOX green staining as shown by the two experimental setups (**Figure 43**).

Cortical actin filament networks act as a physical impediment to plasma membrane rupture and DNA release into the extracellular environment, and early disassembly of the actin cytoskeleton acts to remove this impediment. In this context, NMII crosslinking functions as a stabilizer of the actin network (Taneja et al., 2020; Weissenbruch et al., 2021). Together, these data suggest that the uneven and punctuated accumulation of highly stable NMII-A structures (**Figure 40** and **Figure 42**) may alter the overall mechanics of the actomyosin cortex by creating regions of

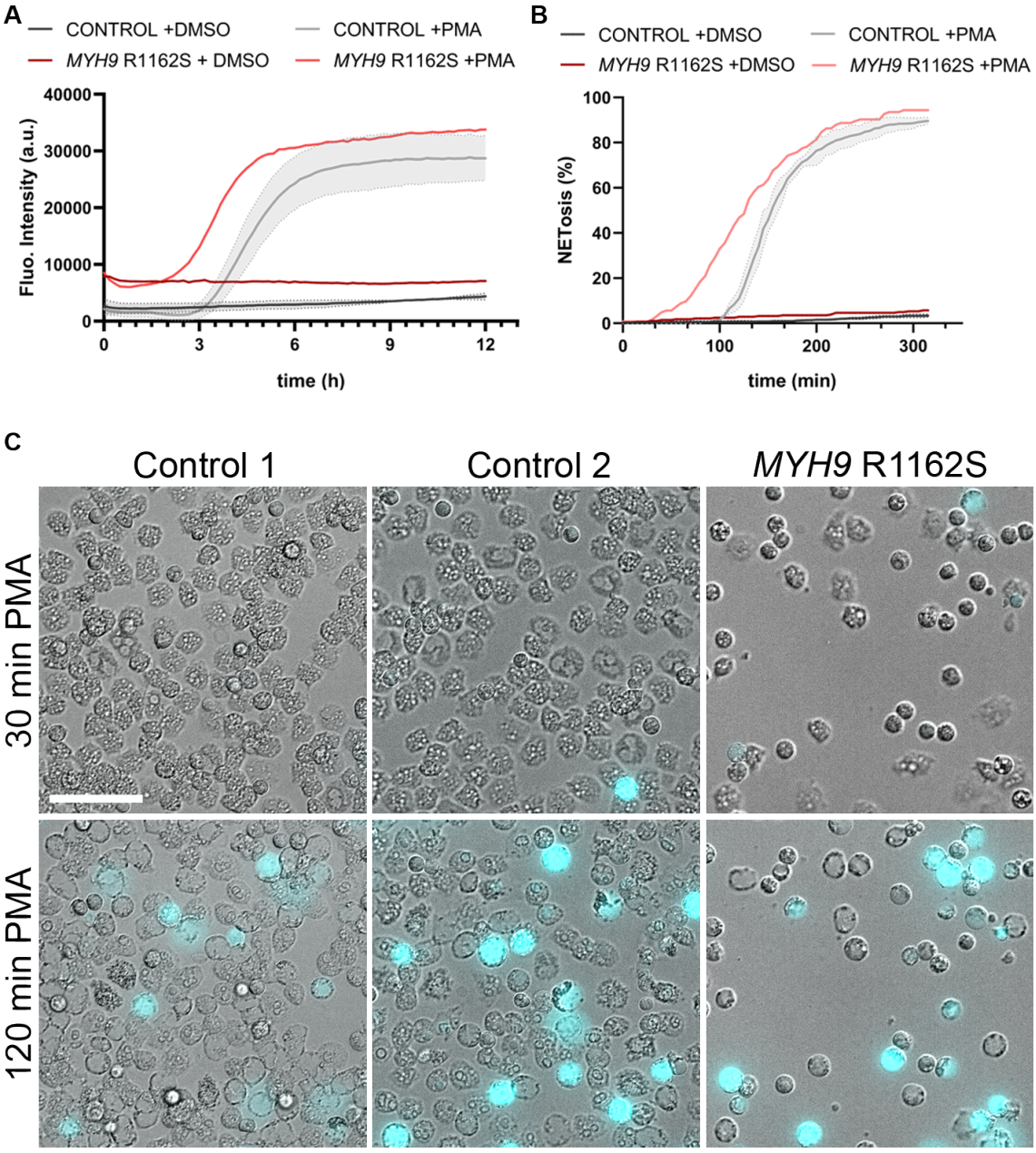

Figure 43: ***MYH9*-R1162S neutrophils display an early onset of NETosis.** **(A)** Kinetics of SYTOX green (1 µM) fluorescence detection of NETosis in response to 300 nM PMA. For control conditions, data are the mean ± SD of 8 healthy donors in 4 independent experiments, one of which included the *MYH9* R1162S patient. **(B)** Quantification of the percentage of NETosis from a time-lapse video relative to the total number of cells on the microscopic field. Cells were incubated with DMSO or PMA 300 nM and imaged for 5,5h. Sytox green (250 nM) was added to imaging medium. N= 360 (control 1), 258 (control 2) and 124 (*MYH9*) cells in the PMA-stimulated condition, and at least 300 cells in the non-stimulated (DMSO) condition. **(C)** Representative fluorescent images from the time lapse video. Note that the number of NETosis is similar between the three experimental conditions, but there is a smaller number of neutrophils per microscopic field in the case of *MYH9* patient, indicating a higher percentage of NETosis at 120 minutes. Bar = 50µm.

higher rigidity than others. This can compromise cellular integrity, as suggested by the increase SYTOX green staining in control conditions of neutrophils bearing the R1162S mutation (**Figure 43**), and favor DNA projection.

5 Discussion

5.1 The role of RLC Y155 phosphorylation in NMII regulation

In the first chapter of this thesis, we demonstrate that phosphorylation of residue Y155 of the RLC inhibits NMII assembly at the leading edge. This novel phosphorylation constitutes a mechanism through which pro-migratory signals, e.g. growth factors, control the spatial organization of actomyosin structures of different stability that is necessary for mesenchymal cells to develop migratory front-rear polarity.

In non-muscle cells, actin and NMII appear in two major states: non-filamentous and filamentous. Filamentous actomyosin can be structurally divided into small and dynamic bundles, and large and stable bundles (Cramer et al., 1997; Vicente-Manzanares et al., 2008). The relative proportion of each population depends on the conditions of the cellular microenvironment. For example, a large amount of stable actomyosin bundles increases the mechanical resistance of cells (Kassianidou and Kumar, 2015). It also enables the establishment of long-lasting cellular morphologies. Conversely, small and dynamic bundles predominate in rapidly moving cells.

The intracellular distribution of actomyosin bundles of different stability ultimately controls the ability of the cells to become stably polarized and respond efficiently to migratory signals. This hinges on the assembly competence of NMII, which largely depends on the phosphorylation of NMII on S19 (and T18) of the RLC (Ikebe, 2008). Our previous findings established that T18/S19 phosphorylation effectively controls the ability of NMII to form large and stable actomyosin bundles, thereby dictating front-rear polarity, and the ability of the cell to form elongated focal adhesions in bi-dimensional substrates (Vicente-Manzanares and Horwitz, 2010;

Vicente-Manzanares et al., 2008). Here, Y155 emerges as a crucial residue that controls the incorporation of RLC into the NMII hexamer.

We have demonstrated that Y155 phosphorylation impairs RLC association with MHCII to form NMII hexamers. Y155E phospho-mimetic mutant mimics this behavior, which is consistent with a decreased interaction with the heavy chain of myosin II. Y155E is neither able to compete with endogenous RLC for the heavy chain nor its overexpression rescues the effects generated by RLC knockdown. RLC Y155E does not restore the loss of MHCII-A and MHCII-B expression caused by depletion of endogenous RLC, suggesting that its affinity for MHCII-A/B is so low that it does not stabilize NMII hexamers, even the soluble, non-filamentous (10S) conformation. This is likely due to its inability to associate with the heavy chain enough to maintain the intra-molecular interactions that support the compact conformation of myosin II (Salzameda et al., 2006; Heissler et al., 2021; Yang et al., 2020).

5.1.1 The Y155 residue is important for the interaction of RLC with MHCII

Comparison of overexpression and knockdown + rescue experiments with RLC Y142 and Y155 phosphomimetic and non-phosphorylatable mutants also reveals the structural relevance of residue Y155 in the interaction between RLC and myosin heavy chain. While Y142 mutants could readily exchange and locate in filaments in overexpression (indicating that they efficiently compete with the endogenous form), Y155F localization in filaments only occurs in the context of the knockdown of the endogenous RLC, where competition with wild type form is eliminated, suggesting that Y155F interaction with the heavy chain is affected to some degree.

The interaction of Y155F RLC with the heavy chain is sufficient to ensure the stability of the heavy chain and rescue its expression, and the formation of myosin II mini-filaments; but it does not support formation of large and stable bundles. In agreement, Y155F RLC is modestly phosphorylated on S19, and even more modestly on T18/S19 in response to adhesion. Although the low phosphorylation of RLC Y155F on S19 and T18+S19 is likely enough to restore some NMII-dependent effects, for example nascent adhesion formation, it is clearly insufficient to generate the required amount of large and stable actomyosin filaments that supports adhe-

sion maturation and define front-rear migratory polarity (Vicente-Manzanares and Horwitz, 2010; Vicente-Manzanares et al., 2008). This strongly suggests that myosin filaments containing RLC Y155F are less stable and smaller than those containing wild type RLC, pointing out the relevance of this residue in the stability of the hexamer. It also indicates that highly dynamic, small myosin filaments are sufficient to drive nascent adhesion formation. In this regard, the RLC Y155F rescue phenotype is similar to that observed when MHCII-B was depleted. In these cells, we also observed a complete loss of front-back polarity, impaired migration and focal adhesion maturation, but no effect on nascent adhesions (Lo et al., 2004; Vicente-Manzanares et al., 2007).

It is important to delineate the mechanism through which Y155 controls the interaction of RLC with the MHCII to form a functional NMII hexamer. Our data are consistent with a model in which Y155 would function as an allosteric switch that enables the cell to use RLC to form assembly-competent NMII only when Y155 is not phosphorylated. We use the word "allosteric" because Y155 does not localize in the region that controls NMII function through phosphorylation, i.e. the N-terminus. The N-terminus has been difficult to resolve by cryo-EM until recently owing to its flexibility. A recent study resolved the N-terminus of RLC partially, only from residue 14 (Heissler et al., 2021). Y155 localizes to the C-terminal lobe of RLC. There are two pieces of data that support Y155 function through phosphorylation and its role in the interaction with the heavy chain. First, Taylor and colleagues' cryo-EM data show that, in smooth muscle myosin II, RLC Y155 is solvent-accessible (Baumann et al., 2012). Second, Heissler and coworkers have shown that the C-terminal ends of both RLC adopt a clamp-like conformation that stabilizes the interaction with their respective hooks of the lever arms in the folded conformation, suggesting a role for this region in the formation and stabilization of the 10S structure (Heissler et al., 2021). Together with the observations described here, these data suggest that Y155 phosphorylation could prevent the RLC from adopting a conformation that allows RLC binding to the heavy chain. In this regard, we could not detect phospho-Y155 RLC associated to MHCII, supporting this hypothesis.

The main function of RLC is to enable the formation and control the function of the NMII hexamer. NMII is a hyper-abundant protein in most cells. In parallel to the development of this work, and in collaboration with Henry Higgs' lab in Dar-

mouth, we have measured the number of NMII molecules in individual cells, which are over 2×10^7 total molecules (the three paralogs) per individual U2OS cell (Kage et al., 2022). Thus, any post-translational modification would lead primarily to the regulation of NMII, since it is its main binding partner and it is broadly expressed in every cell type. However, it could be interesting to consider other binding partners of RLC that could, as in the previous example, be affected to a lesser degree by RLC regulatory modifications. Whether this new mode of regulation through Y155 phosphorylation also affects RLC interaction with other binding partners remains unexplored.

5.1.2 NMII is not the only partner of RLC

One of the key findings of this work is that RLC phosphorylation in Y155 takes place in the context of free, unbound RLC. The fact that RLC is not in the context of NMII hexamer when phosphorylated in Y155 suggest that this phosphorylation can potentially have other functions unrelated to conventional myosins. Although the most canonical and primary binding partners are class II myosins, there are other unconventional myosins (Bird et al., 2014; Bookwalter et al., 2014) and non-myosin binding partners (Bajaj et al., 2009; Bruneau et al., 2022) for RLC, as reviewed in (Heissler and Sellers, 2015).

For example, the unconventional Myosin 18A (Myo18A) has the closest similarity to NMII among myosin superfamily and binds ELC and RLC (Guzik-Lendrum et al., 2013). It has a motor-like domain, with actin binding but no ATPase activity, a neck region with the IQ motifs for the light chains, and a coiled-coil domain that allows its dimerization. However, it cannot organize into higher order structures and instead assembles within NMII filaments. Additionally, Myo18A has N- and C-terminal domains that increase its repertoire of binding partners (Furusawa et al., 2000; Mori et al., 2003).

In this study we described that unlike NMII, RLC knockdown does not affect Myo18A expression levels. Nevertheless, the fact that RLC is not essential for Myo18A stability does not rule out a possible regulatory function on Myo18A. An impaired interaction between RLC and Myo18A heavy chain can still affect myosin structure stability, promoting its disassembly from NMII filaments. In fact, one of the proposed functions for Myo18A is to increase of the repertoire of binding

partners of NMII through hybrid filaments via the protein-protein interaction sites present within its N and C termini (Billington et al., 2015).

Additionally, there are other non-myosin binding partners, such as NMDA type glutamate receptor, that only binds RLC when it is free and not in the context of NMII hexamer. This suggest that the NMDA-RLC interaction is not a mechanism for localization of NMII, that could have myosin-unrelated functions. In this case, RLC phosphorylation on S19 disrupts its interaction with NMDA-type glutamate receptor, which results in a delay in the delivery of the receptors to the cell membrane, indicating a role in receptor traffic (Bajaj et al., 2009).

5.1.3 Proposed model for Y155 regulation

Assembled NMII filaments localize outside of the lamellipodium, because NMII activation and myosin filament formation inhibit protrusion by increasing actin retrograde flow (Gardel et al., 2008; Ponti et al., 2004; Vicente-Manzanares et al., 2011). By locally reducing the pool of assembled, activation-competent NMII in this region, Y155 phosphorylation could *de facto* inhibit NMII assembly. This is particularly important in light of the fact that RTKs can also activate NMII via S19 phosphorylation; hence the same stimulus triggers paradoxical, protrusive and anti-protrusive, signals. We propose that, in active, protruding lamellipodia, Y155 phosphorylation by growth factors is locally dominant, preventing NMII assembly. Later on, lamellipodia stalls because the effect of growth factors to trigger S19 phosphorylation becomes dominant, promoting NMII filament assembly, traction stress and adhesion elongation. An alternative mechanism of NMII inactivation through phosphorylation of S1 of the RLC by PKC could also contribute to locally inactivate NMII assembly (Asokan et al., 2014).

Our data are consistent with a model in which phosphorylation of Y155 inhibits the incorporation of RLC into the NMII hexamer in the lamellipodium. The model depicted in **Figure 44** summarizes our current view. In steady-state, filamentous NMII undergoes extensive homeostatic RLC exchange with the free fraction of RLC, as shown by FRAP (Watanabe et al., 2007). Such exchange is essential for the stability of the NMII filaments. Upon growth factor stimulation in the vicinity of a region rich in actomyosin filaments (**Figure 44**, center), i.e. non-protrusive, free RLC (shown as a small cyan ball) would become locally phosphorylated on

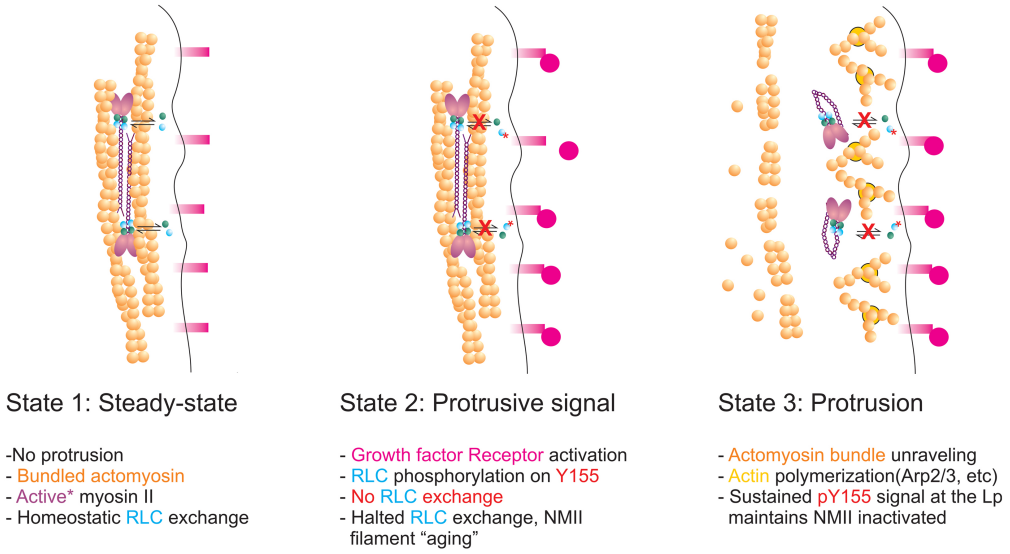

Figure 44: A model of regulation of NMII assembly by Y155 in the lamellipodium. Left image represents an edge of the cell in steady-state, in the absence of stimulus and with fully formed actomyosin bundles that prevent spontaneous protrusion. The key concept is that their bundle maintenance requires homeostatic RLC exchange of the NMII filaments with the free RLC fraction (indicated by bidirectional black arrows); upon growth factor stimulation (middle image), RLC becomes phosphorylated on Y155 (red asterisk), effectively lowering the affinity of RLC for NMII and thus blocking the homeostatic exchange of RLC (red Xs); as a consequence, NMII filaments cannot exchange RLC and eventually disassemble (right panel). The region is now devoid of assembled NMII and thereby protrusion permissive.

Y155, greatly reducing its affinity for NMII hexamers and impeding its exchange. As a consequence, NMII filaments in this subcellular region would no longer be exchanging fresh RLC and would disassemble, making this region permissive for protrusion. If the region is devoid of actomyosin filaments at the beginning of the stimulation, this mechanism would ensure that no myosin would become activated during the protrusive phase of the cellular response to growth factors.

5.1.4 Myosin deterrence: the need for NMII disassembly

It is important to note that Y155 phosphorylation constitutes a conceptually novel mechanism of NMII regulation that locally controls NMII assembly. Unlike the other modes of NMII regulation, which mainly affect the ATPase domain of the heavy chain or the stability of the myosin assemblies, this mechanism controls the actual population of NMII available for assembly. Conversely, other mechanisms, e.g. targeting the tail domain of myosin heavy chain, would be intrinsically reversible. Examples include the phosphorylation of S1943 (Dulyaninova et al., 2007) of MHCII-

A or S1935 of MHCII-B (Juanes-Garcia et al., 2015); or tail-mediated interactions with regulatory proteins such as Lgl (Dahan et al., 2012).

The regulatory mechanisms that target the tail of myosin heavy chain control the assembly state of NMII either by promoting NMII disassembly or blocking its assembly. However, they do not inhibit NMII activity, nor potential NMII functions that would not require fully assembled actomyosin filaments. This is not the case of Y155 phosphorylation. By diminishing the interaction with the heavy chain, Y155 phosphorylation compromises the stability of NMII hexamer, or discourages its formation. In fact, Y155 phosphorylation constitutes a mass action-dependent mechanism of myosin II inhibition, which decreases the actual amount of myosin II available for assembly at protrusive regions. Phosphorylation of RLC on Y155 in the lamellipodial region would ensure, locally, effective actin polymerization by the complete inhibition of myosin II activity or assembly, until signaling through S19 on assembled NMII becomes dominant. Exchange with Y155-unphosphorylated RLC and subsequent S19 phosphorylation triggers the conformational extension of the 10S molecule, which frees the catalytic domains otherwise covered in the folded structure (Craig et al., 1983; Heissler et al., 2021; Scholey et al., 1980; Suzuki et al., 1978). Additional phosphorylation on T18 stabilizes the extended conformation (Ikebe et al., 1988), and thus NMII localization into more stable filaments (Vicente-Manzanares and Horwitz, 2010; Vicente-Manzanares et al., 2008).

Another mechanism of functional regulation is the phosphorylation on S1 of RLC. This has been detected in free RLC (Nishikawa et al., 1984) but also in the context of the hexamer (Ikebe et al., 1986). In this case, the phosphorylation diminishes myosin ability to bind actin-filaments and reduces MLCK-dependent phosphorylations on S19 and T18/S19 (Ikebe et al., 1986). Together with phosphorylation of S19, S1 phosphorylation acts directly on NMI activity.

In summary, our work reveals a novel mode of NMII regulation, defining three major levels: 1) NMII availability (Y155, RLC); 2) NMII activity (S1, S19, T18/S19, RLC); 3) NMII assembly (S1943(A), S1935(B), protein-protein interactions, MHCII). Nevertheless, it seems clear that the regulation of NMII assembly state lies at the center of the ability of cells to respond and adapt to different stimuli. In fact, the pool of NMII monomers appears to be a limiting step for the assembly of myosin filaments (Beach et al., 2017) and the endpoint of many myosin II regulatory signals

by inducing NMII disassembly. In line with this, Y155 phosphorylation would represent another mechanism to control the amount of NMII available to assemble by maintaining RLC in a soluble, non-filamentous state, which could be exchanged to form a competent NMII hexamer upon dephosphorylation. All the signals described above induce the reorganization of actomyosin structures (van Leeuwen et al., 1999) and endow the cytoskeletal plasticity necessary for migration (Friedl and Wolf, 2010) in response to grow factors (Even-Faitelson and Ravid, 2006), or in processes such as mast cell degranulation (Ludowyke et al., 2006) and upon stimulation of platelets and the Jurkat T cell line (Kawamoto et al., 1989; Moussavi et al., 1993).

However, disassembly signals that allow the quick adaptation and reorganization of the cytoskeletal machinery have also been associated with a pathological behavior. Y155 phosphorylation was originally described in carcinoma cells in response to growth factors (Gallis et al., 1983). These signals would also support the loss of cell polarity and cell-cell contacts, a pro-tumor, pro-migratory behavior (Betapudi et al., 2011; Dulyaninova et al., 2007; Even-Faitelson et al., 2005; Ivkovic et al., 2012; Middelbeek et al., 2012) and the promotion of epithelial to mesenchymal transition (Beach et al., 2011).

5.2 The cellular alterations of *MYH9* mutations

The first part of this discussion illustrates the diversity of mechanisms that regulate NMII function at different molecular levels. Some of these signals do not modify the catalytic properties of NMII, but target instead the ability of the molecule to form, or remain in, filaments. This reflects the relevance of the assembly – disassembly cycle in the execution of NMII cellular functions, contributing to the definition of the mechanical properties of actomyosin arrays.

In line with this, NMII paralogs display significant differences in their ability to form filaments as well as their behavior. NMII-A assembles and disassembles faster than NMII-B. This property seems to endow this paralog with the ability to actively generate filaments that generate contraction and transmissible forces (Sandquist and Means, 2008; Vicente-Manzanares et al., 2008). On the other hand, NMII-B-containing filaments generate less traction, but form structures built for tension-bearing processes. This notion is supported by the fact that filamentous NMII-B displays slower FRAP rates and larger immobile fractions that become

even more stable under load (Nagy et al., 2013; Rosenfeld et al., 2003).

The paralog composition of different actomyosin structures is also part of a dynamic continuum in which specific populations of filaments are precursors of new populations with different functions. For example, we showed that the first observable population of actomyosin filaments in lamellae mainly contains NMII-A (Choi et al., 2008; Vicente-Manzanares et al., 2011). In the absence of additional assembly, NMII-A-only containing filaments disassemble (Vicente-Manzanares et al., 2011), explaining why a large population of lamellar adhesions undergoes turnover (Webb et al., 2004). Incidentally, cellular forces are higher in regions located closer to the cell edges (Legant et al., 2013), that is, containing filaments mainly decorated with NMII-A. These structures also show higher recovery rates by FRAP (Baird et al., 2017), indicating that a continuous exchange of NMII molecules is necessary for force generation.

Conversely, some NMII-A filaments serve as "templates" for the assembly of NMII-B, contributing to their stabilization and the conversion from highly contractile filaments into load-bearing structures, i.e. stress fibers (Vicente-Manzanares et al., 2011). Photo-bleaching experiments reveal that these structures display low myosin and actin exchange, only logical as tension bearing structures benefit from structural stability. These observations have been confirmed and reproduced in a number of cell types and studies (Shutova et al., 2017; Tojkander et al., 2015; Weissenbruch et al., 2022).

The combination of these observations, the dynamics of the NMII paralogs in filamentous structures, traction force experiments and direct comparison with muscle myosin kinetics indicates that contraction requires fast cycling, whereas structure-related tension buildup benefits from slow cycling. At 30 µM actin, NMII-A displays a $K_{ATPase} \sim 10$ µM (Hu et al., 2002; Kim et al., 2005), which is very similar to the cardiac α ("fast") isoform (*MYH6*) and not that different from the fast muscle isoform IIa (*MYH2*) (Johnson et al., 2019). Their duty ratios are also in the same range, which means that NMII-A kinetic parameters are similar to those of fast contracting muscle myosins; its function is, after all, to generate contraction, albeit in non-muscle cells. Conversely, NMII-B kinetic parameters are comparable to those of embryonic myosin (*MYH3*), with a $K_{ATPase} \sim 3$ µM (approximately 3 times lower than that of NMII-A), limited actin motility and a high duty ratio (Johnson et al., 2019; Kovacs et al., 2007). *MYH3* deficiency causes alterations in the myo-

genic/myoblastic cell pools and causes scoliosis, a structural defect in an anatomical location (the spine) bearing high load (Agarwal et al., 2020).

Although of considerable biochemical interest, similarities between these parameters cannot be extrapolated to the cellular level, mainly due to the fact that both NMII-A and NMII-B form very small filaments (6-30 hexamers) compared to the much higher order (thousands of hexamers) of sarcomeric structures formed by *MYH2*, *MYH3* and *MYH6*, used before for comparison.

We propose a model in which NMII filament stability depends on two factors that, while related, are fundamentally independent: i) myosin-myosin interactions within filaments, which mainly depend on the susceptibility of the molecule to cycle between the extended and the folded conformation; ii) the interaction of the myosin filament with multiple actin filaments (**Figure 45**).

Let us consider a bipolar filament made of NMII-A. It contains one myosin-myosin bond corresponding to the anti-parallel interaction of the tail and four myosin-actin bonds corresponding to two heads on each hexamer. Assuming the duty ratio of NMII-A to be 5%, the probability of this filament to be bound to actin through at least one head is ∼18% at any given time. Also, the exchange of NMII-A in filaments as measured by FRAP, which gauges the tendency of the molecule to fold back into 10S (Sprague et al., 2004), indicates that, on average, a NMII-A molecule has a 60% probability of reverting back to 10S at a given moment.

Considering the same scenario for a NMII-B filament reveals interesting differences. NMII-B has a duty ratio of at least 20%, which means that the probability of the filament being bound to actin by at least one head is much higher (∼56%) than that of NMII-A. In addition, FRAP rates indicate that NMII-B has only a 30% probability of reverting back to 10S. If we theoretically ascribe the same value to both components, actin binding and filament stability (whether this is the case is currently unknown), we can estimate that a NMII-A bipolar filament is roughly six times more prone to disassemble through actin dissociation or return to 10S than a NMII-B bipolar filament. Of course, larger filaments (remember that NMII filaments contain 6-30 hexamers) display increased stability due to a larger number of attachments. It is also important that these interactions may be modified under load (Kovacs et al., 2007). However, this simple model illustrates how the relative contribution of each paralog defines the stability and/or contractility of the actomyosin structure in which they participate. This feature ultimately ascribes

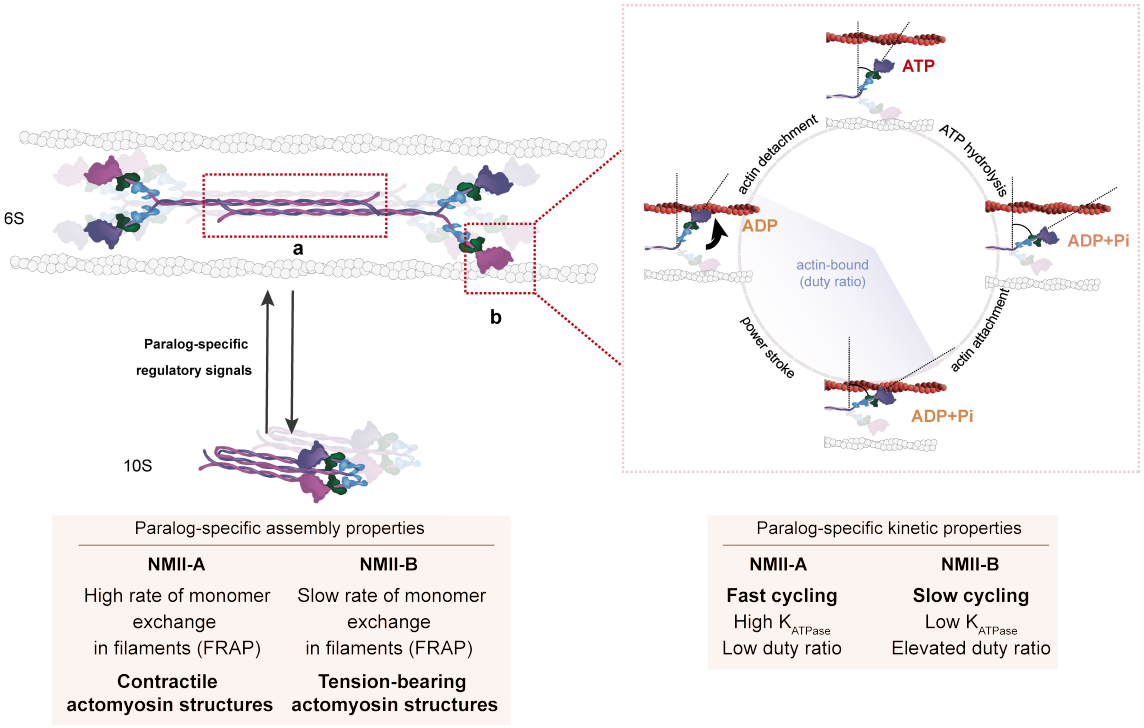

Figure 45: Non-muscle myosin II integrated dynamic circle. The filament stability of NMII paralogs result from a combination of **(a)** myosin-myosin interactions through the tail and **(b)** myosin-actin interactions during the catalytic cycle. Both determine the specific behavior of NMII paralogs and the mechanical properties of actomyosin structures in which they participate.

paralog-specific functions to paralog-decorated structures, some of which are altered if part of the NMII-A bears disease-causing mutations. In the next section, we will discuss how the continuum of *MYH9* mutations target the integrated dynamics of NMII-A (**Figure 45**), how it translates to the cellular context and how it may lead to the onset of highly specific pathologies despite the widespread and high expression of the molecule.

5.2.1 Structural modifications

Regarding motor mutations, alterations in this domain could affect actin binding and force generation at different levels of the ATPase cycle, as explained in terms of the swinging cross-bridge model (**Figure 45b**). For example, the R702C mutation renders a NMII-A that displays approximately 25% of ATPase activity and *in vitro* actin filament motility (Hu et al., 2002). The same authors reported that the N93K mutation lowered the ATPase activity of NMII-A to less than 10% of the original, with no observable actin motility (Hu et al., 2002).

Our results indicate that the mutation does not severely affect the enzymatic activity of NMII-A. However, this mutation, albeit rare, associates with severe macrothrombocytopenia, bi-lateral sensorineural hearing loss for high tones and proteinuria (Seri et al., 2003). *In vitro*, we found that the motor domain possesses ∼80% of the activity of the wild type form in terms of ATPase activity and actin filament motility (this thesis). These data indicate that the effect observed by some of these mutants cannot be ascribed to major alterations in their catalytic activity, and that some other mechanism might be dominating its cellular dynamics.

In addition to the structural changes of the motor domain during ATPase cycle (**Figure 45b**), myosin undergoes large-scale spatial rearrangements as part of the switch between the auto-inhibited, folded and the assembly-competent conformations. To maintain either of these states, additional interactions are required between domains that are very distant in terms of primary structure, i.e. intramolecular interactions in the 10S form; or in different NMII molecules, i.e. intermolecular interactions in the 6S form to assemble NMII minifilaments.

Recently, the structure of the 10S conformation of smooth muscle myosin (which harbors high homology with non-muscle myosin II) has been described using high-resolution cryoEM (4–9 Å). These data reveal the establishment of several interactions between distant parts of the molecule that support the folded conformation of the molecule (Heissler et al., 2021; Yang et al., 2020). Yang and coworkers also mapped several mutations described in smooth muscle and non-muscle myosin II (which included *MYH9* mutations) that localize to potential key regions that clamp myosin II in the folded, inhibited conformation. These regions, with the equivalent residues in NMII-A, are illustrated in **Figure 46** (Yang et al., 2020).

Concerning the mutations studied in this thesis, we can observe that residues N93 and R705 lie in regions of potentially close interactions with segment 2 (blue) and segment 3 (pink) of the tail, respectively (**Figure 46**). In line with this, residue D1424 is located in segment 2 and lies in proximity to residues N93 and R705, also in the same region of contact with the blocked head (**Figure 46**). In addition, residue R1162 locates precisely in the first hinge region of the tail. E1841, in segment 3, is in a region in which it could potentially interact with segment 1 and 2 and stabilize the molecule by tail interactions.

Before these seminal studies, the only predicted interactions of residues N93 and R702 concerned residues in the SH1 and converter subdomains, both within the

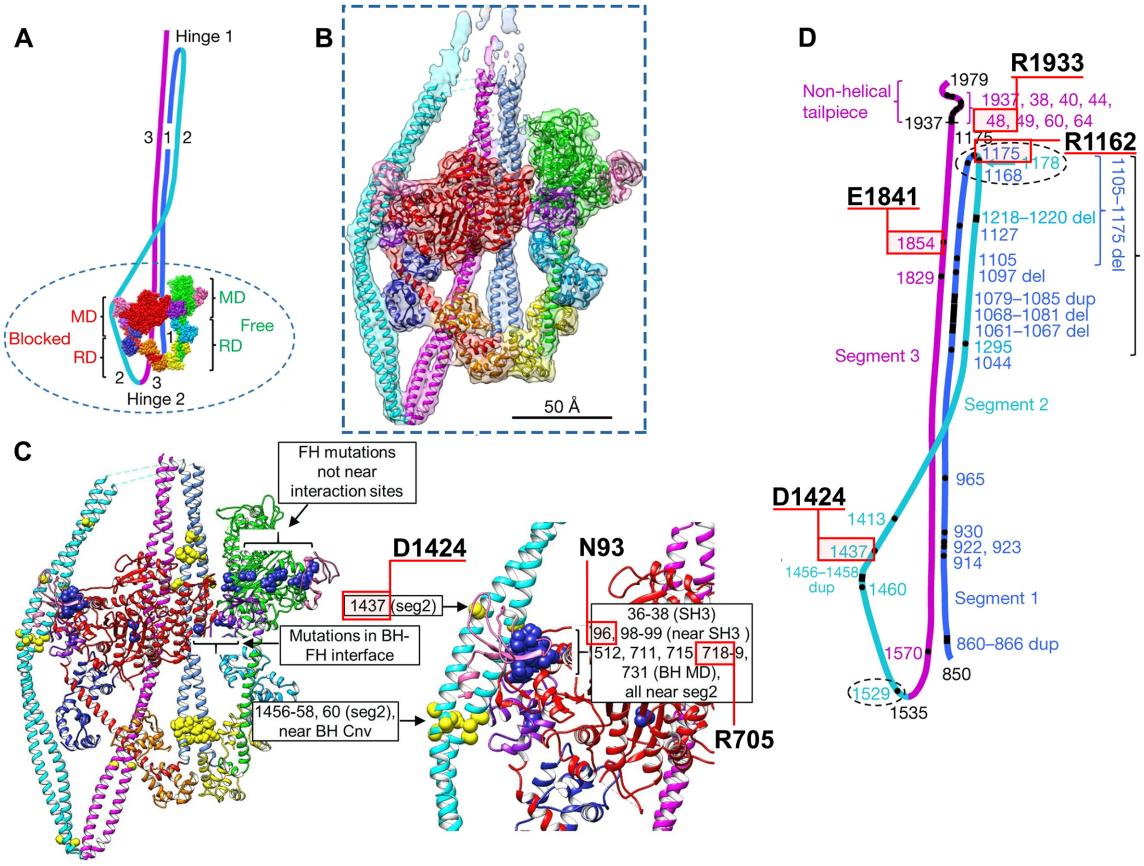

Figure 46: Cryo-EM structure of the inhibited (10S) form of myosin II. (A) Overview of 10S molecule, showing two heads and folded tail. Heads comprise N-terminal halves of heavy chains (red, green), ELCs (blue, cyan) and RLCs (orange, yellow). C-terminal halves of heavy chains combine to form the coiled-coil tail, folded at two hinges, creating tail segments 1, 2 and 3. SH3 and converter regions of motor domains are depicted in pink and purple respectively. MD, motor domain; RD, regulatory domain. The inhibition occurs through the interaction of the actin-binding region of one head (the blocked head (BH)) with the ATP-binding region of the other (the free head (FH)), through head interactions with the three segments of the tail (seg1, seg2 and seg3) and through the interactions of the tail with itself. **(B)** Cryo-EM map fitted with refined atomic model (PDB 6XE9). **(C)** Refined model showing locations of disease-causing mutations in smooth muscle and non-muscle myosin II plotted onto the atomic model (motor domain mutations in blue, tail mutations in yellow). Enlargements of mutation regions relevant for this thesis. Proximity of BH converter domain (purple) and SH3 domain (pink) to seg2 mutations, and of BH SH3 and MD mutations to seg2. **(D)** Locations of all tail mutations (heads omitted for clarity). Ellipses, mutations that could affect folding at hinges; long bracket, clustering of mutations in the three tail segments presumed to interact with each other in the 10S structure—these may affect stability of the folded molecule. Numbers are amino acid positions: black, ends of the coiled-coil (850–1937), the two hinges (1175, 1535), and the C terminus (1979); amino acids 1938–1979 form a non-helical tailpiece; colored numbers indicate positions of point, duplication or deletion mutations. Highlighted in red squares are the mutations studied in this thesis. In bold, the corresponding residues in the sequence of MHCII-A. Figures and footnotes are extracted from (Yang et al., 2020), with some additions relevant for this thesis.

motor region (Hu et al., 2002; Seri et al., 2000). These results suggest the possibility that mutations in the head domain may affect the conformational deployment of the molecule, rather than its enzymatic activity and/or actin binding. In this regard, the localization of *MYH9* mutations on the 3D structure strongly suggests that these residues participate in the maintenance of the compact conformation, and that their alteration would modify its stability. Whether these mutations increase or decrease the stability of the compact conformation is still an open question, although the decreased dissociation rates from filaments observed by FRAP and photo-conversion suggest that the return to the 10S state is not favored.

The resolution of 10S structure in such detail provides new insight into the alterations produced by these mutations, integrating and highlighting other aspects of myosin II dynamics (**Figure 45**). These considerations add up to the possible effects that these mutations have on the function of the domains in which they are in, and also provide a suitable explanation as to why mutations in disparate parts of the molecule have comparable biological effects. For example, the end of the coiled coil and the non-helical tail control NMII assembly in minifilaments: one residue in the non-helical tail domain of MHCII-A (S1943) impairs filament formation when phosphorylated (Dulyaninova et al., 2007). Egelhoff and co-workers generated a mutant form of MHCII-A in which the non-helical domain was deleted, and showed that such mutant myosin appeared over-assembled (Breckenridge et al., 2009). In a similar manner, mutants E1841K and R1933X (the latter is, *de facto*, a truncated form of MHCII-A) could stabilize NMII-A in the assembly state and trigger over-assembly.

The presence of other NMII paralogs or the architecture of the actomyosin structures can potentially modify the outcome of NMII-A-containing structures. NMII-B can copolymerize with NMII-A (Kaufmann and Schwarz, 2020; Shutova et al., 2017) and increase NMII-A stability in filaments (Shutova et al., 2017). Additionally, the paralogs could be part of thick, aligned and stable actin bundles; or participate in the dynamic networks associated to the cellular cortex. These factors and others could potentially demand a specific behavior on NMII-A, something that *MYH9* mutants may not be able to fulfill.

5.2.2 Cellular effects

As discussed above, analysis of the cellular effects of NMII-A mutants reveals quite similar outcomes for all the mutations studied, despite affecting different domains of the heavy chain. All the mutations seem to stabilize the mutant form of NMII-A in filaments, as demonstrated by the decreased dissociation rates from actomyosin filaments shown by FRAP and photo-conversion. It is possible that the different mutants could stabilize the filamentous form through different mechanisms. Motor domain mutations could extend NMII binding to actin filaments by having slower rates in different steps of the ATPase cycle (i.e., phosphate release or ADP exchange). For coiled-coil-localized mutations D1424H and R1162S, and given the electrostatic nature of the interactions that form the MHCII dimer (Cohen and Parry, 1998; Dulyaninova and Bresnick, 2013; Ricketson et al., 2010), it could be argued that the charge modifications caused by these mutations could stabilize the interaction. However, given the localization of these residues in the 10S conformation (**Figure 46**), it also seems feasible that these mutations decrease the stability of the compact conformation, making the return to the 10S state thermodynamically less favorable and therefore increasing their residence within filaments.

In addition to slower dissociation rates for all the selected NMII-A mutants, FRAP and photo-conversion data revealed higher immobile fractions (i.e., subpopulations of NMII molecules bound for longer periods of time to actin filaments) for NMII-A mutants with alterations affecting the end of the coiled-coil region and the non-helical tail, i.e. E1841K and R1933X. This strongly suggests that these mutants induce an over-assembly of NMII-A by altering (E1841K) or deleting (R1933X), the regulatory regions that mediate NMII disassembly (Breckenridge et al., 2009; Dulyaninova et al., 2007; Juanes-Garcia et al., 2015).

Such alterations could also explain their segregation and enrichment to more central actomyosin structures in U2OS and COS-7 cells, as it happens with the sorting mechanism of NMII-A and NMII-B paralogs in a physiological context (Kolega, 2003; Vicente-Manzanares et al., 2007). NMII-A mutants would remain more time bound to actin filaments, segregating to more central and posterior actomyosin structures. In this regard, actin-associated NMII is driven to the rear of the cell by the strong retrograde flow established at the leading edge of migrating cells (Liu et al., 2015). A model emerges in which wild type NMII-A rapidly assembles and disassembles

at the leading edge of migrating cells, similar to a salmon swimming upstream a river. The mutants would display a reduced ability to disassemble rapidly due to: i) increased duty ratio (head mutants); ii) increased filament stability or inability to revert to folded conformation (tail mutants and maybe some head mutants too).

Additionally, the dynamics of NMII mutants in spreading COS-7 showed the same segregation effect than in steady-state conditions: the wild type form was more abundant than NMII-A mutants in regions closer to the cell edges where *de novo* assembly of NMII minifilaments occurred. This effect could be due to two non-excluding possibilities: i) the mutants have a defect in the nucleation process, which renders them unable to incorporate to NMII minifilaments as readily as the wild type form; or/and ii) the mutants segregate rapidly from the wild type form (as discussed above).

If the mutants have a defect of the nucleation process, the analysis of TIRF movies will not reveal it. Although the location of all the mutants (behind the wild type and further away from the leading edge) was robust, there was a significant variability in the degree of overlap with the wild type form. We found spreading cells in which the mutants locate to the first wild type NMII-A minifilaments distinguishable by TIRF, although with less abundance. We also found other cells in which they incorporated to pre-formed wild type NMII-A minifilaments. Those differences could be due to variability in the spreading state of the cell, or expression levels. The smaller estimated k^*_{on} for all the NMII-A mutants could support the hypothesis of a defect in NMII nucleation process. However, a suitable approach to address this problem would require other technological approaches, such as TIRF-SIM (Total internal reflection fluorescence-structured illumination microscopy) or STED. TIRF-SIM has already been used for the bulk measure of NMII populations (monomers, dimers, multimers)(Beach et al., 2017; Fenix et al., 2016) and could reveal the relative proportion of homo-dimers and hetero-dimers between the wild type and the mutant form of NMII-A.

Another possibility is that the mutants segregate rapidly from the wild type form in these regions. We postulate that the increased interaction with actin and/or increased myosin filament stability (see above) induces a rapid segregation of the mutant from the wild type form, which has a more transient interaction with actin and/or forms more labile minifilaments in this model. This process is necessarily quick, since segregation would start at the beginning of cell spreading and actin

retrograde flow is very fast at the leading edge (25 nm/s) (Gardel et al., 2008), which would induce the rapid segregation of the two forms. This means that by the time we begin imaging the cells, and taking into consideration that we capture cells already spreading, segregation may have happened already and the distribution of the mutant and wild type NMII-A may be close to steady state.

A third, non-excluding, possibility is that an affected 10S conformation may jeopardize the recycling and transport of NMII to the cell edges, therefore diminishing the monomer concentration of the mutant in those regions. This remains unexplored in live cells.

5.2.3 Refinements of the ICS analysis

The differences in the intensity levels in TIRF time-lapse videos prevented us from obtaining useful data regarding the degree of aggregation, as described in the Results section. These differences could be due to several reasons:

1. The fluorescent ligands for HaloTag and the EGFP have different quantum yields. In this scenario (equal amounts of Halotag and EGFP), the fluorescent Halotag molecules would emit more photons than the EGFP ones, therefore leading to an over-estimation of the concentration of HaloTag-tagged protein. This was initially corrected in the calculation of the intensity by the known parameters of Halotag ligands and EGFP, mainly the extinction coefficient and the quantum yield, parameters that define the brightness of a fluorescent molecule (see section 3.3.9 of Materials and Methods). However, the values for the extinction and quantum yield coefficients were obtained from published works that calculated these parameters in ethanol (and not in an aqueous medium) (Grimm et al., 2017; Patterson et al., 1997). In the absence of these values obtained in physiological medium, the ethanol-based correction of the differential brightness could distort the estimate of the intensity and therefore the degree of aggregation.

2. The other source of variability is the expression levels of both molecules, since they are exogenously expressed. Initially we expected that this fact would be self-corrected based on the density measurements. The initial reasoning was that high expression levels should yield high density values, since there would be more molecules in the media and therefore differences in the expression levels would be

corrected by this parameter. However, careful analysis of cells co-expressing wild type MHCII-A with both fluorescent tags reveals that that is not the case. The density of individual clusters or "filaments" appears to be independent of expression levels; therefore, the calculation of the degree of aggregation is very sensitive to differences in the expression levels between the co-transfected constructions.

One possibility to overcome this problem is to define a ratio of intensity between the HaloTag and EGFP tags that reflects similar expression levels. For that, we plan to co-transfect COS-7 cells (naturally devoid of NMII-A, so there is no confounding population of non-fluorescent filaments) with the wild type form of NMII-A coupled to EGFP or coupled to HaloTag. After mixing both populations (GFP^+ and $Halotag^+$) in the same coverslip and staining with an antibody for the tail of NMII-A coupled to a fluorochrome, or a secondary antibody (this will label equally both the wild type and the mutant in a separate channel, e.g. far-red, except in the case of the R1933X, which lacks the antibody recognition epitope), we will select cells with the same intensity in the far-red (antibody staining) channel, and measure the intensity levels of cells in the HaloTag or EGFP channels. We will perform these experiments in the same conditions as in the time-lapse videos (i.e. in aqueous solution instead of self-curing mounting medium). By correlating the intensity of the far-red channel with that of the other two channels, we will generate a "ratiometric ruler" that can be used to normalize the differences in brightness in aqueous solution, thus correlating them to specific levels of expression that can be translated from sample to sample under the same illumination conditions.

Additionally, there are several aspects of the segmentation process that may limit the information that we can obtain from the time-lapse videos. Since COS-7 cells form filamentous structures that are unsuitable for ICS analysis (such as central bundles and concatenated transversal arches), we cannot skip the segmentation step when analyzing these cells. Conversely, MEG-01 cells do not form complex, filament-based structures such as transverse arches or stress fibers, thereby constituting a better model to reveal differences in the aggregation state of NMII-A mutants. In these cells, the differences in the degree of aggregation are obvious for the E1841K mutant, but others may have more subtle differences, which may be revealed by this type of semi-quantitative analysis.

5.2.4 The contractility of mutant NMII-A-decorated filaments

While all the mutants included in this study support adhesion assembly, they all display defective adhesion maturation. This suggests that the filaments they are part of are less contractile (or transmit contraction poorly), since myosin-generated forces trigger adhesion growth forces (Chrzanowska-Wodnicka and Burridge, 1996; Dumbauld et al., 2010; Vicente-Manzanares et al., 2007). Interestingly, this observation extends to mutants of the coiled-coil region and the non-helical tailpiece despite having, theoretically, an actin binding and ATPase activity intact, circling back to the notion that the ability of NMII to undergo cycles of assembly-disassembly is an essential part of its ability to exert force.

Let us consider the case of the mutants of the coiled-coil region and the non-helical tail domain. Since these mutants remain longer in actomyosin filaments, they should go through the swinging cross bridge cycle several times; likely more than the wild type form, before disassembling. However, and although further experiments will be needed to address this in a more direct way (i.e., traction force microscopy), these filaments seem to be less contractile.

One possibility is that the NMII-A mutants display reduced phosphorylation of their associated RLC on S19 and T18/S19. Phosphorylation of these residues boosts ATPase activity (Adelstein and Conti, 1975; Ikebe et al., 1988). This possibility is currently being addressed in the lab. In this regard, Pal and coworkers demonstrated that megakaryocytes bearing NMII-A E1841K mutant in heterozygosis display similar RLC S19 phosphorylation levels than wild type megakaryocytes (Pal et al., 2020). However, the possibility that these mutants display reduced phosphorylation is difficult to justify within the current state of the art. This would mean that these mutants are lower affinity substrates for MLCK or ROCK compared to the wild type form. One possibility is that filamentous NMII is actually a poor substrate for these kinases. In fact, a tail-less, monomeric fragment of smooth muscle myosin II (heavy meromyosin subfragment-1, abbreviated as HMMII-S1), which only contains the motor domain and the binding regions for the light chains, support *in vitro* RLC phosphorylation (Ikebe and Hartshorne, 1985b). We have also observed RLC phosphorylation of a tail-less, dimeric form of NMII-A and NMII-B (heavy meromyosin, HMMII-A and II-B) (Hu et al., 2002; Kim et al., 2005). These data

indicate that RLC phosphorylation may occur in the context of non-polymerized, soluble NMII. What others and we have not addressed is whether non-polymeric myosin II is a better or worse substrate for these kinases than filamentous NMII. If soluble NMII turns out to be a better substrate for these kinases than filamentous NMII, it would boost the argument that efficient contraction requires cycles of filament assembly and disassembly. Another possibility is that the soluble and filamentous forms of NMII offer different accessibility to MYPT1, a phosphatase that specifically dephosphorylates RLC (Hartshorne et al., 2004).

5.2.5 The case of the N93K mutation

As discussed elsewhere in this study, the N93K mutation had been shown to display only 4% of the maximal ATPase activity of wild type NMII-A and did not translocate actin filaments in *in vitro* motility assays (Hu et al., 2002). This supported the attractive possibility that this mutant was in fact a passive actin cross-linker with no contractile function (Alieva et al., 2019; Choi et al., 2008; Taneja and Burnette, 2019). Here, we demonstrate that the motor domain of this mutant has a catalytic activity close to that of the wild type form (80%), contrary to the previous observations. Our data is supported by the cellular data which localize this mutant anterior to the *bona fide* non contractile MHCHII-B(R709C)/A chimera, suggesting that the N93K mutant can exert some degree of contraction.

In both experimental designs, the *in vitro* assays were performed using the heavy meromyosin (HMM) construct of non-muscle myosin II, which is dimeric as it retains part of the coiled-coil domain (see Introduction, **Figure 1**).

The upgraded resolution of the 10S structure by cryo-EM (Heissler et al., 2021; Yang et al., 2020) suggests that N93 have structural functions, possibly interacting with distal parts of the tail. Data from Hu and coworkers may have resulted from the fact that the HMMII construct could have forced the already constrained structural stability of the molecule, resulting in a dysfunctional protein that may have jeopardized the *in vitro* studies. A possible strategy to address this problem is to use a shorter fragment, e.g. the recombinant HMM-subfragment-1, for the *in vitro* kinetic characterization of the N93K mutant. HMM-S1 only contains the motor domain and the regions for the binding of the light chains and does not dimerize, although it supports interaction with the ELC and RLC (see Introduction, **Figure**

1). This removes any possible steric constraints caused by the tails, focusing exclusively on the catalytic activity of the head domain. These experiments are currently underway in the laboratory.

The point that needs to be made is that the kinetic defect observed in this mutant (around 20% loss of activity) does not justify the phenotype observed in the carriers of the mutation, or the cellular phenotypes described in this thesis. Based on the data presented here, we postulate that the effect of the N93K mutant is likely due a combination of the reduction of its contractile activity and an altered ability to refold into 10S conformation. While the data presented here do not conclusively demonstrate this, they strongly suggest this possibility; hence further research will try to yield conclusive data in this regard.

This hypothesis, i.e. N93K displays not only a mild impairment of catalytic activity, but also conformational alterations that add on, or synergize, to elicit a more dramatic phenotype than any of the two defects alone, is supported by the stable behavior in filaments (immobile fractions in FRAP analysis). It is also consistent with the increased interaction of the mutant with UNC45a, which catalyzes NMII folding in filaments (Lehtimaki et al., 2017b). Whether increased interaction with UNC45a is specific for N93K mutant or could be displayed by the other mutants is currently not known. Since UNC45a interacts with the head domain of MHCII for NMII folding, it could be specific for motor domain mutations.

The interpretation of the *in vitro* filamentation assays, in which we observed no difference between wild type and N93K, is that the mutant assembles in minifilaments as efficiently as the wild type form, and that the increased stability observed by FRAP is a consequence of its embedding within the actomyosin structure; and not due to enhanced filamentation. This is consistent with the fact that its assembly domain is unaltered. This indicates that the manifestation of the effect of the mutation is only noticeable upon its incorporation into fully formed filaments, i.e. requiring both actin and myosin filaments. In the filamentation (ultracentrifugation) assay, most of the actin is removed. The starting material of the assay is mostly 10S NMII that spontaneously forms filaments in low-salt conditions even in the absence of actin.

Conversely, mutations in the assembly domain (i.e., E1841K and R1933X) may directly affect the assembly properties of NMII-A. In this regard, the mutant E1841K forms thicker and longer NMII-A filaments *in vitro* (Pal et al., 2020).

We also observed that, when co-assembled in filaments, mutants with large immobile fractions (for example, N93K and R1933X) increase the stability of the wild type form (in this context, they decrease the ability of wild type NMII-A to exchange in and out of filaments measured by FRAP). Most likely, the increased stability of the mutant extends the overall half-life of the minifilaments, delaying filament disassembly by increasing the stability of the myosin-myosin interaction and thus increasing the duty ratio of the whole filament. One possibility is that the wild type form establishes stronger interactions with these NMII mutants through the tail domains. However, this is unlikely in the case of the N93K mutant, as its tail domain is intact. In summary, our data are consistent with a model in which both components (actin binding and myosin binding) contribute to the stability of the NMII filaments, and strongly suggest that the dominant effect of the N93K mutation resides in its effect on the conformational extension of the NMII-A hexamer (10S→6S) and not its catalytic activity.

5.2.6 A model for the genotype-phenotype correlations of *MYH9* patients

The careful examination of the molecular effect of these mutations may help explaining the genotype-phenotype correlations exhibited by *MYH9* mutation carriers. *MYH9* patients bearing mutations in exons encoding the motor domain had, in general, more severe thrombocytopenia and are at higher risk of developing extra-hematological damage, i.e. nephropathy and deafness, than patients with mutations affecting the tail domain or non-helical tailpiece (Pecci et al., 2018, 2008).

Conversely, patients carrying tail domain mutations exhibit larger protein aggregates in neutrophils (Pecci et al., 2018; Savoia et al., 2010). This means that the degree of protein aggregation does not necessarily correlate with the severity of the syndrome. It can thus be postulated that deafness, cataracts and nephropathy are not exclusively due to the appearance of protein deposits in relevant cells, e.g. renal podocytes (nephropathy) or cochlear cells (deafness). To our knowledge, the onset of protein aggregates in cells other than neutrophils has not been addressed.

An attractive model to reconcile these data is that the head domain mutants form mixed filaments with the wild type more readily than the tail mutants. This possibility is based on the fact that head domains have intact assembly domains,

whereas tail mutants do not. In a simple model (i.e. ignoring conformational readiness to deploy as discussed above), one wild type NMII-A hexamer would have the same capability to form a dimer with a head mutant as with another wild type hexamer. Conversely, it would have a reduced ability to form a dimer with a tail mutant.

For example, E1841 residue lies in the assembly critical domain (ACD, see Introduction, **Figure 1**) of MHCII (Ricketson et al., 2010). The domain contains the highest concentration of positive charge amino acids in the tail and it is sufficient to drive NMII assembly (Cohen and Parry, 1998). Assembly takes place by generating a unique positive charge surface in this region, that would interact with several negative charged segments of adjacent parallel and antiparallel heavy chains from other monomers (Ricketson et al., 2010). Introduction of a lysine (K) instead of a glutamic acid (E) increases the net positive charge of this region of the hexamer, which would increase its binding strength to a negatively charged region in other neighbour interacting hexamers.

Together, i) the big aggregates of NMII-A on neutrophils bearing the E1841K mutation (see Introduction, **Figure 5**), ii) the thicker filaments formed by this mutant *in vitro* (Pal et al., 2020) and iii) the slower exchange observed by FRAP and photoconversion (this thesis), indicate that, indeed, E1841 residue could function act as a local charge dampener designed to avoid charge-dependent over-stabilization. In this sense, E1841 limits the local accumulation of positive-residues interacting with negative regions in the tail of neighbor monomers. The mutation of this residue to lysine would further stabilize the interaction at the assembly interface and would explain the over-assembly phenotype of this mutant (**Figure 47**).

In this context, filaments containing NMII-A E1841K would be much more stable. Although tail mutants, e.g. R1933X, slow down disassembly of NMII-A wild type from the filament, the mutant itself likely has a slower turnover than that of wild type in the same filament (compare data in **Figure 30C**, right panels) which was obtained with filaments made of the mutant alone vs. in the presence of NMII-A wild type (**Figure 30C**, left panels). These differences underlie the progressive accumulation of filaments enriched in the mutant and globally less prone to disassemble. In this regard, N93K, which is a motor domain mutant, has a comparable effect to that of R1933X on wild type exchange, further indicating that the N93K mutation may induce filamentation alterations beyond its effect on the ATPase activity

```
SP|P35579|MYH9_HUMAN   QAACKQVRRTEKKLKDVLLQV 1851
SP|P35580|MYH10_HUMAN  AAANKLVRRTEKKLKEIFMQV 1858
SP|Q7Z406|MYH14_HUMAN  ILSGKLVRRAEKRLKEVVLQV 1875
SP|P35749|MYH11_HUMAN  QAATKSLKQKDKKLKEILLQV 1858
SP|P10587|MYH11_CHICK  QAAAKTLRQKDKKLKDALLQV 1864
SP|O08638|MYH11_MOUSE  QAATKSLKQKDKKLKEVLLQV 1858
                         : * ::: ::::*:  :*.
```

Figure 47: Sequence alignment of a segment of the ACD domain. NMII-A, NMII-B and NMII-C correspond to *MYH9*, *MYH10* and *MYH14*, respectively. *MYH11* encodes smooth muscle myosin. Symbols in last row: "*" perfect alignment, ":" a site belonging to a group exhibiting strong similarity and "." a site belonging to a group exhibiting weak similarity. In bold, residue E1841 from *MYH9*. Light blue and light red indicate conserved amino acids with positive and negative charge. Note that the negatively charged E1841 residue locates in a region rich in positively charged amino acids. Modification of a figure from (Yang et al., 2020).

The differential behavior between motor and tail domain mutations becomes apparent in a controlled system of naturally limited filamentation, e.g. amoeboid cells. Our filament segregation data was obtained in COS-7 and U2OS cells, which are mesenchymal or mesenchymal-like and form adhesions and actomyosin cables upon adhesion to fibronectin. Conversely, amoeboid cells do not form large adhesions or stress fibers in the same conditions. Such cells (we have used MEG-01 megakaryocytes) display clear differences between head and tail mutants. Cells co-expressing wild type NMII-A and a head domain mutant displayed a modestly higher degree of protein aggregation than those expressing wild type alone. However, the aggregates contain both wild type and mutant NMII-A. Conversely, cells co-expressing wild type NMII-A and a tail domain (E1841K) form large aggregates that mainly contain the mutant. Our interpretation is that the head domain mutant "drags" the wild type to the aggregates, whereas the tail domain mutant does not because it will segregate strongly into more stable structures in actomyosin bundles or "aggregates" in cells with actomyosin networks with low cortical tension (**Figure 48**).

This has important implications to explain the correlation between genotype and phenotype. Head domain mutants are likely more deleterious because they likely co-segregate with the wild type form, particularly in static structures, e.g. podosomes, or sensory organs (eye, ear), locally affecting NMII-A-dependent functions. Conversely, the lower affinity of the wild type for the tail mutants may decrease the amount of mutant myosin at critical junctures, decreasing its ability to cause structural damage.

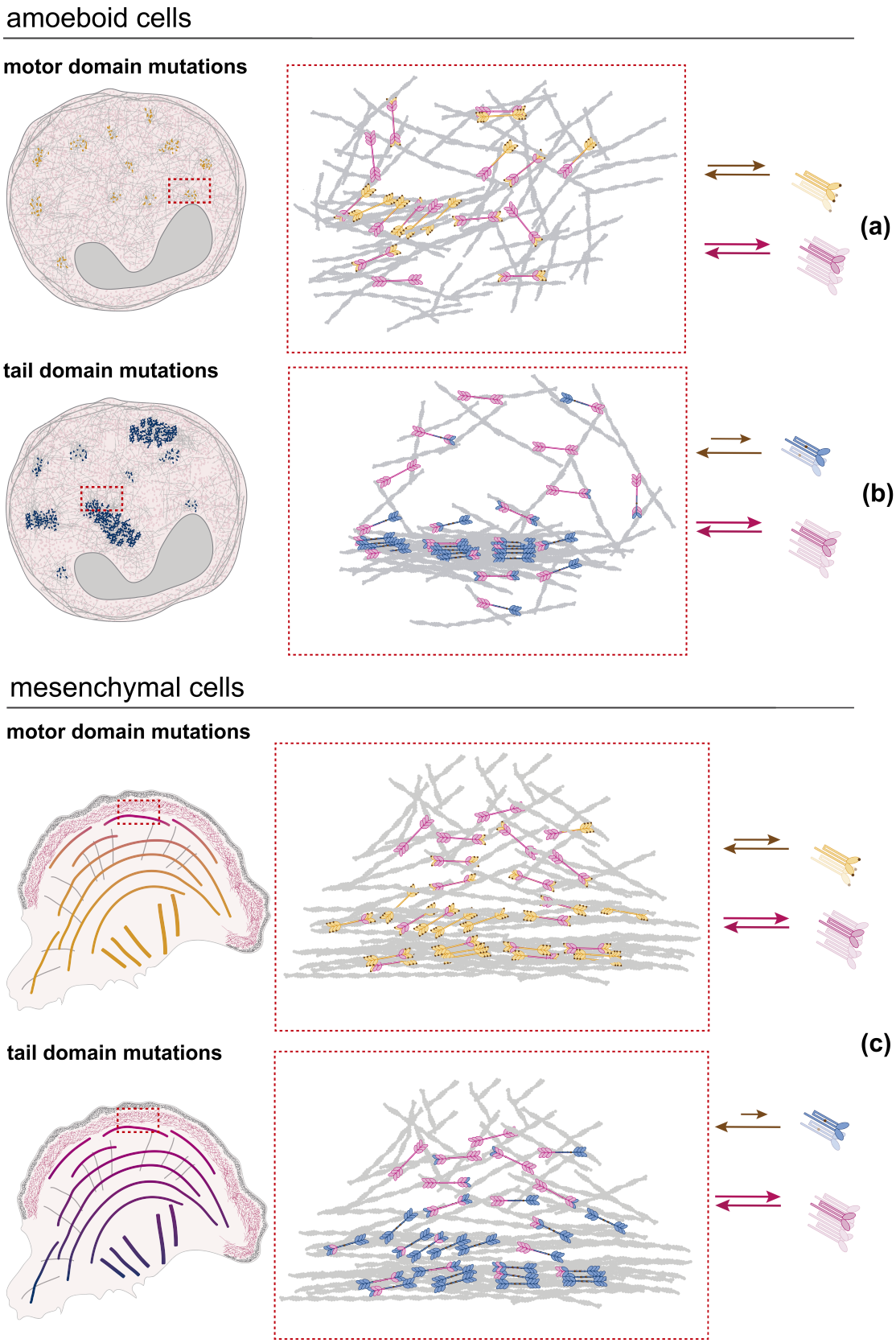

Figure 48: Schematic model of the dynamics of *MYH9* mutations in two filamentous contexts. (See caption next page).

Figure 48 (page 141): **Schematic model of the dynamics of *MYH9* mutations in two filamentous contexts.** In amoeboid cells, NMII exchanges fast in filaments. **(a)** Motor domain (orange) mutations do not affect the assembly domain, thus mutants form filaments with the wild type (magenta) with similar probability. **(b)** Tail domain (blue) mutations affect the assembly domain, thus mutants form filaments with wild type (magenta) with decreased probability. In mesenchymal cells, the exchange of NMII in filaments is slower, preventing the emergence of differences in the subcellular segregation among mutations. **(c)** The more stable nature of actomyosin fibers accommodate the slower dynamic behavior of both the tail and motor domain mutations.

In the case of platelet segregation in megakaryocytes, the defect on platelet biogenesis seems to operate at different levels. First, *MYH9* MKs have a defective migration from the bone marrow to the periphery of the vasculature independent of the affected domain on NMII-A (Pal et al., 2020), therefore fewer MKs would reach the bloodstream and contribute to the proplatelet pool. Secondly, *in vitro* studies with MKs derived from *MYH9*-RD patients show a defect on the branching leading to proplatelet formation, which would contribute to the thrombocytopenia effect (Pecci et al., 2009). In a control situation, MKs seems to downregulate the assembly state of NMII-A through phosphorylation of tail of the heavy chain, probably to generate a more compliant cell cortex (Chang et al., 2007; Shin et al., 2011; Spinler et al., 2015). Increased permanence of the *MYH9* mutants in filaments provides a rigidity effect that would be detrimental for membrane branching. Interestingly, when excised from the MKs, the size of these proplatelets is similar to control proplatelets since excision seems to rely on shear-dependent processes rather than on NMII-dependent contractility (Spinler et al., 2015).

Therefore, the largest effect on the variable severity of the macrothrombocytopenia and its correlation to *MYH9* motor or tail domain variants appears to act at the level of proplatelet cytofission in the bloodstream. This process seems to be dependent on NMII-A contractility (Spinler et al., 2015).

In this context, the head mutants would co-localize with the wild type form to a larger extent than the tail mutants in MKs (as also seen in MEG-01 cells), with a substantial fraction of the head mutant segregating to the proplatelet that gets excised by shear. This would decrease the local amount of functional NMII in the proplatelet, which may trigger cytofission failure in the bloodstream. Conversely, the higher permanence of the tail mutants in filaments and/or aggregates would result in a decreased soluble fraction that can be incorporated to the proplatelets.

In fact, Pecci and coworkers demonstrated that in *MYH9* patients with deletions

in the non-helical tail of NMII-A, the mutant form did not segregate into platelets (Pecci et al., 2005). In this case, only 50% of fully functional NMII-A was present, which is likely insufficient to enable the optimal cytofission in the bloodstream.

This subtle mechanistic difference would result in the same platelet defect (macrothrombocytopenia, as observed), but an increased probability that the head domain mutants cause a more severe macrothrombocytopenia phenotypes and extra-hematological damage, consistent with the current state of the art.

5.2.7 Leukocyte alterations in *MYH9* R1162S mutation carriers

To our knowledge, we demonstrate for the first time that the Döhle-like inclusion bodies observed in neutrophils are in fact the result of over-assembly, or defective disassembly, of NMII-A. This finding does not seem exclusive of the R1162S mutation, since other studies, e.g. Rocco and coworkers, described the presence of aggregates with "cross-striated appearance" in *MYH9* patients with a duplication in the gene (p.E1066_A1072dup) (De Rocco et al., 2009).

The phenotype of defective disassembly is consistent with NMII-A R1162S reduced FRAP turnover rates in the COS-7 cell line, and would explain the relationship between the size of the aggregates and the location of the mutation within the heavy chain, which is widely used as a diagnostic tool of *MYH9*-RD (Pecci et al., 2018; Savoia et al., 2010). Mutations in the assembly domain (E1841K and R1933X), which have the highest immobile fractions/stability in filaments, also display the largest aggregates in this cell type. Conversely, motor domain mutants cause a modest accumulation of small aggregates in neutrophils, which suggest that they may not have a deep alteration of the assembly properties *per se* since the assembly domain is intact. This is in good agreement with our model, in which the motor domain mutations would segregate more efficiently with the wild type form than the tail mutations, causing a more severe malfunction, while tail mutations would segregate to more stable structures.

Additionally, these data indicate that the aggregates are not the result of misfolded protein, at least not initially. Whether it would later become a degradation problem is yet to be addressed. The fact that we did not observe differences in the degradative process in COS-7 cells does not rule out this possibility, since these cells

already display a filamentous structure, which could harbor the more stable NMII-A mutants and keep them away from the cellular protein degradation machinery without disturbing additional components.

The accelerated NETosis onset observed in *MYH9* neutrophils points out to an overall compromised cellular integrity rather than an improved NETosis capacity. Most likely, the incorporation of a mutant NMII-A with slower turnover rates to cortical actomyosin networks would compromise the overall stability of the structure, affecting the homogeneous distribution of NMII, and therefore the generation of NMII-dependent forces. Additionally, a decreased NMII contractile capacity (consistent with a reduction in the rates of assembly -disassembly) would also affect myosin-driven actin filament turnover, thereby adding up to the defect in cortical and cellular integrity by compromising the correct regeneration of actin filaments. This is consistent with the increase in SYTOX green staining in *MYH9* neutrophils even in unstimulated conditions. A similar defect in overall cortical integrity might be the reason why *MYH9* R1192S dendritic cells in 3D collagen gels displayed frequent events of cellular shedding.

However, aggregates in this cell type could not be observed, at least in 2D substrates, where these cells display a filamentous and "sarcomeric-like" ("stacked") organization. Nor could we observe them in T cells, despite these cells only display cortical actomyosin networks.

We think that this could be explained by the presence of other NMII paralogs (e.g., NMII-B) in T cells (Millán-Salanova, unpublished) and dendritic cells (this thesis). Neutrophils only express NMII-A (Marigo et al., 2004; Maupin et al., 1994). Expression of NMII-B may introduce a level of additional stability in the actomyosin cytoskeleton that would help harbor the more stable NMII-A mutants. Additionally, measurements of cortical tension indicates that the actin cortex in these cell types is fundamentally different: granulocytes are characterized for displaying one of the lowest cortical tensions as measured by micropipette aspiration assays $\sim$ 30-35 pN/µm (Salbreux et al., 2012) while T cells display $\sim$ 70 pN/µm (Guo et al., 2012). Fibroblasts range in the order of 600 pN/µm (Salbreux et al., 2012). This could be due to differences in the crosslinker composition or the filament density of the actin network. Likewise, the presence of NMII-B in actomyosin structures prevents the disassembly of the cortex by NMII-A-driven tension and enables the buildup of higher cortical tensions (Taneja et al., 2020; Weissenbruch et al., 2021). The alter-

ations of the dynamics of NMII-A mutants may be less evident in cells capable of generating more stable actomyosin structures that harbor higher cellular tension.

The morphology of neutrophils on bi-dimensional substrates upon stimulation with fMLP indicates that NMII localizes properly at the back in polarized cells. However, its organization is clearly aberrant. These structures would probably lack the contractile capacity for, for example, nucleus translocation (Thomas et al., 2015), which is consistent with their decreased migration through pores in transmigration assays.

Defective contractile activity also supports the defective adhesive behavior of dendritic cells. In general, adhesion requires the interplay between integrin-dependent adhesive structures (focal complexes and podosomes) with actomyosin filaments (Rafiq et al., 2019b). Podosomes appear to self-assemble by default under low traction forces, while focal adhesions critically depend on the existence of such forces. The relative abundance of podosomes and focal adhesions is controlled, among other factors, by the activity of NMII, which stimulates the formation of sarcomeric-like structures and focal adhesions (Rafiq et al., 2019a). Consistent with this idea, reduced contractile activity in DCs would lead to the over-assembly of podosome structures and a defective spreading on fibronectin substrates. Additionally, it could be responsible for the slower migratory speed of *MYH9* mDCs in 3D collagen gels, which also require NMII activity for migration through confined environments (Barbier et al., 2019). The persistence of *MYH9* mDCs migratory trajectories may be consistent with a decreased ability to disassemble NMII at the back, leaving the cell unable to reorganize the actin cytoskeleton to change polarity. This effect is not significant in mDCs carrying the *MYH9* R1162S variant, but it is worth considering for other *MYH9* mutations, particularly the ones from the assembly domain. Nevertheless, further experiments to better address this must include immature mDCs, which are characterized for their random migration and in which the persistence effect should be more evident.

The fact that *MYH9* R1162S T cells displayed an increased area of spreading and polarization is consistent with a decrease in NMII-A mediated contractile activity due to reduced assembly-disassembly cycles. In these cells, NMII activity seems to mediate the uncoupling of adhesive structures to the substrate (Morin et al., 2008; Smith et al., 2003), and an inhibition of NMII contractile activity induces over-adherence in 2D substrates (Millán-Salanova, unpublished)(Jacobelli et al., 2010).

Together, this data shows the existence of morphological and functional alterations in leukocyte populations carrying *MYH9* R1162S mutation that may lead to their suboptimal functioning, and therefore explain the recurrent infections described in those patients. Given the importance of NMII to preserve cellular integrity at the most basic level, one could assume that the defect would be most probably at the neutrophil level, since the presence of other NMII paralog in other leukocyte populations may lessen the defects of a mutant NMII-A. Nevertheless, further characterization of other *MYH9* variants is needed to verify this effect, which otherwise might remain overlooked.

6 Conclusions

Part 1

1. RLC silencing results in a reduction of MHCII-A and MHCII-B expression and the loss of focal adhesion assembly and front-back polarity.

2. Aberrant cell function by RLC deletion is restored by both Y142 mutations studied; only partially by a Y155 non-phosphorylatable mutant, and not restored at all by a Y155 phospho-mimetic mutant.

3. Phosphorylation of Y155 impedes RLC interaction with the heavy chain of non-muscle myosin II and impairs formation of functional myosin hexamers.

4. Phospho-Y155 RLC mainly appears at the lamellipodia in response to growth factors, where it could prevent the assembly of functional NMII filaments in the first stages of protrusion.

Part 2

1. *MYH9* mutations targeting the motor, coiled-coil and non-helical tail domains of NMII-A cause a decreased turnover rate of NMII from actomyosin filaments, although likely through different mechanisms.

2. Increased stability of the mutants is also transferred to wild type hexamers within the same filament.

3. The cellular effects caused by these mutations depend on the filamentous state of the cell.

(a) In mesenchymal-like cells, all the mutants localize to more stable actomyosin filaments with decreased contractile capacity.

(b) In amoeboid-like cells, the motor domain mutant N93K co-localizes with wild type NMII-A in small aggregates, while the assembly domain mutant E1841K segregate into larger and aberrant actomyosin structures that rarely contain wild type NMII-A.

4. Contrary to previous belief and despite affecting a critical position between the S1 helix and converter stretch of NMII-A, the N93K mutation has a minor effect on the contractile activity of the motor domain.

5. Primary leukocyte populations from an *MYH9* patient carrying R1162S mutation displayed several morphological and functional alterations. An over-assembly of mutant NMII-A underlies the appearance of the Döhle-like inclusion bodies that are typical features of *MYH9* neutrophils. T cells and dendritic cells show alterations in their adhesive behavior. Additionally, dendritic cells and neutrophils show altered migratory capabilities, as well as functional defects consistent with impaired cellular integrity.

7 Conclusiones

Part 1

1. El silenciamiento de RLC provoca la disminución de los niveles de expresión de MHCII-A y MHCII-B, la pérdida de adhesiones focales y de la polaridad anteroposterior.

2. La expresión de los mutantes del residuo Y142 recupera los efectos celulares causados por la disminución de RLC. El mutante no fosforilable de Y155 solo recupera estos efectos parcialmente, mientras que el mutante fosfomimético de Y155 no los corrige.

3. La fosforilación del residuo Y155 impide la interacción de la RLC con la cadena pesada de la miosina no muscular, evitando la formación de hexámeros funcionales de miosina.

4. La RLC fosforilada en el residuo Y155 aparece principalmente en el lamelipodio en respuesta a factores de crecimiento, donde podría prevenir el ensamblaje de filamentos funcionales de NMII durante las primeras fases de la protrusión.

Part 2

1. Las mutaciones del gen *MYH9* que afectan al dominio motor, helicoidal y no helicoidal de NMII-A causan una reducción del intercambio de NMII-A en filamentos, aunque probablemente por mecanismos distintos.

2. La mayor estabilidad de los mutantes se transmite a los hexámeros de la forma salvaje de NMII-A que comparten el filamento con estos mutantes.

3. Los efectos celulares causados por este tipo de mutaciones dependen del estado de filamentación de la célula.

   (a) En células mesenquimales, todos los mutantes se localizan en estructuras más estables de actomiosina con una capacidad contráctil reducida.

   (b) En células ameboides, el mutante del dominio motor N93K colocaliza en pequeños agregados con la forma salvaje de NMII-A; mientras que el mutante del dominio de ensamblaje E1841K aparece en estructuras más grandes y aberrantes de actomiosina que raramente contienen la forma salvaje de NMII-A.

4. Contrariamente a observaciones previas, y a pesar de localizarse en una posición crítica entre la hélice S1 y la región convertidora de NMII-A, el mutante N93K presenta un defecto menor en la actividad contráctil del dominio motor.

5. Los leucocitos primarios obtenidos de un paciente con la mutación R1162S en el gen *MYH9* muestran varias alteraciones morfológicas y funcionales. Los cuerpos de inclusión característicos de neutrófilos con afectación en el gen *MYH9* son el resultado de un ensamblaje exacerbado de NMII-A. Los linfocitos T y las células dendríticas muestran alteraciones en su comportamiento adhesivo. Finalmente, las células dendríticas y los neutrófilos muestran una migración alterada, y defectos funcionales consistentes con problemas de integridad celular.

Appendix A: Image Correlation Spectroscopy analysis

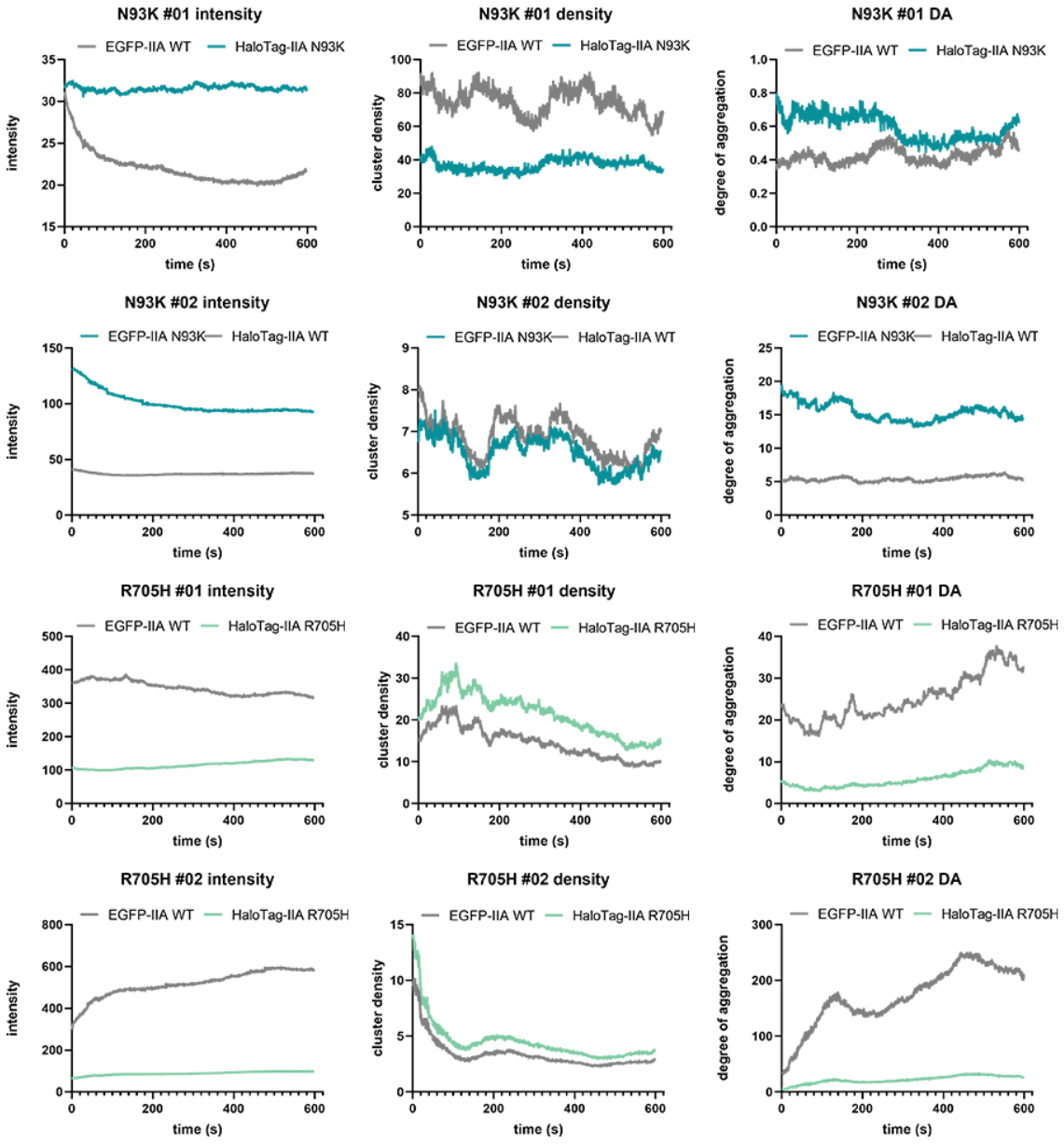

Figure 49: See caption at page 153

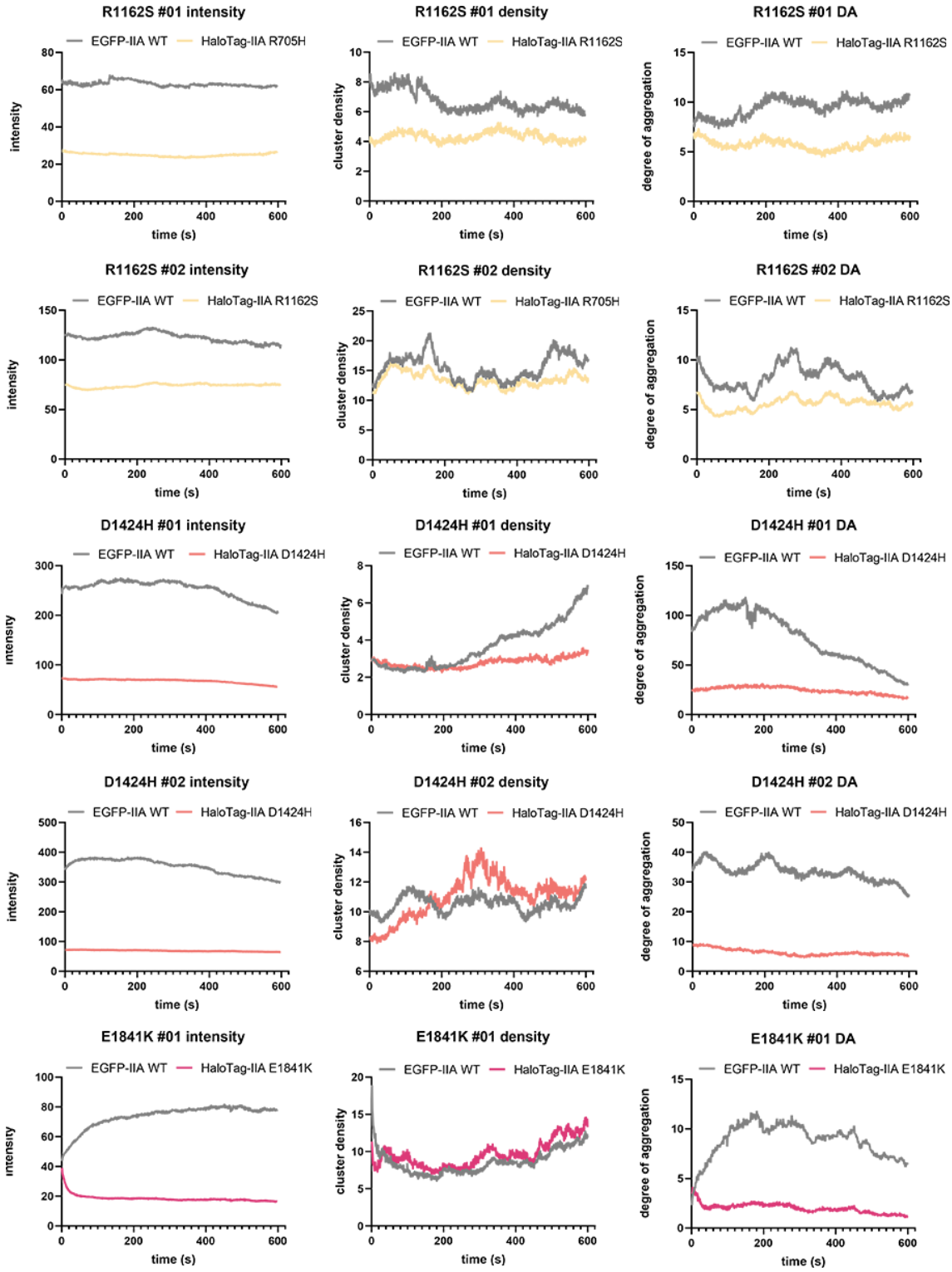

Figure 49 (continuation): See caption at page 153

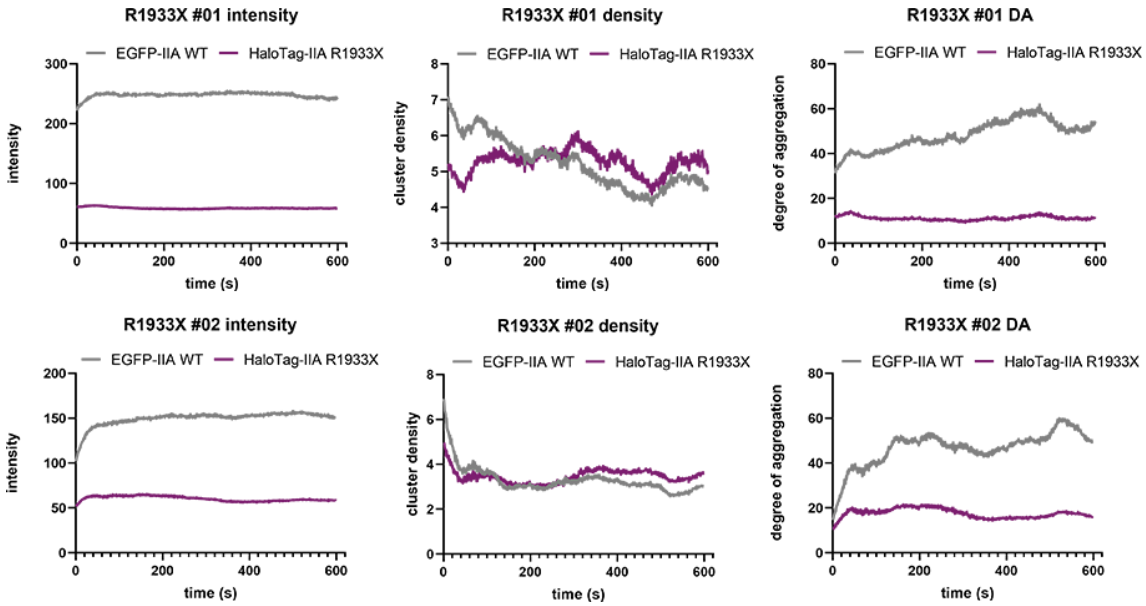

Figure 49: ICS analysis of NMII-A mutants. ICS analysis of TIRF images of COS-7 cells co-transfected with MHCII-A WT and MHCII-A mutants coupled to EGFP or HaloTag, stained with Janelia Fluor®-585 (50 nM) for 1 h, and imaged immediately after seeded in fibronectin-coated coverslips (3 µm/ml). Two cells were analyzed per mutant condition.

Appendix B: Publications and funding

B.1 Publications related to this work

1. C. Llorente-González, González-Rodríguez M, Vicente-Manzanares M. 2021. Targeting cytoskeletal phosphorylation in cancer. Explor. Target Antitumor Ther. 2:292-308.
   DOI: 10.37349/etat.2021.00047.

2. Asensio-Juárez, G., C. Llorente-González, and M. Vicente-Manzanares. 2020. Linking the landscape of MYH9-related diseases to the molecular mechanisms that control non-muscle myosin II-A function in cells. Cells. 9:e1458.
   DOI: 10.3390/cells9061458.

3. Aguilar-Cuenca, R.*, C. Llorente-González*, J.R. Chapman, V.C. Talayero, M. Garrido-Casado, C. Delgado-Arévalo, M. Millán-Salanova, J. Shabanowitz, D.F. Hunt, J.R. Sellers, S.M. Heissler, and M. Vicente-Manzanares. 2020. Tyrosine Phosphorylation of the Myosin Regulatory Light Chain Controls Non-muscle Myosin II Assembly and Function in Migrating Cells. Curr. Biol. 30:2446-2458.e2446. DOI: 10.1016/j.cub.2020.04.057. * denotes equal contribution

4. Rodriguez-Fdez, S., C. Citterio, L.F. Lorenzo-Martin, J. Baltanas-Copado, C. Llorente-González, S. Corbalan-Garcia, M. Vicente-Manzanares, and X.R. Bustelo. 2019. Phosphatidylinositol Monophosphates Regulate Optimal Vav1 Signaling Output. Cells. 8:1649. DOI: 10.3390/cells8121649.

5. Juanes-Garcia, A., C. Llorente-González, and M. Vicente-Manzanares. 2017. Non Muscle Myosin II. In Encyclopedia of Signaling Molecules. S. Choi, editor. Springer, New York. DOI: 10.1007/978-1-4614-6438-9_101734-1.

6. Aguilar-Cuenca, R., C. Llorente-González, C. Vicente, and M. Vicente-Manzanares. 2017. Microfilament-coordinated adhesion dynamics drives single cell migration and shapes whole tissues. F1000Research. 6:160. DOI: 10.12688/f1000research.10356.1.

7. Juanes-García A, C. Llorente-González, Vicente-Manzanares M. 2016. Molecular control of non-muscle myosin II assembly. Oncotarget. 7(5):5092-3. DOI: 10.18632/oncotarget.6936.

B.2 Funding

This Ph.D. thesis has been supported by:

1. Predoctoral grant from Junta de Castilla y Léon.

2. Funding from "Mechanical determinants of cell migration and immune interactions SAF2014-54705-R MINECO" and "Mechanical and chemical determinants of cell migration, division and leukemic cancers PID2020-116232RB-I00 MINECO".

List of abbreviations

ACD: assembly critical domain.
ADP: adenosine diphosphate.
AR: aspect ratio.
Arp2/3: actin-related proteins 2/3.
ATCC: American Tissue Culture Collection.
ATP: adenosine triphosphate.
BSA: bovine serum albumin.
BH: blocked head.
CCLx: C-C motif chemokine ligand (number)
CDx: cluster of differentiation (number).
CH_3CO_2K: potassium acetate.
CKII: casein kinase II.
CLAHE: contrast limited adaptive histogram equalization.
CXCLx: C-X-C motif chemokine ligand (number).
CXCRx: C-X-C motif chemokine receptor (number).
D: Aspartic acid
DMSO: dimethyl sulfoxide.
DNA: deoxyribonucleic acid.
DSF: dorsal stress fibers.
E: glutamic acid
ECM: extracellular matrix.
(E)GFP: (enhanced) green fluorescent protein.
EGF: epidermal growth factor.
EGFR: epidermal growth factor receptor.
EGTA: ethylene glycol-bis(β-aminoethyl ether)-N,N,N',N'-tetraacetic acid.
ELC: essential light chain.
ERM: ezrin–radixin–moesin.
FBS: fetal bovine serum.
FC: flow cytometry.
F_{eq}: concentration of free binding molecules.
FH: free head.
fMLP: N-Formylmethionyl-leucyl-phenylalanine.
FRAP: fluorescence recovery after photobleaching.
G: goat.
H: histidine
HMM: heavy meromyosin.
HPLC: high performance liquid chromatography.
HRP: horseradish peroxidase.
Hspx: heat-shock protein (number).
ICS: Image Correlation Microscopy
IF: immunofluorescence.
Ig: immunoglobulin.
IL: interleukin.
IPTG:isopropyl β- D -1-thiogalactopyranoside.

IVK: *in vitro* kinase assay.

K: lysine

K: exponential rate of recovery.

kDa: kiloDalton.

K_{off} : dissociation constant.

K_{on}: association constant.

KLH: Keyhole limpet hemocyanin

LPS: lipopolysaccharides.

mDC: monocyte-derived dendritic cell.

M: mouse.

MD: motor domain.

MFI: mean of fluorescence intensity

Mg: magnesium.

$MgCl_2$: magnesium chloride.

MHCII-A/B/C: non-muscle myosin II heavy chain isoform A/B/C.

MK: megakaryocyte.

MLCK: myosin light-chain kinase.

$MnCl_2$: manganese chloride.

MOPS: 3-(N-Morpholino)propanesulfonic acid.

MYH9-RD: *MYH9*-related diseases.

MYPT1: myosin phosphatase target subunit 1.

N: Asparagine.

NA: numerical aperture.

NE: nuclear envelope.

NEAA: non-essential amino acids.

NET: neutrophil extracellular trap.

NHT: non-helical tailpiece.

NMDA: N-methyl-D-aspartate.

NMII: non-muscle myosin II.

P: plateau.

PBMCs: peripheral blood mononuclear cells.

PBS: phosphate buffered saline.

PBSst: PBS staining buffer.

PC: photo-conversion.

PCR: polymerase chain reaction.

PFA: paraformaldehyde.

PHA-L: phytohemagglutinin-L.

Pi: inorganic phosphate.

PKC: protein kinase C.

PMA: Phorbol 12-myristate 13-acetate.

PMN: polymorphonuclear neutrophil.

P/S: penicillin and streptomycin.

PVDF: polyvinylidene fluoride.

R: arginine

RD: related diseases.

RLC: regulatory light chain.

RhoA: Ras homolog gene family, member A.

RNA: ribonucleic acid.

ROCK: Rho associated coiled coil kinase.

ROS: reactive oxygen species.

RT: room temperature.

S: serine

S: concentration of free binding sites on the filament.

SDF-1: stromal cell-derived factor -1

SDS-PAGE: sodium dodecyl sulfate polyacrylamide gel electrophoresis.

shRNA: short hairpin RNA.

siRNA: small interfering RNA.

SMMII: Smooth muscle myosin II

T: threonin

TA: transverse arcs.

TBS: tris-buffered saline.

TFA: trifluoroacetic acid.

TFS: Thermo Fisher Scientific

TIRF: total internal reflection fluorescence.

TPR: tetratricopeptide repeat.

TRPM7: transient receptor potential melastatin 7.

UV: ultraviolet.

VSF: ventral stress fibers.

WB: Western blot.

WL: white light.

WT: wild type.

Y: tyrosine.

Bibliography

Adelstein, R. S. and Conti, M. A. (1975). Phosphorylation of platelet myosin increases actin-activated myosin ATPase activity. Nature **256**, 597–8.

Agarwal, M., Sharma, A., Kumar, P., Kumar, A., Bharadwaj, A., Saini, M., Kardon, G. and Mathew, S. J. (2020). Myosin heavy chain-embryonic regulates skeletal muscle differentiation during mammalian development. Development **147**, dev184507.

Agarwal, P. and Zaidel-Bar, R. (2019). Diverse roles of non-muscle myosin II contractility in 3D cell migration. Essays Biochem **63**, 497–508.

Aguilar-Cuenca, R., Llorente-González, C., Chapman, J. R., Talayero, V., Garrido-Casado, M., Delgado-Arévalo, C., Millán-Salanova, M., Shabanowitz, J., Hunt, D. F., Sellers, J. R., Heissler, S. M. and Vicente-Manzanares, M. (2020). Tyrosine Phosphorylation of the Myosin Regulatory Light Chain Controls Non-muscle Myosin II Assembly and Function in Migrating Cells. Curr Biol **30**, 2446–2458.e6.

Akiyama, S. K. (2013). Purification of fibronectin. Curr Protoc Cell Biol **60**, Unit 10–5.

Alamo, L., Ware, J. S., Pinto, A., Gillilan, R. E., Seidman, J. G., Seidman, C. E. and Padron, R. (2017). Effects of myosin variants on interacting-heads motif explain distinct hypertrophic and dilated cardiomyopathy phenotypes. Elife **6**, e71888.

Alcalai, R., Seidman, J. G. and Seidman, C. E. (2008). Genetic basis of hypertrophic cardiomyopathy: from bench to the clinics. J Cardiovasc Electrophysiol **19**, 104–10.

Alieva, N. O., Efremov, A. K., Hu, S., Oh, D., Chen, Z., Natarajan, M., Ong, H. T., Jegou, A., Romet-Lemonne, G., Groves, J. T., Sheetz, M. P., Yan, J. and Bershadsky, A. D. (2019). Myosin IIA and formin dependent mechanosensitivity of filopodia adhesion. Nat Commun **10**, 3593.

Almutawa, W., Smith, C., Sabouny, R., Smit, R. B., Zhao, T., Wong, R., Lee-Glover, L., Desrochers-Goyette, J., Ilamathi, H. S., Care4Rare Canada, C., Suchowersky, O., Germain, M., Mains, P. E., Parboosingh, J. S., Pfeffer, G., Innes, A. M. and Shutt, T. E. (2019). The R941L mutation in MYH14 disrupts mitochondrial fission and associates with peripheral neuropathy. EBioMedicine **45**, 379–392.

Althaus, K. and Greinacher, A. (2010). MYH-9 Related Platelet Disorders: Strategies for Management and Diagnosis. Transfus Med Hemother **37**, 260–267.

Alvarado, J., Sheinman, M., Sharma, A., MacKintosh, F. C. and Koenderink, G. H. (2013). Molecular motors robustly drive active gels to a critically connected state. Nat Phys **9**, 591–597.

Amano, M., Ito, M., Kimura, K., Fukata, Y., Chihara, K., Nakano, T., Matsuura, Y. and Kaibuchi, K. (1996). Phosphorylation and activation of myosin by Rho-associated kinase (Rho-kinase). J Biol Chem **271**, 20246–9.

Anderson, A. E., Swan, D. J., Sayers, B. L., Harry, R. A., Patterson, A. M., von Delwig, A.,

Robinson, J. H., Isaacs, J. D. and Hilkens, C. M. (2009). LPS activation is required for migratory activity and antigen presentation by tolerogenic dendritic cells. J Leukoc Biol **85**, 243–50.

Anderson, M. J., Pham, V. N., Vogel, A. M., Weinstein, B. M. and Roman, B. L. (2008). Loss of unc45a precipitates arteriovenous shunting in the aortic arches. Dev Biol **318**, 258–67.

Aoki, T., Kunishima, S., Yamashita, Y., Minamitani, K. and Ota, S. (2018). Macrothrombocytopenia With Congenital Bilateral Cataracts: A Phenotype of MYH9 Disorder With Exon 24 Indel Mutations. J Pediatr Hematol Oncol **40**, 76–78.

Arganda-Carreras, I., Kaynig, V., Rueden, C., Eliceiri, K. W., Schindelin, J., Cardona, A. and Sebastian Seung, H. (2017). Trainable Weka Segmentation: a machine learning tool for microscopy pixel classification. Bioinformatics **33**, 2424–2426.

Asensio-Juárez, G., Llorente-Gonzalez, C. and Vicente-Manzanares, M. (2020). Linking the landscape of MYH9-related diseases to the molecular mechanisms that control non-muscle myosin II-A function in cells. Cells **9**, e1458.

Asokan, S. B., Johnson, H. E., Rahman, A., King, S. J., Rotty, J. D., Lebedeva, I. P., Haugh, J. M. and Bear, J. E. (2014). Mesenchymal chemotaxis requires selective inactivation of myosin II at the leading edge via a noncanonical PLCgamma/PKCalpha pathway. Dev Cell **31**, 747–60.

Atilgan, E., Wirtz, D. and Sun, S. X. (2006). Mechanics and dynamics of actin-driven thin membrane protrusions. Biophys J **90**, 65–76.

Atkinson, S. J. and Stewart, M. (1992). Molecular interactions in myosin assembly. Role of the 28-residue charge repeat in the rod. J Mol Biol **226**, 7–13.

Baird, M. A., Billington, N., Wang, A., Adelstein, R. S., Sellers, J. R., Fischer, R. S. and Waterman, C. M. (2017). Local pulsatile contractions are an intrinsic property of the myosin 2A motor in the cortical cytoskeleton of adherent cells. Mol Biol Cell **28**, 240–251.

Bajaj, G., Zhang, Y., Schimerlik, M. I., Hau, A. M., Yang, J., Filtz, T. M., Kioussi, C. and Ishmael, J. E. (2009). N-methyl-D-aspartate receptor subunits are non-myosin targets of myosin regulatory light chain. J Biol Chem **284**, 1252–66.

Balduini, C. L., Pecci, A. and Savoia, A. (2011). Recent advances in the understanding and management of MYH9-related inherited thrombocytopenias. Br J Haematol **154**, 161–74.

Barbier, L., Saez, P. J., Attia, R., Lennon-Dumenil, A. M., Lavi, I., Piel, M. and Vargas, P. (2019). Myosin II Activity Is Selectively Needed for Migration in Highly Confined Microenvironments in Mature Dendritic Cells. Front Immunol **10**, 747.

Barral, J. M., Hutagalung, A. H., Brinker, A., Hartl, F. U. and Epstein, H. F. (2002). Role of the myosin assembly protein UNC-45 as a molecular chaperone for myosin. Science **295**, 669–71.

Bastida, J. M., Lozano, M. L., Benito, R., Janusz, K., Palma-Barqueros, V., Del Rey, M., Hernandez-Sanchez, J. M., Riesco, S., Bermejo, N., Gonzalez-Garcia, H., Rodriguez-Alen, A., Aguilar, C., Sevivas, T., Lopez-Fernandez, M. F., Marneth, A. E., van der Reijden, B. A., Morgan, N. V., Watson, S. P., Vicente, V., Hernandez-Rivas, J. M., Rivera, J. and Gonzalez-Porras, J. R. (2018). Introducing high-throughput sequencing into mainstream genetic diagnosis practice in inherited platelet disorders. Haematologica **103**, 148–162.

Baumann, B. A., Taylor, D. W., Huang, Z., Tama, F., Fagnant, P. M., Trybus, K. M. and Taylor, K. A. (2012). Phosphorylated smooth muscle heavy meromyosin shows an open conformation linked to activation. J Mol Biol **415**, 274–87.

Beach, J. R., Bruun, K. S., Shao, L., Li, D., Swider, Z., Remmert, K., Zhang, Y., Conti, M. A., Adelstein, R. S., Rusan, N. M., Betzig, E. and Hammer, J. A. (2017). Actin dynamics and

competition for myosin monomer govern the sequential amplification of myosin filaments. Nat Cell Biol **19**, 85–93.

Beach, J. R., Hussey, G. S., Miller, T. E., Chaudhury, A., Patel, P., Monslow, J., Zheng, Q., Keri, R. A., Reizes, O., Bresnick, A. R., Howe, P. H. and Egelhoff, T. T. (2011). Myosin II isoform switching mediates invasiveness after TGF-beta-induced epithelial-mesenchymal transition. Proc Natl Acad Sci U S A **108**, 17991–6.

Berg, J. S., Powell, B. C. and Cheney, R. E. (2001). A millennial myosin census. Mol Biol Cell **12**, 780–94.

Betapudi, V., Gokulrangan, G., Chance, M. R. and Egelhoff, T. T. (2011). A proteomic study of myosin II motor proteins during tumor cell migration. J Mol Biol **407**, 673–86.

Billington, N., Beach, J. R., Heissler, S. M., Remmert, K., Guzik-Lendrum, S., Nagy, A., Takagi, Y., Shao, L., Li, D., Yang, Y., Zhang, Y., Barzik, M., Betzig, E., Hammer, J. A., r. and Sellers, J. R. (2015). Myosin 18A coassembles with nonmuscle myosin 2 to form mixed bipolar filaments. Curr Biol **25**, 942–8.

Bird, J. E., Takagi, Y., Billington, N., Strub, M. P., Sellers, J. R. and Friedman, T. B. (2014). Chaperone-enhanced purification of unconventional myosin 15, a molecular motor specialized for stereocilia protein trafficking. Proc Natl Acad Sci U S A **111**, 12390–5.

Biro, M., Romeo, Y., Kroschwald, S., Bovellan, M., Boden, A., Tcherkezian, J., Roux, P. P., Charras, G. and Paluch, E. K. (2013). Cell cortex composition and homeostasis resolved by integrating proteomics and quantitative imaging. Cytoskeleton (Hoboken) **70**, 741–54.

Blanchoin, L., Boujemaa-Paterski, R., Sykes, C. and Plastino, J. (2014). Actin dynamics, architecture, and mechanics in cell motility. Physiol Rev **94**, 235–63.

Bookwalter, C. S., Kelsen, A., Leung, J. M., Ward, G. E. and Trybus, K. M. (2014). A Toxoplasma gondii class XIV myosin, expressed in Sf9 cells with a parasite co-chaperone, requires two light chains for fast motility. J Biol Chem **289**, 30832–30841.

Bovellan, M., Romeo, Y., Biro, M., Boden, A., Chugh, P., Yonis, A., Vaghela, M., Fritzsche, M., Moulding, D., Thorogate, R., Jegou, A., Thrasher, A. J., Romet-Lemonne, G., Roux, P. P., Paluch, E. K. and Charras, G. (2014). Cellular control of cortical actin nucleation. Curr Biol **24**, 1628–1635.

Breckenridge, M. T., Dulyaninova, N. G. and Egelhoff, T. T. (2009). Multiple regulatory steps control mammalian nonmuscle myosin II assembly in live cells. Mol Biol Cell **20**, 338–47.

Bridgman, P. C., Dave, S., Asnes, C. F., Tullio, A. N. and Adelstein, R. S. (2001). Myosin IIB is required for growth cone motility. J Neurosci **21**, 6159–69.

Bruneau, A., Delaunay, J. L., Durand-Schneider, A. M., Vauthier, V., Ben Saad, A., Aoudjehane, L., El Mourabit, H., Morichon, R., Falguieres, T., Gautheron, J., Housset, C. and Ait-Slimane, T. (2022). MRCK-Alpha and Its Effector Myosin II Regulatory Light Chain Bind ABCB4 and Regulate Its Membrane Expression. Cells **11**, 617.

Brunet, S., Zimmermann, T., Reynaud, E. G., Vernos, I., Karsenti, E. and Pepperkok, R. (2006). Detection and quantification of protein-microtubules interactions using green fluorescent protein photoconversion. Traffic **7**, 1283–9.

Bulinski, J. C., Odde, D. J., Howell, B. J., Salmon, T. D. and Waterman-Storer, C. M. (2001). Rapid dynamics of the microtubule binding of ensconsin in vivo. J Cell Sci **114**, 3885–97.

Burgess, S. A., Yu, S., Walker, M. L., Hawkins, R. J., Chalovich, J. M. and Knight, P. J. (2007).

Structures of smooth muscle myosin and heavy meromyosin in the folded, shutdown state. J Mol Biol **372**, 1165–78.

Burnette, D. T., Manley, S., Sengupta, P., Sougrat, R., Davidson, M. W., Kachar, B. and Lippincott-Schwartz, J. (2011). A role for actin arcs in the leading-edge advance of migrating cells. Nat Cell Biol **13**, 371–81.

Burridge, K. and Wittchen, E. S. (2013). The tension mounts: stress fibers as force-generating mechanotransducers. J Cell Biol **200**, 9–19.

Cai, Y., Biais, N., Giannone, G., Tanase, M., Jiang, G., Hofman, J. M., Wiggins, C. H., Silberzan, P., Buguin, A., Ladoux, B. and Sheetz, M. P. (2006). Nonmuscle myosin IIA-dependent force inhibits cell spreading and drives F-actin flow. Biophys J **91**, 3907–20.

Canzi, P., Pecci, A., Manfrin, M., Rebecchi, E., Zaninetti, C., Bozzi, V. and Benazzo, M. (2016). Severe to profound deafness may be associated with MYH9-related disease: report of 4 patients. Acta Otorhinolaryngol Ital **36**, 415–420.

Chang, Y., Aurade, F., Larbret, F., Zhang, Y., Le Couedic, J. P., Momeux, L., Larghero, J., Bertoglio, J., Louache, F., Cramer, E., Vainchenker, W. and Debili, N. (2007). Proplatelet formation is regulated by the Rho/ROCK pathway. Blood **109**, 4229–36.

Chen, D., Li, S., Singh, R., Spinette, S., Sedlmeier, R. and Epstein, H. F. (2012). Dual function of the UNC-45b chaperone with myosin and GATA4 in cardiac development. J Cell Sci **125**, 3893–903.

Choi, C. K., Vicente-Manzanares, M., Zareno, J., Whitmore, L. A., Mogilner, A. and Horwitz, A. R. (2008). Actin and alpha-actinin orchestrate the assembly and maturation of nascent adhesions in a myosin II motor-independent manner. Nat Cell Biol **10**, 1039–50.

Chow, D., Srikakulam, R., Chen, Y. and Winkelmann, D. A. (2002). Folding of the striated muscle myosin motor domain. J Biol Chem **277**, 36799–807.

Chrzanowska-Wodnicka, M. and Burridge, K. (1996). Rho-stimulated contractility drives the formation of stress fibers and focal adhesions. J Cell Biol **133**, 1403–15.

Clark, K., Middelbeek, J., Dorovkov, M. V., Figdor, C. G., Ryazanov, A. G., Lasonder, E. and van Leeuwen, F. N. (2008). The alpha-kinases TRPM6 and TRPM7, but not eEF-2 kinase, phosphorylate the assembly domain of myosin IIA, IIB and IIC. FEBS Lett **582**, 2993–7.

Cohen, C. and Parry, D. A. (1998). A conserved C-terminal assembly region in paramyosin and myosin rods. J Struct Biol **122**, 180–7.

Conti, M. A. and Adelstein, R. S. (2008). Nonmuscle myosin II moves in new directions. J Cell Sci **121**, 11–8.

Conti, M. A., Even-Ram, S., Liu, C., Yamada, K. M. and Adelstein, R. S. (2004). Defects in cell adhesion and the visceral endoderm following ablation of nonmuscle myosin heavy chain II-A in mice. J Biol Chem **279**, 41263–6.

Craig, R., Smith, R. and Kendrick-Jones, J. (1983). Light-chain phosphorylation controls the conformation of vertebrate non-muscle and smooth muscle myosin molecules. Nature **302**, 436–9.

Craig, R. and Woodhead, J. L. (2006). Structure and function of myosin filaments. Curr Opin Struct Biol **16**, 204–12.

Cramer, L. P., Siebert, M. and Mitchison, T. J. (1997). Identification of novel graded polarity

actin filament bundles in locomoting heart fibroblasts: implications for the generation of motile force. J Cell Biol **136**, 1287–305.

Cremo, C. and Hartshorne, D. (2007). Smooth-muscle myosin II. *In* Myosins: A Superfamily of Molecular Motors. pp. 171–222. L.M. Coluccio, editor. Watertown: Springer.

Dahan, I., Yearim, A., Touboul, Y. and Ravid, S. (2012). The tumor suppressor Lgl1 regulates NMII-A cellular distribution and focal adhesion morphology to optimize cell migration. Mol Biol Cell, **23**, 591–601.

Dasbiswas, K., Hu, S., Schnorrer, F., Safran, S. A. and Bershadsky, A. D. (2018). Ordering of myosin II filaments driven by mechanical forces: experiments and theory. Philos Trans R Soc Lond B Biol Sci, **373**, 20170114.

de la Fuente, H., Mittelbrunn, M., Sanchez-Martin, L., Vicente-Manzanares, M., Lamana, A., Pardi, R., Cabanas, C. and Sanchez-Madrid, F. (2005). Synaptic clusters of MHC class II molecules induced on DCs by adhesion molecule-mediated initial T-cell scanning. Mol Biol Cell, **16**, 3314–22.

De Rocco, D., Pujol-Moix, N., Pecci, A., Faletra, F., Bozzi, V., Balduini, C. L. and Savoia, A. (2009). Identification of the first duplication in MYH9-related disease: A hot spot for unequal crossing-over within exon 24 of the MYH9 gene. Eur J Med Genet, **52**, 191–194.

De Rocco, D., Zieger, B., Platokouki, H., Heller, P. G., Pastore, A., Bottega, R., Noris, P., Barozzi, S., Glembotsky, A. C., Pergantou, H., Balduini, C. L., Savoia, A. and Pecci, A. (2013). MYH9-related disease: five novel mutations expanding the spectrum of causative mutations and confirming genotype/phenotype correlations. Eur J Med Genet, **56**, 7–12.

Deutsch, S., Rideau, A., Bochaton-Piallat, M. L., Merla, G., Geinoz, A., Gabbiani, G., Schwede, T., Matthes, T., Antonarakis, S. E. and Beris, P. (2003). Asp1424Asn MYH9 mutation results in an unstable protein responsible for the phenotypes in May-Hegglin anomaly/Fechtner syndrome. Blood, **102**, 529–34.

Diaz, R., Nguewa, P. A., Parrondo, R., Perez-Stable, C., Manrique, I., Redrado, M., Catena, R., Collantes, M., Penuelas, I., Diaz-Gonzalez, J. A. and Calvo, A. (2010). Antitumor and antiangiogenic effect of the dual EGFR and HER-2 tyrosine kinase inhibitor lapatinib in a lung cancer model. BMC Cancer, **10**, 188.

Dong, F., Li, S., Pujol-Moix, N., Luban, N. L., Shin, S. W., Seo, J. H., Ruiz-Saez, A., Demeter, J., Langdon, S. and Kelley, M. J. (2005). Genotype-phenotype correlation in MYH9-related thrombocytopenia. Br J Haematol, **130**, 620–7.

Dulyaninova, N. G. and Bresnick, A. R. (2013). The heavy chain has its day: regulation of myosin-II assembly. Bioarchitecture, **3**, 77–85.

Dulyaninova, N. G., House, R. P., Betapudi, V. and Bresnick, A. R. (2007). Myosin-IIA heavy-chain phosphorylation regulates the motility of MDA-MB-231 carcinoma cells. Mol Biol Cell, **18**, 3144–55.

Dulyaninova, N. G., Malashkevich, V. N., Almo, S. C. and Bresnick, A. R. (2005). Regulation of myosin-IIA assembly and Mts1 binding by heavy chain phosphorylation. Biochemistry, **44**, 6867–76.

Dumbauld, D. W., Shin, H., Gallant, N. D., Michael, K. E., Radhakrishna, H. and Garcia, A. J. (2010). Contractility modulates cell adhesion strengthening through focal adhesion kinase and assembly of vinculin-containing focal adhesions. J Cell Physiol, **223**, 746–56.

Dunois-Larde, C., Capron, C., Fichelson, S., Bauer, T., Cramer-Borde, E. and Baruch, D. (2009).

Exposure of human megakaryocytes to high shear rates accelerates platelet production. Blood, **114**, 1875–83.

Eckly, A., Strassel, C., Freund, M., Cazenave, J. P., Lanza, F., Gachet, C. and Leon, C. (2008). Abnormal megakaryocyte morphology and proplatelet formation in mice with megakaryocyte-restricted MYH9 inactivation. Blood, **113**, 3182–9.

Engelhardt, V. and Lyubimova, M. (1939). Myosin and adenosinetriphosphatase. Nature, **144**, 668–669.

Ennomani, H., Letort, G., Guerin, C., Martiel, J. L., Cao, W., Nedelec, F., De La Cruz, E. M., Thery, M. and Blanchoin, L. (2016). Architecture and Connectivity Govern Actin Network Contractility. Curr Biol, **26**, 616–26.

Etard, C., Roostalu, U. and Strahle, U. (2008). Shuttling of the chaperones Unc45b and Hsp90a between the A band and the Z line of the myofibril. J Cell Biol, **180**, 1163–75.

Even-Faitelson, L. and Ravid, S. (2006). PAK1 and aPKCzeta regulate myosin II-B phosphorylation: a novel signaling pathway regulating filament assembly. Mol Biol Cell, **17**, 2869–81.

Even-Faitelson, L., Rosenberg, M. and Ravid, S. (2005). PAK1 regulates myosin II-B phosphorylation, filament assembly, localization and cell chemotaxis. Cell Signal, **17**, 1137–48.

Fenix, A. M., Taneja, N., Buttler, C. A., Lewis, J., Van Engelenburg, S. B., Ohi, R. and Burnette, D. T. (2016). Expansion and concatenation of nonmuscle myosin IIA filaments drive cellular contractile system formation during interphase and mitosis. Mol Biol Cell, **27**, 1465–1478.

Friedl, P. and Wolf, K. (2010). Plasticity of cell migration: a multiscale tuning model. J Cell Biol, **188**, 1–9.

Fritzsche, M., Lewalle, A., Duke, T., Kruse, K. and Charras, G. (2013). Analysis of turnover dynamics of the submembranous actin cortex. Mol Biol Cell, **24**, 757–67.

Fujita-Becker, S., Reubold, T. F. and Holmes, K. C. (2006). The actin-binding cleft: functional characterisation of myosin II with a strut mutation. J Muscle Res Cell Motil, **27**, 115–23.

Furlano, M., Arlandis, R., Venegas, M. D. P., Novelli, S., Crespi, J., Bullich, G., Ayasreh, N., Remacha, A., Ruiz, P., Lorente, L., Ballarin, J., Matamala, A., Ars, E. and Torra, R. (2019). MYH9 Associated nephropathy. Nefrologia, **39**, 133–140.

Furusawa, T., Ikawa, S., Yanai, N. and Obinata, M. (2000). Isolation of a novel PDZ-containing myosin from hematopoietic supportive bone marrow stromal cell lines. Biochem Biophys Res Commun, **270**, 67–75.

Gallis, B., Edelman, A. M., Casnellie, J. E. and Krebs, E. G. (1983). Epidermal growth factor stimulates tyrosine phosphorylation of the myosin regulatory light chain from smooth muscle. J Biol Chem, **258**, 13089–93.

Gardel, M. L., Sabass, B., Ji, L., Danuser, G., Schwarz, U. S. and Waterman, C. M. (2008). Traction stress in focal adhesions correlates biphasically with actin retrograde flow speed. J Cell Biol, **183**, 999–1005.

Garrido-Casado, M., Asensio-Juarez, G. and Vicente-Manzanares, M. (2021). Nonmuscle Myosin II Regulation Directs Its Multiple Roles in Cell Migration and Division. Annu Rev Cell Dev Biol, **37**, 285–310.

Gazda, L., Pokrzywa, W., Hellerschmied, D., Lowe, T., Forne, I., Mueller-Planitz, F., Hoppe, T. and Clausen, T. (2013). The myosin chaperone UNC-45 is organized in tandem modules to support myofilament formation in C. elegans. Cell, **152**, 183–95.

Geach, T. J. and Zimmerman, L. B. (2010). Paralysis and delayed Z-disc formation in the Xenopus tropicalis unc45b mutant dicky ticker. BMC Dev Biol, **10**, 75.

Geisterfer-Lowrance, A. A., Kass, S., Tanigawa, G., Vosberg, H. P., McKenna, W., Seidman, C. E. and Seidman, J. G. (1990). A molecular basis for familial hypertrophic cardiomyopathy: a beta cardiac myosin heavy chain gene missense mutation. Cell, **62**, 999–1006.

Golomb, E., Ma, X., Jana, S. S., Preston, Y. A., Kawamoto, S., Shoham, N. G., Goldin, E., Conti, M. A., Sellers, J. R. and Adelstein, R. S. (2004). Identification and characterization of nonmuscle myosin II-C, a new member of the myosin II family. J Biol Chem, **279**, 2800–8.

Gordon, A. M., Homsher, E. and Regnier, M. (2000). Regulation of contraction in striated muscle. Physiol Rev, **80**, 853–924.

Grimm, J. B., Muthusamy, A. K., Liang, Y., Brown, T. A., Lemon, W. C., Patel, R., Lu, R., Macklin, J. J., Keller, P. J., Ji, N. and Lavis, L. D. (2017). A general method to fine-tune fluorophores for live-cell and in vivo imaging. Nat Methods, **14**, 987–994.

Guha, M., Zhou, M. and Wang, Y. L. (2005). Cortical actin turnover during cytokinesis requires myosin II. Curr Biol, **15**, 732–6.

Guo, Q., Park, S. and Ma, H. (2012). Microfluidic micropipette aspiration for measuring the deformability of single cells. Lab Chip, **12**, 2687–95.

Guzik-Lendrum, S., Heissler, S. M., Billington, N., Takagi, Y., Yang, Y., Knight, P. J., Homsher, E. and Sellers, J. R. (2013). Mammalian myosin-18A, a highly divergent myosin. J Biol Chem, **288**, 9532–48.

Han, K. H., Lee, H., Kang, H. G., Moon, K. C., Lee, J. H., Park, Y. S., Ha, I. S., Ahn, H. S., Choi, Y. and Cheong, H. I. (2011). Renal manifestations of patients with MYH9-related disorders. Pediatr Nephrol, **26**, 549–55.

Hartshorne, D. J., Ito, M. and Erdodi, F. (2004). Role of protein phosphatase type 1 in contractile functions: myosin phosphatase. J Biol Chem, **279**, 37211–4.

Haviv, L., Gillo, D., Backouche, F. and Bernheim-Groswasser, A. (2008). A cytoskeletal demolition worker: myosin II acts as an actin depolymerization agent. J Mol Biol, **375**, 325–30.

Heissler, S. M., Arora, A. S., Billington, N., Sellers, J. R. and Chinthalapudi, K. (2021). Cryo-EM structure of the autoinhibited state of myosin-2. Sci Adv, **7**, eabk3273.

Heissler, S. M., Chinthalapudi, K. and Sellers, J. R. (2015). Kinetic characterization of the sole nonmuscle myosin-2 from the model organism Drosophila melanogaster. FASEB J, **29**, 1456–66.

Heissler, S. M. and Manstein, D. J. (2011). Comparative kinetic and functional characterization of the motor domains of human nonmuscle myosin-2C isoforms. J Biol Chem, **286**, 21191–202.

Heissler, S. M. and Sellers, J. R. (2015). Four things to know about myosin light chains as reporters for non-muscle myosin-2 dynamics in live cells. Cytoskeleton (Hoboken), **72**, 65–70.

Heissler, S. M. and Sellers, J. R. (2016). Kinetic Adaptations of Myosins for Their Diverse Cellular Functions. Traffic, **17**, 839–59.

Henderson, C. J., Aleo, E., Fontanini, A., Maestro, R., Paroni, G. and Brancolini, C. (2005). Caspase activation and apoptosis in response to proteasome inhibitors. Cell Death Differ, **12**, 1240–54.

Hinz, B., Mastrangelo, D., Iselin, C. E., Chaponnier, C. and Gabbiani, G. (2001). Mechanical tension controls granulation tissue contractile activity and myofibroblast differentiation. Am J Pathol, **159**, 1009–20.

Hiraiwa, T. and Salbreux, G. (2016). Role of Turnover in Active Stress Generation in a Filament Network. Phys Rev Lett, **116**, 188101.

Hiramatsu, K., Nishio, S.-y., Kitajiri, S.-i., Kitano, T., Moteki, H., Usami, S.-i. and on behalf of the Deafness Gene Study Consortium (2021). Prevalence and Clinical Characteristics of Hearing Loss Caused by MYH14 Variants. Genes, **12**, 1623.

Horvath, A. I., Gyimesi, M., Varkuti, B. H., Kepiro, M., Szegvari, G., Lorincz, I., Hegyi, G., Kovacs, M. and Malnasi-Csizmadia, A. (2020). Effect of allosteric inhibition of non-muscle myosin 2 on its intracellular diffusion. Sci Rep, **10**, 13341.

Hotulainen, P. and Lappalainen, P. (2006). Stress fibers are generated by two distinct actin assembly mechanisms in motile cells. J Cell Biol, **173**, 383–94.

Hu, A., Wang, F. and Sellers, J. R. (2002). Mutations in human nonmuscle myosin IIA found in patients with May-Hegglin anomaly and Fechtner syndrome result in impaired enzymatic function. J Biol Chem, **277**, 46512–7.

Hu, S., Grobe, H., Guo, Z., Wang, Y. H., Doss, B. L., Pan, M., Ladoux, B., Bershadsky, A. D. and Zaidel-Bar, R. (2019). Reciprocal regulation of actomyosin organization and contractility in nonmuscle cells by tropomyosins and alpha-actinins. Mol Biol Cell, **30**, 2025–2036.

Ikebe, M. (2008). Regulation of the function of mammalian myosin and its conformational change. Biochem Biophys Res Commun, **369**, 157–64.

Ikebe, M. and Hartshorne, D. J. (1985a). Phosphorylation of smooth muscle myosin at two distinct sites by myosin light chain kinase. J Biol Chem, **260**, 10027–31.

Ikebe, M. and Hartshorne, D. J. (1985b). Proteolysis of smooth muscle myosin by Staphylococcus aureus protease: preparation of heavy meromyosin and subfragment 1 with intact 20 000-dalton light chains. Biochemistry, **24**, 2380–7.

Ikebe, M., Hartshorne, D. J. and Elzinga, M. (1986). Identification, phosphorylation, and dephosphorylation of a second site for myosin light chain kinase on the 20,000-dalton light chain of smooth muscle myosin. J Biol Chem, **261**, 36–9.

Ikebe, M., Koretz, J. and Hartshorne, D. J. (1988). Effects of phosphorylation of light chain residues threonine 18 and serine 19 on the properties and conformation of smooth muscle myosin. J Biol Chem, **263**, 6432–7.

Ivkovic, S., Beadle, C., Noticewala, S., Massey, S. C., Swanson, K. R., Toro, L. N., Bresnick, A. R., Canoll, P. and Rosenfeld, S. S. (2012). Direct inhibition of myosin II effectively blocks glioma invasion in the presence of multiple motogens. Mol Biol Cell, **23**, 533–42.

Jacobelli, J., Friedman, R. S., Conti, M. A., Lennon-Dumenil, A. M., Piel, M., Sorensen, C. M., Adelstein, R. S. and Krummel, M. F. (2010). Confinement-optimized three-dimensional T cell amoeboid motility is modulated via myosin IIA-regulated adhesions. Nat Immunol, **11**, 953–61.

Jiang, J., Woulfe, D. S. and Papoutsakis, E. T. (2014). Shear enhances thrombopoiesis and formation of microparticles that induce megakaryocytic differentiation of stem cells. Blood, **124**, 2094–103.

Jo, M., Thomas, K. S., O'Donnell, D. M. and Gonias, S. L. (2003). Epidermal growth factor receptor-dependent and -independent cell-signaling pathways originating from the urokinase receptor. J Biol Chem, **278**, 1642–6.

Johnson, C. A., Walklate, J., Svicevic, M., Mijailovich, S. M., Vera, C., Karabina, A., Leinwand, L. A. and Geeves, M. A. (2019). The ATPase cycle of human muscle myosin II isoforms:

Adaptation of a single mechanochemical cycle for different physiological roles. J Biol Chem, **294**, 14267–14278.

Juanes-Garcia, A., Chapman, J. R., Aguilar-Cuenca, R., Delgado-Arevalo, C., Hodges, J., Whitmore, L. A., Shabanowitz, J., Hunt, D. F., Horwitz, A. R. and Vicente-Manzanares, M. (2015). A regulatory motif in nonmuscle myosin II-B regulates its role in migratory front-back polarity. J Cell Biol, **209**, 23–32.

Jung, H. S., Billington, N., Thirumurugan, K., Salzameda, B., Cremo, C. R., Chalovich, J. M., Chantler, P. D. and Knight, P. J. (2011). Role of the tail in the regulated state of myosin 2. J Mol Biol, **408**, 863–78.

Jung, H. S., Komatsu, S., Ikebe, M. and Craig, R. (2008). Head-head and head-tail interaction: a general mechanism for switching off myosin II activity in cells. Mol Biol Cell, **19**, 3234–42.

Junt, T., Schulze, H., Chen, Z., Massberg, S., Goerge, T., Krueger, A., Wagner, D. D., Graf, T., Italiano, J. E., J., Shivdasani, R. A. and von Andrian, U. H. (2007). Dynamic visualization of thrombopoiesis within bone marrow. Science, **317**, 1767–70.

Kage, F., Vicente-Manzanares, M., McEwan, B. C., Kettenbach, A. N. and Higgs, H. N. (2022). Myosin II proteins are required for organization of calcium-induced actin networks upstream of mitochondrial division. Mol Biol Cell, **33**, ar63.

Kassianidou, E. and Kumar, S. (2015). A biomechanical perspective on stress fiber structure and function. Biochim Biophys Acta, **1853**, 3065–74.

Kaufmann, T. L. and Schwarz, U. S. (2020). Electrostatic and bending energies predict staggering and splaying in nonmuscle myosin II minifilaments. PLoS Comput Biol, **16**, e1007801.

Kawamoto, S., Bengur, A. R., Sellers, J. R. and Adelstein, R. S. (1989). In situ phosphorylation of human platelet myosin heavy and light chains by protein kinase C. J Biol Chem, **264**, 2258–65.

Kelkar, M., Bohec, P. and Charras, G. (2020). Mechanics of the cellular actin cortex: From signalling to shape change. Curr Opin Cell Biol, **66**, 69–78.

Kelley, C. A., Sellers, J. R., Gard, D. L., Bui, D., Adelstein, R. S. and Baines, I. C. (1996). Xenopus nonmuscle myosin heavy chain isoforms have different subcellular localizations and enzymatic activities. J Cell Biol, **134**, 675–87.

Kelley, M. J., Jawien, W., Ortel, T. L. and Korczak, J. F. (2000). Mutation of MYH9, encoding non-muscle myosin heavy chain A, in May-Hegglin anomaly. Nat Genet, **26**, 106–8.

Khalilgharibi, N., Fouchard, J., Asadipour, N., Barrientos, R., Duda, M., Bonfanti, A., Yonis, A., Harris, A., Mosaffa, P., Fujita, Y., Kabla, A., Mao, Y., Baum, B., Munoz, J. J., Miodownik, M. and Charras, G. (2019). Stress relaxation in epithelial monolayers is controlled by the actomyosin cortex. Nat Phys, **15**, 839–847.

Kiboku, T., Katoh, T., Nakamura, A., Kitamura, A., Kinjo, M., Murakami, Y. and Takahashi, M. (2013). Nonmuscle myosin II folds into a 10S form via two portions of tail for dynamic subcellular localization. Genes Cells, **18**, 90–109.

Kim, K. Y., Kovacs, M., Kawamoto, S., Sellers, J. R. and Adelstein, R. S. (2005). Disease-associated mutations and alternative splicing alter the enzymatic and motile activity of nonmuscle myosins II-B and II-C. J Biol Chem, **280**, 22769–75.

Kimura, K., Ito, M., Amano, M., Chihara, K., Fukata, Y., Nakafuku, M., Yamamori, B., Feng, J., Nakano, T., Okawa, K., Iwamatsu, A. and Kaibuchi, K. (1996). Regulation of myosin phosphatase by Rho and Rho-associated kinase (Rho-kinase). Science, **273**, 245–8.

Koenderink, G. H. and Paluch, E. K. (2018). Architecture shapes contractility in actomyosin networks. Curr Opin Cell Biol, **50**, 79–85.

Kolega, J. (2003). Asymmetric distribution of myosin IIB in migrating endothelial cells is regulated by a rho-dependent kinase and contributes to tail retraction. Mol Biol Cell, **14**, 4745–57.

Komatsu, S. and Ikebe, M. (2007). The phosphorylation of myosin II at the Ser1 and Ser2 is critical for normal platelet-derived growth factor induced reorganization of myosin filaments. Mol Biol Cell, **18**, 5081–5090.

Kovacs, M., Thirumurugan, K., Knight, P. J. and Sellers, J. R. (2007). Load-dependent mechanism of nonmuscle myosin 2. Proc Natl Acad Sci U S A, **104**, 9994–9.

Kovacs, M., Wang, F., Hu, A., Zhang, Y. and Sellers, J. R. (2003). Functional divergence of human cytoplasmic myosin II: kinetic characterization of the non-muscle IIA isoform. J Biol Chem, **278**, 38132–40.

Krendel, M. and Mooseker, M. S. (2005). Myosins: tails (and heads) of functional diversity. Physiology (Bethesda), **20**, 239–51.

Kuhns, D. B., Priel, D. A. L., Chu, J. and Zarember, K. A. (2015). Isolation and Functional Analysis of Human Neutrophils. Curr Protoc Immunol, **111**, 7.23.1–7.23.16.

Kunishima, S., Kojima, T., Matsushita, T., Tanaka, T., Tsurusawa, M., Furukawa, Y., Nakamura, Y., Okamura, T., Amemiya, N., Nakayama, T., Kamiya, T. and Saito, H. (2001). Mutations in the NMMHC-A gene cause autosomal dominant macrothrombocytopenia with leukocyte inclusions (May-Hegglin anomaly/Sebastian syndrome). Blood, **97**, 1147–9.

Kunishima, S., Matsushita, T., Kojima, T., Sako, M., Kimura, F., Jo, E. K., Inoue, C., Kamiya, T. and Saito, H. (2003). Immunofluorescence analysis of neutrophil nonmuscle myosin heavy chain-A in MYH9 disorders: association of subcellular localization with MYH9 mutations. Lab Invest, **83**, 115–22.

Kunishima, S. and Saito, H. (2010). Advances in the understanding of MYH9 disorders. Curr Opin Hematol, **17**, 405–10.

Lalwani, A. K., Goldstein, J. A., Kelley, M. J., Luxford, W., Castelein, C. M. and Mhatre, A. N. (2000). Human nonsyndromic hereditary deafness DFNA17 is due to a mutation in nonmuscle myosin MYH9. Am J Hum Genet, **67**, 1121–8.

Landsverk, M. L. and Epstein, H. F. (2005). Genetic analysis of myosin II assembly and organization in model organisms. Cell Mol Life Sci, **62**, 2270–82.

Landsverk, M. L., Li, S., Hutagalung, A. H., Najafov, A., Hoppe, T., Barral, J. M. and Epstein, H. F. (2007). The UNC-45 chaperone mediates sarcomere assembly through myosin degradation in Caenorhabditis elegans. J Cell Biol, **177**, 205–10.

Laporte, D., Ojkic, N., Vavylonis, D. and Wu, J. Q. (2012). alpha-Actinin and fimbrin cooperate with myosin II to organize actomyosin bundles during contractile-ring assembly. Mol Biol Cell, **23**, 3094–110.

Lee, D. H. and Goldberg, A. L. (1998). Proteasome inhibitors: valuable new tools for cell biologists. Trends Cell Biol, **8**, 397–403.

Legant, W. R., Choi, C. K., Miller, J. S., Shao, L., Gao, L., Betzig, E. and Chen, C. S. (2013). Multidimensional traction force microscopy reveals out-of-plane rotational moments about focal adhesions. Proc Natl Acad Sci U S A, **110**, 881–6.

Lehtimaki, J., Hakala, M. and Lappalainen, P. (2017a). Actin Filament Structures in Migrating Cells. Handb Exp Pharmacol, **235**, 123–152.

Lehtimaki, J. I., Fenix, A. M., Kotila, T. M., Balistreri, G., Paavolainen, L., Varjosalo, M., Burnette, D. T. and Lappalainen, P. (2017b). UNC-45a promotes myosin folding and stress fiber assembly. J Cell Biol, **216**, 4053–4072.

Lehtimäki, J. I., Rajakylä, E. K., Tojkander, S. and Lappalainen, P. (2021). Generation of stress fibers through myosin-driven reorganization of the actin cortex. eLife, **10**, e60710.

Li, Y., Li, M., Weigel, B., Mall, M., Werth, V. P. and Liu, M. L. (2020). Nuclear envelope rupture and NET formation is driven by PKCalpha-mediated lamin B disassembly. EMBO Rep, **21**, e48779.

Liang, Y. and Walczak, P. (2021). Long term intravital single cell tracking under multiphoton microscopy. J Neurosci Methods, **349**, 109042.

Liu, X., Billington, N., Shu, S., Yu, S. H., Piszczek, G., Sellers, J. R. and Korn, E. D. (2017). Effect of ATP and regulatory light-chain phosphorylation on the polymerization of mammalian nonmuscle myosin II. Proc Natl Acad Sci U S A, **114**, E6516–E6525.

Liu, X., Shu, S., Billington, N., Williamson, C. D., Yu, S., Brzeska, H., Donaldson, J. G., Sellers, J. R. and Korn, E. D. (2016). Mammalian Nonmuscle Myosin II Binds to Anionic Phospholipids with Concomitant Dissociation of the Regulatory Light Chain*. J Biol Chem, **291**, 24828–24837.

Liu, Y. J., Le Berre, M., Lautenschlaeger, F., Maiuri, P., Callan-Jones, A., Heuze, M., Takaki, T., Voituriez, R. and Piel, M. (2015). Confinement and low adhesion induce fast amoeboid migration of slow mesenchymal cells. Cell, **160**, 659–72.

Liu, Z., Ho, C. H. and Grinnell, F. (2014). The different roles of myosin IIA and myosin IIB in contraction of 3D collagen matrices by human fibroblasts. Exp Cell Res, **326**, 295–306.

Lo, C. M., Buxton, D. B., Chua, G. C., Dembo, M., Adelstein, R. S. and Wang, Y. L. (2004). Nonmuscle myosin IIb is involved in the guidance of fibroblast migration. Mol Biol Cell, **15**, 982–9.

Ludowyke, R. I., Elgundi, Z., Kranenburg, T., Stehn, J. R., Schmitz-Peiffer, C., Hughes, W. E. and Biden, T. J. (2006). Phosphorylation of nonmuscle myosin heavy chain IIA on Ser1917 is mediated by protein kinase C beta II and coincides with the onset of stimulated degranulation of RBL-2H3 mast cells. J Immunol, **177**, 1492–9.

Ma, X. and Adelstein, R. S. (2014). The role of vertebrate nonmuscle Myosin II in development and human disease. Bioarchitecture, **4**, 88–102.

Ma, X., Bao, J. and Adelstein, R. S. (2007). Loss of cell adhesion causes hydrocephalus in nonmuscle myosin II-B-ablated and mutated mice. Mol Biol Cell, **18**, 2305–12.

Ma, X., Jana, S. S., Conti, M. A., Kawamoto, S., Claycomb, W. C. and Adelstein, R. S. (2010). Ablation of nonmuscle myosin II-B and II-C reveals a role for nonmuscle myosin II in cardiac myocyte karyokinesis. Mol Biol Cell, **21**, 3952–62.

Ma, X., Kawamoto, S., Hara, Y. and Adelstein, R. S. (2004). A point mutation in the motor domain of nonmuscle myosin II-B impairs migration of distinct groups of neurons. Mol Biol Cell, **15**, 2568–79.

Ma, X., Uchida, Y., Wei, T., Liu, C., Adams, R. H., Kubota, Y., Gutkind, J. S., Mukouyama, Y. S. and Adelstein, R. S. (2020). Nonmuscle myosin 2 regulates cortical stability during sprouting angiogenesis. Mol Biol Cell, **31**, 1974–1987.

Mabuchi, I. and Okuno, M. (1977). The effect of myosin antibody on the division of starfish blastomeres. J Cell Biol, **74**, 251–63.

Marigo, V., Nigro, A., Pecci, A., Montanaro, D., Di Stazio, M., Balduini, C. L. and Savoia, A. (2004). Correlation between the clinical phenotype of MYH9-related disease and tissue distribution of class II nonmuscle myosin heavy chains. Genomics, **83**, 1125–33.

Maupin, P., Phillips, C. L., Adelstein, R. S. and Pollard, T. D. (1994). Differential localization of myosin-II isozymes in human cultured cells and blood cells. J Cell Sci, **107**, 3077–90.

McFadden, W. M., McCall, P. M., Gardel, M. L. and Munro, E. M. (2017). Filament turnover tunes both force generation and dissipation to control long-range flows in a model actomyosin cortex. PLoS Comput Biol, **13**, e1005811.

McLachlan, A. D. and Karn, J. (1983). Periodic features in the amino acid sequence of nematode myosin rod. J Mol Biol, **164**, 605–26.

Merrill, R. A., Song, J., Kephart, R. A., Klomp, A. J., Noack, C. E. and Strack, S. (2019). A robust and economical pulse-chase protocol to measure the turnover of HaloTag fusion proteins. J Biol Chem, **294**, 16164–16171.

Middelbeek, J., Kuipers, A. J., Henneman, L., Visser, D., Eidhof, I., van Horssen, R., Wieringa, B., Canisius, S. V., Zwart, W., Wessels, L. F., Sweep, F. C., Bult, P., Span, P. N., van Leeuwen, F. N. and Jalink, K. (2012). TRPM7 Is Required for Breast Tumor Cell Metastasis. Cancer Res, **72**, 4250–4261.

Mii, Y., Nakazato, K., Pack, C.-G., Ikeda, T., Sako, Y., Mochizuki, A., Taira, M. and Takada, S. (2021). Quantitative analyses reveal extracellular dynamics of Wnt ligands in *Xenopus* embryos. eLife, **10**, e55108.

Mitchell, E. J., Karn, J., Brown, D. M., Newman, A., Jakes, R. and Kendrick-Jones, J. (1989). Regulatory and essential light-chain-binding sites in myosin heavy chain subfragment-1 mapped by site-directed mutagenesis. J Mol Biol, **208**, 199–205.

Miyazaki, K., Kunishima, S., Fujii, W. and Higashihara, M. (2009). Identification of three in-frame deletion mutations in MYH9 disorders suggesting an important hot spot for small rearrangements in MYH9 exon 24. Eur J Haematol, **83**, 230–4.

Mooseker, M. and Foth, B. J. (2007). The structural and functional diversity of the myosin family of actin-based molecular motors. *In* Myosins: A Superfamily of Molecular Motors., pp. 1–34. L.M. Coluccio, editor. Watertown: Springer.

Moreno-Arotzena, O., Borau, C., Movilla, N., Vicente-Manzanares, M. and Garcia-Aznar, J. M. (2015). Fibroblast Migration in 3D is Controlled by Haptotaxis in a Non-muscle Myosin II-Dependent Manner. Ann Biomed Eng, **43**, 3025–39.

Mori, K., Furusawa, T., Okubo, T., Inoue, T., Ikawa, S., Yanai, N., Mori, K. J. and Obinata, M. (2003). Genome structure and differential expression of two isoforms of a novel PDZ-containing myosin (MysPDZ) (Myo18A). J Biochem, **133**, 405–13.

Morin, N. A., Oakes, P. W., Hyun, Y. M., Lee, D., Chin, Y. E., King, M. R., Springer, T. A., Shimaoka, M., Tang, J. X., Reichner, J. S. and Kim, M. (2008). Nonmuscle myosin heavy chain IIA mediates integrin LFA-1 de-adhesion during T lymphocyte migration. J Exp Med, **205**, 195–205.

Morone, N., Fujiwara, T., Murase, K., Kasai, R. S., Ike, H., Yuasa, S., Usukura, J. and Kusumi, A. (2006). Three-dimensional reconstruction of the membrane skeleton at the plasma membrane interface by electron tomography. J Cell Biol, **174**, 851–62.

Moussavi, R. S., Kelley, C. A. and Adelstein, R. S. (1993). Phosphorylation of vertebrate nonmuscle and smooth muscle myosin heavy chains and light chains. Mol Cell Biochem, **127-128**, 219–27.

Mukhina, S., Wang, Y. L. and Murata-Hori, M. (2007). Alpha-actinin is required for tightly regulated remodeling of the actin cortical network during cytokinesis. Dev Cell, **13**, 554–65.

Murrell, M. P. and Gardel, M. L. (2012). F-actin buckling coordinates contractility and severing in a biomimetic actomyosin cortex. Proc Natl Acad Sci U S A, **109**, 20820–5.

Nagy, A., Takagi, Y., Billington, N., Sun, S. A., Hong, D. K., Homsher, E., Wang, A. and Sellers, J. R. (2013). Kinetic characterization of nonmuscle myosin IIb at the single molecule level. J Biol Chem, **288**, 709–22.

Nakasawa, T., Takahashi, M., Matsuzawa, F., Aikawa, S., Togashi, Y., Saitoh, T., Yamagishi, A. and Yazawa, M. (2005). Critical regions for assembly of vertebrate nonmuscle myosin II. Biochemistry, **44**, 174–83.

Neubert, E., Meyer, D., Rocca, F., Gunay, G., Kwaczala-Tessmann, A., Grandke, J., Senger-Sander, S., Geisler, C., Egner, A., Schon, M. P., Erpenbeck, L. and Kruss, S. (2018). Chromatin swelling drives neutrophil extracellular trap release. Nat Commun, **9**, 3767.

Nishikawa, M., Sellers, J. R., Adelstein, R. S. and Hidaka, H. (1984). Protein kinase C modulates in vitro phosphorylation of the smooth muscle heavy meromyosin by myosin light chain kinase. J Biol Chem, **259**, 8808–14.

Obenauer, J. C., Cantley, L. C. and Yaffe, M. B. (2003). Scansite 2.0: Proteome-wide prediction of cell signaling interactions using short sequence motifs. Nucleic Acids Res, **31**, 3635–41.

Pal, K., Nowak, R., Billington, N., Liu, R., Ghosh, A., Sellers, J. R. and Fowler, V. M. (2020). Megakaryocyte migration defects due to nonmuscle myosin IIA mutations underlie thrombocytopenia in MYH9-related disease. Blood, **135**, 1887–1898.

Park, I., Han, C., Jin, S., Lee, B., Choi, H., Kwon, J. T., Kim, D., Kim, J., Lifirsu, E., Park, W. J., Park, Z. Y., Kim, D. H. and Cho, C. (2011). Myosin regulatory light chains are required to maintain the stability of myosin II and cellular integrity. Biochem J, **434**, 171–80.

Parker, F. and Peckham, M. (2020). Disease mutations in striated muscle myosins. Biophys Rev, **12**, 887–894.

Patterson, G. H., Knobel, S. M., Sharif, W. D., Kain, S. R. and Piston, D. W. (1997). Use of the green fluorescent protein and its mutants in quantitative fluorescence microscopy. Biophys J, **73**, 2782–90.

Pecci, A., Biino, G., Fierro, T., Bozzi, V., Mezzasoma, A., Noris, P., Ramenghi, U., Loffredo, G., Fabris, F., Momi, S., Magrini, U., Pirastu, M., Savoia, A., Balduini, C., Gresele, P. and Italian Registry for, M. Y. H. r. d. (2012). Alteration of liver enzymes is a feature of the MYH9-related disease syndrome. PLoS One, **7**, e35986.

Pecci, A., Canobbio, I., Balduini, A., Stefanini, L., Cisterna, B., Marseglia, C., Noris, P., Savoia, A., Balduini, C. L. and Torti, M. (2005). Pathogenetic mechanisms of hematological abnormalities of patients with MYH9 mutations. Hum Mol Genet, **14**, 3169–78.

Pecci, A., Klersy, C., Gresele, P., Lee, K. J., De Rocco, D., Bozzi, V., Russo, G., Heller, P. G., Loffredo, G., Ballmaier, M., Fabris, F., Beggiato, E., Kahr, W. H., Pujol-Moix, N., Platokouki, H., Van Geet, C., Noris, P., Yerram, P., Hermans, C., Gerber, B., Economou, M., De Groot, M., Zieger, B., De Candia, E., Fraticelli, V., Kersseboom, R., Piccoli, G. B., Zimmermann, S., Fierro, T., Glembotsky, A. C., Vianello, F., Zaninetti, C., Nicchia, E., Guthner, C., Baronci, C., Seri, M., Knight, P. J., Balduini, C. L. and Savoia, A. (2014). MYH9-related disease: a novel

prognostic model to predict the clinical evolution of the disease based on genotype-phenotype correlations. Hum Mutat, **35**, 236–47.

Pecci, A., Ma, X., Savoia, A. and Adelstein, R. S. (2018). MYH9: Structure, functions and role of non-muscle myosin IIA in human disease. Gene, **664**, 152–167.

Pecci, A., Malara, A., Badalucco, S., Bozzi, V., Torti, M., Balduini, C. L. and Balduini, A. (2009). Megakaryocytes of patients with MYH9-related thrombocytopenia present an altered proplatelet formation. Thromb Haemost, **102**, 90–6.

Pecci, A., Panza, E., Pujol-Moix, N., Klersy, C., Di Bari, F., Bozzi, V., Gresele, P., Lethagen, S., Fabris, F., Dufour, C., Granata, A., Doubek, M., Pecoraro, C., Koivisto, P. A., Heller, P. G., Iolascon, A., Alvisi, P., Schwabe, D., De Candia, E., Rocca, B., Russo, U., Ramenghi, U., Noris, P., Seri, M., Balduini, C. L. and Savoia, A. (2008). Position of nonmuscle myosin heavy chain IIA (NMMHC-IIA) mutations predicts the natural history of MYH9-related disease. Hum Mutat, **29**, 409–17.

Pellegrin, S. and Mellor, H. (2007). Actin stress fibres. J Cell Sci, **120**, 3491–9.

Petersen, N. O., Hoddelius, P. L., Wiseman, P. W., Seger, O. and Magnusson, K. E. (1993). Quantitation of membrane receptor distributions by image correlation spectroscopy: concept and application. Biophys J, **65**, 1135–46.

Ponti, A., Machacek, M., Gupton, S. L., Waterman-Storer, C. M. and Danuser, G. (2004). Two distinct actin networks drive the protrusion of migrating cells. Science, **305**, 1782–6.

Price, M. G., Landsverk, M. L., Barral, J. M. and Epstein, H. F. (2002). Two mammalian UNC-45 isoforms are related to distinct cytoskeletal and muscle-specific functions. J Cell Sci, **115**, 4013–23.

Raab, M., Swift, J., Dingal, P. C., Shah, P., Shin, J. W. and Discher, D. E. (2012). Crawling from soft to stiff matrix polarizes the cytoskeleton and phosphoregulates myosin-II heavy chain. J Cell Biol, **199**, 669–83.

Rafiq, N. B. M., Grenci, G., Lim, C. K., Kozlov, M. M., Jones, G. E., Viasnoff, V. and Bershadsky, A. D. (2019a). Forces and constraints controlling podosome assembly and disassembly. Philos Trans R Soc Lond B Biol Sci, **374**, 20180228.

Rafiq, N. B. M., Nishimura, Y., Plotnikov, S. V., Thiagarajan, V., Zhang, Z., Shi, S., Natarajan, M., Viasnoff, V., Kanchanawong, P., Jones, G. E. and Bershadsky, A. D. (2019b). A mechano-signalling network linking microtubules, myosin IIA filaments and integrin-based adhesions. Nat Mater, **18**, 638–649.

Reichl, E. M., Ren, Y., Morphew, M. K., Delannoy, M., Effler, J. C., Girard, K. D., Divi, S., Iglesias, P. A., Kuo, S. C. and Robinson, D. N. (2008). Interactions between myosin and actin crosslinkers control cytokinesis contractility dynamics and mechanics. Curr Biol, **18**, 471–80.

Remijsen, Q., Vanden Berghe, T., Wirawan, E., Asselbergh, B., Parthoens, E., De Rycke, R., Noppen, S., Delforge, M., Willems, J. and Vandenabeele, P. (2011). Neutrophil extracellular trap cell death requires both autophagy and superoxide generation. Cell Res, **21**, 290–304.

Reymann, A. C., Boujemaa-Paterski, R., Martiel, J. L., Guerin, C., Cao, W., Chin, H. F., De La Cruz, E. M., Thery, M. and Blanchoin, L. (2012). Actin network architecture can determine myosin motor activity. Science, **336**, 1310–4.

Ricketson, D., Johnston, C. A. and Prehoda, K. E. (2010). Multiple tail domain interactions stabilize nonmuscle myosin II bipolar filaments. Proc Natl Acad Sci U S A, **107**, 20964–9.

Riedl, J., Crevenna, A. H., Kessenbrock, K., Yu, J. H., Neukirchen, D., Bista, M., Bradke, F., Jenne, D., Holak, T. A., Werb, Z., Sixt, M. and Wedlich-Soldner, R. (2008). Lifeact: a versatile marker to visualize F-actin. Nat Methods, **5**, 605–7.

Rosenfeld, S. S., Xing, J., Chen, L. Q. and Sweeney, H. L. (2003). Myosin IIb is unconventionally conventional. J Biol Chem, **278**, 27449–55.

Salbreux, G., Charras, G. and Paluch, E. (2012). Actin cortex mechanics and cellular morphogenesis. Trends Cell Biol, **22**, 536–45.

Salzameda, B., Facemyer, K. C., Beck, B. W. and Cremo, C. R. (2006). The N-terminal lobes of both regulatory light chains interact with the tail domain in the 10 S-inhibited conformation of smooth muscle myosin. J Biol Chem, **281**, 38801–11.

Sandquist, J. C. and Means, A. R. (2008). The C-terminal tail region of nonmuscle myosin II directs isoform-specific distribution in migrating cells. Mol Biol Cell, **19**, 5156–67.

Sanger, J. W., Kang, S., Siebrands, C. C., Freeman, N., Du, A., Wang, J., Stout, A. L. and Sanger, J. M. (2005). How to build a myofibril. J Muscle Res Cell Motil, **26**, 343–54.

Saposnik, B., Binard, S., Fenneteau, O., Nurden, A., Nurden, P., Hurtaud-Roux, M. F., Schlegel, N. and French, M. Y. H. n. (2014). Mutation spectrum and genotype-phenotype correlations in a large French cohort of MYH9-Related Disorders. Mol Genet Genomic Med, **2**, 297–312.

Savoia, A., De Rocco, D., Panza, E., Bozzi, V., Scandellari, R., Loffredo, G., Mumford, A., Heller, P. G., Noris, P., De Groot, M. R., Giani, M., Freddi, P., Scognamiglio, F., Riondino, S., Pujol-Moix, N., Fabris, F., Seri, M., Balduini, C. L. and Pecci, A. (2010). Heavy chain myosin 9-related disease (MYH9 -RD): neutrophil inclusions of myosin-9 as a pathognomonic sign of the disorder. Thromb Haemost, **103**, 826–32.

Savoia, A., De Rocco, D. and Pecci, A. (2017). MYH9 gene mutations associated with bleeding. Platelets, **28**, 312–315.

Schiffhauer, E. S., Luo, T., Mohan, K., Srivastava, V., Qian, X., Griffis, E. R., Iglesias, P. A. and Robinson, D. N. (2016). Mechanoaccumulative Elements of the Mammalian Actin Cytoskeleton. Curr Biol, **26**, 1473–1479.

Schiffhauer, E. S., Ren, Y., Iglesias, V. A., Kothari, P., Iglesias, P. A. and Robinson, D. N. (2019). Myosin IIB assembly state determines its mechanosensitive dynamics. J Cell Biol, **218**, 895–908.

Schindelin, J., Arganda-Carreras, I., Frise, E., Kaynig, V., Longair, M., Pietzsch, T., Preibisch, S., Rueden, C., Saalfeld, S., Schmid, B., Tinevez, J. Y., White, D. J., Hartenstein, V., Eliceiri, K., Tomancak, P. and Cardona, A. (2012). Fiji: an open-source platform for biological-image analysis. Nat Methods, **9**, 676–82.

Schneider, C. A., Rasband, W. S. and Eliceiri, K. W. (2012). NIH Image to ImageJ: 25 years of image analysis. Nat Methods, **9**, 671–5.

Scholey, J. M., Taylor, K. A. and Kendrick-Jones, J. (1980). Regulation of non-muscle myosin assembly by calmodulin-dependent light chain kinase. Nature, **287**, 233–5.

Schramek, D., Sendoel, A., Segal, J. P., Beronja, S., Heller, E., Oristian, D., Reva, B. and Fuchs, E. (2014). Direct in vivo RNAi screen unveils myosin IIa as a tumor suppressor of squamous cell carcinomas. Science, **343**, 309–13.

Sellers, J. R. (2000). Myosins: a diverse superfamily. Biochim Biophys Acta, **1496**, 3–22.

Seri, M., Cusano, R., Gangarossa, S., Caridi, G., Bordo, D., Lo Nigro, C., Ghiggeri, G. M., Ravazzolo, R., Savino, M., Del Vecchio, M., d'Apolito, M., Iolascon, A., Zelante, L. L., Savoia,

A., Balduini, C. L., Noris, P., Magrini, U., Belletti, S., Heath, K. E., Babcock, M., Glucksman, M. J., Aliprandis, E., Bizzaro, N., Desnick, R. J. and Martignetti, J. A. (2000). Mutations in MYH9 result in the May-Hegglin anomaly, and Fechtner and Sebastian syndromes. The May-Hegglin/Fechtner Syndrome Consortium. Nat Genet, **26**, 103–5.

Seri, M., Pecci, A., Di Bari, F., Cusano, R., Savino, M., Panza, E., Nigro, A., Noris, P., Gangarossa, S., Rocca, B., Gresele, P., Bizzaro, N., Malatesta, P., Koivisto, P. A., Longo, I., Musso, R., Pecoraro, C., Iolascon, A., Magrini, U., Rodriguez Soriano, J., Renieri, A., Ghiggeri, G. M., Ravazzolo, R., Balduini, C. L. and Savoia, A. (2003). MYH9-related disease: May-Hegglin anomaly, Sebastian syndrome, Fechtner syndrome, and Epstein syndrome are not distinct entities but represent a variable expression of a single illness. Medicine (Baltimore), **82**, 203–15.

Shin, J. W., Buxboim, A., Spinler, K. R., Swift, J., Christian, D. A., Hunter, C. A., Leon, C., Gachet, C., Dingal, P. C., Ivanovska, I. L., Rehfeldt, F., Chasis, J. A. and Discher, D. E. (2014). Contractile forces sustain and polarize hematopoiesis from stem and progenitor cells. Cell Stem Cell, **14**, 81–93.

Shin, J. W., Swift, J., Spinler, K. R. and Discher, D. E. (2011). Myosin-II inhibition and soft 2D matrix maximize multinucleation and cellular projections typical of platelet-producing megakaryocytes. Proc Natl Acad Sci U S A, **108**, 11458–63.

Shutova, M. S., Asokan, S. B., Talwar, S., Assoian, R. K., Bear, J. E. and Svitkina, T. M. (2017). Self-sorting of nonmuscle myosins IIA and IIB polarizes the cytoskeleton and modulates cell motility. J Cell Biol, **216**, 2877–2889.

Shutova, M. S. and Svitkina, T. M. (2018). Mammalian nonmuscle myosin II comes in three flavors. Biochem Biophys Res Commun, **506**, 394–402.

Smith, A., Bracke, M., Leitinger, B., Porter, J. C. and Hogg, N. (2003). LFA-1-induced T cell migration on ICAM-1 involves regulation of MLCK-mediated attachment and ROCK-dependent detachment. J Cell Sci, **116**, 3123–33.

Spinler, K. R., Shin, J. W., Lambert, M. P. and Discher, D. E. (2015). Myosin-II repression favors pre/proplatelets but shear activation generates platelets and fails in macrothrombocytopenia. Blood, **125**, 525–33.

Spira, F., Cuylen-Haering, S., Mehta, S., Samwer, M., Reversat, A., Verma, A., Oldenbourg, R., Sixt, M. and Gerlich, D. W. (2017). Cytokinesis in vertebrate cells initiates by contraction of an equatorial actomyosin network composed of randomly oriented filaments. eLife, **6**, e30867.

Sprague, B. L., Pego, R. L., Stavreva, D. A. and McNally, J. G. (2004). Analysis of binding reactions by fluorescence recovery after photobleaching. Biophys J, **86**, 3473–95.

Spudich, J. A. (2001). The myosin swinging cross-bridge model. Nat Rev Mol Cell Biol, **2**, 387–92.

Srikakulam, R., Liu, L. and Winkelmann, D. A. (2008). Unc45b forms a cytosolic complex with Hsp90 and targets the unfolded myosin motor domain. PLoS One, **3**, e2137.

Sunstrom, N. A., Baig, M., Cheng, L., Payet Sugyiono, D. and Gray, P. (1998). Recombinant insulin-like growth factor-I (IGF-I) production in Super-CHO results in the expression of IGF-I receptor and IGF binding protein 3. Cytotechnology, **28**, 91–100.

Suzuki, H., Onishi, H., Takahashi, K. and Watanabe, S. (1978). Structure and function of chicken gizzard myosin. J Biochem, **84**, 1529–42.

Suzuki, H., Stafford, W. F., r., Slayter, H. S. and Seidel, J. C. (1985). A conformational transition in gizzard heavy meromyosin involving the head-tail junction, resulting in changes in sedimentation coefficient, ATPase activity, and orientation of heads. J Biol Chem, **260**, 14810–7.

Svitkina, T. M., Verkhovsky, A. B., McQuade, K. M. and Borisy, G. G. (1997). Analysis of the actin-myosin II system in fish epidermal keratocytes: mechanism of cell body translocation. J Cell Biol, **139**, 397–415.

Szymanski, P. T. and Goyal, R. K. (1999). Calponin binds to the 20-kilodalton regulatory light chain of myosin. Biochemistry, **38**, 3778–84.

Tabibzadeh, N., Fleury, D., Labatut, D., Bridoux, F., Lionet, A., Jourde-Chiche, N., Vrtovsnik, F., Schlegel, N. and Vanhille, P. (2019). MYH9-related disorders display heterogeneous kidney involvement and outcome. Clin Kidney J, **12**, 494–502.

Takeda, K., Kishi, H., Ma, X., Yu, Z. X. and Adelstein, R. S. (2003). Ablation and mutation of nonmuscle myosin heavy chain II-B results in a defect in cardiac myocyte cytokinesis. Circ Res, **93**, 330–7.

Takei, H., Araki, A., Watanabe, H., Ichinose, A. and Sendo, F. (1996). Rapid killing of human neutrophils by the potent activator phorbol 12-myristate 13-acetate (PMA) accompanied by changes different from typical apoptosis or necrosis. J Leukoc Biol, **59**, 229–40.

Talayero, V. C. and Vicente-Manzanares, M. (2021). Multiparametric Analysis of Focal Adhesions in Bidimensional Substrates. Methods Mol Biol, **2217**, 27–37.

Tan, I., Yong, J., Dong, J. M., Lim, L. and Leung, T. (2008). A tripartite complex containing MRCK modulates lamellar actomyosin retrograde flow. Cell, **135**, 123–36.

Taneja, N., Bersi, M. R., Baillargeon, S. M., Fenix, A. M., Cooper, J. A., Ohi, R., Gama, V., Merryman, W. D. and Burnette, D. T. (2020). Precise Tuning of Cortical Contractility Regulates Cell Shape during Cytokinesis. Cell Rep, **31**, 107477.

Taneja, N. and Burnette, D. T. (2019). Myosin IIA drives membrane bleb retraction. Mol Biol Cell, **30**, 1051–1059.

Thebault, S., Alexander, R. T., Tiel Groenestege, W. M., Hoenderop, J. G. and Bindels, R. J. (2009). EGF increases TRPM6 activity and surface expression. J Am Soc Nephrol, **20**, 78–85.

Thiam, H. R., Wong, S. L., Qiu, R., Kittisopikul, M., Vahabikashi, A., Goldman, A. E., Goldman, R. D., Wagner, D. D. and Waterman, C. M. (2020). NETosis proceeds by cytoskeleton and endomembrane disassembly and PAD4-mediated chromatin decondensation and nuclear envelope rupture. Proc Natl Acad Sci U S A, **117**, 7326–7337.

Thomas, D. G., Yenepalli, A., Denais, C. M., Rape, A., Beach, J. R., Wang, Y. L., Schiemann, W. P., Baskaran, H., Lammerding, J. and Egelhoff, T. T. (2015). Non-muscle myosin IIB is critical for nuclear translocation during 3D invasion. J Cell Biol, **210**, 583–94.

Tojkander, S., Gateva, G., Husain, A., Krishnan, R. and Lappalainen, P. (2015). Generation of contractile actomyosin bundles depends on mechanosensitive actin filament assembly and disassembly. Elife, **4**, e06126.

Tojkander, S., Gateva, G. and Lappalainen, P. (2012). Actin stress fibers–assembly, dynamics and biological roles. J Cell Sci, **125**, 1855–64.

Trybus, K. M. and Lowey, S. (1984). Conformational states of smooth muscle myosin. Effects of light chain phosphorylation and ionic strength. J Biol Chem, **259**, 8564–71.

Tullio, A. N., Accili, D., Ferrans, V. J., Yu, Z. X., Takeda, K., Grinberg, A., Westphal, H., Preston, Y. A. and Adelstein, R. S. (1997). Nonmuscle myosin II-B is required for normal development of the mouse heart. Proc Natl Acad Sci U S A, **94**, 12407–12.

Tullio, A. N., Bridgman, P. C., Tresser, N. J., Chan, C. C., Conti, M. A., Adelstein, R. S. and

Hara, Y. (2001). Structural abnormalities develop in the brain after ablation of the gene encoding nonmuscle myosin II-B heavy chain. J Comp Neurol, **433**, 62–74.

Tuzovic, L., Yu, L., Zeng, W., Li, X., Lu, H., Lu, H. M., Gonzalez, K. D. and Chung, W. K. (2013). A human de novo mutation in MYH10 phenocopies the loss of function mutation in mice. Rare Dis, **1**, e26144.

van Leeuwen, F. N., van Delft, S., Kain, H. E., van der Kammen, R. A. and Collard, J. G. (1999). Rac regulates phosphorylation of the myosin-II heavy chain, actinomyosin disassembly and cell spreading. Nat Cell Biol, **1**, 242–8.

Vasquez, C. G., Heissler, S. M., Billington, N., Sellers, J. R. and Martin, A. C. (2016). Drosophila non-muscle myosin II motor activity determines the rate of tissue folding. Elife, **5**, e20828.

Verver, E. J., Topsakal, V., Kunst, H. P., Huygen, P. L., Heller, P. G., Pujol-Moix, N., Savoia, A., Benazzo, M., Fierro, T., Grolman, W., Gresele, P. and Pecci, A. (2016). Nonmuscle Myosin Heavy Chain IIA Mutation Predicts Severity and Progression of Sensorineural Hearing Loss in Patients With MYH9-Related Disease. Ear Hear, **37**, 112–20.

Vicente-Manzanares, M. and Horwitz, A. R. (2010). Myosin light chain mono- and diphosphorylation differentially regulate adhesion and polarity in migrating cells. Biochem Biophys Res Commun, **402**, 537–42.

Vicente-Manzanares, M., Koach, M. A., Whitmore, L., Lamers, M. L. and Horwitz, A. F. (2008). Segregation and activation of myosin IIB creates a rear in migrating cells. J Cell Biol, **183**, 543–54.

Vicente-Manzanares, M., Newell-Litwa, K., Bachir, A. I., Whitmore, L. A. and Horwitz, A. R. (2011). Myosin IIA/IIB restrict adhesive and protrusive signaling to generate front-back polarity in migrating cells. J Cell Biol, **193**, 381–96.

Vicente-Manzanares, M., Zareno, J., Whitmore, L., Choi, C. K. and Horwitz, A. F. (2007). Regulation of protrusion, adhesion dynamics, and polarity by myosins IIA and IIB in migrating cells. J Cell Biol, **176**, 573–80.

Vogel, S. K., Petrasek, Z., Heinemann, F. and Schwille, P. (2013). Myosin motors fragment and compact membrane-bound actin filaments. Elife, **2**, e00116.

Voudouri, K., Berdiaki, A., Tzardi, M., Tzanakakis, G. N. and Nikitovic, D. (2015). Insulin-like growth factor and epidermal growth factor signaling in breast cancer cell growth: focus on endocrine resistant disease. Anal Cell Pathol (Amst), **2015**, 975495.

Wang, A., Ma, X., Conti, M. A. and Adelstein, R. S. (2011). Distinct and redundant roles of the non-muscle myosin II isoforms and functional domains. Biochem Soc Trans, **39**, 1131–5.

Wang, Y., Li, M., Stadler, S., Correll, S., Li, P., Wang, D., Hayama, R., Leonelli, L., Han, H., Grigoryev, S. A., Allis, C. D. and Coonrod, S. A. (2009). Histone hypercitrullination mediates chromatin decondensation and neutrophil extracellular trap formation. J Cell Biol, **184**, 205–13.

Watanabe, T., Hosoya, H. and Yonemura, S. (2007). Regulation of myosin II dynamics by phosphorylation and dephosphorylation of its light chain in epithelial cells. Mol Biol Cell, **18**, 605–16.

Webb, D. J., Donais, K., Whitmore, L. A., Thomas, S. M., Turner, C. E., Parsons, J. T. and Horwitz, A. F. (2004). FAK-Src signalling through paxillin, ERK and MLCK regulates adhesion disassembly. Nat Cell Biol, **6**, 154–61.

Weissenbruch, K., Fladung, M., Grewe, J., Baulesch, L., Schwarz, U. S. and Bastmeyer, M. (2022). Nonmuscle myosin IIA dynamically guides regulatory light chain phosphorylation and assembly of nonmuscle myosin IIB. Eur J Cell Biol, **101**, 151213.

Weissenbruch, K., Grewe, J., Hippler, M., Fladung, M., Tremmel, M., Stricker, K., Schwarz, U. S. and Bastmeyer, M. (2021). Distinct roles of nonmuscle myosin II isoforms for establishing tension and elasticity during cell morphodynamics. Elife, **10**, e71888.

Wendt, T., Taylor, D., Messier, T., Trybus, K. M. and Taylor, K. A. (1999). Visualization of head-head interactions in the inhibited state of smooth muscle myosin. J Cell Biol, **147**, 1385–90.

Wiedenmann, J., Ivanchenko, S., Oswald, F., Schmitt, F., Rocker, C., Salih, A., Spindler, K. D. and Nienhaus, G. U. (2004). EosFP, a fluorescent marker protein with UV-inducible green-to-red fluorescence conversion. Proc Natl Acad Sci U S A, **101**, 15905–10.

Wilson, C. A., Tsuchida, M. A., Allen, G. M., Barnhart, E. L., Applegate, K. T., Yam, P. T., Ji, L., Keren, K., Danuser, G. and Theriot, J. A. (2010). Myosin II contributes to cell-scale actin network treadmilling through network disassembly. Nature, **465**, 373–7.

Wiseman, P. W. and Petersen, N. O. (1999). Image correlation spectroscopy. II. Optimization for ultrasensitive detection of preexisting platelet-derived growth factor-beta receptor oligomers on intact cells. Biophys J, **76**, 963–77.

Wohlgemuth, S. L., Crawford, B. D. and Pilgrim, D. B. (2007). The myosin co-chaperone UNC-45 is required for skeletal and cardiac muscle function in zebrafish. Dev Biol, **303**, 483–92.

Wong, A. J., Pollard, T. D. and Herman, I. M. (1983). Actin filament stress fibers in vascular endothelial cells in vivo. Science, **219**, 867–9.

Yamamoto, K., Otomo, K., Nemoto, T., Ishihara, S., Haga, H., Nagasaki, A., Murakami, Y. and Takahashi, M. (2019). Differential contributions of nonmuscle myosin IIA and IIB to cytokinesis in human immortalized fibroblasts. Exp Cell Res, **376**, 67–76.

Yang, S., Lee, K. H., Woodhead, J. L., Sato, O., Ikebe, M. and Craig, R. (2019). The central role of the tail in switching off 10S myosin II activity. J Gen Physiol, **151**, 1081–1093.

Yang, S., Tiwari, P., Lee, K. H., Sato, O., Ikebe, M., Padron, R. and Craig, R. (2020). Cryo-EM structure of the inhibited (10S) form of myosin II. Nature, **588**, 521–525.

Zhang, H., Webb, D. J., Asmussen, H. and Horwitz, A. (2003). Synapse formation is regulated by the signaling adaptor GIT1. J Cell Biol, **161**, 131–142.

Zhang, Y., Chen, K., Sloan, S. A., Bennett, M. L., Scholze, A. R., O'Keeffe, S., Phatnani, H. P., Guarnieri, P., Caneda, C., Ruderisch, N., Deng, S., Liddelow, S. A., Zhang, C., Daneman, R., Maniatis, T., Barres, B. A. and Wu, J. Q. (2014). An RNA-sequencing transcriptome and splicing database of glia, neurons, and vascular cells of the cerebral cortex. J Neurosci, **34**, 11929–47.

Zhang, Y., Liu, C., Adelstein, R. S. and Ma, X. (2018). Replacing nonmuscle myosin 2A with myosin 2C1 permits gastrulation but not placenta vascular development in mice. Mol Biol Cell, **29**, 2326–2335.